Departamento de Física Atómica, Molecular y Nuclear
Facultad de Ciencias Físicas
Universidad Complutense de Madrid

SECCIONES EFICACES, OBSERVABLES DE POLARIZACIÓN Y RESPUESTAS NUCLEARES EN REACCIONES $A(\vec{e}, e'\vec{p})B$

Memoria de Tesis Doctoral realizada por
Javier Rodríguez Vignote
para optar al grado de Doctor en Física

Trabajo dirigido por el profesor *D. José Manuel Udías Moinelo*

MADRID 2005

Índice General

Capítulo 1

Introducción, estado actual de los estudios de $(\vec{e}, e'\vec{p})$ y objetivos

La dispersión de electrones por núcleos es uno de los métodos más eficaces, y por tanto más usado, para estudiar la estructura nuclear [1–5]. El bombardeo de núcleos con haces de electrones para obtener secciones eficaces de dispersión u otros observables, permite conocer con gran detalle la constitución interna de los núcleos y cómo están distribuidos en ellos los nucleones.

Las ventajas de la utilización de electrones como proyectiles son principalmente las que siguen:

1. Las sondas leptónicas, al no sufrir la interacción fuerte, atraviesan el interior de los núcleos perturbándolos apenas. El estudio de la estructura nuclear mediante el bombardeo de partículas cuya principal interacción con el núcleo es la fuerte, tiene la desventaja añadida de enmascarar el objeto del estudio con efectos propios de la reacción en sí. En este sentido, es claro que el paso de un leptón por el interior del núcleo es más "limpio" y como sonda, los electrones son, por tanto, mucho más adecuados.

2. La interacción principal que rige un proceso de dispersión electrón-núcleo es la interacción electromagnética. De nuevo esto es una ventaja, ya que la teoría que describe este tipo de interacción, la electrodinámica cuántica, es bien conocida y permite resolver de forma exacta la parte de la reacción correspondiente al proyectil, o dicho con otras palabras, conocer con la precisión deseada lo que sucede en el vértice leptónico.

De igual modo, la electrodinámica cuántica admite un tratamiento perturbativo, dado que viene caracterizada por una constante de acoplamiento, α, cuyo valor es relativamente pequeño ($\alpha \simeq \frac{1}{137}$). Gracias al pequeño valor de la constante α, se pueden describir las reacciones con electrones de forma suficientemente fiable a primer orden en teoría de perturbaciones, lo que llamaremos a partir de ahora "aproximación de Born de primer orden".

El diagrama de Feynman que caracteriza a la reacción consiste en este caso del intercambio de un único fotón entre el proyectil y el blanco, caracterizado por momento y energía transferida $\boldsymbol{q}$ y ω respectivamente. Este fotón virtual puede tener un cuadrimomento arbitrario, siempre dentro del rango $Q^2 = \boldsymbol{q}^2 - \omega^2 > 0$, lo cual permite más posibilidades de estudio que las que proporcionan fotones reales, para los cuales estamos limitados a $Q^2 = 0$.

Históricamente, las medidas elásticas de dispersión de electrones han servido para determinar los factores de forma de los nucleones y las distribuciones de carga nucleares. Dispersión elástica quiere decir que toda la energía transferida se invierte en incrementar la energía cinética del blanco sin producir ninguna excitación. El blanco permanece en el mismo estado que tenía [2]. La sección eficaz elástica tiene un pico muy marcado bajo las condiciones cinemáticas adecuadas. Para un núcleo blanco de masa M_A en reposo, la sección eficaz elástica se obtiene cuando el cuadrimomento y la energía transferida satisfacen la siguiente relación:

$$\omega = \frac{Q^2}{2M_A}\,. \tag{1.1}$$

Si fijamos un valor cualquiera del momento transferido q y vamos incrementando poco a poco el valor de la energía transferida ω, llegará un momento en que se sobrepasa la región elástica y la energía del fotón virtual que interacciona con el núcleo será suficiente para excitarlo o, incluso, desmembrarlo en dos o más componentes. Al llegar a esta zona del espectro, el número de canales o procesos que contribuyen a la sección eficaz aumentan de forma que no sólo es posible detectar simplemente el electrón dispersado, lo que llamaremos reacción (e, e'), sino también hacer medidas de secciones eficaces en las que se detectan simultáneamente el electrón dispersado y una, o más, partículas arrancadas del núcleo blanco.

Las medidas en coincidencia son más problematicas que las del tipo (e, e') debido a que tienen una tasa de conteo mucho más baja y además, para tener una buena relación señal ruido y coincidencias frente a no coincidencias (*concidence/singles rate*), precisan de un

haz de electrones de alta intensidad y elevado ciclo de trabajo, incluso aceleradores de ciclo de trabajo continuo. Estas dificultades experimentales han sido completamente resueltas en los aceleradores de electrones modernos situados en los laboratorios de Saclay [6], NIKHEF [7], Bates-MIT [8], Mainz [9] y más recientemente Jlab [10–12] y en el futuro GSI [13–15].

1.1 Dispersion $(\vec{e}, e'\vec{p})$ en condiciones exclusivas

Según el estudio que queramos realizar, interesará trabajar en un régimen de energías u otro. En esta tesis nos vamos a limitar a la llamada zona cuasielástica y, a su vez, nos centraremos en el estudio de las reacciones $(\vec{e}, e'\vec{p})$. En estas reacciones se detectan en coincidencia el electrón dispersado y un protón arrancado del núcleo blanco. A su vez, el proyectil (electrón) puede estar polarizado y se puede medir la polarización del nucleón detectado [16–18].

La región del espectro más adecuada para realizar este estudio viene caracterizada por unos valores del momento y energía transferidas tales que, obviamente, son suficientes como para arrancar un nucleón del interior del núcleo blanco, pero no tan grandes como para ser capaces de producir piones o excitación de resonancias nucleónicas, que se correspondería con una zona del espectro fuera de los objetivos de esta tesis doctoral. Esta zona del espectro se denomina "zona cuasielástica" (ver figura 1.1) y en ella se dan las condiciones adecuadas para que el fotón virtual interaccione directamente con los nucleones individuales que componen el núcleo blanco, sin ser necesario considerar los posibles grados de libertad internos de los mismos.

Mediante las sondas electromagneticas podemos seleccionar momentos transferidos con una longitud de onda de de Broglie asociada mucho menores que las del sistema nuclear, del orden o inferiores al tamaño de un nucleon. En estas condiciones, si además la relación entre la energía y el momento transferido es compatible con la dispersión elástica de fotones por nucleones, es decir, trasladamos la expresión dada por la Eq. (1.1) a nucleones en reposo:

$$\omega \simeq \frac{Q^2}{2M}\,, \tag{1.2}$$

con M ahora la masa de un nucleón, no la del núcleo blanco en su conjunto M_A como antes, estaríamos en la región elástica para nucleones libres. La contribucion de este proceso dominará ampliamente sobre todos los demás y estaremos centrándonos en la zona del

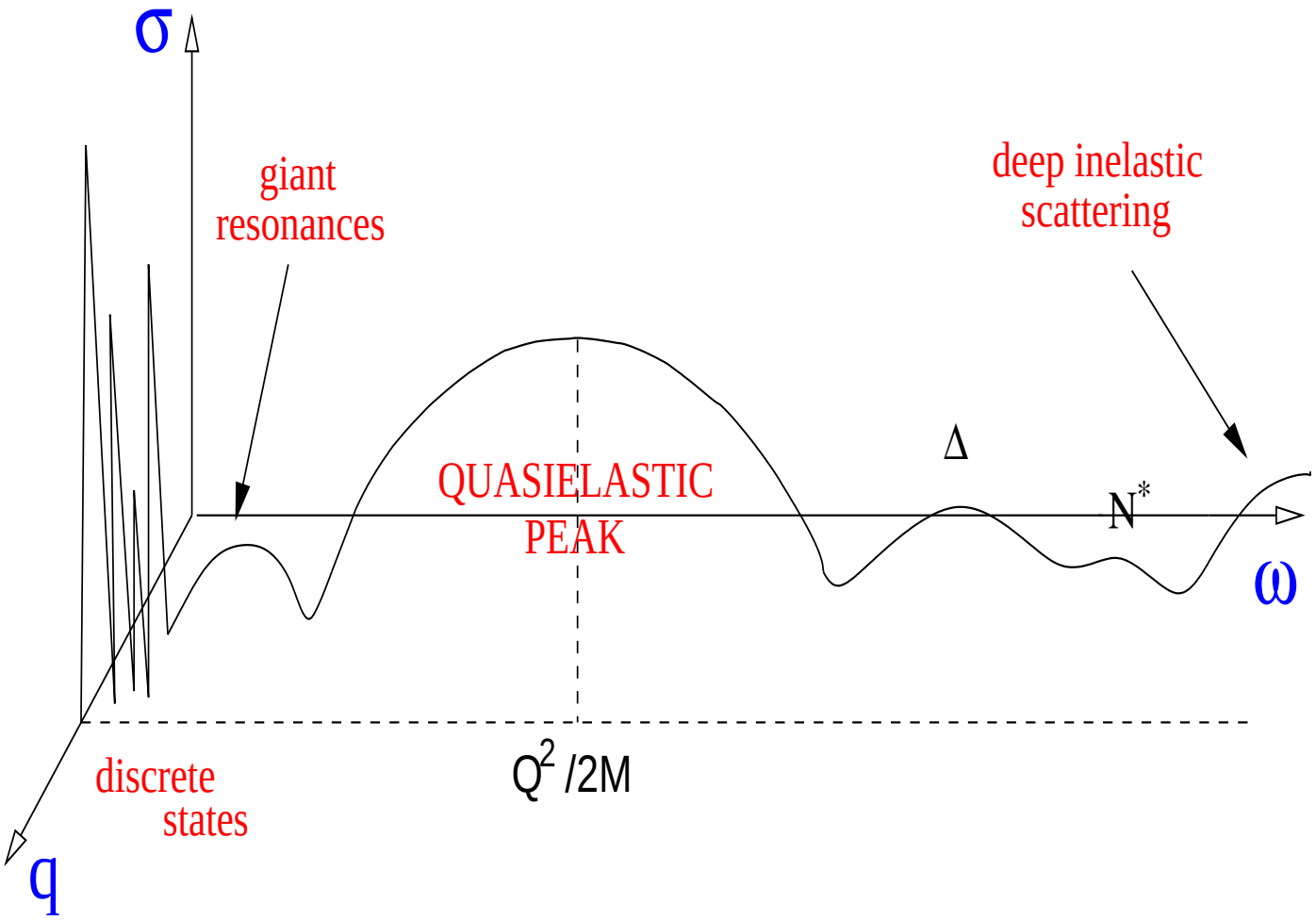

Figura 1.1: Sección eficaz de dispersión de electrones por un núcleo, frente a la energía transferida ω, para un valor fijo del momento transferido q.

espectro denominada "pico cuasielástico" [2,19]. En tal caso, la sección eficaz de la reacción vendrá caracterizada por un máximo distinto al de la zona elástica, mucho más ancho que el primero debido a que los nucleones en el interior del núcleo no están en reposo y no tienen por qué satisfacer la relación característica de toda partícula que se encuentra en la "capa de masas" (*onshell*: $E^2 = \boldsymbol{p}^2 + M^2$) [20]. Trabajar en esta zona del espectro es adecuado para determinar propiedades monoparticulares, como las predicciones del modelo de capas para las energías y funciones de onda de los nucleones. Definiendo la variable $x = \frac{Q^2}{2M\omega}$, los valores de x en torno a la unidad se corresponderán con dispersion cuasielástica de nucleones.

El experimento puede ser aún más selectivo si realizamos medidas exclusivas, es decir, medidas en las que se determinan todos los canales que contribuyen al proceso observado.

Así por ejemplo, las medidas elásticas son exclusivas porque al detectar el electrón y determinar con precisión su energía y momento, sabemos que coincide con la energía inicial menos la de retroceso del sistema nuclear y no falta ninguna energía más, es decir, no hay energía "perdida"en la reacción o *missing energy* E_m. Por tanto, al núcleo no se le ha transferido más que momento y la energía cinética adquirida se corresponde precisamente con el momento que ha ganado. El núcleo queda en el mismo estado que tenía antes de la reacción. Conocemos, pues, todo lo que ha pasado en la reacción, lo que da pie al término exclusivo.

En el caso cuasielástico, en el que se arranca un nucleón, la medida precisa de la energía del protón y del electron permite determinar cuánta energía se lleva el núcleo residual. Si dicha energía no es suficiente como para arrancar más que un nucleón, entonces sabemos con seguridad que hemos detectado las partículas suficientes (todas menos una) como para reconstruir el balance de energías y momentos. El núcleo residual no se ha fragmentado y podemos utilizar la regla de conservación de momento para, a partir del momento transferido conocido, determinar cuánta energía cinética, T_B, ha ganado el núcleo residual y, tras realizar el balance de energía, conocer cuál es la energia desaparecida E_m [19]

$$E_m = \omega - T_F - T_B + T_A = M + M_B - M_A\,, \tag{1.3}$$

con T_F (T_A) la energía cinética del nucleón detectado (blanco), respectivamente. Es decir, conocemos con precisión cuál es el estado en el que ha quedado el núcleo residual. Es, de nuevo, una medida exclusiva porque conocemos el canal preciso por el cual ha tenido lugar la reacción y el balance de energía y momento completo.

Al momento lineal del blanco, $\boldsymbol{p}_A$, menos el momento del núcleo residual, $\boldsymbol{p}_B$, que podemos determinar a partir de la conservacion del momento total, se le denomina, por analogía con la energía desaparecida, momento desaparecido (*missing momentum* $\boldsymbol{p}_m$) [1–4]. Tenemos condiciones exclusivas siempre que la energía transferida sea igual o superior a la energía de separación del primer protón – si no, no se darían las condiciones necesarias para posibilitar las reacciones $(e, e'p)$ – y además esta energía no supere el umbral a partir del cual hay energía suficiente para que, además del protón, se pueda arrancar otra partícula, o bien se fisione el núcleo, o procesos similares. En núcleos estables doblemente mágicos, normalmente el siguiente proceso en energía en el que se rompe el núcleo en más de un fragmento corresponde a aquél en que se arranca un segundo nucleón.

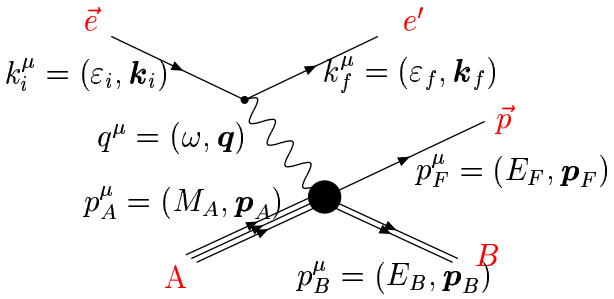

Figura 1.2: *Diagrama de Feynman del proceso $A(\vec{e}, e'\vec{p})B$ en la aproximación de Born.*

1.2 Aproximación de Impulso

Las medidas de $(e, e'p)$ en concidencia bajo condiciones exclusivas y con cinemática cuasielástica, como las que hemos descrito anteriormente, se pueden analizar con confianza en la llamada aproximación de impulso. Así se ha comprobado en numerosas y satisfactorias comparaciones de las predicciones teóricas con los datos experimentales [21–25].

La aproximación de impulso presupone que el fotón que intercambian el electrón y el blanco interacciona única y exclusivamente con un nucleón del blanco, posteriormente arrancado y detectado en coincidencia con el electrón dispersado. Los demás nucleones son meros espectadores que participan sólo a través de la posible interacción con el nucleón arrancado mientras recorre el medio nuclear antes de escapar de su influencia. Esta interacción es lo que llamaremos Interacción de Estados Finales, FSI, *Final State Interaction*.

En la aproximación de impulso, por tanto, el que hemos denominado como momento desaparecido $\boldsymbol{p}_m$, se corresponde con el momento inicial que posee el nucleón con el que interacciona el fotón en el interior del blanco. Esto implica que mediante medidas de secciones eficaces de tipo $(e, e'p)$ se puede determinar la distribución de momento de los nucleones en el interior de los núcleos.

1.3 Cinemática de los procesos $(\vec{e}, e'\vec{p})$ exclusivos

En la figura 1.2 se representa el diagrama de Feynman correspondiente a la reacción $(e, e'p)$ bajo la aproximación de Born de intercambio de un fotón. Un electrón de cuadrimomento $k_i^\mu = (\varepsilon_i, \boldsymbol{k}_i)$ intercambia un fotón $q^\mu = (\omega, \boldsymbol{q})$ con un núcleo de masa M_A y cuadrimomento $p_A^\mu = (E_A, \boldsymbol{p}_A)$. El electrón es dispersado hacia un estado final de cuadri-

momento $k_f^\mu = (\varepsilon_f, \boldsymbol{k}_f)$. A su vez, se detecta en coincidencia un protón de cuadrimomento $p_F^\mu = (E_F, \boldsymbol{p}_F)$ arrancado al núcleo blanco. Al tratarse de un proceso exclusivo sabemos, aunque no lo detectemos, que existe otra única partícula en el estado final, el núcleo residual, con cuadrimomento $p_B^\mu = (E_B, \boldsymbol{p}_B)$. Las leyes de conservación del cuadrimomento en ambos vértices y en el proceso global implican las siguientes relaciones:

$$\boldsymbol{k}_i - \boldsymbol{k}_f = \boldsymbol{q} = \boldsymbol{p}_F + \boldsymbol{p}_B - \boldsymbol{p}_A \,, \tag{1.4}$$

$$\varepsilon_i - \varepsilon_f = \omega = E_F + E_B - E_A \,. \tag{1.5}$$

A lo largo de toda la tesis presupondremos que la energía de los electrones es mucho mayor que su masa, por lo que podremos utilizar con total confianza el llamado límite ultrarrelativista para los electrones ($m_e = 0$). Bajo esta aproximación $\varepsilon_i = k_i$ y $\varepsilon_f = k_f$.

A la hora de elegir un sistema de referencia con respecto al cual fijar las variables cinemáticas, es frecuente tomar un sistema con núcleo blanco en reposo, es decir, $E_A = M_A$ y $\boldsymbol{p}_A = \boldsymbol{0}$. A su vez, el sistema de coordenadas que se emplea normalmente para la descripción del proceso suele elegirse de modo que el plano que forman los vectores $\boldsymbol{k}_i$ y $\boldsymbol{k}_f$, también llamado plano de dispersión, coincida con el plano xz. La dirección del eje z viene dada por el momento transferido $\boldsymbol{q}$. El triedro que define este sistema es entonces:

$$\boldsymbol{u}_z = \frac{\boldsymbol{q}}{q} \,, \quad \boldsymbol{u}_y = \frac{\boldsymbol{k}_i \times \boldsymbol{k}_f}{|\boldsymbol{k}_i \times \boldsymbol{k}_f|} \,, \quad \boldsymbol{u}_x = \boldsymbol{u}_y \times \boldsymbol{u}_z \,. \tag{1.6}$$

De igual modo, el momento del nucleon emitido junto con el momento transferido, definen otro plano, que se conoce como plano de dispersion del nucleón o plano de reacción. Ambos planos forman un ángulo ϕ_F entre sí, como se puede apreciar en la figura 1.3.

En los casos en que $\phi_F = 0°, 180°$, los dos planos de dispersión, el de electrones y el de nucleones, coinciden y la cinemática se denomina coplanar o "en el plano" (*in-plane*), que es la más utilizada en los experimentos.

El número N de variables cinemáticas independientes en los procesos $(e, e'p)$ es igual a seis [2]. Esto es muy sencillo de determinar a partir del número total de variables cinemáticas que definen el estado de las partículas intervinientes en la reacción y el número de cantidades conservadas impuesto por las leyes de la relatividad especial. Las masas del núcleo blanco, electrones y protón detectado son conocidas y, al tratarse de partículas "libres", necesariamente han de estar sobre la capa de masas. Por tanto, el número de variables cinemáticas necesario para determinar su cuadrimomento es de tres, en lugar de cuatro. El núcleo residual también se encuentra sobre su capa de masas, pero a diferencia

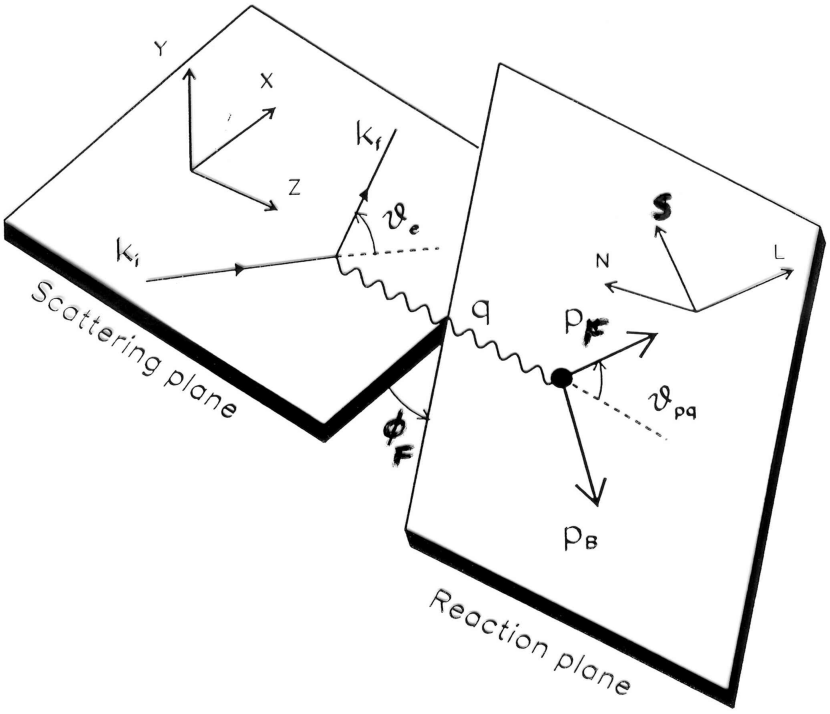

Figura 1.3: *Representación esquemática del proceso* $A(e, e'p)B$.

de las otras partículas, al no ser detectado, su masa no viene fijada *a priori*, por lo cual es un parámetro libre más y las variables cinemáticas necesarias para describir el cuadrimomento del núcleo residual son, por tanto, cuatro. Del conjunto de estas variables hay que restarle el número de parámetros conservados que caracterizan a un grupo de Lorentz-Poincaré: cuatro que corresponden a las traslaciones, tres más para las rotaciones y otros tres para los *boosts*. Tenemos pues $N = 3 \times 4 + 4 \times 1 - 10 = 6$.

Desde un punto de vista teórico es irrelevante cuáles seis, de entre todas las posibles variables cinemáticas, fijemos para determinar las demás. Varias son las elecciones más usuales. Lo más habitual, para simplificar el análisis posterior de las secciones eficaces de este proceso, es mantener constante la energía desaparecida E_m y barrer un determinado rango del momento desaparecido p_m. De este modo podemos probar hasta qué punto es fiable el modelo de capas del núcleo blanco. Fijar E_m bajo la aproximación de impulso antes descrita, es equivalente a decir que el protón detectado se encuentra en una capa determinada antes de ser arrancado del núcleo blanco. Al comparar después la sección eficaz teórica con la medida experimentalmente, observaremos en general que ambas tienen una dependencia en p_m similar, diferenciándose *grosso modo* sólo en un factor de escala. Este

factor de escala, al que denominaremos factor espectroscópico S_α, representa la desviación real entre la estructura del núcleo y el modelo de partículas independientes considerado *a priori*. Cúanto más próximo sea S_α a la unidad, más correcta será la descripción del núcleo mediante el modelo de capas elegido. Si el factor de escala es menor que la unidad, indica que no encontramos a todos los nucleones que se debiera en las condiciones seleccionadas, normalmente a la energía desaparecida compatible con arrancar el nucleón de una capa determinada. Esto implica que los nucleones no están "todo el tiempo" donde el modelo de capas indica o, dicho de otra manera, que el solape de la función de ondas del núcleo real y la del modelo de capas no es del 100%. Un factor espectroscópico cercano al 100% indica un solape amplio entre la funcion de ondas de campo medio (modelo de capas) y el núcleo real. El modelo de capas del núcleo predice con notable éxito gran parte de la fenomenología nuclear, pero hasta ahora la mejor prueba gráfica de la existencia de capas en el núcleo se ha obtenido mediante experimentos $(e, e'p)$ como se muestra en la figura 1.4 [26]. Podemos observar como las capas mas "externas", las que pueden ser exploradas en cinemáticas exclusivas, quedan perfectamente demarcadas.

De las cuatro variables que nos restan para describir completamente la cinemática de la reacción, dos elecciones lógicas son la energía del haz de electrones incidente, ε_i, y el ángulo que forman el plano de reacción con el de dispersión de electrones, ϕ_F. Lo más usual, como ya hemos dicho, es trabajar en cinemática coplanar con $\phi_F = 0°$ ó $\phi_F = 180°$. En esta tesis, salvo excepciones contadas, ésta ha sido la elección usada. Además, en las figuras a la hora de pintar la sección eficaz frente p_m, y salvo que se especifique lo contrario, hemos seguido el convenio estándar de considerar $p_m > 0$ cuando $\phi_F = 180°$ y $p_m < 0$ cuando $\phi_F = 0°$ [3].

Normalmente, para simplificar el análisis de las secciones eficaces de este proceso, se suelen fijar algunas de las variables de la cinemática y se mide la seccion eficaz (u otros observables) para la misma energía desaparecida pero variando el momento desaparecido. Esta variación del momento desaparecido puede obtenerse manteniendo el momento transferido y el momento del nucleón arrancado en la misma dirección, lo que se llama cinemática "paralela" (o "antiparalela"), con lo cual para variar el momento desaparecido se ha de variar el momento transferido. También se puede mantener el momento transferido q y la energía transferida ω fijos en el valor adecuado para mantener constante la energía desaparecida, lo que se suele denominar cinematica con q-ω constante. En los artículos y libros más antiguos, también se le denomina cinemática perpendicular [4].

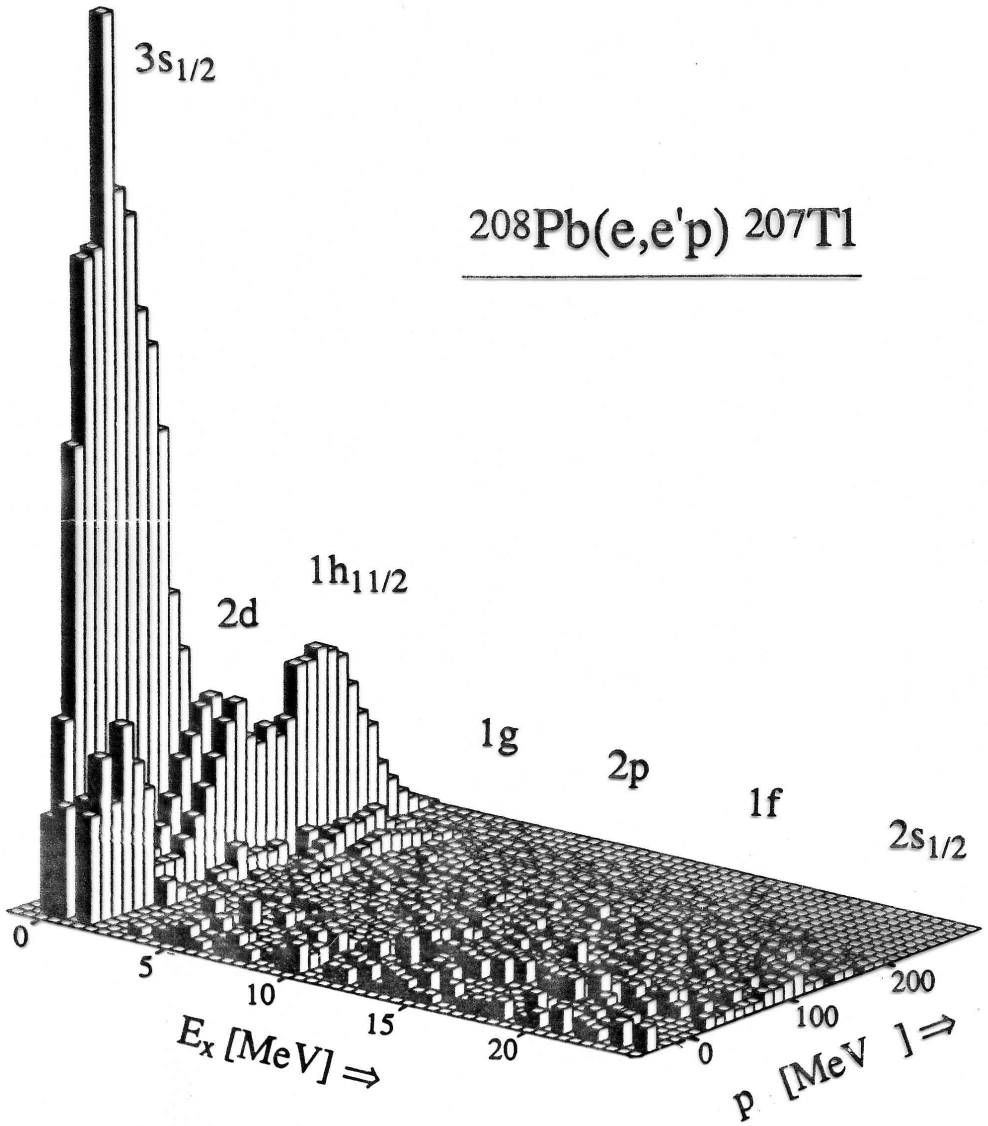

Figura 1.4: Sección eficaz reducida frente a la energía y momento desaparecidos [26].

1.4 Corriente hadrónica

En la aproximación de impulso relativista de ondas distorsionadas, RDWIA, la corriente hadrónica viene descrita por la siguiente amplitud a un cuerpo [16, 19, 21, 25, 27]:

$$J^{\mu}(\omega, \boldsymbol{q}) = \int d\boldsymbol{p}\, \overline{\psi}_F^{s_F}(\boldsymbol{p}+\boldsymbol{q}) \widehat{J}^{\mu} \psi_{\kappa_b}^{\mu_b}(\boldsymbol{p})\,, \tag{1.7}$$

donde ω y $\boldsymbol{q}$ son la energía y momento del fotón virtual intercambiado, $\psi_{\kappa_b}^{\mu_b}$ y $\psi_F^{s_F}$ son las funciones de onda del nucleón inicial ligado, con el que interacciona el fotón, y del protón final detectado, respectivamente. $\widehat{J}^{\mu}$ es el operador de corriente determinado a partir del operador de corriente utilizado en la dispersión libre de electrones por protones. Debido al caracter *off-shell* del protón ligado, se consideran dos formas distintas del operador denominadas $CC1$ y $CC2$. Ambas son totalmente equivalentes para nucleones libres o *on-shell* [28]:

$$\widehat{J}^{\mu}_{CC1} = (F_1 + F_2)\gamma^{\mu} - \frac{F_2}{2M}(P_I + P_F)^{\mu}\,, \tag{1.8}$$

$$\widehat{J}^{\mu}_{CC2} = F_1\gamma^{\mu} + \frac{iF_2}{2M}\sigma^{\mu\nu}q_{\nu}\,, \tag{1.9}$$

donde F_1 y F_2 son los factores de forma de Dirac y Pauli, respectivamente, y $P_I^{\mu} = (E_I, \boldsymbol{p}_I) = (\sqrt{(\boldsymbol{p}_F - \boldsymbol{q})^2 + M^2}, \boldsymbol{p}_F - \boldsymbol{q})$.

La función de onda del nucleón ligado es un cuadriespinor con momento angular total $j_b = |\kappa_b| - 1/2$ y tercera componente μ_b, solución de una ecuación de Dirac con potenciales escalares-vectoriales (S-V) procedentes de un Lagrangiano relativista con términos mesónicos escalares y vectoriales [5, 29]. Su expresión en el espacio de momentos es

$$\psi_{\kappa_b}^{\mu_b}(\boldsymbol{p}) = \frac{1}{(2\pi)^{3/2}} \int d\boldsymbol{r} e^{-i\boldsymbol{p}\cdot\boldsymbol{r}} \psi_{\kappa_b}^{\mu_b}(\boldsymbol{r}) = (-i)^{\ell_b} \begin{pmatrix} g_{\kappa_b}(p) \\ S_{\kappa_b} f_{\kappa_b}(p) \dfrac{\boldsymbol{\sigma}\cdot\boldsymbol{p}}{p} \end{pmatrix} \Phi_{\kappa_b}^{\mu_b}(\widehat{\boldsymbol{p}})\,, \tag{1.10}$$

siendo $\Phi_{\kappa_b}^{\mu_b}(\widehat{\boldsymbol{p}})$ un biespinor de momento angular j_b bien definido

$$\Phi_{\kappa_b}^{\mu_b}(\widehat{\boldsymbol{p}}) = \sum_{m_{\ell_b} h} \langle \ell_b m_{\ell_b} \frac{1}{2} h | j_b \mu_b \rangle Y_{\ell_b}^{\mu_b}(\widehat{\boldsymbol{p}}) \chi_{\frac{1}{2}}^{h}\,, \tag{1.11}$$

con $\ell_b = \kappa_b$ si $\kappa_b > 0$ y $\ell_b = -\kappa_b - 1$ si $\kappa_b < 0$.

La función de onda para el protón final es una solución de una ecuación de Dirac con potenciales S-V ópticos [30–32] para un nucleón dispersado con momento asintótico $\boldsymbol{p}_F$ y proyección de espín s_F, su expresión es

$$\psi_F^{s_F}(\boldsymbol{p}) = 4\pi \sqrt{\frac{E_F + M}{2E_F}} \sum_{\kappa\mu m} e^{-i\delta_{\kappa}^{*}} i^{\ell} \langle \ell m \frac{1}{2} s_F | j\mu \rangle Y_{\ell}^{m*}(\widehat{\boldsymbol{p}}_F) \psi_{\kappa}^{\mu}(\boldsymbol{p})\,. \tag{1.12}$$

Como el potencial óptico es en general complejo, los desfasajes y las funciones radiales también lo son y la funcion de onda $\psi^{\mu}_{\kappa}(\boldsymbol{p})$ viene dada por

$$\psi^{\mu}_{\kappa}(\boldsymbol{p}) = (-i)^{\ell} \begin{pmatrix} g^{*}_{\kappa}(p) \\ S_{\kappa} f^{*}_{\kappa}(p) \frac{\boldsymbol{\sigma}\cdot\boldsymbol{p}}{p} \end{pmatrix} \Phi^{\mu}_{\kappa}(\widehat{\boldsymbol{p}}) \,. \tag{1.13}$$

La corriente hadrónica y las funciones de respuesta nucleares, que como veremos en la siguiente sección caracterizan la sección eficaz del proceso, se relacionan por las expresiones deducidas en el apéndice.

1.5 Sección eficaz y funciones de respuesta

La derivación formal de la sección eficaz se encuentra en el apéndice. Suponemos que la función de onda de los electrones está bien descrita mediante una onda plana, por tanto la seccion eficaz en el laboratorio (para un protón final polarizado a lo largo de una dirección cualquiera) se puede escribir en términos de las llamadas funciones de respuesta como sigue [16, 17, 27]:

$$\begin{aligned} \frac{d\sigma}{d\varepsilon_f d\Omega_f d\Omega_F} &= \frac{E_F p_F}{(2\pi)^3} \sigma_M f_{rec} \frac{1}{2} \Big\{ v_L \left(R^L + R^L_n \widehat{S}_n \right) + v_T \left(R^T + R^T_n \widehat{S}_n \right) \\ &+ v_{TL} \left[\left(R^{TL} + R^{TL}_n \widehat{S}_n \right) \cos\phi_F + \left(R^{TL}_l \widehat{S}_l + R^{TL}_s \widehat{S}_s \right) \sin\phi_F \right] \\ &+ v_{TT} \left[\left(R^{TT} + R^{TT}_n \widehat{S}_n \right) \cos 2\phi_F + \left(R^{TT}_l \widehat{S}_l + R^{TT}_s \widehat{S}_s \right) \sin 2\phi_F \right] \\ &+ h \Big\{ v_{TL'} \left[\left(R^{TL'}_l \widehat{S}_l + R^{TL'}_s \widehat{S}_s \right) \cos\phi_F + \left(R^{TL'} + R^{TL'}_n \widehat{S}_n \right) \sin\phi_F \right] \\ &+ v_{T'} \left[R^{T'}_l \widehat{S}_l + R^{T'}_s \widehat{S}_s \right] \Big\} \Big\} \,, \end{aligned} \tag{1.14}$$

donde σ_M es la sección eficaz de Mott (ver apéndice), $\{\varepsilon_f, \Omega_f\}$ son la energía y el ángulo sólido correspondientes al electrón dispersado y $\Omega_F = (\theta_F, \phi_F)$ el ángulo sólido para el protón final. El factor f_{rec}, deducido en el apéndice, es un factor de retroceso del núcleo residual y viene determinado por la expresión:

$$f^{-1}_{rec} = \left| 1 - \frac{E_F}{E_B} \frac{\boldsymbol{p}_B \cdot \boldsymbol{p}_F}{p^2_F} \right| \tag{1.15}$$

siendo $\boldsymbol{p}_B$ y E_B el momento y energía del núcleo residual respectivamente. Los factores cinemáticos v_α se deducen en el apéndice. Del mismo modo, también se puede ver en el apéndice la relación que existe entre las funciones de respuesta y el llamado tensor hadrónico, que contiene toda la información dinámica correspondiente al vértice nuclear. En las funciones de respuesta polarizadas la dependencia en la polarización del nucleón

detectado viene determinada por las componentes $\widehat{S}_k$ $(k = l, n, s)$ del espín $(\boldsymbol{s}_F)_R$ del nucleón final, en el sistema de referencia en el que dicho nucleón está en reposo, a lo largo de las direcciones:

$$\boldsymbol{l} = \frac{\boldsymbol{p}_F}{p_F}\,, \quad \boldsymbol{n} = \frac{\boldsymbol{q} \times \boldsymbol{p}_F}{|\boldsymbol{q} \times \boldsymbol{p}_F|}\,, \quad \boldsymbol{s} = \boldsymbol{n} \times \boldsymbol{l}\,. \tag{1.16}$$

De las dieciocho funciones de respuesta mediante las cuales queda completamente descrita la sección eficaz del proceso $(\vec{e}, e'\vec{p})$ en el caso más general posible, no todas son distintas de cero en todas las condiciones experimentales [3,17]. En la tabla 1.1 se muestra cuáles se anulan cuando el electrón inicial no está polarizado, cuando restringimos el estudio a la cinemática coplanar $(\phi_F = 0°, 180°)$, cuando no se tiene en cuenta la interacción entre el protón arrancado y el núcleo residual o cuando el momento del protón saliente es paralelo al momento transferido [2,3].

Otra forma de expresar la sección eficaz en términos de las asimetrías de polarización, las cuales son cocientes entre diferentes clases de funciones de respuesta, es [3,18,27]

$$\frac{d\sigma}{d\varepsilon_f d\Omega_f d\Omega_F} = \frac{\sigma_0}{2}\left[1 + P_n\widehat{S}_n + P_l\widehat{S}_l + P_s\widehat{S}_s + h\left(A + P'_n\widehat{S}_n + P'_l\widehat{S}_l + P'_s\widehat{S}_s\right)\right]\,, \tag{1.17}$$

siendo σ_0 la sección eficaz completamente despolarizada, A la asimetría del helicidad del haz incidente y P_k (P'_k) las polarizaciones inducidas (transferidas) respectivamente [3,18, 27]. En función de la sección eficaz, estos observables pueden escribirse como sigue:

$$\sigma_0 = \frac{1}{2}\sum_{h,s_N} d\sigma(h, s_F)\,, \tag{1.18}$$

donde $d\sigma(h, s_F)$ denota de forma simplificada la sección eficaz diferencial $d\sigma/(d\varepsilon_f d\Omega_f d\Omega_F)$ y s_F representa la proyección del espín del nucleón saliente,

$$A = \frac{\sigma(h=1) - \sigma(h=-1)}{\sigma(h=1) + \sigma(h=-1)}, \tag{1.19}$$

siendo $\sigma(h) = \sum_{s_F} d\sigma(h, s_F)$,

$$P_k = \frac{\sigma(s_k=1) - \sigma(s_k=-1)}{\sigma(s_k=1) + \sigma(s_k=-1)}, \tag{1.20}$$

donde $\sigma(s_k) = \frac{1}{2}\sum_h d\sigma(h, s_k)$ y s_k es la proyección del espín del nucleón saliente en una cierta dirección $k = l, n, s$. Análogamente, las polarizaciones transferidas P'_k vienen dadas por

$$P'_k = \frac{[d\sigma(h=1, s_k=1) - d\sigma(h=-1, s_k=1)] - [d\sigma(h=1, s_k=-1) - d\sigma(h=-1, s_k=-1)]}{[d\sigma(h=1, s_k=1) + d\sigma(h=-1, s_k=1)] + [d\sigma(h=1, s_k=-1) + d\sigma(h=-1, s_k=-1)]}. \tag{1.21}$$

Es sencillo comprobar que en cinemática coplanar las únicas componentes que sobreviven de las dos polarizaciones son P_n, P'_l y P'_s [17].

Respuestas	$h = 0$	$\phi_F = 0, 180°$	PWIA	paralela
R^L	S	S	S	S
R^T	S	S	S	S
R^{TT}	S	S	S	N
R^{TL}	S	S	S	N
$R^{TL'}$	N	N	N	N
R_l^{TT}	S	N	N	N
R_l^{TL}	S	N	N	N
$R_l^{TL'}$	N	S	S	N
$R_l^{T'}$	N	S	S	S
R_s^{TT}	S	N	N	N
R_s^{TL}	S	N	N	S
$R_s^{TL'}$	N	S	S	S
$R_s^{T'}$	N	S	S	N
R_n^L	S	S	N	N
R_n^T	S	S	N	N
R_n^{TT}	S	S	N	N
R_n^{TL}	S	S	N	S
$R_n^{TL'}$	N	N	S	S

Tabla 1.1: *Propiedades de las funciones de respuesta en procesos $A(\vec{e}, e'\vec{N})B$. S significa que la respuesta no se anula en la circunstancia impuesta, mientras N significa que es nula.*

En el ámbito de la dispersión de protones por núcleos, las medidas de observables de polarización del nucleón emitido, así como del protón utilizado como blanco, fueron frecuentes, especialmente a energías intermedias. También se hicieron muchos estudios sobre el "poder de análisis" A_y y la función de rotacion de spin Q [33]. Con blancos no polarizados, la sección eficaz, A_y y Q forman el conjunto completo de observables que pueden adquirirse en dispersión elástica y determinan de forma "exacta" todos los parámetros del modelo, frecuentemente basado en potenciales ópticos, utilizado para describir dichos procesos elásticos.

En dispersión de electrones por núcleos, la utilización de un analizador mágnetico (Stern-Gerlach) para poder medir el momento magnético del protón emitido, representa un desafío experimental importante, dado que la eficiencia del espectrómetro de protones se reduce en al menos un orden de magnitud al introducir el polarímetro. En el caso cuasielástico, eligiendo la cinemática de forma adecuada, podemos seleccionar qué condiciones ha de cumplir el nucleón que arrancamos del núcleo, en cuanto a su momento y su energía de ligadura. La medida de la sección eficaz permite determinar la distribución de momentos en el núcleo, como hemos dicho anteriormente, y la medida de los observables de polarización suministra el mapa de espín del nucleón arrancado en el núcleo blanco (polarización transferida) y del intercambio de espín/momento magnético del nucleón arrancado al atravesar el medio nuclear (polarización inducida). La primera permite estudiar con un detalle nunca antes visto, la distribucion de carga y espín (momento magnético) del nucleón en el núcleo blanco y las segunda proporciona información adicional sobre la interacción del protón con el núcleo residual en el estado final; interacción de estados finales.

1.6 Objetivos y estructura de la tesis

Basándonos en los trabajos previos sobre reacciones $(e, e'p)$ realizados por el grupo de Física Nuclear de Madrid y colaboradores [19, 21–23, 34–36], en esta tesis doctoral se pretenden satisfacer los siguientes objetivos:

- Completar el formalismo relativista desarrollado por el citado grupo, extendiéndolo a las reacciones $(\vec{e}, e'\vec{p})$ y calculando todos los observables de polarización.
- Comparar con los datos y experimentos pasados y presentes, con el fin de determinar la fiabilidad del modelo.

- Realizar una comparación detallada de los cálculos relativistas y no relativistas, para establecer las razones de las diferencias observadas entre ambos formalismos.

- Asegurar el marco teórico del proceso de reacción con el fin de poder utilizar los datos experimentales para obtener información sobre las propiedades de los nucleones en el medio nuclear.

Con este fin y siguiendo la normativa vigente de la Universidad Complutense de Madrid respecto a la publicación de tesis doctorales que contemplen distintas publicaciones, hemos estructurado la presente del siguiente modo: El primer capítulo, que aquí concluye, consiste en una introducción con una revisión del estado actual del tema de la tesis doctoral. Este capítulo se ve completado mediante un apéndice donde se desarrolla formalmente el cálculo de la sección eficaz de la reacción $A(\vec{e}, e'\vec{p})B$. Los capítulos del 2 al 8 consisten en la presentación de diferentes publicaciones a las que ha dado lugar el trabajo de investigación del doctorando. En el capítulo 2 se estudian las propiedades de factorización de los observables más relevantes para el estudio de los procesos $A(\vec{e}, e'\vec{p})B$ bajo distintas aproximaciones. En el capítulo 3 se presenta un análisis de las secciones eficaces medidas por diferentes grupos experimentales en ^{16}O [37–39] y se comparan con los cálculos relativistas de ondas distorsionadas desarrollados por nuestro grupo. En el capítulo 4 se estudia la reacción $^{4}He(e, e'p)^{3}H$. En los capítulos 5 y 6 se analizan los observables de polarización, las polarizaciones inducidas en el capítulo 5 y las polarizaciones transferidas en el capítulo 6. Los capítulos 7 y 8 consisten en un estudio del cociente entre las polarizaciones transferidas, particularizado a la reacción $^{4}He(\vec{e}, e'\vec{p})^{3}H$, con el objetivo de buscar evidencias sobre las posibles modificaciones en las propiedades de los nucleones producidas por el medio nuclear. En el capítulo 9 se muestra una discusión integradora de todas las publicaciones presentadas y, por último, en el capítulo 10 se presentan las conclusiones a las que ha dado lugar esta tesis. Al final de cada capítulo se encuentra una bibliografía con todos los artículos que se citan en cada uno de ellos.

Bibliografía

[1] S. Boffi, C. Giusti, F.D. Pacati, Phys. Rep. **226**, 1 (1993);

[2] S. Boffi, C. Giusti, F.D. Pacati, M. Radici, *Electromagnetic Response of Atomic Nuclei* (Oxford University Press, Oxford, 1996).

[3] J.J. Kelly, Adv. Nucl. Phys. **23**, 75 (1996).

[4] S. Frullani and J. Mougey, Adv. Nucl. Phys. **14**, 1 (1985).

[5] J.D. Walecka, *Electron Scattering for Nuclear and Nucleon Structure* (Cambridge University Press, 2001).

[6] P. Leconte *et al.*, Nucl. Instrum. Meth. **169**, 401 (1980)

[7] C. de Vries *et al.*, Nucl. Instrum. Meth. **223**, 1 (1984).

[8] R.J. Woo, Ph.D. thesis, College of William and Mary, 1996.

[9] K.I. Blomqvist *et al.*, Nucl. Inst. Meth. **A403**, 263 (1998).

[10] A. Saha, W. Bertozzi, R. W. Lourie, L. B. Weinstein, Experiment Proposal E89-003, Jefferson Laboratory 1989

[11] K. G. Fissum *et al.*, MIT-LNS Internal Report 2/97, Massachusetts Institute of Technology 1997

[12] K. G. Fissum *et al.*, Phys. Rev. C **70**, 034606 (2004).

[13] *Technical Proposal for the Design, Construction, Commissioning and Operation of R^3B. A universal setup for kinematical complete measurements of Reactions with Reltivistic Radioactive Beams*, Spokerperson: Thomas Aumman, por la colaboración R3B. Presentada al PAC de FAIR, para el proyecto del Nuevo GSI, 2005.

[14] *Technical Proposal for the Design, Construction, Commissioning and Operation of the EXL project (Exotic nuclei studied in light-ion induced reactions at the NESR storage ring)*, Spokerperson Marielle Chartier, por la colaboración EXL. Presentada al PAC de FAIR, para el proyecto del Nuevo GSI, 2005.

[15] *Technical Proposal for the Design, Construction, Commissioning and Operation of the ELISE setup*, Spokerperson Haik Simon, por la colaboración Elise. Presentada al PAC de FAIR, para el proyecto del Nuevo GSI, 2005.

[16] A. Picklesimer and J.W. Van Orden, Phys. Rev. C **35**, 266 (1987)

[17] A. Picklesimer and J.W. Van Orden, Phys. Rev. C **40**, 290 (1989).

[18] M.C. Martínez, J.R. Vignote, J.A. Caballero, T.W. Donnelly, E. Moya de Guerra, J.M. Udías, Phys. Rev. C **69**, 034604 (2004)

[19] J.M. Udías, Ph.D. thesis, CSIC, Madrid, 1993.

[20] J.D. Bjorken and S.D. Drell, *Relativistic Quantum Mechanics* (McGraw-Hill, New York, 1964).

[21] J.M Udías, P. Sarriguren, E. Moya de Guerra, E. Garrido, J.A. Caballero, Phys. Rev. C **48**, 2731 (1993).

[22] J.M. Udías, P. Sarriguren, E. Moya de Guerra, J.A. Caballero, Phys. Rev. C **53**, R1488 (1996).

[23] J.M. Udías, J.A. Caballero, E. Moya de Guerra, J.E. Amaro, T.W. Donnelly, Phys. Rev. Lett. **83**, 5451 (1999).

[24] J.M. Udías, J.R. Vignote, Phys. Rev. C **62**, 034302 (2000).

[25] J.M. Udías, J.A. Caballero, E. Moya de Guerra, J.R. Vignote, A. Escuderos, Phys. Rev. C **64**, 024614 (2001).

[26] E.N.M. Quint, Ph.D. thesis, Amsterdam, 1988.

[27] Javier R. Vignote, M.C. Martínez, J.A. Caballero, E. Moya de Guerra, J.M. Udías, Phys. Rev. C **70**, 044608 (2004).

[28] T. de Forest, Nucl. Phys. **A392**, 232 (1983); F. Halzen and A.D. Martin, *Quarks & Leptons: An Introductory Course in Modern Particle Physics* (John Wiley & Sons, New York, 1984), 177, ejercicio 8.7.

[29] J.D. Walecka, Ann. Phys. **83**, 491 (1974).

[30] E.D. Cooper, S. Hama, B.C. Clark, R.L. Mercer, Phys. Rev. C **47**, 297 (1993).

[31] C.J. Horowitz, Phys. Rev. C **31**, 1340 (1985); D.P. Murdock and C.J. Horowitz, Phys. Rev. C **35**, 1442 (1987).

[32] C.J. Horowitz, D.P. Murdock, B.D. Serot, *Computational Nuclear Physics* (Springer, Berlin, 1991).

[33] H. Feshbach, *Theoretical Nuclear Physics Nuclear Reactions* (John Wiley & Sons, New York, 1992).

[34] J.M Udías, P. Sarriguren, E. Moya de Guerra, E. Garrido, J.A. Caballero, Phys. Rev. **C51**, 3246 (1995).

[35] J.E. Amaro, J.A. Caballero, T.W. Donnelly, A.M. Lallena, E. Moya de Guerra, J.M. Udías, Nucl. Phys. **A 602**, 263 (1996).

[36] J.A. Caballero, T.W. Donnelly, E. Moya de Guerra, J.M. Udías, Nucl. Phys. **A632**, 323 (1998); **A643**, 189 (1998).

[37] L. Chinitz *et al.*, Phys. Rev. Lett. **67**, 568 (1991).

[38] C.M. Spaltro, H.P. Blok, E. Jans, L. Lapikás, M. van der Schaar, G. van der Steenhoven, P.K.A. de Witt Huberts, Phys. Rev. C **48**, 2385 (1993).

[39] M. Leuschner *et al.*, Phys. Rev. C **49**, 955 (1994).

Capítulo 2

Factorización

PHYSICAL REVIEW C **70**, 044608 (2004)

$A(\vec{e}, e'\vec{p})B$ responses: From bare nucleons to complex nuclei

Javier R. Vignote[1], M.C. Martínez[2], J.A. Caballero[2], E. Moya de Guerra[3], and J.M. Udías[1]

[1]*Departamento de Física Atómica, Molecular y Nuclear, Universidad Complutense de Madrid, E-28040 Madrid, Spain*

[2]*Departamento de Física Atómica, Molecular y Nuclear, Universidad de Sevilla, Apartado postal 1065, E-41080 Sevilla, Spain*

[3]*Instituto de Estructura de la Materia, CSIC, Serrano 123, E-28006 Madrid, Spain*

We study the occurrence of factorization in polarized and unpolarized observables in coincidence quasi-elastic electron scattering. Starting with the relativistic distorted wave impulse approximation, we reformulate the effective momentum approximation and show that the latter leads to observables which factorize under some specific conditions. Within this framework, the role played by final state interactions and, in particular, by the spin-orbit term is explored. Connection with the nonrelativistic formalism is studied in depth. Numerical results are presented to illustrate the analytical derivations and to quantify the differences between factorized and unfactorized approaches.

PACS number(s): 25.30.Rw, 24.10.Jv, 21.60.Cs

2.1 Introduction

Quasielastic $(e, e'p)$ reactions have provided over the years an enormous wealth of information on nuclear structure, particularly, on single particle degrees of freedom: energies, momentum distributions and spectroscopic factors of nucleons inside nuclei [1–3]. In recent years important efforts have been devoted to provide more realistic theoretical descriptions of these processes [4–16]. However, there are still uncertainties associated to the various ingredients that enter in the reaction dynamics: final state interactions (FSI), off-shell effects, nuclear correlations, relativistic degrees of freedom or meson exchange currents (MEC). These ingredients affect the evaluation of electron scattering observables and hence lead to ambiguities in the information on the nuclear and nucleon structure that can be extracted from experiments. In recent years, electron beam polarization as well as polarization degrees of freedom for the outgoing nucleon can be measured, what makes it possible to extract a new wealth of observables from quasielastic $(\vec{e}, e'\vec{p})$ reactions. For instance ratios of transferred polarizations are used to measure ratios of nucleon form factors.

One of the basic results which has made $(e, e'p)$ reactions so appealing for investigations of single particle properties is the factorized approach [1, 17, 18]. Within this approximation, the $(e, e'p)$ differential cross section factorizes into a single-nucleon cross section, describing electron proton scattering, and a spectral function which gives the probability to find a proton in the target nucleus with selected values of energy and momentum compatible with the kinematics of the process. The simplicity of the factorized result makes it possible to get a clear image of the physics contained in the problem. Even being known that factorization does not hold in general, it is often assumed that the breakdown of factorization is not too severe, and then it is still commonplace to use factorized calculations for few body systems or for inclusive scattering. The importance of factorization lies on the fact that the interpretation of experimental data is still usually based on this property by defining an *effective* spectral function that is extracted from experiment in the form of a reduced cross section. Assuming that factorization holds at least approximately, reduced cross section would yield information on momentum distributions of the nucleons inside the nucleus. On the other hand, these momentum distributions would cancel when taking ratios of cross sections and consequently these ratios might give information on the electromagnetic form factors of the nucleons [19, 20].

In spite of the importance of the factorization assumption, there have been however

almost no formal (and very few quantitative) studies of its validity. So far, it has been shown by different authors [3, 18, 21] that in the nonrelativistic case and when using plane waves to describe the ejected nucleon (PWIA), factorization holds exactly for the *unpolarized cross section*. When interactions in the final state are included (DWIA), then certain further assumptions are needed to recover the factorized result [3]. The meaning and importance of the additional assumptions required to attain a factorized result has not been quantitatively studied thoroughly.

In the relativistic case, factorization of the unpolarized cross section is broken even without FSI, due to the negative energy components of the bound nucleon wave function [18, 21]. A quantitative estimate of the breakdown of factorization is lacking for the relativistic case when taking into account FSI.

Furthermore, there has not been any study of the validity of the factorization picture for polarization observables, even though this factorized picture is implicitly assumed when using ratios of transferred polarizations to determine nucleon form factors [19, 20].

Within a nonrelativistic framework, the breakdown of factorization has been usually interpreted as due to the spin-orbit dependent optical potentials. We note however, that other effects such as the Coulomb distortion of the electron waves, and contributions beyond the impulse approximation (IA) such as MEC, play also a role in breaking factorization. In the particular case of the plane wave limit (i.e., neglecting FSI between the ejected proton and the residual nucleus) factorization is strictly satisfied in IA at the level of the transition amplitude [3, 18]. This contrasts strongly with the relativistic formalism, where the enhancement of the lower components of the bound nucleon wave function destroys factorization of the transition amplitude even in the case of no FSI. Hence, an important difference between relativistic and nonrelativistic approaches already emerges in the plane wave limit. Whereas factorization holds in nonrelativistic PWIA, it does not in the relativistic plane wave impulse approximation (RPWIA), which includes negative-energy components in the bound nucleon wave function [18, 21].

As mentioned above, the mechanism that breaks factorization has been only established for the unpolarized cross section in the nonrelativistic approach. Here we explore such mechanisms for both polarized and unpolarized observables starting from the more complex relativistic distorted wave impulse approximation (RDWIA) and making simplifying assumptions that lead to factorization. We make also the connection with the nonrelativistic framework and present conclusions that are valid in both relativistic and nonrelativistic cases. It is important to point out that most of the $(e, e'p)$ experiments

performed recently involved energies and momenta high enough to make compulsory the use of relativistic nucleon dynamics. Within this context, the RDWIA, which incorporates kinematical and dynamical relativistic effects, has proved its capability to explain polarized and unpolarized $(e, e'p)$ experimental data [6, 9–11]. Starting from the RDWIA, the effective momentum approximation (EMA-noSV), originally introduced by Kelly [22], is reformulated here paying special attention to aspects concerned with the property of factorization. In addition, an analysis is made of the various assumptions that lead to *factorized* polarized and unpolarized observables and which are mainly linked to the spin-orbit dependence of the problem. Finally, a quantitative estimate of the validity (or breakdown) of factorization is made for different observables that are commonly extracted from $(e, e'p)$ experiments.

The paper is organized as follows: in Sec. 2.2 we outline the basic RDWIA formalism and revisit the EMA-noSV approach, emphasizing its connection with the factorized approximation. In Sec. 2.3 we present our analysis for polarized and unpolarized observables, deriving the specific conditions which lead to *factorization*. In Sec. 2.4 we concentrate on reduced cross sections and connect them to the momentum distributions. Results for polarized and unpolarized observables are presented in Sec. 2.5. Numerical calculations performed within different approaches are compared. Finally, in Sec. 2.6 we draw our conclusions.

2.2 Relativistic distorted wave impulse approximation (RDWIA)

The RDWIA has been described in detail in previous works (see for instance [6, 11]). In this section we limit our attention to those aspects needed for later discussion of the results presented. In RDWIA the one body nucleon current

$$J^{\mu}(\omega, \boldsymbol{q}) = \int d\boldsymbol{p}\, \overline{\psi}_F^{s_F}(\boldsymbol{p}+\boldsymbol{q}) \widehat{J}^{\mu} \psi_{\kappa_b}^{\mu_b}(\boldsymbol{p})\,, \tag{2.1}$$

where ω and $\boldsymbol{q}$ are the energy and momentum of the exchanged virtual photon, is calculated with relativistic $\psi_{\kappa_b}^{\mu_b}$ and $\psi_F^{s_F}$ wave functions for initial bound and final outgoing nucleons, respectively, and with relativistic nucleon current operator $\widehat{J}^{\mu}$.

The bound state wave function is a four-spinor with well defined angular momentum quantum numbers κ_b, μ_b corresponding to the shell under consideration. In momentum

space it is given by

$$\psi^{\mu_b}_{\kappa_b}(\boldsymbol{p}) = \frac{1}{(2\pi)^{3/2}} \int d\boldsymbol{r} e^{-i\boldsymbol{p}\cdot\boldsymbol{r}} \psi^{\mu_b}_{\kappa_b}(\boldsymbol{r}) = (-i)^{\ell_b} \begin{pmatrix} g_{\kappa_b}(p) \\ S_{\kappa_b} f_{\kappa_b}(p) \frac{\boldsymbol{\sigma}\cdot\boldsymbol{p}}{p} \end{pmatrix} \Phi^{\mu_b}_{\kappa_b}(\widehat{\boldsymbol{p}}) \,, \tag{2.2}$$

which is the eigenstate of total angular momentum $j_b = |\kappa_b| - 1/2$, and $\Phi^{\mu_b}_{\kappa_b}(\widehat{\boldsymbol{p}})$ are the spinor harmonics

$$\Phi^{\mu_b}_{\kappa_b}(\widehat{\boldsymbol{p}}) = \sum_{m_{\ell_b} h} \langle \ell_b m_{\ell_b} \frac{1}{2} h | j_b \mu_b \rangle Y^{\mu_b}_{\ell_b}(\widehat{\boldsymbol{p}}) \chi^h_{\frac{1}{2}} \,, \tag{2.3}$$

with $\ell_b = \kappa_b$ if $\kappa_b > 0$ and $\ell_b = -\kappa_b - 1$ if $\kappa_b < 0$.

The wave function for the outgoing proton is a solution of the Dirac equation containing scalar (S) and vector (V) optical potentials [6, 7]. For a nucleon scattered with asymptotic momentum $\boldsymbol{p}_F$ and spin projection s_F, its expression is

$$\psi^{s_F}_F(\boldsymbol{p}) = 4\pi \sqrt{\frac{E_F + M}{2E_F}} \sum_{\kappa\mu m} e^{-i\delta^*_\kappa} i^\ell \langle \ell m \frac{1}{2} s_F | j \mu \rangle Y^{m*}_\ell(\widehat{\boldsymbol{p}}_F) \psi^\mu_\kappa(\boldsymbol{p}) \,. \tag{2.4}$$

As the optical potential may be in general complex the phase shifts and radial functions are also complex, and the wave function $\psi^\mu_\kappa(\boldsymbol{p})$ is given by

$$\psi^\mu_\kappa(\boldsymbol{p}) = (-i)^\ell \begin{pmatrix} g^*_\kappa(p) \\ S_\kappa f^*_\kappa(p) \frac{\boldsymbol{\sigma}\cdot\boldsymbol{p}}{p} \end{pmatrix} \Phi^\mu_\kappa(\widehat{\boldsymbol{p}}) \,. \tag{2.5}$$

Assuming plane waves for the electron (treated in the extreme relativistic limit), the differential cross section for outgoing nucleon polarized $A(\vec{e}, e'\vec{p})B$ reactions can be written in the laboratory system in the general form

$$\frac{d\,\sigma}{d\varepsilon_f d\,\Omega_f d\,\Omega_F} = \frac{E_F p_F}{(2\pi)^3} \sigma_M f_{rec}\, \omega_{\mu\nu} W^{\mu\nu} \,, \tag{2.6}$$

where σ_M is the Mott cross section, $\{\varepsilon_f, \Omega_f\}$ are the energy and solid angle corresponding to the scattered electron and $\Omega_F = (\theta_F, \phi_F)$ the solid angle for the outgoing proton. The factor f_{rec} is the usual recoil factor $f^{-1}_{rec} = |1 - (E_F/E_B)(\boldsymbol{p}_B \cdot \boldsymbol{p}_F)/p^2_F|$, being $\boldsymbol{p}_B$ and E_B the momentum and energy of the residual nucleus, respectively. Finally, $\omega_{\mu\nu}$ is the familiar leptonic tensor that can be decomposed into its symmetric (helicity independent) and antisymmetric (helicity dependent) parts and $W^{\mu\nu}$ is the hadronic tensor which contains all of the hadronic dynamics of the process. The latter is defined from bilinear combinations of the one body nucleon current matrix elements given in Eq. (2.1), as

$$W^{\mu\nu} = \frac{1}{2j_b + 1} \sum_{\mu_b} J^{\mu*}(\omega, \boldsymbol{q}) J^\nu(\omega, \boldsymbol{q}) \,. \tag{2.7}$$

The cross section can be also written in terms of hadronic responses by making use of the general properties of the leptonic tensor. For $(\vec{e}, e'\vec{p})$ reactions with the incoming electron polarized and the final nucleon polarization also measured, a total set of eighteen response functions contribute to the cross section. Its general expression is written in the form

$$\begin{aligned}
\frac{d\sigma}{d\varepsilon_f d\Omega_f d\Omega_F} &= \frac{E_F p_F}{(2\pi)^3}\sigma_M f_{rec}\frac{1}{2}\left\{v_L\left(R^L + R_n^L\widehat{S}_n\right) + v_T\left(R^T + R_n^T\widehat{S}_n\right)\right. \\
&+ v_{TL}\left[\left(R^{TL} + R_n^{TL}\widehat{S}_n\right)\cos\phi_F + \left(R_l^{TL}\widehat{S}_l + R_s^{TL}\widehat{S}_s\right)\sin\phi_F\right] \\
&+ v_{TT}\left[\left(R^{TT} + R_n^{TT}\widehat{S}_n\right)\cos 2\phi_F + \left(R_l^{TT}\widehat{S}_l + R_s^{TT}\widehat{S}_s\right)\sin 2\phi_F\right] \\
&+ h\left\{v_{TL'}\left[\left(R_l^{TL'}\widehat{S}_l + R_s^{TL'}\widehat{S}_s\right)\cos\phi_F + \left(R^{TL'} + R_n^{TL'}\widehat{S}_n\right)\sin\phi_F\right]\right. \\
&+ \left.\left. v_{T'}\left[R_l^{T'}\widehat{S}_l + R_s^{T'}\widehat{S}_s\right]\right\}\right\}\,, \qquad (2.8)
\end{aligned}$$

where v_α are the usual electron kinematical factors [5, 11] and $h = \pm 1$ is the incident electron helicity. The polarized and unpolarized nuclear response functions are constructed directly by taking the appropriate components of the hadronic tensor $W^{\mu\nu}$ (see Ref. [5] for their explicit expressions). The cross section dependence on the recoil nucleon polarization is specified by the components $\widehat{S}_k$ $(k = l, n, s)$ of the ejected proton rest frame spin $(\boldsymbol{s}_F)_R$ along the directions: $\boldsymbol{l} = \boldsymbol{p}_F/p_F$, $\boldsymbol{n} = (\boldsymbol{q}\times\boldsymbol{p}_F)/|\boldsymbol{q}\times\boldsymbol{p}_F|$ and $\boldsymbol{s} = \boldsymbol{n}\times\boldsymbol{l}$.

To finish this section and in order to ease the analysis of the results, the cross section can be also expressed in terms of the usual polarization asymmetries, which are given as ratios between different classes of response functions,

$$\frac{d\sigma}{d\varepsilon_f d\Omega_f d\Omega_F} = \frac{\sigma_0}{2}\left[1 + P_n\widehat{S}_n + P_l\widehat{S}_l + P_s\widehat{S}_s + h\left(A + P'_n\widehat{S}_n + P'_l\widehat{S}_l + P'_s\widehat{S}_s\right)\right]\,, \qquad (2.9)$$

with σ_0 the unpolarized cross section, A the electron analyzing power, and P_k (P'_k) the induced (transferred) polarizations.

2.2.1 Factorization and effective momentum approximation

In nonrelativistic PWIA, the $(e, e'p)$ unpolarized cross section factorizes in the form

$$\left(\frac{d\sigma}{d\varepsilon_f d\Omega_f d\Omega_F}\right)^{PWIA} = E_F p_F f_{rec}\,\sigma_{ep}\,N_{NR}(\boldsymbol{p}_m)\,, \qquad (2.10)$$

where σ_{ep} is the bare electron-proton cross section usually taken as σ_{cc1} (or σ_{cc2}) of de Forest [23], and $N_{NR}(\boldsymbol{p}_m)$ is the *non relativistic momentum distribution* that represents

the probability of finding a proton in the target nucleus with missing momentum $\boldsymbol{p}_m$, compatible with the kinematics of the reaction. It is well known that the factorized result in Eq. (2.10) comes from an oversimplified description of the reaction mechanism. FSI, as well as Coulomb distortion of the electron wave functions, destroys in general factorization. In fact, most current descriptions of exclusive $(e, e'p)$ reactions involve unfactorized calculations. However, the simplicity of the factorized result makes it very useful to analyze and interpret electron scattering observables in terms of single particle properties of bound nucleons. Therefore it is common to quote *experimental reduced cross section* or *effective momentum distribution* on the basis of the experimental unpolarized cross section as

$$\rho^{exp}(\boldsymbol{p}_m) = \frac{\left(\frac{d\sigma}{d\varepsilon_f d\Omega_f d\Omega_F}\right)^{exp}}{E_F p_F f_{rec}\, \sigma_{ep}} \,. \tag{2.11}$$

A similar expression can be used for the theoretical reduced cross section,

$$\rho^{th}(\boldsymbol{p}_m) = \frac{\left(\frac{d\sigma}{d\varepsilon_f d\Omega_f d\Omega_F}\right)^{th}}{E_F p_F f_{rec}\, \sigma_{ep}} \,, \tag{2.12}$$

constructed from the the theoretical unpolarized $(e, e'p)$ cross section, independently of whether it is calculated within a relativistic or nonrelativistic formalism. We will say that the factorization property is satisfied by $\rho^{th}(\boldsymbol{p}_m)$ when the theoretical unpolarized cross section factors out exactly σ_{ep}, and then, the theoretical reduced cross section does not depend on it.

As we will demonstrate later in this paper, factorization is not a property exclusive of the nonrelativistic PWIA approach. It is well known that, due to the negative energy components of the bound proton wave function, factorization is not satisfied even in RPWIA [18]. However, if we neglect the contribution from the negative energy components, the unpolarized cross section factorizes to a similar expression as in Eq. (2.10).

Starting from a fully relativistic calculation of the nuclear current, in what follows we explore the most general conditions under which factorization is recovered. First, it is important to note that in order to extract the elementary cross section "σ_{ep}" from the general relativistic theory (RDWIA), the upper and lower components of the relativistic wave functions that enter in Eq. (2.1) must be forced to satisfy the "free" relationship with momenta determined by asymptotic kinematics at the nucleon vertex, that is

$$\psi_{down}(\boldsymbol{p}) = \frac{\boldsymbol{\sigma}\cdot\boldsymbol{p}_{as}}{E_{as}+M}\psi_{up}(\boldsymbol{p}) \,, \tag{2.13}$$

with $E_{as} = \sqrt{\boldsymbol{p}_{as}^2 + M^2}$ and $\boldsymbol{p}_{as}$ the asymptotic momentum corresponding to each nucleon. In what follows we discuss this condition (2.13) in the nonrelativistic language.

The nonrelativistic formalism is based on bispinors $\chi(\boldsymbol{p})$ solutions of Schrödinger-like equations. Generally, the nonrelativistic formalism can be analyzed using the following semirelativistic (SR) four-spinor

$$\psi^{SR}(\boldsymbol{p}) = \frac{1}{\sqrt{N}} \begin{pmatrix} \chi(\boldsymbol{p}) \\ \frac{\boldsymbol{\sigma}\cdot\boldsymbol{p}}{E+M}\chi(\boldsymbol{p}) \end{pmatrix} , \tag{2.14}$$

to be introduced in Eq. (2.1) in order to calculate a relativistic-like nucleon current amplitude. In this way the relativistic kinematics is fully taken into account and no expansions in p/M are needed. The one body nucleon current matrix element takes then the following form:

$$J^{\mu}(\omega, \boldsymbol{q}) = \int d\boldsymbol{p}\, \chi_F^{s_F\,\dagger}(\boldsymbol{p}+\boldsymbol{q}) \widehat{J}^{\mu}_{eff}(\boldsymbol{p}, \boldsymbol{q}) \chi_{j_b}^{\mu_b}(\boldsymbol{p}) \,, \tag{2.15}$$

with $\widehat{J}^{\mu}_{eff}(\boldsymbol{p}, \boldsymbol{q})$ now an effective (2x2) current operator that occurs between bispinor wave functions $\chi_F^{s_F}$ ($\chi_{j_b}^{\mu_b}$) for the outgoing (bound) nucleon respectively.

The calculation of the nuclear amplitude using four-spinors like the one written in Eq. (2.14), implies removal of the enhancement of the lower components that is present in the four-spinors of Eqs. (2.2) and (2.4). This is a well known fact present in nonrelativistic calculations, but this alone is not enough to get factorization. It is also required the use of exactly the same nuclear current operator as in a free electron-proton scattering. In Eq. (2.15) then, the non-truncated effective current operator must be evaluated at the asymptotic momentum values, leading to

$$J^{\mu}(\omega, \boldsymbol{q}) = \int d\boldsymbol{p}\, \chi_F^{s_F\,\dagger}(\boldsymbol{p}+\boldsymbol{q}) \widehat{J}^{\mu}_{eff}(\boldsymbol{p}_F - \boldsymbol{q}, \boldsymbol{q}) \chi_{j_b}^{\mu_b}(\boldsymbol{p}) \,. \tag{2.16}$$

One can show that this condition is implicit in one of the necessary assumptions introduced in Ref. [3] to recover factorization in the nonrelativistic case.

In a relativistic calculation, the assumptions written in Eq. (2.13) set up the so-called Effective Momentum Approximation with no Scalar and Vector terms (EMA-noSV)*, originally introduced by Kelly [22], to which we will refer in what follows as EMA. The EMA approximation in the relativistic framework, or the nonrelativistic calculation based on Eq. (2.16), are essentially the same conditions which are necessary to recover factorization, in either formalism. These conditions are necessary but not sufficient and in what

*The factorization property could be also analyzed within the framework of the asymptotic projection approach (see Refs. [9, 11, 16] for details)

follows, we concentrate on the EMA case to study additional assumptions needed to obtain factorization.

In EMA, the bound nucleon wave function in momentum space is given by

$$\psi_{\kappa_b}^{\mu_b\,EMA}(\boldsymbol{p}) = (-i)^{\ell_b} \begin{pmatrix} g_{\kappa_b}(p) \\ \frac{\boldsymbol{\sigma}\cdot\boldsymbol{p}_I}{E_I+M} g_{\kappa_b}(p) \end{pmatrix} \Phi_{\kappa_b}^{\mu_b}(\widehat{\boldsymbol{p}})\,, \tag{2.17}$$

with $E_I = \sqrt{\boldsymbol{p}_I^2 + M^2}$ and $\boldsymbol{p}_I = \boldsymbol{p}_F - \boldsymbol{q}$. Likewise the outgoing relativistic distorted wave function in Eq. (2.5) becomes

$$\psi_{\kappa}^{\mu\,EMA}(\boldsymbol{p}) = (-i)^{\ell} \begin{pmatrix} g_{\kappa}^*(p) \\ \frac{\boldsymbol{\sigma}\cdot\boldsymbol{p}_F}{E_F+M} g_{\kappa}^*(p) \end{pmatrix} \Phi_{\kappa}^{\mu}(\widehat{\boldsymbol{p}})\,. \tag{2.18}$$

Introducing these expressions into the equation of the one body nucleon current matrix element (Eq. (2.1)), we get

$$\begin{aligned} J_{EMA}^{\mu} &= \sum_{sh} \left[\overline{u}(\boldsymbol{p}_F, s)\widehat{J}^{\mu} u(\boldsymbol{p}_I, h)\right] \sum_{\kappa\mu m} \langle \ell m \frac{1}{2} s_F | j\mu\rangle Y_{\ell}^{m*}(\widehat{\boldsymbol{p}}_F) \\ &\times \sum_{m_{\ell_b} m_\ell} \langle \ell_b m_{\ell_b} \frac{1}{2} h | j_b \mu_b\rangle \langle \ell m_\ell \frac{1}{2} s | j\mu\rangle U_{\kappa_b\, m_{\ell_b}}^{\kappa\, m_\ell}(\boldsymbol{p}_F, \boldsymbol{q}) \\ &\equiv \sum_{sh} J_{bare}^{\mu}(\boldsymbol{p}_F s, \boldsymbol{p}_I h) A_{sh}^{\mu_b}(\boldsymbol{p}_F, \boldsymbol{q})\,, \end{aligned} \tag{2.19}$$

where we have written both nucleon wave functions in terms of free positive energy Dirac spinors and we have introduced the bare nucleon current matrix element

$$J_{bare}^{\mu}(\boldsymbol{p}_F s, \boldsymbol{p}_I h) = \overline{u}(\boldsymbol{p}_F, s)\widehat{J}^{\mu} u(\boldsymbol{p}_I, h)\,, \tag{2.20}$$

with the term $U_{\kappa_b\, m_{\ell_b}}^{\kappa\, m_\ell}(\boldsymbol{p}_F, \boldsymbol{q})$ given by

$$U_{\kappa_b\, m_{\ell_b}}^{\kappa\, m_\ell} = \frac{8\pi M}{\sqrt{2E_F(E_I+M)}} (-i)^{\ell_b} \int d\boldsymbol{p}\, g_{\kappa_b}(p) g_{\kappa}^*(|\boldsymbol{p}+\boldsymbol{q}|) Y_{\ell_b}^{m_{\ell_b}}(\widehat{\boldsymbol{p}}) Y_{\ell}^{m_\ell *}(\widehat{\boldsymbol{p}+\boldsymbol{q}}) e^{i\delta_\kappa}\,, \tag{2.21}$$

and the amplitude

$$A_{sh}^{\mu_b}(\boldsymbol{p}_F, \boldsymbol{q}) = \sum_{\kappa\mu m} \langle \ell m \frac{1}{2} s_F | j\mu\rangle Y_{\ell}^{m*}(\widehat{\boldsymbol{p}}_F) \sum_{m_{\ell_b} m_\ell} \langle \ell_b m_{\ell_b} \frac{1}{2} h | j_b \mu_b\rangle \langle \ell m_\ell \frac{1}{2} s | j\mu\rangle U_{\kappa_b\, m_{\ell_b}}^{\kappa\, m_\ell}(\boldsymbol{p}_F, \boldsymbol{q}) \tag{2.22}$$

The result in Eq. (2.19) defines the nucleon current in EMA, and is our starting point for the analysis of the conditions that may lead to *factorized* observables. Notice that J_{EMA}^{μ} involves a sum over initial and final spin projections $(s,\, h)$ of the bare nucleon current, times an amplitude that depends on the bound and ejected nucleon wave functions.

Factorization in J^{μ}_{EMA} occurs if $A^{\mu_b}_{sh}(\boldsymbol{p}_F,\boldsymbol{q})$ does not depend on the spin variables s and h.

Before entering into a detailed discussion of the observables, it is important to stress again that factorization may only be achieved assuming EMA and/or asymptotic projection, i.e., neglecting dynamical enhancement of the lower components in the nucleon wave functions. This is a priori assumed within some nonrelativistic calculations.

2.3 Analysis of observables within EMA

In this section we investigate the conditions that lead to factorization of polarized and unpolarized observables. Response functions, transverse-longitudinal asymmetry, electron analyzing power, as well as induced and transferred polarizations are examined. The analysis is made directly at the level of the hadronic tensor which, within the EMA approach, can be written in the following way:

$$\begin{aligned} W^{\mu\nu}_{EMA} &= \frac{1}{2j_b+1}\sum_{\mu_b}\left(J^{\mu}_{EMA}\right)^* J^{\nu}_{EMA} \\ &= \sum_{ss'}\sum_{hh'}\left[J^{\mu}_{bare}(\boldsymbol{p}_F s,\boldsymbol{p}_I h)\right]^* J^{\nu}_{bare}(\boldsymbol{p}_F s',\boldsymbol{p}_I h') \\ &\times \frac{1}{2j_b+1}\sum_{\mu_b}\left[A^{\mu_b}_{sh}(\boldsymbol{p}_F,\boldsymbol{q})\right]^* A^{\mu_b}_{s'h'}(\boldsymbol{p}_F,\boldsymbol{q})\,. \end{aligned} \tag{2.23}$$

Note that in Eq. (2.23) s, s' are the spin variables corresponding to the outgoing nucleon, while h, h' correspond to the bound nucleon.

In order to simplify the analysis that follows, the general expression of the hadronic tensor can be written in a more compact form as

$$W^{\mu\nu}_{EMA} = \sum_{ss'}\sum_{hh'}\mathcal{W}^{\mu\nu}_{ss',hh'}X^{s_F}_{ss',hh'}(\boldsymbol{p}_F,\boldsymbol{q})\,, \tag{2.24}$$

where we have introduced a general bare-nucleon tensor $\mathcal{W}^{\mu\nu}_{ss',hh'}$,

$$\mathcal{W}^{\mu\nu}_{ss',hh'} = \left(J^{\mu}_{bare}\right)^* J^{\nu}_{bare} = \left[\overline{u}(\boldsymbol{p}_F,s)\widehat{J}^{\mu}u(\boldsymbol{p}_I,h)\right]^*\left[\overline{u}(\boldsymbol{p}_F,s')\widehat{J}^{\nu}u(\boldsymbol{p}_I,h')\right]\,, \tag{2.25}$$

and a general spin dependent momentum distribution function $X^{s_F}_{ss',hh'}$,

$$\begin{aligned} X^{s_F}_{ss',hh'}(\boldsymbol{p}_F,\boldsymbol{q}) &= \frac{1}{2j_b+1}\sum_{\mu_b}\left[A^{\mu_b}_{sh}(\boldsymbol{p}_F,\boldsymbol{q})\right]^* A^{\mu_b}_{s'h'}(\boldsymbol{p}_F,\boldsymbol{q}) \\ &= \frac{1}{2j_b+1}\sum_{\mu_b}\sum_{\kappa\mu m}\sum_{\kappa'\mu' m'}\langle \ell m\tfrac{1}{2}s_F|j\mu\rangle\langle \ell' m'\tfrac{1}{2}s_F|j'\mu'\rangle Y^{m}_{\ell}(\widehat{\boldsymbol{p}}_F)Y^{m'*}_{\ell'}(\widehat{\boldsymbol{p}}_F) \end{aligned}$$

$$\times \sum_{m_{\ell_b} m_\ell} \sum_{m'_{\ell_b} m'_\ell} \langle \ell_b m_{\ell_b} \frac{1}{2} h | j_b \mu_b \rangle \langle \ell m_\ell \frac{1}{2} s | j \mu \rangle \langle \ell_b m'_{\ell_b} \frac{1}{2} h' | j_b \mu_b \rangle \langle \ell' m'_\ell \frac{1}{2} s' | j' \mu' \rangle$$

$$\times U^{\kappa\, m_\ell *}_{\kappa_b\, m_{\ell_b}}(\boldsymbol{p}_F, \boldsymbol{q})\, U^{\kappa'\, m'_\ell}_{\kappa_b\, m'_{\ell_b}}(\boldsymbol{p}_F, \boldsymbol{q})\,. \tag{2.26}$$

Making use of general symmetry properties (see Appendix A), the bare-nucleon tensor in Eq. (2.25) can be decomposed into terms which are symmetric and antisymmetric under interchange of μ and ν. Each of these terms shows a different dependence on the spin variables: ss' and/or hh'. Explicitly, the bare nucleon tensor can be written in the form

$$\mathcal{W}^{\mu\nu}_{ss',hh'} = \mathcal{S}^{\mu\nu}\, \delta_{ss'}\, \delta_{hh'} + \mathcal{A}^{\mu\nu}_{hh'}\, \delta_{ss'} + \mathcal{A}^{\mu\nu}_{ss'}\, \delta_{hh'} + \mathcal{S}^{\mu\nu}_{ss',\, hh'}\,, \tag{2.27}$$

where $\mathcal{S}$ ($\mathcal{A}$) refers to symmetric (antisymmetric) tensors. Notice that the first (symmetric) term in Eq. (2.27) does not depend on the initial bound neither on the final outgoing nucleon spin variables; the antisymmetric second (third) term depends solely on the initial (final) spin projections; finally, the fourth (symmetric) term presents dependence on both initial and final nucleon spin projections simultaneously. This bare-nucleon tensor would lead to the σ_{ep} cross section in Eq. (2.10).

The general result for the bare nucleon tensor given in Eq. (2.27) constitutes the starting point for the analysis of factorization for polarized as well as unpolarized observables. In what follows we explore the specific conditions, linked to the spin dependence in the problem, that lead to *factorized* results. We investigate separately the role played by the dependence on the initial and/or final nucleon spin variables. As we show in next subsections, the factorization property at the level of spin-averaged squared matrix elements is intimately connected with the spin dependence: a bound nucleon in a s-wave or, in general, no spin-orbit coupling effects on the radial nucleon wave functions, may lead for some specific observables to exactly *factorized* results. As it is clear from the analogy between Eq. (2.16) and Eq. (2.1) with the input from Eq. (2.13), the analysis of spin dependence here and in what follows is also valid for the nonrelativistic case.

2.3.1 No spin-orbit in the initial state

The general expression of $X^{s_F}_{ss',hh'}$ (2.26) is greatly simplified for no spin-orbit in the initial state or, more generally in LS coupling. For instance in the case of nucleon knockout from s-shells the orbital angular momentum $\ell_b = 0$ and the spin dependent momentum distribution is simply given by

$$X^{s_F}_{ss',hh'}(\boldsymbol{p}_F, \boldsymbol{q}) = N^{s_F}_{ss'}(\boldsymbol{p}_F, \boldsymbol{q})\, \delta_{hh'}\,, \tag{2.28}$$

with

$$N^{s_F}_{ss'}(\boldsymbol{p}_F,\boldsymbol{q}) = \frac{1}{2j_b+1}\sum_{\kappa\mu m}\sum_{\kappa'\mu' m'}\langle \ell m \frac{1}{2} s_F | j\mu\rangle\langle \ell' m' \frac{1}{2} s_F | j'\mu'\rangle Y^m_\ell(\widehat{\boldsymbol{p}}_F) Y^{m'*}_{\ell'}(\widehat{\boldsymbol{p}}_F) \times \sum_{m_\ell m'_\ell}\langle \ell m_\ell \frac{1}{2} s | j\mu\rangle\langle \ell' m'_\ell \frac{1}{2} s' | j'\mu'\rangle U^{\kappa\, m_\ell *}_{-1\,0}(\boldsymbol{p}_F,\boldsymbol{q})\, U^{\kappa'\, m'_\ell}_{-1\,0}(\boldsymbol{p}_F,\boldsymbol{q})\,. \quad (2.29)$$

In the case of no spin-orbit coupling with $\ell_b \neq 0$ waves, a similar reduction to Eq. (2.28) follows after summation of the spin dependent momentum distribution X on $j_b = \ell_b \pm 1/2$.

Making use of Eqs. (2.27) and (2.28), the hadronic tensor in EMA becomes

$$W^{\mu\nu}_{EMA} = \sum_{ss'} N^{s_F}_{ss'}\left[\sum_h \mathcal{W}^{\mu\nu}_{ss',hh}\right] = \sum_{ss'} N^{s_F}_{ss'}\left[\mathcal{S}^{\mu\nu}\,\delta_{ss'} + \mathcal{A}^{\mu\nu}_{ss'}\right] = \mathcal{S}^{\mu\nu}\sum_s N^{s_F}_{ss} + \sum_{ss'} N^{s_F}_{ss'}\mathcal{A}^{\mu\nu}_{ss'}\,. \quad (2.30)$$

From this result it clearly emerges that those responses coming from the symmetric tensor $\mathcal{S}^{\mu\nu}$ factorize, while the ones coming from the antisymmetric part do not. Let us signal out more precisely what factorization really means in this situation.

First, note that the momentum distribution function $\sum_s N^{s_F}_{ss}$ that multiplies the symmetric tensor depends on the outgoing nucleon spin s_F. In the case when recoil nucleon polarization is not measured, an extra sum in s_F has to be carried out and hence the momentum distribution, which is independent of s_F, gives rise to the unpolarized responses R^L, R^T, R^{TL} and R^{TT} in Eq. (2.8). On the other hand, if the spin of the outgoing proton is measured via a polarimeter placed along a fixed direction ($\boldsymbol{l}$, $\boldsymbol{n}$ or $\boldsymbol{s}$), the momentum distribution, now dependent on the final spin, contributes to the induced polarized responses: R^L_n, R^T_n, $R^{TL}_{n,l,s}$ and $R^{TT}_{n,l,s}$. Hence, in the case of no spin-orbit coupling in the initial bound state, both types of responses (unpolarized and induced polarized) factorize, but each kind of response factorizes with a different momentum distribution function. Then, the induced polarization asymmetries P_k ($k = l, n, s$), which are basically given by the ratio between the induced polarized responses R^α_k and the unpolarized ones R^α, will differ from the bare result. On the contrary, the momentum distribution functions cancel when taking a ratio between two responses of the same kind, i.e., a ratio between two induced polarized responses along a specific direction, or a ratio between two unpolarized responses. Therefore such ratios would coincide with the bare results. This property can be expressed in the general form

$$\frac{R^\alpha_k}{R^\beta_k} = \frac{R^\alpha}{R^\beta} = \frac{\mathcal{R}^\alpha}{\mathcal{R}^\beta}\,, \quad (2.31)$$

where $\alpha, \beta = L, T, TL$ or TT and $k = l, n, s$ fixes the recoil nucleon polarization direction. The functions $\mathcal{R}^{\alpha,\beta}$ represent the bare-nucleon responses, also usually named single-nucleon responses [21]. The result in Eq. (2.31) explains also why the A_{TL} asymmetry, which is obtained from the difference of electron unpolarized cross sections measured at $\phi_F = 0°$ and $\phi_F = 180°$ divided by the sum, is identical to the bare asymmetry in this case. In terms of response functions we may write

$$A_{TL} = \frac{v_{TL} R^{TL}}{v_L R^L + v_T R^T + v_{TT} R^{TT}} = \frac{v_{TL} \mathcal{R}^{TL}}{v_L \mathcal{R}^L + v_T \mathcal{R}^T + v_{TT} \mathcal{R}^{TT}} = A_{TL}^{bare} \,. \tag{2.32}$$

To complete the discussion, we note that the electron analyzing power and transferred polarization asymmetries involve responses coming from the antisymmetric part of the tensor (2.30), which do not factorize, divided by unpolarized responses obtained from the symmetric tensor term. Therefore the behaviour of A and P'_k will differ from the bare one. The amount of discrepancy between the factorized and unfactorized calculations of different observables is discussed in Sec. 2.5.

2.3.2 No spin-orbit in the final state

Let us consider now the case of no spin-orbit coupling effects on the radial wave function of the outgoing proton. In this case neither δ_κ nor g_κ in Eqs. (2.4), (2.18) depend on j. After some algebra (see Appendix B for details), this condition leads to $s = s' = s_F$ in the bare-nucleon tensor, and therefore the momentum distribution depends only on the hh' spin variables of the initial nucleon. The hadronic tensor is then given by

$$W^{\mu\nu}_{EMA} = \sum_{hh'} \mathcal{W}^{\mu\nu}_{s_F s_F, hh'} \widetilde{N}_{hh'}(\boldsymbol{p}_F, \boldsymbol{q}) \,, \tag{2.33}$$

where the momentum distribution function $\widetilde{N}_{hh'}(\boldsymbol{p}_F, \boldsymbol{q})$ is defined in Eq. (2.56) of Appendix B. Using the decomposition in Eq. (2.27), we can write the following expression

$$W^{\mu\nu}_{EMA} = \left[\mathcal{S}^{\mu\nu} + \mathcal{A}^{\mu\nu}_{s_F s_F}\right] \sum_h \widetilde{N}_{hh} + \sum_{hh'} \left[\mathcal{S}^{\mu\nu}_{s_F s_F, hh'} + \mathcal{A}^{\mu\nu}_{hh'}\right] \widetilde{N}_{hh'}. \tag{2.34}$$

The analysis of how polarized or unpolarized responses behave with respect to factorization emerges straightforwardly from Eq. (2.34). Let us discuss each case separately:

- Unpolarized responses: R^L, R^T, R^{TL} and R^{TT}. They do not depend on spin and come from the symmetric part of the tensor, i.e., they are given by $\mathcal{S}^{\mu\nu} \sum_h \widetilde{N}_{hh}$, and hence factorize exactly. This result coincides with that one obtained in the nonrelativistic study of Ref. [3].

- Transferred polarization responses: $R_{l,s}^{T'}$ and $R_{l,s,n}^{TL'}$. They come from the antisymmetric part of the tensor and depend on the final proton spin polarization, i.e., $\mathcal{A}_{s_F s_F}^{\mu\nu} \sum_h \widetilde{N}_{hh}$, in exactly the same form as displayed in Eq. (2.27). Consequently, these responses also factorize.

- Fifth response $R^{TL'}$. It comes from the antisymmetric part of the tensor and does not depend on the recoil nucleon spin, i.e., it is given by $\sum_{hh'} \widetilde{N}_{hh'} \mathcal{A}_{hh'}^{\mu\nu}$ and clearly does not factorize.

- Induced polarized responses: R_n^L, R_n^T, $R_{n,l,s}^{TL}$ and $R_{n,l,s}^{TT}$. They come from the symmetric tensor part and depend explicitly on the spin polarization of the outgoing proton, i.e., they are constructed from $\sum_{hh'} \widetilde{N}_{hh'} \mathcal{S}_{s_F s_F, hh'}^{\mu\nu}$, and consequently do not factorize.

Once the behaviour of the response functions is established, the asymmetries and polarization ratios can be easily analyzed. The case of A_{TL}, which only depends on the unpolarized responses, reduces to A_{TL}^{bare} (see Eq. (2.32)). A similar comment applies also to the transferred nucleon polarizations P_l', P_s' and P_n'. Notice that the momentum distribution function involved in the unpolarized and transferred polarized responses is the same and hence, it cancels when forming the polarization ratios. The electron analyzing power A and induced asymmetries P_k, given in terms of responses which do not factorize, should differ from the bare calculations.

As a particular case of no spin-orbit in the final nucleon wave function, it is worth to explore the plane wave limit for the outgoing nucleon. In this case (see Eq. (2.58) in Appendix B), the momentum distribution $\widetilde{N}_{hh'}^{PW}$ is diagonal and independent on h, thus the fifth response $R^{TL'}$ vanishes since $\sum_h \mathcal{A}_{hh}^{\mu\nu} = 0$. Similarly, the induced polarization responses do not contribute because $\sum_h \mathcal{S}_{s_F s_F, hh}^{\mu\nu} = 0$.

2.3.3 No spin-orbit in both initial and final states

To finish with this analysis, let us consider the case of no spin-orbit coupling in the initial nor in the final state. In this situation, factorization already comes out at the level of the nuclear current matrix element. Note that $\ell_b = 0$ in Eq. (2.54) of Appendix B, leads to $h = \mu_b$ and the matrix element simply reads

$$J_{EMA}^{\mu} = \overline{u}(\boldsymbol{p}_F, s_F) \widehat{J}^{\mu} u(\boldsymbol{p}_I, \mu_b)\, U_{-1}^0(\boldsymbol{p}_F, \boldsymbol{q})\,, \tag{2.35}$$

where U^0_{-1} is defined in Eq. (2.55). This result resembles the situation occurring in the free case. From the current (2.35) the hadronic tensor can be written in the form

$$W^{\mu\nu}_{EMA} = \frac{1}{2}\left|U^0_{-1}(\boldsymbol{p}_F,\boldsymbol{q})\right|^2 \sum_{\mu_b} \mathcal{W}^{\mu\nu}_{s_F s_F,\mu_b\mu_b} = \frac{1}{2}\left|U^0_{-1}(\boldsymbol{p}_F,\boldsymbol{q})\right|^2 \left(\mathcal{S}^{\mu\nu} + \mathcal{A}^{\mu\nu}_{s_F s_F}\right) . \tag{2.36}$$

Then all responses (polarized and unpolarized) factorize with the same momentum distribution. Note also that the whole dependence on the nucleon polarization s_F is contained in the antisymmetric tensor. This implies that the polarized induced responses must be zero. Furthermore, since $\sum_{s_F} \mathcal{A}^{\mu\nu}_{s_F s_F} = 0$ the unpolarized fifth response $R^{TL'}$ also vanishes.

2.4 Reduced cross sections and momentum distributions

Starting from a shell model approach, the relativistic (vector) momentum distribution is defined as follows:

$$N(p_I) = \frac{1}{2j_b+1}\sum_{\mu_b} \psi^{\mu_b\dagger}_{\kappa_b}(\boldsymbol{p}_I)\psi^{\mu_b}_{\kappa_b}(\boldsymbol{p}_I) = \frac{1}{4\pi}\left[g^2_{\kappa_b}(p_I) + f^2_{\kappa_b}(p_I)\right] . \tag{2.37}$$

Using the EMA approximation means projecting out the negative energies components of the bound proton wave function, obtaining then the relativistic EMA momentum distribution:

$$N^{EMA}(p_I) = \frac{1}{2j_b+1}\sum_{\mu_b} \psi^{\mu_b EMA\dagger}_{\kappa_b}(\boldsymbol{p}_I)\psi^{\mu_b EMA}_{\kappa_b}(\boldsymbol{p}_I) = \frac{1}{4\pi}\frac{2E_I}{E_I+M} g^2_{\kappa_b}(p_I) , \tag{2.38}$$

this expression reduces to the nonrelativistic momentum distribution in the proper limit because of its lack of contribution from negative energies.

In general, in a nonrelativistic formalism, the momentum distribution is defined from bispinors $\chi^{\mu_b}_{j_b}(\boldsymbol{r})$, solutions of Schrödinger-like equation:

$$N_{NR}(p_I) = \frac{1}{2j_b+1}\sum_{\mu_b} \chi^{\mu_b\dagger}_{j_b}(\boldsymbol{p}_I)\chi^{\mu_b}_{j_b}(\boldsymbol{p}_I) , \tag{2.39}$$

with $\chi^{\mu_b}_{j_b}(\boldsymbol{p}_I)$ the Fourier transform of $\chi^{\mu_b}_{j_b}(\boldsymbol{r})$,

$$\chi^{\mu_b}_{j_b}(\boldsymbol{p}_I) = \frac{1}{(2\pi)^{3/2}}\int d\boldsymbol{r}\, e^{-i\boldsymbol{p}_I\cdot\boldsymbol{r}}\, \chi^{\mu_b}_{j_b}(\boldsymbol{r}) . \tag{2.40}$$

Now, in nonrelativistic PWIA, the wave function for the ejected proton in the $\boldsymbol{r}$-space is

$$\chi^{s_F PW}_F(\boldsymbol{r}) = e^{i\boldsymbol{p}_F\cdot\boldsymbol{r}}\, \chi^{s_F}_{\frac{1}{2}} , \tag{2.41}$$

and looking at the the Fourier transform in Eq. (2.40), it is natural to define a nonrelativistic distorted wave amplitude as follows:

$$\chi_{DW}(\boldsymbol{p}_F, \boldsymbol{q}) \equiv \frac{1}{(2\pi)^{3/2}} \int d\boldsymbol{r}\, \chi_F^{s_F\dagger}(\boldsymbol{r})\, e^{i\boldsymbol{q}\cdot\boldsymbol{r}}\, \chi_{j_b}^{\mu_b}(\boldsymbol{r})\,. \tag{2.42}$$

Two observations are worth mentioning:

1. $\chi_{DW}(\boldsymbol{p}_F, \boldsymbol{q})$ is an amplitude, not a bispinor.

2. If the final proton wave function is a plane wave, the following relationship is satisfied:

$$\sum_{s_F} |\chi_{PW}(\boldsymbol{p}_F, \boldsymbol{q})|^2 = \chi_{j_b}^{\mu_b\dagger}(\boldsymbol{p}_I)\chi_{j_b}^{\mu_b}(\boldsymbol{p}_I)\,. \tag{2.43}$$

So, we can define a nonrelativistic distorted momentum distribution

$$\rho_{DW}^{NR}(\boldsymbol{p}_F, \boldsymbol{q}) = \frac{1}{2j_b+1} \sum_{\mu_b} \sum_{s_F} |\chi_{DW}(\boldsymbol{p}_F, \boldsymbol{q})|^2\,, \tag{2.44}$$

that takes into account FSI, and has the property that we recover the nonrelativistic momentum distribution in Eq. (2.39) in the plane wave limit.

Let us generalize the above expression to the relativistic case. We request that we recover from it the relativistic EMA momentum distribution of Eq. (2.38) when there is not FSI and the initial wave function is evaluated within EMA. For that purpose we define a relativistic distorted wave amplitude,

$$\psi_{DW}(\boldsymbol{p}_F, \boldsymbol{q}) \equiv \frac{K}{(2\pi)^{3/2}} \int d\boldsymbol{r}\, \psi_F^{s_F\dagger}(\boldsymbol{r})\, e^{i\boldsymbol{q}\cdot\boldsymbol{r}}\, \psi_{\kappa_b}^{\mu_b}(\boldsymbol{r}) = \frac{K}{(2\pi)^{3/2}} \int d\boldsymbol{p}\, \psi_F^{s_F\dagger}(\boldsymbol{p}+\boldsymbol{q})\psi_{\kappa_b}^{\mu_b}(\boldsymbol{p}) \tag{2.45}$$

with $K = \sqrt{(2E_IE_F)/(E_IE_F + \boldsymbol{p}_I\cdot\boldsymbol{p}_F + M^2)}$, so that the relativistic distorted momentum distribution is given by this amplitude squared after sum and average over initial and final spins,

$$\rho_{DW}(\boldsymbol{p}_F, \boldsymbol{q}) = \frac{1}{2j_b+1} \sum_{\mu_b} \sum_{s_F} |\psi_{DW}(\boldsymbol{p}_F, \boldsymbol{q})|^2\,. \tag{2.46}$$

It is easy to check that $\rho_{DW}(\boldsymbol{p}_F, \boldsymbol{q})$ coincides with the relativistic EMA momentum distribution Eq. (2.38), when one takes EMA approximation for the initial wave function and the plane wave limit for the final one,

$$\rho_{PW}^{EMA}(\boldsymbol{p}_F, \boldsymbol{q}) = N^{EMA}(p_I)\,. \tag{2.47}$$

It is also important to remark that $\rho_{DW}(\boldsymbol{p}_F, \boldsymbol{q})$ coincides with the corresponding reduced cross section of Eq. (2.12) whenever there is factorization.

2.5 Numerical results

To show quantitatively the effects introduced by the different approaches to the general description of $(\vec{e}, e'\vec{p})$ reactions, we compare our fully RDWIA calculations with the EMA results, exploring also the effects introduced by the spin variables in the initial and final nucleon states. The results presented in this section illustrate and reinforce the conclusions reached in the preceding sections concerning the factorization properties.

Guided by the factorization properties one may focus on two different aspects in the analysis of observables.

1. On the one hand, one may factor out the elementary electron-proton electromagnetic cross section, in order to isolate and investigate nuclear properties like momentum distributions.

   To the extent that factorization holds the reduced cross section will follow the momentum distribution. In the first part of this section we compare factorized and unfactorized results for the reduced cross section to the momentum distribution. We show how the different ingredients that break factorization may obscure the extraction of momentum distributions.

   First of all, we note that since FSI modify the response of the ejected nucleon, it is more adequate to compare reduced cross sections with distorted momentum distributions (as defined in the previous section). This is done in Fig. 2.1 that we discuss below.

2. On the other hand, one may take ratios between observables to cancel out the dependence on the momentum distribution, in order to isolate and investigate intrinsic nucleon properties in the nuclear medium, like nucleon form factors.

In Fig. 2.1 we present reduced cross sections at quasielastic kinematics for three cases: complete RDWIA approach (solid line), EMA (dashed line) and EMA with no spin dependence in the final state, referred to as EMA-noLS (dotted line). We also show by a thin solid line the distorted momentum distributions (ρ_{DW}, Eq. (2.46)) which are equivalent to what one would obtain from a factorized approach to RDWIA. Note that up to $|p_m|$ of around 250 MeV/c, the factorized approach ρ_{DW} follows reasonably well the full calculation. Actually in this p_m range, EMA and EMA-noLS are also reasonable approximations to the complete calculation. However, at $|p_m| > 250$ MeV/c the full approach produces

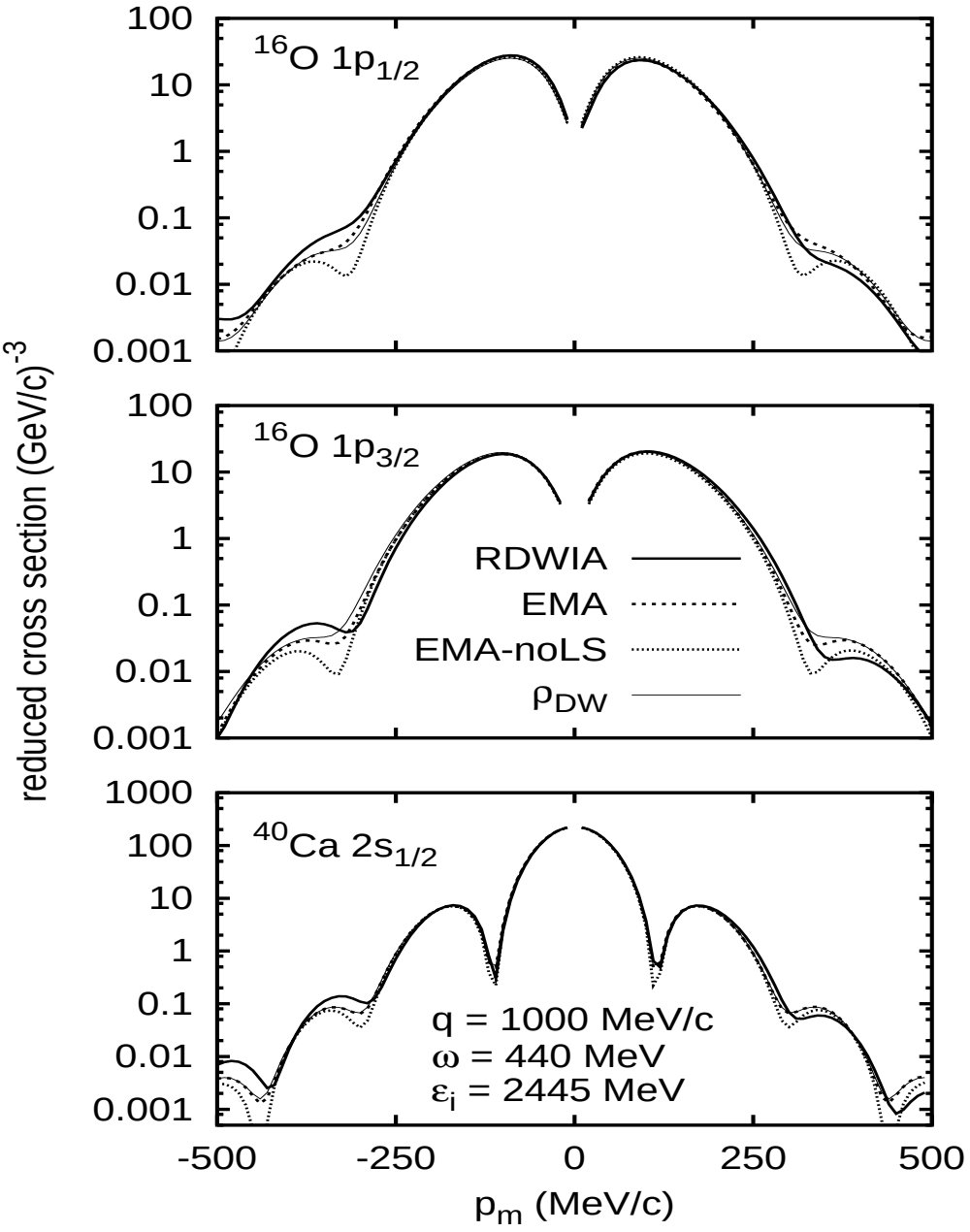

Figura 2.1: Reduced cross section for proton knockout from $1p_{1/2}$ (upper panel) and $1p_{3/2}$ (middle panel) in ^{16}O and from $2s_{1/2}$ in ^{40}Ca (lower panel). RDWIA calculations (solid line) are compared to EMA (short-dashed line) and EMA-noLS (dotted line) results. The corresponding relativistic distorted wave momentum distribution is also plotted (thin solid line). Negative (positive) p_m values correspond to $\phi_F = 0°$ (180°) respectively.

more reduced cross section for $p_m < 0$ than for $p_m > 0$, leading to a much larger asymmetry in this region as we would see in Fig. 2.2. We also note that differences between complete RDWIA reduced cross section and ρ_{DW} (hence deviations from factorization) are more noticeable at $|p_m| > 250$ MeV/c in the $p_m < 0$ region. Nonrelativistic calculations would generally yield results on the line of the EMA ones presented here. Note also that, the reduced cross section in EMA practically coincides with ρ_{DW} for the $s_{1/2}$ orbital in ^{40}Ca, and even in the ^{16}O $p_{1/2}$ and $p_{3/2}$ orbitals the reduced cross sections in EMA and ρ_{DW} are rather close in the whole p_m range.

In Figs. 2.2 to 2.4 we show the TL asymmetry, electron analyzing power, induced polarization and transferred polarizations, respectively, for proton knockout from the $p_{1/2}$ (left panels), $p_{3/2}$ (middle) in ^{16}O and $s_{1/2}$ (right) shells in ^{40}Ca. Results are computed for CC2 current operator and Coulomb gauge. The bound nucleon wave function corresponds to the set NLSH [24–27] and the outgoing nucleon wave function has been derived using the EDAIO relativistic optical potential parameterization [28]. As in the previous figure, the selected kinematics corresponds to the experimental conditions of the experiments E89003 and E89033 performed at Jlab [29–31]. This is (q, ω) constant kinematics with $q = 1$ GeV/c, $\omega = 440$ MeV and the electron beam energy fixed to $\varepsilon_i = 2.445$ GeV. Coplanar kinematics, with $\phi_F = 0°$, are chosen for computing the polarization asymmetries. Therefore, as $P_l = P_s = P'_n = 0$ when $\phi_F = 0°$, they are not plotted. In each graph, we show five curves corresponding to the following approaches: RDWIA (solid), RDWIA but without spin-orbit coupling in the final nucleon state, denoted as RDWIA-noLS (dashed), EMA (short-dashed), EMA-noLS (dotted), and finally the *factorized* result (dash-dotted).

As shown in Sec. 2.3, factorization only holds within the EMA approach and assuming specific conditions on the spin dependence in the problem. In Table 2.1 we summarize the basic assumptions within EMA that lead to factorization for the different observables. To simplify the discussion of the results that follows we consider each observable separately.

The asymmetry A_{TL}, presented in Fig. 2.2, shows that factorization emerges within EMA in the case of the $s_{1/2}$ shell (where EMA, EMA-noLS and *factorized* results coincide). For spin-orbit dependent bound states ($p_{1/2}$ and $p_{3/2}$), factorization emerges only when there is no spin-orbit coupling in the final state (EMA-noLS coincides with *factorized* results). Also note that the oscillatory behaviour shown by A_{TL} in RDWIA and in RDWIA-noLS is almost entirely lost within EMA, even when there is no factorization. This reflects the crucial role played by the dynamical enhancement of the lower components of the nucleon wave functions for this observable. The spin dependence in the final

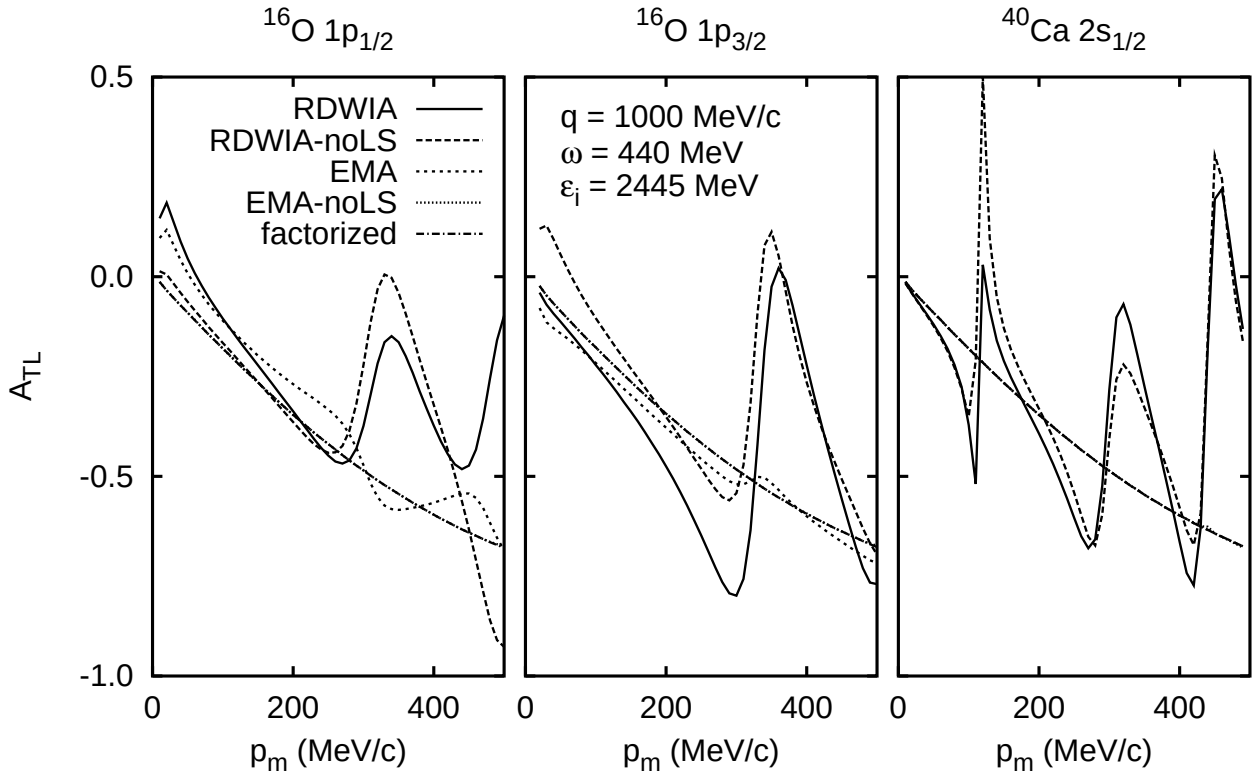

Figura 2.2: A_{TL} asymmetry for proton knockout from $1p_{1/2}$ (left panel) and $1p_{3/2}$ (middle panel) in ^{16}O and from $2s_{1/2}$ in ^{40}Ca (right panel). RDWIA calculations (solid line) are compared to RDWIA-noLS (dashed line), EMA (short-dashed line), EMA-noLS (dotted line) and factorized (dash-dotted line) results. The EMA-noLS calculation coincides in all panels with the factorized (A_{TL}^{bare}) result. In the right hand panel EMA, as well as EMA-noLS, coincides with the factorized (A_{TL}^{bare}).

	no LS initial	no LS final	no LS both
A_{TL}	A_{TL}^{bare}	A_{TL}^{bare}	A_{TL}^{bare}
A	—	—	0
P_n	—	—	0
P_l	—	—	0
P_s	—	—	0
P'_n	—	$P_n^{'bare}$	$P_n^{'bare}$
P'_l	—	$P_l^{'bare}$	$P_l^{'bare}$
P'_s	—	$P_s^{'bare}$	$P_s^{'bare}$

Tabla 2.1: Properties of factorization of different observables using the EMA approximation and turning off the spin-orbit coupling in the initial wave function (first column), in the final wave function (second column) or in both simultaneously (third column).

nucleon state modifies significantly the values of A_{TL} even at low missing momentum, but preserves its general oscillatory structure, compare for instance RDWIA vs RDWIA-noLS or EMA vs EMA-noLS.

The electron analyzing power A is presented in Fig. 2.3. This observable is zero in coplanar kinematics so the azimuthal angle is fixed to $\phi_F = 225°$ in Fig. 2.3, but the remarks that follow also apply to other $\phi_F \neq 0°, 180°$ values. As we demonstrated in Sec. 2.3, the fifth response $R^{TL'}$ involved in A only factorizes if there is no spin-orbit contribution in the initial and final nucleon wave functions. Moreover, in such situation $R^{TL'} = 0$ and hence $A = 0$, as occurs for $s_{1/2}$ shell within EMA-noLS in Fig. 2.3. From a careful inspection of Fig. 2.3 we also observe that the main differences between the various approaches come from the spin-orbit term in the final state. Note that the discrepancy between RDWIA and EMA (or likewise between RDWIA-noLS and EMA-noLS) is significantly smaller than the discrepancy between RDWIA and RDWIA-noLS (or EMA vs EMA-noLS). In all of the cases with $A \neq 0$, oscillations survive. The behaviour of A contrasts with the one observed for the asymmetry A_{TL}. This is due to the fact that factorization is broken down already at the EMA level even in the $s_{1/2}$ shell.

The induced polarization P_n is presented in Fig. 2.4. Here the discussion of results follows similar trends to the previous one on A. Factorization requires no spin dependence in any of the nucleon wave functions, being the induced polarized responses equal to zero

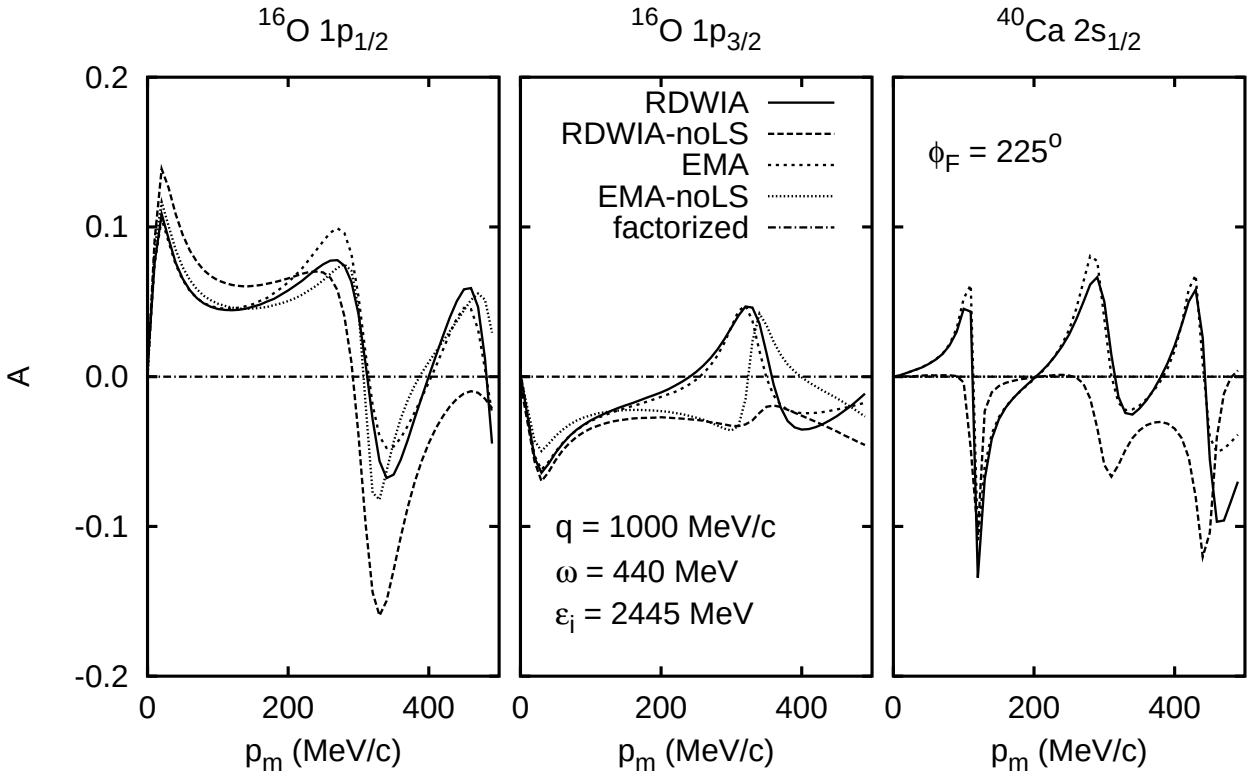

Figura 2.3: Electron analyzing power A at (q, ω) constant kinematics and azimuthal angle $\phi_F = 225°$. The labeling of the curves is as in Fig. 2.2. For this observable factorization is only achieved in the EMA-noLS curve on the right hand panel. See text for details.

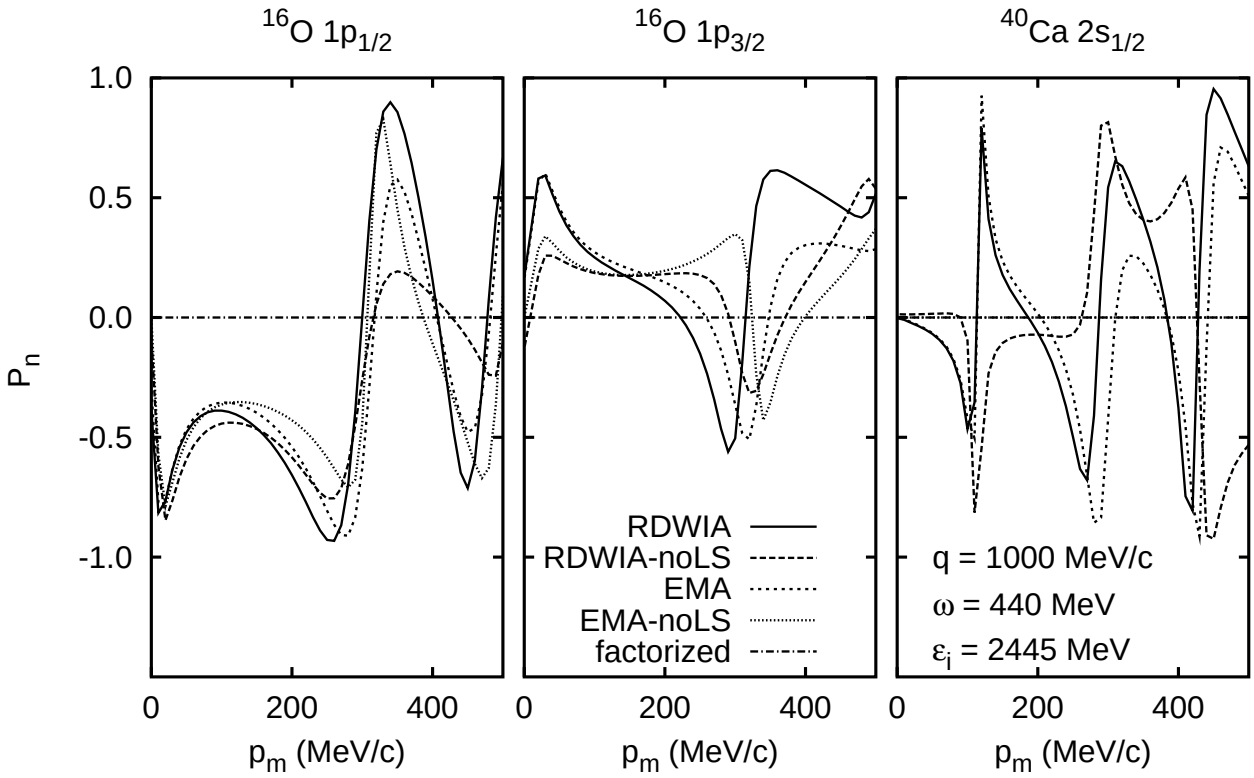

Figura 2.4: Induced polarization P_n at coplanar kinematics with $\phi_F = 0°$. Kinematics and labeling as in Fig. 2.2. Only the EMA-noLS calculation for a $s_{1/2}$ shell factorizes.

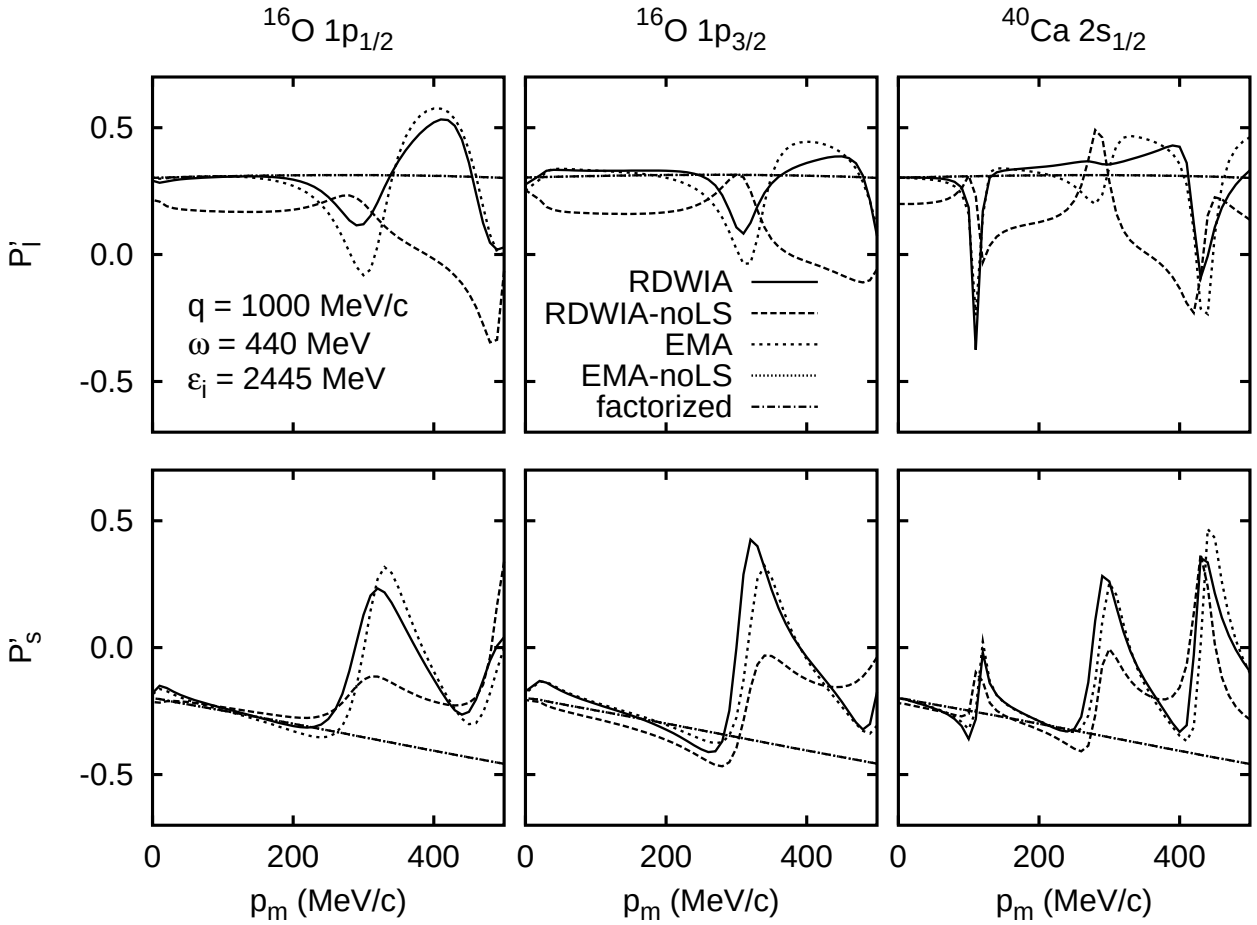

Figura 2.5: Longitudinal transferred polarization P'_l (top panels) and sideways transferred polarization P'_s (bottom panels) at coplanar kinematics ($\phi_F = 0°$). In this case, factorization is obtained within the EMA approach when there is no spin-orbit coupling in the final state (EMA-noLS, dotted line).

in such a case (notice that P_n is zero in the plane wave limit). In any other situation factorization breaks down and P_n shows strong oscillations in all cases. Again, it is important to point out that the behaviour of the RDWIA calculation is qualitatively followed by the EMA approach, differing much more from the RDWIA-noLS or EMA-noLS. This reveals the important effects introduced by the spin-orbit coupling in the optical potential for polarized observables, contrary to what happens for the unpolarized A_{TL}.

The comment above applies also to the transferred polarizations P'_l and P'_s (Fig. 2.5) for which RDWIA and EMA approaches give rise to rather similar oscillating (unfactorized) results. On the contrary, RDWIA-noLS, which is also unfactorized, deviates significantly from RDWIA due to the crucial role of the spin-orbit dependence in the final state. Finally, EMA-noLS coincides with the bare asymmetries showing a flat behaviour without oscillations. This is in accord with the findings in Sec. 2.3.2, where we demonstrated that the unpolarized R^α and transferred polarized $R^{\alpha'}_{l,s}$ responses factorize with the same momentum distribution function (see Table 2.1 and Eq. (2.34)).

2.6 Summary and conclusions

A systematic study of the property of factorization in quasielastic $(\vec{e}, e'\vec{p})$ reactions has been presented. Starting from a RDWIA analysis, we have reformulated the EMA approach and studied the conditions which are needed to get factorization. In this context, we have explored the role of the spin-orbit coupling in the initial and/or final nucleon states and its influence on the breakdown of factorization.

From our general study we conclude that exact factorization only emerges within the EMA approach, i.e., neglecting the dynamical enhancement of the lower components in the nucleon wave functions by using Eq. (2.13). Furthermore, additional restrictions on the spin dependence in the problem are necessary to get factorization in the case of polarized observables.

Within the EMA approach, the factorization properties of various $(\vec{e}, e'\vec{p})$ responses and asymmetries are as follows (see also Table 2.1):

The unpolarized R^α responses factorize to a single, polarization independent, momentum distribution when the initial *or* the final nucleon wave functions are independent on spin-orbit coupling (i.e., depend on ℓ but not on j). As a consequence, the A_{TL} asymmetry is in these cases given by the bare-nucleon A_{TL}^{bare} asymmetry.

The fifth response $R^{TL'}$ (and consequently A), depending on electron beam polarization, never factorizes, but becomes zero when both initial and final nucleon wave functions are independent on spin-orbit coupling, as well as in the nonrelativistic plane wave limit (PWIA).

The transferred polarization responses $R_k^{\alpha'}$ factorize when the final nucleon wave function is independent on j. Consequently the transferred polarizations are in this case given by the bare-nucleon ones, independent on whether the initial state may or may not depend on spin-orbit coupling.

The induced polarized responses R_k^{α} do not factorize even when the final nucleon wave function is independent on j, unless the initial wave function is also independent on j, in which case R_k^{α} become zero. If the final wave function depends on spin-orbit coupling but the initial wave function does not, the induced polarized responses factorize with a polarization-dependent momentum distribution different from the unpolarized one. Therefore, as stated in Eq. (2.31), a new factorization property emerges when there is no spin-orbit coupling in the initial state.

From our numerical calculations a clear difference in the behaviour of polarized and unpolarized observables comes out. In the case of the unpolarized A_{TL} asymmetry, its general structure is not substantially modified by the final spin-orbit dependence, being much more affected by the lower components of the nucleon states. The *strong* oscillations in A_{TL} within RDWIA practically vanish in EMA. On the contrary, the polarized asymmetries A, P_n and $P'_{l,s}$, present a very strong sensitivity to the final spin dependence, while the general structure of the RDWIA results is preserved by the EMA calculations.

As a general conclusion, we can say that observables that require less extra assumptions (apart from EMA) to factorize, are more sensitive to any ingredient of the calculation that breaks factorization. Such observables are good candidates to test the elements of any model/calculation, as it is the case of the A_{TL} asymmetry.

In spite of the fact that factorization is not reached when realistic calculations are made, we show that the reduced cross sections extracted from fully unfactorized calculations follow the factorized distorted momentum distribution quite well for moderate values of the missing momentum, where the bulk of the cross section lies. Then, reduced cross sections and integrated quantities directly related to them, like nuclear transparencies or inclusive cross sections, are reasonably predicted by the factorized scheme, as long as one remains at quasielastic kinematics. We may conclude that the unpolarized cross section

follows closely the factorized calculation that takes FSI into account. In other words, in spite of the breakdown of factorization of the cross section introduced by FSI and by negative energy components of the relativistic model, one may still extract a meaningful effective momentum distribution within this formalism.

While the bulk of the cross section factorizes to a good approximation, ratios of cross sections like A_{TL} or polarizations are very sensitive to the ingredients of the calculation that break factorization. This is why in particular the A_{TL} observable is very sensitive to the negative energy components of the wave functions, and provides a plausible signature of the relativistic dynamics.

Contrary to A_{TL}, polarizations are much more sensitive to the spin-orbit properties of the upper components of the wave functions than to the dynamical enhancement of the lower components. Yet, RDWIA transferred polarizations closely match the factorized results in certain p_m ranges. This suggests that measuring transferred polarizations in those ranges may safely explore modifications of the nucleon form factor ratios in the nuclear medium.

Acknowledgements

The authors thank T.W. Donnelly for his helpful comments. This work was partially supported by funds provided by DGI (Spain) under Contracts Nos. BFM2002-03315, BFM2002-03562, FPA2002-04181-C04-04 and BFM2003-04147-C02-01 and by the Junta de Andalucía (Spain). J.R.V. and M.C.M. acknowledge financial support from the Consejería de Educación de la Comunidad de Madrid and the Fundación Cámara (University of Sevilla), respectively.

Appendix A

In this appendix we present in more detail the hadronic bare-nucleon tensor (2.25), which can be written using traces in the form

$$\mathcal{W}^{\mu\nu}_{ss',hh'} = Tr\left[\overline{\widehat{J}}^{\,\mu} u(\boldsymbol{p}_F, s)\overline{u}(\boldsymbol{p}_F, s')\widehat{J}^{\nu} u(\boldsymbol{p}_I, h')\overline{u}(\boldsymbol{p}_I, h)\right] , \tag{2.48}$$

where we use the notation $\overline{\widehat{J}}^{\mu} \equiv \gamma^0 \widehat{J}^{\mu\dagger}\gamma^0$.

Making use of the following relation [17, 18]

$$u(\boldsymbol{p},s)\overline{u}(\boldsymbol{p},s') = \frac{\delta_{ss'} + \gamma_5 \not{\varphi}_{ss'}}{2} \frac{\not{P} + M}{2M}\,, \tag{2.49}$$

with $\varphi^{\mu}_{ss'}$ a pseudovector defined as $\varphi^{\mu}_{ss'} = \overline{u}(\boldsymbol{p},s')\gamma^{\mu}\gamma^5 u(\boldsymbol{p},s)$ which reduces to the four spin S^{μ} in the diagonal case, i.e., $\varphi^{\mu}_{ss} = S^{\mu}$, the bare nucleon tensor reads

$$\begin{aligned}
\mathcal{W}^{\mu\nu}_{ss',hh'} &= \frac{1}{16M^2} Tr\left[\overline{\widehat{J}}^{\,\mu}(\not{P}_F + M)\widehat{J}^{\nu}(\not{P}_I + M)\right]\delta_{ss'}\,\delta_{hh'} \\
&+ \frac{1}{16M^2} Tr\left[\overline{\widehat{J}}^{\,\mu}(\not{P}_F + M)\widehat{J}^{\nu}\gamma_5\not{\varphi}_{hh'}(\not{P}_I + M)\right]\delta_{ss'} \\
&+ \frac{1}{16M^2} Tr\left[\overline{\widehat{J}}^{\,\mu}\gamma_5\not{\varphi}_{ss'}(\not{P}_F + M)\widehat{J}^{\nu}(\not{P}_I + M)\right]\delta_{hh'} \\
&+ \frac{1}{16M^2} Tr\left[\overline{\widehat{J}}^{\,\mu}\gamma_5\not{\varphi}_{ss'}(\not{P}_F + M)\widehat{J}^{\nu}\gamma_5\not{\varphi}_{hh'}(\not{P}_I + M)\right]\,.
\end{aligned} \tag{2.50}$$

This result is expressed in a compact form in Eq. (2.27).

Appendix B

Let us consider the case of no spin-orbit coupling in the final nucleon wave function. This means that the radial functions g_{κ} and δ_{κ} depend only on l but not on j. Then the upper component of the wave function is given by

$$\begin{aligned}
\psi^{s_F}_{F,up}(\boldsymbol{p}) &= 4\pi\sqrt{\frac{E_F + M}{2E_F}}\sum_{\ell m} e^{-i\delta^*_{\ell}} Y^{m*}_{\ell}(\widehat{\boldsymbol{p}}_F) g^*_l(p) \sum_{j\mu}\langle \ell m \frac{1}{2} s_F | j\mu\rangle \Phi^{\mu}_{\kappa}(\widehat{\boldsymbol{p}}) \\
&= G(\boldsymbol{p},\boldsymbol{p}_F)\chi_{s_F}
\end{aligned} \tag{2.51}$$

with

$$G(\boldsymbol{p},\boldsymbol{p}_F) = 4\pi\sqrt{\frac{E_F + M}{2E_F}}\sum_{\ell m} e^{-i\delta^*_{\ell}} Y^{m*}_{\ell}(\widehat{\boldsymbol{p}}_F) g^*_l(p) Y^{m}_{\ell}(\widehat{\boldsymbol{p}})\,. \tag{2.52}$$

The resulting wave function for the ejected proton is then

$$\psi^{s_F\,EMA}_{F}(\boldsymbol{p}) = \sqrt{\frac{2M}{E_F + M}} G(\boldsymbol{p},\boldsymbol{p}_F) u(\boldsymbol{p}_F, s_F)\,. \tag{2.53}$$

Introducing this result into the expression of the current matrix element, we get

$$J^{\mu}_{EMA} = \sum_{m_{\ell_b} h} \langle \ell_b m_{\ell_b} \frac{1}{2} h | j_b \mu_b\rangle \left[\overline{u}(\boldsymbol{p}_F, s_F)\widehat{J}^{\mu} u(\boldsymbol{p}_I, h)\right] U^{m_{\ell_b}}_{\kappa_b}(\boldsymbol{p}_F, \boldsymbol{q}) \tag{2.54}$$

being,

$$U_{\kappa_b}^{m_{\ell_b}}(\boldsymbol{p}_F,\boldsymbol{q}) = \frac{2M}{\sqrt{(E_I+M)(E_F+M)}}(-i)^{\ell_b}\int d\boldsymbol{p}\, G^*(\boldsymbol{p}+\boldsymbol{q},\boldsymbol{p}_F) g_{\kappa_b}(p) Y_{\ell_b}^{m_{\ell_b}}(\widehat{\boldsymbol{p}})\,. \quad (2.55)$$

We observe that the whole dependence on the spin polarization s_F is contained in the Dirac spinor $u(\boldsymbol{p}_F, s_F)$. From Eq. (2.54) we can immediately construct the hadronic tensor $W^{\mu\nu}_{EMA}$, which can be written in the form of Eq. (2.33) with the momentum distribution function given by

$$\widetilde{N}_{hh'}(\boldsymbol{p}_F,\boldsymbol{q}) = \frac{1}{2j_b+1}\sum_{\mu_b}\sum_{m_{\ell_b}m'_{\ell_b}} \langle \ell_b m_{\ell_b}\tfrac{1}{2}h|j_b\mu_b\rangle\langle \ell_b m'_{\ell_b}\tfrac{1}{2}h'|j_b\mu_b\rangle U_{\kappa_b}^{m_{\ell_b}*}U_{\kappa_b}^{m'_{\ell_b}}\,. \quad (2.56)$$

As a particular example, let us consider the case of the plane wave limit without dynamical relativistic effects. In this situation the function $G(\boldsymbol{p},\boldsymbol{p}_F)$ (Eq. (2.52)) simply reduces to

$$G^{PW}(\boldsymbol{p},\boldsymbol{p}_F) = \sqrt{\frac{E_F+M}{2E_F}}(2\pi)^{3/2}\delta^3(\boldsymbol{p}-\boldsymbol{p}_F) \quad (2.57)$$

and the momentum distribution results

$$\widetilde{N}^{PW}_{hh'}(\boldsymbol{p}_F,\boldsymbol{q}) \;=\; \delta_{hh'}\,\frac{M^2}{2E_IE_F}(2\pi)^3\,N^{EMA}(p_I)\,. \quad (2.58)$$

Bibliografía

[1] S. Boffi, C. Giusti, F.D. Pacati, M. Radici, Phys. Rep. **226**, 1 (1993); *Electromagnetic Response of Atomic Nuclei* (Oxford University Press, Oxford, 1996).

[2] J.J. Kelly, Adv. Nucl. Phys. **23**, 75 (1996).

[3] S. Frullani and J. Mougey, Adv. Nucl. Phys. **14**, 1 (1985).

[4] A. Picklesimer and J.W. Van Orden, Phys. Rev. C **35**, 266 (1987)

[5] A. Picklesimer and J.W. Van Orden, Phys. Rev. C **40**, 290 (1989).

[6] J.M Udías, P. Sarriguren, E. Moya de Guerra, E. Garrido, J.A. Caballero, Phys. Rev. C **48**, 2731 (1993).

[7] J.M Udías, P. Sarriguren, E. Moya de Guerra, E. Garrido, J.A. Caballero, Phys. Rev. C **51**, 3246 (1995).

[8] J.M. Udías, P. Sarriguren, E. Moya de Guerra, J.A. Caballero, Phys. Rev. C **53**, R1488 (1996).

[9] J.M. Udías, J.A. Caballero, E. Moya de Guerra, J.E. Amaro, T.W. Donnelly, Phys. Rev. Lett. **83**, 5451 (1999).

[10] J.M. Udías, J.R. Vignote, Phys. Rev. C **62**, 034302 (2000).

[11] J.M. Udías, J.A. Caballero, E. Moya de Guerra, J.R. Vignote, A. Escuderos, Phys. Rev. C **64**, 024614 (2001).

[12] F. Kazemi Tabatabei, J.E. Amaro, J.A. Caballero, Phys. Rev. C **68**, 034611 (2003).

[13] A. Meucci, C. Giusti, and F.D. Pacati, Phys. Rev. C **64**, 014604 (2001); nucl-th/0211023.

[14] A. Meucci, Phys. Rev. C **65**, 044601 (2002).

[15] J. Ryckebusch, D. Debruyne, W. Van Nespen, S. Janssen, Phys. Rev. C **60**, 034604 (1999).

[16] M.C. Martínez, J.R. Vignote, J.A. Caballero, T.W. Donnelly, E. Moya de Guerra, J.M. Udías, Phys. Rev. C **69**, 034604 (2004)

[17] J.A. Caballero, T.W. Donnelly, G.I. Poulis, Nucl. Phys. **A555**, 709 (1993).

[18] J.A. Caballero, T.W. Donnelly, E. Moya de Guerra, J.M. Udías, Nucl. Phys. **A632**, 323 (1998); **A643**, 189 (1998).

[19] S. Dieterich *et al.,* Phys. Lett. B **500**, 47 (2001).

[20] S. Strauch *et al.,* Phys. Rev. Lett. **91**, 052301 (2003).

[21] M.C. Martínez, J.A. Caballero, T.W. Donnelly, Nucl. Phys. **A707**, 83 (2002); **A707**, 121 (2002).

[22] J.J. Kelly, Phys. Rev. C **56**, 2672 (1997); **59**, 3256 (1999).

[23] T. de Forest, Nucl. Phys. **A392**, 232 (1983).

[24] B.D. Serot, Phys. Lett. B **86**, 146 (1979)

[25] C.J. Horowitz, B.D. Serot, Nucl. Phys. **A368**, 503 (1981).

[26] C.J. Horowitz, D.P. Murdock, B.D. Serot, *Computational Nuclear Physics*, Springer, Berlin (1991).

[27] M.M. Sharma, M.A. Nagarajan, P. Ring, Phys. Lett. B **312**, 377 (1993).

[28] E.D.Cooper, S. Hama, B.C. Clark, R.L. Mercer, Phys. Rev. C **47**, 297 (1993).

[29] JLab Experiment E89-003, Spokespersons: W. Bertozzi, K. Fissum, A. Saha, L. Weinstein, unpublished.

[30] JLab Experiment E89-033, Spokespersons: C.C. Chang, C. Glashausser, S. Nanda, P. Rutt, unpublished.

[31] J. Gao *et al.,* Phys. Rev. Lett. **84**, 3265 (2000).

Capítulo 3

Factores espectroscópicos en $^{16}O(e, e'p)^{15}N$

PHYSICAL REVIEW C **64**, 024614 (2001)

Relativistic mean field approximation to the analysis of $^{16}\mathbf{O}(e,e'p)^{15}\mathbf{N}$ data at $|Q^2| \leq \mathbf{0.4\ (GeV/c)^2}$

J.M. Udías[1], J.A. Caballero[2,3], E. Moya de Guerra[3], Javier R. Vignote[1], and A. Escuderos[3]

[1]*Departamento de Física Atómica, Molecular y Nuclear, Universidad Complutense de Madrid, E-28040 Madrid, Spain*

[2]*Departamento de Física Atómica, Molecular y Nuclear, Universidad de Sevilla, Apdo. 1065, E-41080 Sevilla, Spain*

[3]*Instituto de Estructura de la Materia, CSIC Serrano 123, E-28006 Madrid, Spain*

We use the relativistic distorted wave impulse approximation to analyze data on $^{16}O(e,e'p)^{15}N$ at $|Q^2| \leq 0.4$ (GeV/c)^2 that were obtained by different groups and seemed controversial. Results for differential cross sections, response functions and A_{TL} asymmetry are discussed and compared to different sets of experimental data for proton knockout from $p_{1/2}$ and $p_{3/2}$ shells in ^{16}O. We compare with a nonrelativistic approach to better identify relativistic effects. The present relativistic approach is found to accommodate most of the discrepancy between data from different groups, smoothing a long standing controversy.

PACS number(s): 25.30.Fj; 25.30.Rw; 24.10.-i; 21.60.Cs

3.1 Introduction

Quasielastic $(e, e'p)$ processes are a powerful tool to study bound nucleon properties. Indeed, coincidence $(e, e'p)$ measurements at quasielastic kinematics have provided over the years detailed information on the energies, momentum distributions and spectroscopic factors of bound nucleons. This is so because at quasielastic kinematics the $(e, e'p)$ reaction can be treated with confidence in the impulse approximation, *i.e.*, assuming that the detected knockout proton absorbs the whole momentum (q) and energy (ω) of the exchanged photon (for recent reviews of the subject see ref. [1] and references therein). Until recently most data were concentrated in the low missing momentum range $p_m \leq 300$ MeV/c, where p_m is the recoil momentum of the residual nucleus. In the last years [2] higher p_m-regions are being probed at small missing energies E_m to study further aspects of bound nucleon dynamics and nucleon currents. A substantial amount of theoretical work on $(e, e'p)$ has been carried out on the basis of nonrelativistic approximations to the nucleon current. This is the case of the standard distorted wave impulse approximation (DWIA) [1] that uses a nonrelativistic approximation to the nucleon current operator and wave functions. DWIA has been successfully used over the years [3] to analyze $(e, e'p)$ data using bound and scattered proton wave functions deduced from phenomenological nonrelativistic potentials. The limits of validity of the nonrelativistic DWIA approach are now being studied by Meucci, Giusti and Pacati [4], among others.

In past years we investigated [5–8] nuclear responses and differential cross sections for exclusive quasielastic electron scattering within the framework of relativistic mean field approximations. In the relativistic distorted wave impulse approximation (RDWIA) [5, 9–11] the one-body nucleon current,

$$J^{\mu}_{N}(\omega, \vec{q}) = \int d\vec{p} \bar{\psi}_F(\vec{p} + \vec{q}) \hat{J}^{\mu}_{N}(\omega, \vec{q}) \psi_B(\vec{p}) \ , \tag{3.1}$$

is calculated with relativistic ψ_B and ψ_F wave functions for initial bound and final outgoing nucleons, respectively, and with relativistic nucleon current operator, $\hat{J}^{\mu}_{N}$. The bound state wave function is a four-spinor with well-defined parity and angular momentum quantum numbers, and is obtained by solving the Dirac equation with scalar-vector (S-V) potentials determined through a Hartree procedure from a relativistic Lagrangian with scalar and vector meson terms [12]. The wave function for the outgoing proton is a solution of the Dirac equation containing S-V global optical potentials [13] for a nucleon scattered with asymptotic momentum $\vec{p}_F$. Dirac equations for both scattered and bound wave functions

are solved in coordinate space and their solutions are then transformed to momentum space where necessary.

Eq. (1) sets up the scenario where differences between RDWIA and DWIA are at play. To go from the relativistic to the nonrelativistic approach the one-body (4×4 matrix) current operator is first of all expanded in a basis of free nucleon plane waves. This amounts to a truncation of the nucleon propagator that ignores negative energy solutions of the free Dirac equation. Next, a Pauli reduction [6] is made to transform the current operator into a 2×2 matrix, and an expansion in powers of (q/M) and/or (p/M) (where M is the nucleon mass) is made [14]. Finally the transition nucleon current is calculated as the matrix element between bispinorial, nonrelativistic bound (ϕ_B) and scattered (ϕ_F) wave functions instead of the 4-component ψ_B, ψ_F wave functions. We then cast relativistic effects into:

i) *Kinematical.* These are effects due to the truncation of the current operator to first, or higher order in p/M, q/M. For moderate p/M values the relativized form proposed in [14] gives proper account of such effects.

ii) *Dynamical.* These are effects due to the differences between relativistic and nonrelativistic wave functions which depend not only on the 4-spinor versus 2-spinor structure, but also on the potentials used in the respective Dirac and Schrödinger equations for the bound and scattered nucleon. Salient features of dynamical effects are: a) A dynamical depression of the upper component of the scattered nucleon wave function in the nuclear interior, typically identified as the effect of the Darwin term coming from the derivative of the optical S–V potentials [6]. b) A dynamical enhancement of the lower components, mainly that of the bound nucleon wave function.

So far, we applied successfully RDWIA to ^{208}Pb and ^{40}Ca at low $|Q^2|$ [5, 6], and to ^{16}O at high $|Q^2|$ [8, 15]. The effect caused by the nonlocal Darwin term for ^{40}Ca and ^{208}Pb cases was studied in detail in refs. [5, 6]. The Darwin term causes an apparent enhanced absorption when comparing the RDWIA differential cross section to the DWIA one at moderate p_m values, thus predicting larger spectroscopic factors [5,6,16]. For larger missing momentum values ($p_m/(Mc) \geq 1/3$) the lower components of the relativistic wave functions start to play a more important role, enhancing the higher momentum components of the nucleon wave functions. In previous work [7] we found that RDWIA calculations, compared to standard DWIA, tend to produce lower cross sections at $p_m \leq$ 300 MeV/c and larger cross sections at $p_m \geq 300$ MeV/c, improving agreement [5–7] with experiment.

The effect of the dynamical enhancement of the lower components was studied in RPWIA in refs. [17, 18]. It was also studied in RDWIA in ref. [8] at high $|Q^2|$. In both cases it was found to play a crucial role in the TL responses. Recent data [15] on ^{16}O at high $|Q^2|$ seem to confirm former RDWIA predictions. In particular, the richness shown by the structure of the A_{TL} asymmetry, which is different for $p_{1/2}$ and $p_{3/2}$ shells, is only consistent with predictions of relativistic calculations that include the dynamical enhancement of the lower components of bound Dirac spinors. Moreover, recent data on polarization observables in ^{12}C at $|Q^2| \approx 0.5$ (GeV/c)^2 also agree nicely with RDWIA analysis [19, 20].

For ^{16}O there is an important controversy in the comparison of theory to data at low $|Q^2|$. We refer to the data sets from $1p$-shell proton knockout experiments on ^{16}O performed at Saclay [21] and NIKHEF [22, 23] in various kinematics in late 80's/early 90's. These experiments measured the cross section as a function of missing momentum and, in particular Chinitz *et al.* [21] and Spaltro *et al.* [22], extracted also the TL response and A_{TL} asymmetry at $|Q^2| = 0.3$ (GeV/c)^2 and 0.2 (GeV/c)^2, respectively. The measurements from Chinitz *et al.* were compared to relativistic [21] and nonrelativistic [22] DWIA calculations showing relatively small deviations from theory. On the other hand, the data of Spaltro *et al.* [22] were compared to results from standard nonrelativistic DWIA calculations, and were found to be far from theory. Using nonrelativistic optical potential parameters by Schwandt *et al.* [24], and spectroscopic factors fitted to data in parallel kinematics, Spaltro *et al.* [22] found that the experimental R^{TL} is enhanced by a factor $\simeq 2.05$ for the $1p_{3/2}$ shell and by a factor $\simeq 1.5$ for the $1p_{1/2}$.

Though the large discrepancy between DWIA results and experiment found by Spaltro *et al.* may in part be due to two-body currents, calculations of exchange current effects are still contradictory [25, 26]. Hence, the controversy surrounding the TL response and asymmetry data still persists. In view of forthcoming information on ^{16}O responses from experiments at Jefferson Lab in the near future, it is important to reexamine these sets of data with RDWIA calculations. We investigate whether a systematic fully relativistic analysis of the $(e, e'p)$ data at low $|Q^2|$ may explain the apparent discrepancies between data from Saclay [21] and NIKHEF [22, 23].

The paper is organized as follows: in Sec. 3.2 we summarize the basic formalism needed to describe coincidence electron scattering reactions, paying special attention to the relativistic distorted wave impulse approximation (RDWIA). Section 3.3 contains the theoretical results obtained and their comparison with the experimental data. In Sec. 3.4

we present our conclusions.

3.2 Description of $(e,e'p)$ calculations

The general formalism for exclusive electron scattering reactions has been presented in detail in several previous papers. We refer in particular to Refs. [1, 5, 27]. Here we just summarize the kinematics and focus on those aspects that are of relevance to the points under discussion in this paper. As a guide to the reader we write down the unpolarized cross section in Born approximation assuming plane waves for the incoming and outgoing electron (treated in the extreme relativistic limit),

$$\frac{d\sigma}{d\Omega_e d\varepsilon' d\Omega_F} = K\sigma_{Mott} f_{rec} \left[v_L R^L + v_T R^T + v_{TL} R^{TL} \cos\phi_F + v_{TT} R^{TT} \cos 2\phi_F \right] , \quad (3.2)$$

where ε' and Ω_e are the energy and solid angle corresponding to the scattered electron and $\Omega_F = (\theta_F, \phi_F)$ is the solid angle for the outgoing proton. The factor K is given by $K = |\vec{p}_F| E_F/(2\pi)^3$, with $\vec{p}_F$ the momentum carried by the ejected proton and E_F its energy. The term f_{rec} is the usual recoil factor $f_{rec}^{-1} = |1 - (E_F/E_{A-1})(\vec{p}_{A-1} \cdot \vec{p}_F)/|\vec{p}_F|^2|$, where $\vec{p}_{A-1}$ and E_{A-1} are the momentum and energy of the residual nucleus, respectively. The kinematical factors are $v_L = \lambda^2$, $v_T = \lambda/2 + \tan^2\theta_e/2$, $v_{TT} = \lambda/2$, $v_{TL} = \lambda\sqrt{\lambda + \tan^2\theta_e/2}$ with $\lambda = 1-(\omega/|\vec{q}|)^2$, where ω and $\vec{q}$ are the energy and momentum transfer in the reaction and θ_e the electron scattering angle. The above factors, that contain the dependence on the electron kinematics, coincide with those given in [27, 28] except for a factor $\sqrt{2}$ in the interference TL term. We remark that in refs. [21, 22] a different convention for K was used (see for instance eq. (1) of ref. [22]), which amounts to a factor M/E_F of the responses presented in this work with respect to the ones displayed in [21, 22].

Our calculation of differential cross sections and responses includes also the effect of Coulomb distortion of the incoming and outgoing electron waves. This breaks the simplicity of eq. (3.2), which is however still useful as a guide. Nevertheless, for ^{16}O Coulomb distortion effects in the electron wave functions are tiny (less than 1.5% effect on the cross section).

The hadronic current enters only in the response functions R^α, $\alpha = L, T, TL, TT$ where L and T denote the longitudinal and transverse projections of the nuclear current with respect to the momentum transfer $\vec{q}$, respectively. Note that the response functions can be

separated by performing measurements with different kinematical factors v_α and/or values of the azimuthal angle ϕ_F, while keeping the momentum and energy transfer constant. The response R^{TL} is obtained from differential cross sections at $\phi_F = 0^o$ and 180^o, both in theory and in experiment. Experimental data for the cross section are often presented in terms of *reduced cross sections* or *effective momentum distributions* $\rho(\vec{p}_m)$, obtained by integrating over a particular missing energy peak the differential cross section divided by $K(2\pi)^3\sigma_{ep}$. Thus $\rho(\vec{p}_m)$ is defined by,

$$\rho(\vec{p}_m) = \int_{\Delta E_m} \left(\frac{d\sigma}{d\Omega_e d\varepsilon' d\Omega_F dE_F} / (K(2\pi)^3\sigma_{ep}) \right) dE_m \ . \tag{3.3}$$

The free electron-proton cross section, σ_{ep}, is usually taken as σ_{CC1} of de Forest [29]. One must be aware that the cross section given in eq. (3.2) has a strong dependence in the kinematical variables via K and σ_{ep} which is removed in the reduced cross section. For instance, at the kinematics of the experiment of Chinitz *et al.* [21] ($T_F = 160$ MeV, $|Q^2| = 0.3$ (MeV/c)^2 and $\varepsilon_{beam} = 580$ MeV) a small variation of 5 MeV in T_F and ω (keeping E_m and p_m constant), may change the cross section by as much as 7% and the reduced cross section by less than 2%. In order to minimize kinematical dependences, it is safer to determine spectroscopic factors by scaling the theory to data on reduced cross sections rather than to data on cross sections. This is so because experimentally, a folding and average of the cross sections, responses and/or reduced cross sections is performed over the experimental acceptance, and central values for the kinematical variables are quoted. Theoretical calculations are done for the quoted central values. Due to this, it is not unusual that spectroscopic factors may depend on whether one chooses to set the scale by comparing to reduced cross sections or to differential cross sections, or even to separate responses. In this work we first derive the spectroscopic factor (S_α) from the reduced cross section data. Then we use this same factor to compare to data for the individual responses. In this way the analysis of R^{TL} and other responses is more consistent and meaningful.

Another quantity also obtained by the experimentalists and discussed in next section is the asymmetry A_{TL} given by

$$A_{TL} = \frac{\sigma(\phi_F = 180^\circ) - \sigma(\phi_F = 0^\circ)}{\sigma(\phi_F = 180^\circ) + \sigma(\phi_F = 0^\circ)} \ . \tag{3.4}$$

One can see from eq. (2) that this observable is closely related to R^{TL}, with the advantage that it is free from the scale factor ambiguity.

3.2.1 Relativistic Distorted Wave Impulse Approximation (RDWIA)

In RDWIA the process is described [5] in terms of the one-body nucleon current given in eq. (3.1). The relativistic bound nucleon wave function, ψ_B, is a four-spinor with well defined angular momentum quantum numbers κ, μ, corresponding to the shell under consideration. In coordinate space it is given by:

$$\psi^{\mu}_{\kappa}(\vec{r}) = \begin{pmatrix} g_{\kappa}(r)\phi^{\mu}_{\kappa}(\hat{r}) \\ if_{\kappa}(r)\phi^{\mu}_{-\kappa}(\hat{r}) \end{pmatrix} , \tag{3.5}$$

which is the eigenstate of total angular momentum with eigenvalue $j = |\kappa| - 1/2$,

$$\phi^{\mu}_{\kappa}(\hat{r}) = \sum_{m,\sigma} \langle lm\frac{1}{2}\sigma|j\mu\rangle Y_{lm}(\hat{r})\chi^{1/2}_{\sigma} , \tag{3.6}$$

with $l = \kappa$ if $\kappa > 0$ and $l = -\kappa - 1$ if $\kappa < 0$. The functions f_{κ}, g_{κ} satisfy the usual coupled linear differential equations [5, 30, 31].

The wave function for the outgoing proton, ψ_F, is a scattering solution of the Dirac equation, which includes S–V global optical potentials. This wave function is obtained as a partial wave expansion in configuration space [5, 6]:

$$\psi_F(\vec{r}) = 4\pi\sqrt{\frac{E_F + M}{2E_F V}} \sum_{\kappa,\mu,m} e^{-i\delta^*_{\kappa}} i^l \langle l\ m\ \frac{1}{2}\ \sigma_F|j\ \mu\rangle Y^*_{lm}(\hat{P}_F)\psi^{\mu}_{\kappa}(\vec{r}) , \tag{3.7}$$

where $\psi^{\mu}_{\kappa}(\vec{r})$ are four-spinors of the same form as that in eq. (3.5). The phase-shifts and radial functions are complex because of the complex potential.

The choice of the current operator $\hat{J}^{\mu}$ is to some extent arbitrary (see discussion in refs. [5, 17, 32]). Here we consider the two most popular choices denoted as CC1 and CC2 [29]:

$$\hat{J}^{\mu}_{CC1} = (F_1 + F_2)\gamma^{\mu} - \frac{F_2}{2M}(\overline{P} + P_F)^{\mu} \tag{3.8}$$

$$\hat{J}^{\mu}_{CC2} = F_1\gamma^{\mu} + i\frac{F_2}{2M}\sigma^{\mu\nu}Q_{\nu} , \tag{3.9}$$

where F_1 and F_2 are the nucleon form factors related in the usual way [33] to the electric and magnetic Sachs form factors of the dipole form. The variable $\overline{P}$ in eq. (3.8) is the four-momentum of the initial nucleon for on-shell kinematics, *i.e.*, $\overline{P}^{\mu} = (E(p), \vec{p})$ ($E(p) = \sqrt{\vec{p}^2 + M^2}$ and $\vec{p} = \vec{p}_F - \vec{q}$).

Thus the evaluation of the one-body current matrix element involves the use of 4×4-operators and 4-spinors with negative energy components. This is at variance with the nonrelativistic (DWIA) approximation where a truncated current operator is used [34] and matrix elements are evaluated between bispinorial wave functions (ϕ_B, ϕ_F). Therefore in the discussion of results in next sections we shall refer to relativistic kinematical effects –that have to do with the differences due to the use of the complete relativistic current operator instead of the truncated one– and to relativistic dynamical effects. A way to fully incorporate the kinematical relativistic effects was suggested in ref. [6, 14], and studied in detail in ref. [35] for the reaction $^2H(e, e'p)$.

3.2.2 Remarks on relativistic dynamical effects

As mentioned in the introduction the dynamical effects come from the differences between relativistic and nonrelativistic potentials and wave functions. In ref. [6] we discussed in detail effects on reduced cross sections for ^{208}Pb in parallel kinematics due to differences between the upper components of the four-spinors ψ_B, ψ_F which are Dirac solutions with S-V potentials and the bispinors ϕ_B, ϕ_F which are Schrödinger solutions with standard (Wood-Saxon type) potentials for bound and scattered nucleons.

To illustrate the meaning of this effect we recall that the Dirac equation with S-V potentials

$$(\tilde{E}\gamma_0 - \vec{p}\cdot\vec{\gamma} - \tilde{M})\psi = 0 \tag{3.10}$$

with

$$\tilde{E} = E - V(r) \tag{3.11}$$

$$\tilde{M} = M - S(r) \tag{3.12}$$

$$\psi = \begin{pmatrix} \psi_{up} \\ \psi_{down} \end{pmatrix}, \tag{3.13}$$

can be written either as a system of coupled linear differential equations for ψ_{up}, ψ_{down}, or as a second order differential Schrödinger like-equation for ψ_{up} containing also a first order derivative term (the Darwin term). Furthermore, using the transformation

$$\psi_{up}(r) = K(r)\phi(r), \tag{3.14}$$

the non-local (Darwin) term can be eliminated to obtain a more standard Schrödinger

equation with second derivatives only

$$\left[\frac{-\vec{\nabla}^2}{2M} - U_{DEB}\right]\phi(\vec{r}) = \frac{(E^2-M^2)}{2M}\phi(\vec{r}) \tag{3.15}$$

with U_{DEB} the Dirac equivalent potential [6] with central and spin-orbit terms

$$\begin{aligned}
U_{DEB} &= V_C + V_{SO}\ \vec{\sigma}\cdot\vec{\ell} \\
V_C &= \frac{1}{2M}\left[V^2 - 2EV - S^2 + 2MS + V_D\right] \\
V_D &= \frac{1}{rA}\frac{\partial A}{\partial r} + \frac{1}{2A}\frac{\partial^2 A}{\partial r^2} - \frac{3}{4A^2}\left(\frac{\partial A}{\partial r}\right)^2 \\
V_{SO} &= \frac{1}{2M}\frac{1}{rA}\frac{\partial A}{\partial r} \\
A(r) &= \frac{\tilde{E}+\tilde{M}}{E+M} = K^2(r)\ .
\end{aligned} \tag{3.16}$$

The factor $K(r)$ relating the upper component of the Dirac solution (ψ_{up}) to the solution of the equivalent Schrödinger equation ($\phi(r)$) is called the Darwin factor. As it will be shown in next section, $K(r)$ produces a depletion of the outgoing wave function in the nuclear interior [36, 37].

Another dynamical relativistic effect is that coming from the non-zero overlap with Dirac sea of the Dirac solutions with S-V potentials. The ψ_B, ψ_F wave functions have the general structure

$$\psi(\vec{p}) = \psi^{(+)}(\vec{p}) + \psi^{(-)}(\vec{p})\ , \tag{3.17}$$

where $\psi^{(+)}$ and $\psi^{(-)}$ are the projections on the positive and negative energy solutions of the Dirac equation for free particles:

$$\psi^{(+)}(\vec{p}) = \sum_s u_s(\vec{p})\overline{u}_s(\vec{p})\psi(\vec{p}) = \Lambda_{(+)}(\vec{p})\psi(\vec{p}) \tag{3.18}$$

$$\psi^{(-)}(\vec{p}) = -\sum_s v_s(\vec{p})\overline{v}_s(\vec{p})\psi(\vec{p}) = \Lambda_{(-)}(\vec{p})\psi(\vec{p})\ , \tag{3.19}$$

where we use the notation and conventions of Bjorken and Drell [33], so that the positive and negative energy projectors are

$$\Lambda_{(\pm)}(\vec{p}) = \frac{M \pm \overline{\not{P}}}{2M} \tag{3.20}$$

with $\overline{P}_\mu = (\overline{E}, \vec{p})$ and $\overline{E} = \sqrt{p^2+M^2}$.

The positive and negative energy components of ψ can also be written as

$$\psi^{(+)}(\vec{p}) = \begin{pmatrix} \psi^{(+)}_{up}(\vec{p}) \\ \psi^{(+)}_{down}(\vec{p}) \end{pmatrix} = \sum_s \tilde{\alpha}(\vec{p}, s) u_s(\vec{p}) \tag{3.21}$$

$$\psi^{(-)}(\vec{p}) = \begin{pmatrix} \psi^{(-)}_{up}(\vec{p}) \\ \psi^{(-)}_{down}(\vec{p}) \end{pmatrix} = \sum_s \tilde{\beta}(\vec{p}, s) v_s(\vec{p}) \ . \tag{3.22}$$

Eqs. (3.21,3.22) make it more transparent what are the new ingredients of the relativistic calculation. In particular the difference between ψ_{down} and $\psi^{(+)}_{down}$ is what we call the dynamical enhancement of the down component. Explicit expressions and figures showing $\tilde{\alpha}(p)$ and $\tilde{\beta}(p)$ for several orbitals can be found in ref. [18]. Here we just mention that the dynamical enhancement of the down component is proportional to the nonzero Dirac sea overlap, $\tilde{\beta}(p)$, and that though it is small, it was found to play an important role in the TL response function in the RPWIA calculations presented in ref. [18], and in the RDWIA calculations at high $|Q^2|$ reported in refs. [8,15]. Its role for the present RDWIA calculations is discussed in next section. A way to define an effective 2×2 current operator that includes these dynamical relativistic effects was introduced in ref. [38].

3.2.3 Projected calculation

The sensitivity of the different scattering observables to the negative energy components can be analyzed by constructing properly normalized 4-spinors of the form in eq. (3.18). Then, one can compare the results obtained using the fully relativistic amplitude given in eq. (3.1) with those obtained when the negative energy components are projected out. This is done when the nucleon current is calculated as

$$J^{\mu}_{(++)}(\omega, \vec{q}) = \int d\vec{p} \overline{\psi}^{(+)}_F(\vec{p} + \vec{q}) \hat{J}^{\mu}(\omega, \vec{q}) \psi^{(+)}_B(\vec{p}) \ , \tag{3.23}$$

where $\psi^{(+)}_B$ ($\psi^{(+)}_F$) is the positive-energy projection of ψ_B (ψ_F), *i.e.*,

$$\psi^{(+)}_B(\vec{p}) = \Lambda_{(+)}(\vec{p}) \psi_B(\vec{p}), \quad \psi^{(+)}_F(\vec{p} + \vec{q}) = \Lambda_{(+)}(\vec{p} + \vec{q}) \psi_F(\vec{p} + \vec{q}) \ . \tag{3.24}$$

The dynamical enhancement of the lower components is contained in the current of eq. (3.1), but not in eq. (3.23). It is important to realize that the positive-energy projectors inserted in eq. (3.23) depend on the integration variable $\vec{p}$. One could also neglect this $\vec{p}$-dependence by using projection operators corresponding to asymptotic values of the momenta, *i.e.*, projectors acting on ψ_F and ψ_B respectively, with $P^{\mu}_F = (E_F, \vec{p}_F)$, $P^{\mu}_B =$

$P_F^\mu - \overline{Q}^\mu$ the asymptotic four-momentum of the outgoing and bound nucleon respectively, with $\overline{Q}^\mu = (\overline{\omega}, \vec{q})$ and $\overline{\omega} = E_F - \sqrt{(\vec{p}_F - \vec{q})^2 + M^2}$. We refer to this approach as *asymptotic projection*. This latter projection is almost equivalent to "EMA-noSV" procedure employed in ref. [39], in which the 4-spinors used have upper components identical to the upper components of the Dirac equation solutions, but the lower components are obtained with an additional approximation, the effective momentum approach (EMA). Although EMA-noSV approach also neglects the enhancement of the lower components, it is not at all equivalent to the exact projection method in eqs. (3.23,3.24). The EMA-noSV approach computes the nucleon current with four-spinors that have the same structure than the ones encountered in the scattering of free nucleons, because it enforces the relationship between upper and lower components to be driven by the asymptotic value of the momenta at the nucleon vertex. In particular, the Gordon transformation is exact for EMA-noSV approach. Therefore, CC1 and CC2 operators would lead to identical results within EMA-noSV, provided the same choices for the off-shell values of ω, E, E_F, $\vec{p}$ and $\vec{p}_F$ are made. This would be a strong prerequisite to a factorized calculation, though still not a sufficient condition. In order to keep the drawings in Sec. 3.3 clear enough, we do not show in the figures the results obtained within EMA-noSV, but we shall comment how this approach compares with the fully relativistic and/or the projected one.

3.3 Results and Discussion

In this work we consider three data sets for nucleon knockout from $p_{1/2}$ and $p_{3/2}$ shells in ^{16}O that correspond to kinematical conditions of three different experiments. We summarize them as follows:

Set (a) corresponds to the experiment of Leuschner *et al.* at the Medium Energy Accelerator (MEA) at NIKHEF-K [23]. The coincidence reaction $^{16}O(e,e'p)^{15}N$ was analyzed in quasielastic parallel kinematics at three different beam energies: 304, 456 and 521 MeV. The total kinetic energy of the outgoing proton was around 90 MeV. The spectral function of ^{16}O was measured in the range, $0 < E_m < 40$ MeV and $-180 < p_m < 270$ MeV/c, where E_m and p_m are the missing energy and missing momentum, respectively.

Set (b) corresponds to the experiment performed at the Saclay Linear Accelerator by Chinitz *et al.* [21]. The kinematical setup was constant $|\vec{q}| - \omega$ kinematics. The electron beam energy was $\varepsilon = 580$ MeV, the outgoing proton kinetic energy $T_F = 160$ MeV, and the transfer momentum and energy: $|\vec{q}| = 570$ MeV/c and $\omega = 170$ MeV ($|Q^2| = 0.3$

$(\mathrm{GeV/c})^2$). The missing energy resolution was 1.3 MeV, which made not possible to resolve the $(5/2^+,1/2^+)$ doublet at an excitation energy $E_x = 5.3$ MeV in ^{15}N from the $3/2^-$ state at $E_x = 6.3$ MeV.

Set (c), also in $|\vec{q}| - \omega$ constant kinematics, was obtained by Spaltro *et al.* [22] with the two high-resolution magnetic spectrometers at the medium-energy electron accelerator MEA of NIKHEF-K. Data were measured at momentum and energy-transfer values centered at $(\omega, |\vec{q}|) = (90$ MeV, 460 MeV/c), *i.e.*, close to the center of the quasielastic peak at $|Q^2| \simeq 0.2$ $(\mathrm{GeV/c})^2$. The experiment covered a missing momentum range from 30 to 190 MeV/c. The missing energy resolution was about 180 keV, which made it possible to resolve the $(5/2^+, 1/2^+)$ doublet from the $3/2^-$ state.

Next we discuss our results for spectroscopic factors, reduced cross sections and responses corresponding to these sets of data and kinematical conditions.

In Sec. 3.3.1 we deduce spectroscopic factors from reduced cross sections, that are then used in Sec. 3.3.2 for response functions. Section. 3.3.1 discusses also results corresponding to different relativistic S-V potentials. In our previous work on ^{40}Ca and ^{208}Pb we found that spectroscopic factors were larger than the ones obtained with the nonrelativistic analyses and were very stable when different parameterizations of the S-V potentials for bound (HS, NLSH) [5, 7] and scattered (EDAI, EDAD1, EDAD2, EDAD3) [6] protons were used. We shall see that the case of ^{16}O that we examine here is different in several respects.

3.3.1 Reduced Cross Section and Spectroscopic Factors

Let us first discuss the comparison of theory and experiment on reduced cross sections for set (a) (Leuschner *et al.* [23]). We recall that because of parallel kinematics, for this set the only response functions that contribute to the cross sections are R^L and R^T. Fig. 3.1 shows the reduced cross section for $p_{1/2}$ and $p_{3/2}$ shells. The sign of p_m refers to the projection of the initial nucleon momentum along the direction of the transfer momentum $\vec{q}$. It is defined to be positive for $|\vec{q}| < |\vec{p}_F|$ and negative for $|\vec{q}| > |\vec{p}_F|$. Fully relativistic calculations using the CC1 and CC2 current operators (RCC1, RCC2) are shown by thin and thick lines respectively. Throughout this paper we use the Coulomb gauge. The Landau gauge produces similar results. Gauge ambiguities [40] are rather small for the fully relativistic results in these two gauges [17, 18].

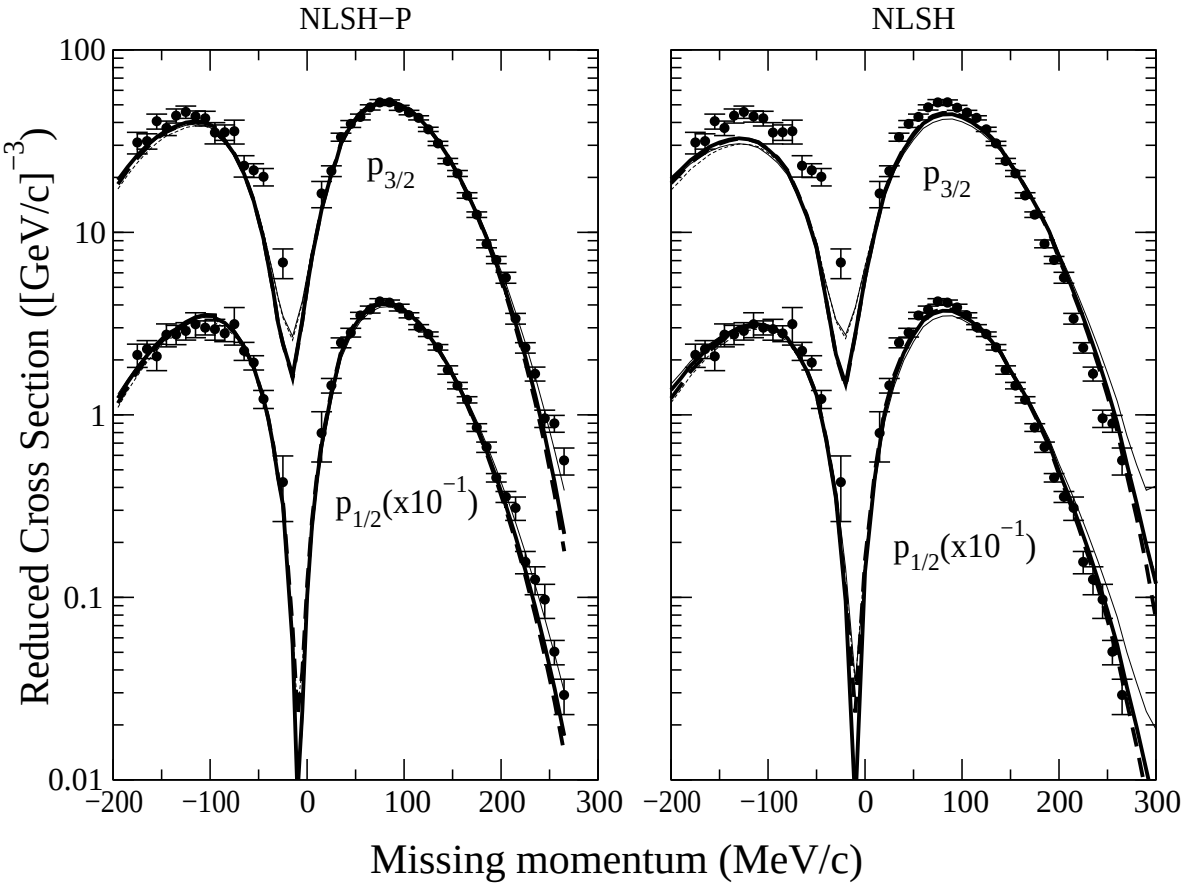

Figura 3.1: Reduced cross sections for proton knockout from $1p_{1/2}$ and $1p_{3/2}$ orbits in ^{16}O versus missing momentum p_m corresponding to the experiment performed by Leuschner *et al.* [23] (set (a)). The bound relativistic proton wave function has been obtained with the NLSH (right panel) and NLSH-P (left panel) parameterization. Theoretical results shown correspond to a fully relativistic calculation using the Coulomb gauge and current operators RCC1 (thin solid line) and RCC2 (thick solid line). The optical potential used is EDAI-O from ref. [13]. Also shown are the results after projecting the bound and scattered proton wave functions over positive-energy states: PCC1 (thin dashed line), PCC2 (thick dashed line). EMA-noSV results (not shown) are practically identical to PCC2 ones. Each curve is scaled by the corresponding spectroscopic factor in Table 3.1.

Spectroscopic factors for each of the two shells are evaluated by scaling theoretical calculations to experimental data. They are listed in Table 3.1 for different choices of wave functions and current operators. In this table we also quote the statistical error within parenthesis and the χ^2 values per degree of freedom.

Results on the right panel in Fig. 3.1 correspond to bound state wave function calculated using the parameters of the set NLSH [41]. Results with the older HS set [12, 31], as well as with the newest NL3 one [42] are similar. For the scattered proton wave function we use the energy-dependent A-independent potential derived by Clark *et al.* [13] for ^{16}O (EDAI-O). Two things are striking in these results that are at variance with the situation we met in previous works on ^{40}Ca and ^{208}Pb [5, 6]:

1. There are clear deviations in the shape of theoretical and experimental effective momentum distributions in the right hand side panel of Fig. 3.1. Actually, the NLSH wave functions have smaller (larger) r.m.s. radii in r-space (p-space) than what is shown experimentally.

2. The spectroscopic factors are small, of the same order or even smaller than non-relativistic ones when Perey factor is included in the latter. As seen in Table 3.1 the spectroscopic factors increase when global A-dependent type (EDAD-1,-2) potentials are used instead of the A-independent potential fitted to ^{16}O (EDAI-O). Moreover, the χ^2 values are large for NLSH bound wave functions independently of the optical potential used.

We have verified that all EDAD-type calculations (EDAD-1,-2,-3) give similar results on reduced cross sections and responses. Compared to EDAI-O they give about $15-20\%$ smaller reduced cross sections with almost identical shapes. Consequently, EDAD-1,-2,-3 spectroscopic factors are $15-20\%$ larger than EDAI-O ones but the χ^2 values are analogous (see Table 3.1). Why this is different from the cases we analyzed in refs. [5, 6] can be easily understood from Fig. 3.2. In this figure we compare the relativistic central potentials (S, V) and Darwin factors (K) corresponding to EDAI-O and to EDAD-1,-2 optical potentials for ^{208}Pb (right panels) and for ^{16}O (left panels). We can see that in the case of ^{16}O, EDAD-1,-2 potentials produce a deeper $K(r)$, *i.e.,* a larger reduction of the scattered wave in the nuclear interior than EDAI-O potential –also, V_C is somewhat more absorptive–, while in the case of ^{208}Pb both are about the same. Consequently, at the energies considered, EDAD-1,-2 potential lead to larger spectroscopic factors than

		NLSH				NLSH-P			
		$p_{1/2}$		$p_{3/2}$		$p_{1/2}$		$p_{3/2}$	
		CC1	CC2	CC1	CC2	CC1	CC2	CC1	CC2
		Relativistic							
EDAI-O	S_α	0.58(1)	0.64(2)	0.45(3)	0.49(3)	0.54(1)	0.58(1)	0.43(1)	0.45(1)
	χ^2/N_{DF}	6.6	4.5	25.3	15.7	1.3	1.3	2.7	3.5
EDAD-1	S_α	0.63(4)	0.72(2)	0.56(3)	0.62(2)	0.58(1)	0.64(1)	0.52(1)	0.55(2)
	χ^2/N_{DF}	9.6	3.7	15	7.2	1.2	1.2	1.2	4.8
EDAD-2	S_α	0.61(4)	0.69(3)	0.53(3)	0.59(2)	0.56(1)	0.62(1)	0.50(1)	0.52(1)
	χ^2/N_{DF}	10	2.6	18	9.2	1.4	1.1	1.7	4.1
		Projected							
EDAI-O	S_α	0.65(2)	0.66(2)	0.51(3)	0.52(3)	0.58(1)	0.59(1)	0.47(1)	0.46(1)
	χ^2/N_{DF}	4.5	3.2	16.9	13.3	1.2	1.6	3.6	4.3
EDAD-1	S_α	0.72(3)	0.74(2)	0.64(3)	0.64(2)	0.64(1)	0.65 (2)	0.57(2)	0.56(2)
	χ^2/N_{DF}	4.0	2.6	7.6	5.9	1.4	1.6	4.4	6.3
EDAD-2	S_α	0.69(3)	0.71(2)	0.61(3)	0.61(3)	0.62(1)	0.63(1)	0.55(2)	0.54(2)
	χ^2/N_{DF}	4.6	3.1	9.7	7.4	1.3	1.5	3.7	5.3

Tabla 3.1: Spectroscopic factors derived from Leuschner's experimental reduced cross sections in ref. [23] (data set (a)) using NLSH and NLSH-P relativistic bound nucleon wave functions, and EDAI-O, EDAD-1 and EDAD-2 relativistic optical potential parameterizations (see text). Results with EDAD-3 are almost identical to the ones with EDAD-1. The numbers within parentheses indicate the statistical error.

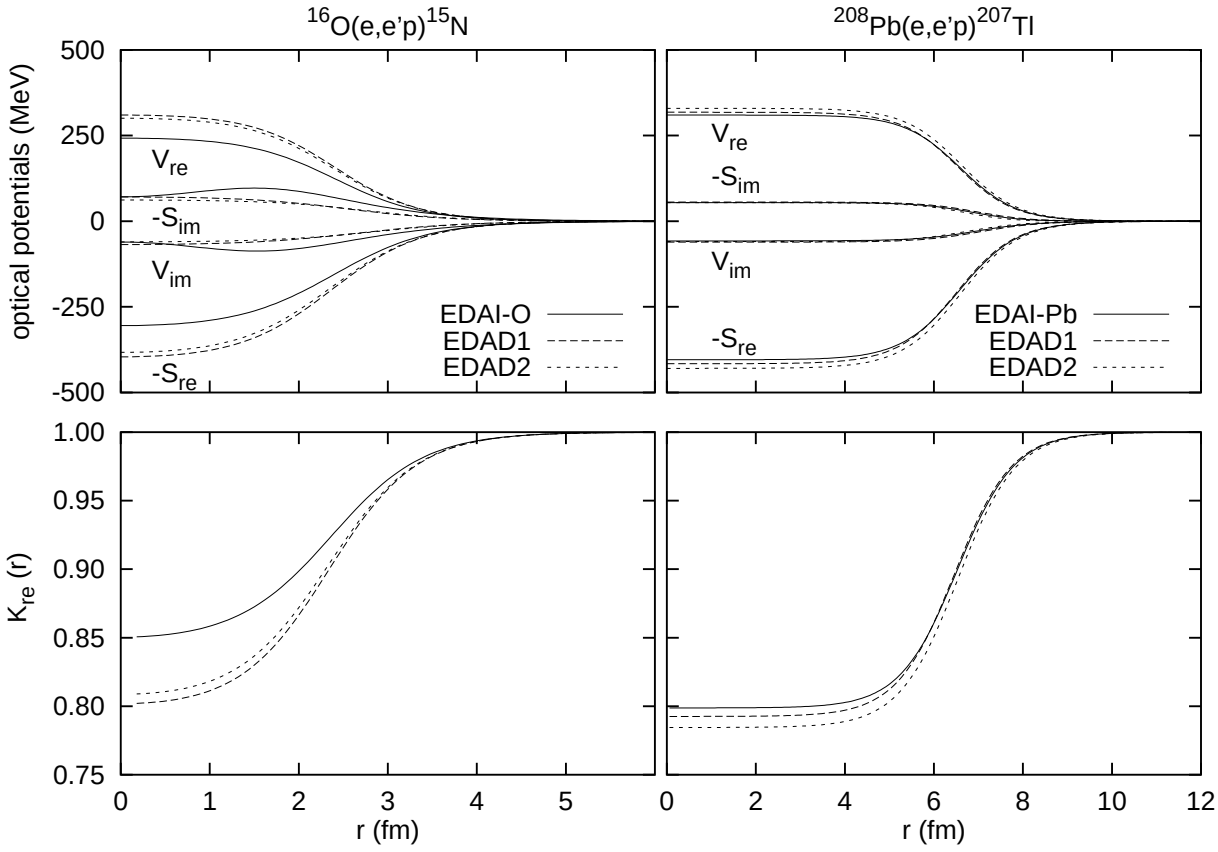

Figura 3.2: Real and imaginary part of the optical potentials (upper panels) and real part of the Darwin factor (lower panels) (the imaginary part is negligible) for ^{16}O (left panels) and ^{208}Pb (right panels).

EDAI-O in ^{16}O, while the two potentials lead to similar spectroscopic factors in ^{208}Pb. The same is true for EDAD-3 and other versions of the relativistic EDAD potentials.

To have a more conclusive determination of ^{16}O spectroscopic factors one would need to constrain the optical potential choice by means of inelastic (p, p') data, in addition to the elastic ones [43]. But this is not available for the small knock-out proton energies ($\sim$ 90 MeV) considered here nor in a fully relativistic framework.

The large χ^2 values in the left part of Table 3.1 for all the optical potentials have to do with the fact that the data do not follow the shape of theoretical reduced cross sections in the right panel of Fig. 3.1. A similar problem has been found for data sets (b) and (c) where the quality of NLSH fits is even worse. This, after all, is not surprising

	$p_{1/2}$			$p_{3/2}$		
	b.e. (MeV)	rms-r (fm)	rms-p (MeV)	b.e. (MeV)	rms-r (fm)	rms-p (MeV)
NLSH	11.4	2.838	175.7	18.8	2.679	185.2
NLSH-P	12.1	3.043	170.6	18.4	2.907	173.6

Tabla 3.2: Comparison of binding energies and rms radius in $p-$ and $r-$ space for the wave functions NLSH [41] and NLSH-P. The contribution from the negative energy components to the norm of the wave function is about 2% in all cases.

because the standard Lagrangians, like NLSH, are fitted to bulk properties of a few heavy nuclei, and one may expect that the predicted r.m.s. radii of ^{16}O orbitals differ somewhat from experiment. Unfortunately, as seen in Table 3.1 this produces large uncertainties in spectroscopic factors. To solve this problem we may adjust the parameters of the relativistic potentials (or Lagrangian) so as to obtain the correct values of the single particle energies and r.m.s. radii for the orbitals considered, in an analogous way to what is usually done in nonrelativistic analyses of $(e,e'p)$ data. This is what we do next.

Compared to data sets (b) and (c), data set (a) has many more data points extending over a larger p_m range. Therefore, this data set can be used much more reliably to determine *simultaneously* spectroscopic factors and r.m.s.r. values. We have then adopted the following strategy: First, we use data set (a) to slightly tune the parameters of the NLSH potential so as to reproduce the experimental binding energies and r.m.s.r. values of the $p_{1/2}$ and $p_{3/2}$ orbitals in ^{16}O, closely resembling the standard nonrelativistic procedure. We denote by NLSH-P the new relativistic potentials and wave functions (see Table 3.2). These new relativistic wave functions are then used to make predictions for the kinematical conditions of data sets (b) and (c).

The NLSH-P wave functions are obtained by changing the parameters of the NLSH Lagrangian so that the radii and depth of the S and V potential wells derived from the Lagrangian are modified in the same proportion. The negative energy content of the resulting bound state wave function is barely changed by this procedure. The rescaling of the depth size and radii of the NLSH-P wells is within 10% of the initial NLSH ones. The improvement obtained in the description of the shapes and quality of the fits is clearly visible in Fig. 3.1 and Table 3.1.

The role played by relativistic dynamical effects is also analyzed from the results presented in Fig. 3.1 and Table 3.1. Each curve in Fig. 3.1 is scaled by the corresponding

spectroscopic factors in Table 3.1. The reduced cross sections evaluated after projecting the bound and scattered proton wave functions over positive energy states (see eq. (3.23)) are shown by thin-dashed (PCC1) and thick-dashed (PCC2) lines. Note that the difference between PCC1 and PCC2 results is very small because the so-called Gordon ambiguities are reduced after projection [17, 18]. The results obtained using the asymptotic values of the momenta in the projection operator as described in Sec. 3.2.3, are almost identical to the PCC2 results and thus are not shown here. Once the global scale factor is taken into account, all the calculations predict a very similar behavior, what indicates that, aside from the Darwin term, the effect of relativistic dynamics in the reduced cross sections is not important in parallel kinematics at low values of $|Q^2|$. This agrees with a recent work by Giusti and collaborators [4]. This observation also agrees with results of some previous works [8, 17, 18] where we saw that the dynamical enhancement of the lower component makes an important effect in the cross section mainly at high missing momentum values and/or in the R^{TL} response function (which *does not contribute in parallel kinematics*), whereas its influence on R^L and R^T is quite modest.

Comparing the fully relativistic results with NLSH-P wave functions for CC1 and CC2, one observes that the differences are at most of the order of $\sim 8\%$. In the case of the projected calculation, we note that the spectroscopic factors are slightly larger than those corresponding to a fully relativistic calculation. This is due to the enhancement of the lower components of the wave functions which is not contained in the projected approximations. Their effect is negligible for CC2 operator and is enhanced by the CC1 choice. We recall that another dynamical relativistic effect, namely the Darwin term, is contained in all the figures and tables shown here. For EDAI-O optical potential this effect amounts to a 10% reduction of the reduced cross section in ^{16}O for the kinematics discussed in this work. This is comparable to the effect of the Perey factor that was included in nonrelativistic DWEEPY calculations [22, 23] while for EDAD-optical potentials this amounts to a 20% reduction.

One thus expects the spectroscopic factors listed in Table 3.1 for EDAI-O in the projected case to be similar to those obtained from fits with standard nonrelativistic DWIA calculations including Perey factors. In this last case the extracted factors for various choices of optical potentials are $0.60 \leq S_\alpha \leq 0.65$ for $p_{1/2}$, and $0.49 \leq S_\alpha \leq 0.60$ for $p_{3/2}$ [23], which are also roughly in agreement with those in Table 3.1 for NLSH-P and EDAD-type potentials.

A smaller spectroscopic factor is expected for the $p_{3/2}$ shell than for the $p_{1/2}$, because

	Set (*b*) Chinitz *et al.* [21]				Set (*c*) Spaltro *et al.* [22]			
	$p_{1/2}$		$p_{3/2}$		$p_{1/2}$		$p_{3/2}$	
	CC1	CC2	CC1	CC2	CC1	CC2	CC1	CC2
EDAI-O (R)	0.54(4)	0.56(3)	0.49(2)	0.51(2)	0.57(3)	0.61(2)	0.56(1)	0.59(2)
EDAI-O (P)	0.59(4)	0.56(4)	0.53(4)	0.53(3)	0.66(2)	0.63(2)	0.61(1)	0.61(2)
EDAD-1 (R)	0.59(4)	0.61(3)	0.53(3)	0.55(3)	0.68(4)	0.72(2)	0.62(2)	0.67(2)
EDAD-1 (P)	0.65(4)	0.62(3)	0.57(5)	0.57(4)	0.79(3)	0.74(3)	0.69(3)	0.69(3)

Tabla 3.3: Spectroscopic factors derived from two different sets of data on experimental reduced cross sections from the full relativistic approach (R) and from the projected one (P). The nomenclature used is the same as in Table 3.1. The numbers within parentheses show the statistical error only. All results correspond to the NLSH-P bound wave function.

the $p_{3/2}$ strength is known to be fragmented into three states: the state considered here at $E_m = 18.4$ MeV, and two weaker peaks at around 22.0 and 22.7 MeV. According to [23, 44] the two higher lying peaks would contain about 10% of the total $p_{3/2}$ strength. The spectroscopic factors determined from data set (*a*) indicate that, taking this extra 10% contribution into account, there is similar $3/2^-$ and $1/2^-$ spectroscopic strength.

In what follows we use the new bound state wave functions (NLSH-P) to make predictions for comparison to the other data sets (*b*) and (*c*). We stress that we have used high quality data to fix the size of the wave function and that because data set (*a*) corresponds to parallel kinematics no experimental information on the R^{TL} response has been employed.

Let us now focus on the spectroscopic factors obtained from reduced cross sections in data sets (*b*) and (*c*). Fig. 3.3 shows the reduced cross sections for $p_{1/2}$ and $p_{3/2}$ shells. Left and right panel correspond respectively to data sets (*b*) and (*c*). As in Fig. 3.1, for each curve a global scale factor has been fitted to the experimental data. The corresponding scale factors and their statistical errors are listed in Table 3.3. Similarly to what we saw for set (*a*), also for sets (*b*) and (*c*) EDAD-type optical potentials give larger spectroscopic factors than EDAI-O (see also Fig. 3.4).

The results for the $p_{3/2}$ shell corresponding to the Saclay experiment (left panel) include the contribution of the $(5/2^+, 1/2^+)$ doublet. We have verified that the change in the shape of the responses or reduced cross section after inclusion of the doublet is small. The main effect of its inclusion is a decrease of the deduced spectroscopic factor for the

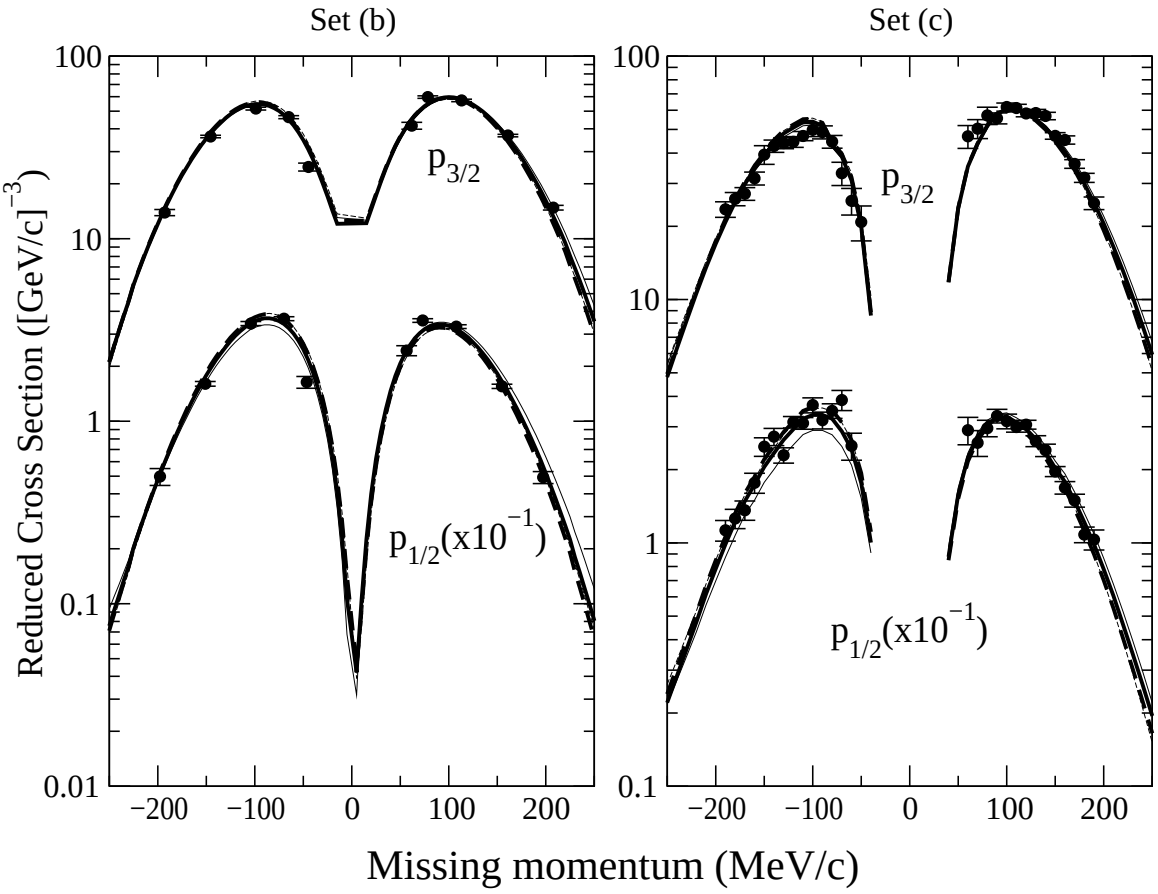

Figura 3.3: Same as Fig. 3.1 for the experiments performed by Chinitz *et al.* [21] (left panel, set (*b*)) and by Spaltro *et al.* [22] (right panel, set (*c*)). In all the cases the NLSH-P relativistic bound proton wave function and EDAI-O optical potential has been used. For $p_{3/2}$ shell in set (*b*) the contribution from the nearby $5/2^+$ and $1/2^+$ states has been taken into account (see text). Each curve is scaled by the corresponding spectroscopic factor in Table 3.3.

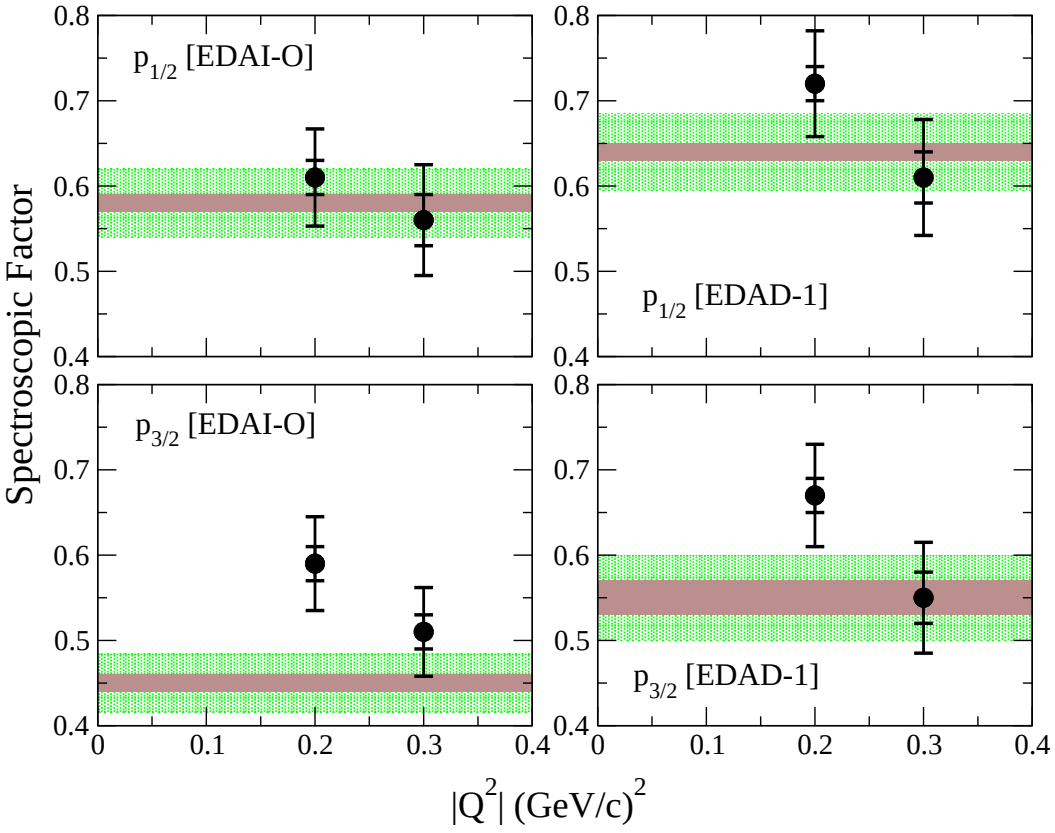

Figura 3.4: Spectroscopic factors derived within the fully relativistic approach from the low-Q^2 data discussed in this work with NLSH-P wave function, CC2 current operator and EDAI-O (left) or EDAD-1 (right) optical potentials. The inner error bars include statistical errors only, the outer one includes also the additional systematic error in the reduced cross sections for each experiment. The bands covering the whole $|Q^2|$ range corresponds to the value obtained from the data set (a) [23], while the dots at $|Q^2| = 0.2$ (GeV/c)^2 and 0.3 (GeV/c)^2 correspond to the data set (c) [22] and set (b) [21], respectively.

$p_{3/2}$ shell of the order of 10%. In ref. [21] the contribution of this doublet was subtracted from the experimental data with a procedure based on a nonrelativistic formalism. We have chosen to use the uncorrected data from ref. [44], and include the contribution from the doublet in our theoretical calculation. The $s-d$ content has been determined through fits to data set (a) for this state [23]. The values of the spectroscopic factors are $S_{1/2+} = 0.034(2)$ (RCC1), 0.034(2) (RCC2), $S_{5/2+} = 0.086(5)$ (RCC1), 0.088(5) (RCC2) (with a χ^2/N_{DF} of the order of 0.5).

Let us now discuss the results corresponding to data set (b) in left panel of Fig. 3.3. As shown, the calculations reproduce in general the experimental data for both shells with the scale factors listed in Table 3.3. Although the various approximations give similar results, we note that the RCC1 (thin solid line) reduced cross sections for the $p_{1/2}$ shell are less symmetrical around $p_m = 0$, a behavior that is not favored by the data. For this data set (b) all the calculations, except RCC1 for the $p_{1/2}$ shell, reproduce well the asymmetry of the reduced cross section. We will return to this point when talking about the TL observables in next section. Finally, it is important to remark that the spectroscopic factors obtained from the data set (b) (Table 3.3) agree, within statistical errors, with those obtained from data set (a) taking into account the systematic error of both experiments: around 5.4% for data set (a) [23] and 6.3% for data set (b) [44].

Concerning set (c) [22] the data on reduced cross sections in right panel of Fig. 3.3 have been obtained from the differential cross sections and detailed kinematics setup in Appendices A and D of ref. [45] (the systematic error for data set (c) reduced cross section is 6% [22]). For the $p_{1/2}$ shell, the reduced cross section is well reproduced by both relativistic and projected calculations, except in the case of the RCC1 calculation (thin solid line) that underestimates the data for negative missing momentum values. This is consistent with the results previously discussed for data set (b). For this shell, the spectroscopic factors that fit data set (c) are larger than the ones derived from data sets (a) or (b), but they are all compatible within statistical errors. In the case of the $p_{3/2}$ shell, although the shape of the cross section is well reproduced by the various calculations, the situation on the spectroscopic factors is clearly different (see Table 3.3). With EDAI-O optical potential the values of the spectroscopic factors that fit the $p_{3/2}$ data on reduced cross sections in set (c) are $25-30\%$ larger than the ones obtained from data set (a). These scale factors are also larger than the ones obtained from data set (b), but in this case the discrepancy is of the order of 15%, which is comparable to the combined systematic and statistical error for these values. EDAD-type potentials not only give larger spectroscopic

factors but also give, on average, better agreement between $p_{3/2}$ spectroscopic factors of the three different sets (a), (b) and (c). This is seen in detail in Tables 3.1 and 3.3 and is further illustrated in Fig. 3.4.

In summary, the shapes of the reduced cross sections are well described by all the RCC2 calculations and data sets, what makes us conclude that we can rely on the spectroscopic factors derived with EDAD-1 and NLSH-P potentials. Thus the differences in the $p_{3/2}$ spectroscopic factors (see Fig. 3.4) obtained with the same ingredients (wave functions, operators and optical potentials) may be attributed either to a global scale variation among the three experiments for the $p_{3/2}$ shell, or to limitations of the theory. Coupled channel contributions or MEC could possibly make a different effect for the three kinematics analyzed in this work.

3.3.2 Response Functions and longitudinal-transverse Asymmetry

In this section we present results for the response functions and asymmetries and compare them to the data in sets (b) and (c) measured at Saclay [21] and NIKHEF [22], respectively. As already mentioned, these two experiments were performed under $|\vec{q}| - \omega$ constant kinematics so that the TL response and asymmetry (R^{TL}, A_{TL}) can be obtained from the cross sections measured at $\phi_F = 0^o$ and $\phi_F = 180^o$ with the other variables (ω, Q^2, E_m, p_m) held constant. Moreover, the response functions $R^L + \frac{q^2}{2Q^2}R^{TT}$ and R^T were also determined for data set (c) [22].

Figs. 3.5 and 3.6 show respectively R^{TL} and A_{TL} for $p_{1/2}$ (upper panels) and $p_{3/2}$ (lower panels) corresponding to set (b) (left panels) and set (c) (right panels). In each panel we present four curves with the same conventions as in previous figures: RCC1 (thin solid), RCC2 (thick solid), PCC1 (thin-dashed) and PCC2 (thick-dashed). Each R^{TL} curve is scaled with the corresponding spectroscopic factor quoted in Table 3.3. As it was also the case for reduced cross sections, there are no appreciable differences in the shapes of curves obtained with the different types of optical potentials. Obviously, the asymmetry A_{TL} is independent on the value of the spectroscopic factor. The results for the $p_{3/2}$ shell in bottom-left panel of Figs. 3.5 and 3.6 include the contribution of the ($5/2^+$,$1/2^+$) doublet as explained for set (b) in previous section. The asymmetry A_{TL} was not produced by the Saclay experiment (set(b)), but we have deduced A_{TL} from the data using the R^{TL} values as well as the cross section data in [44].

In Fig. 3.5 we also show by dotted lines the nonrelativistic results of ref. [22]. For

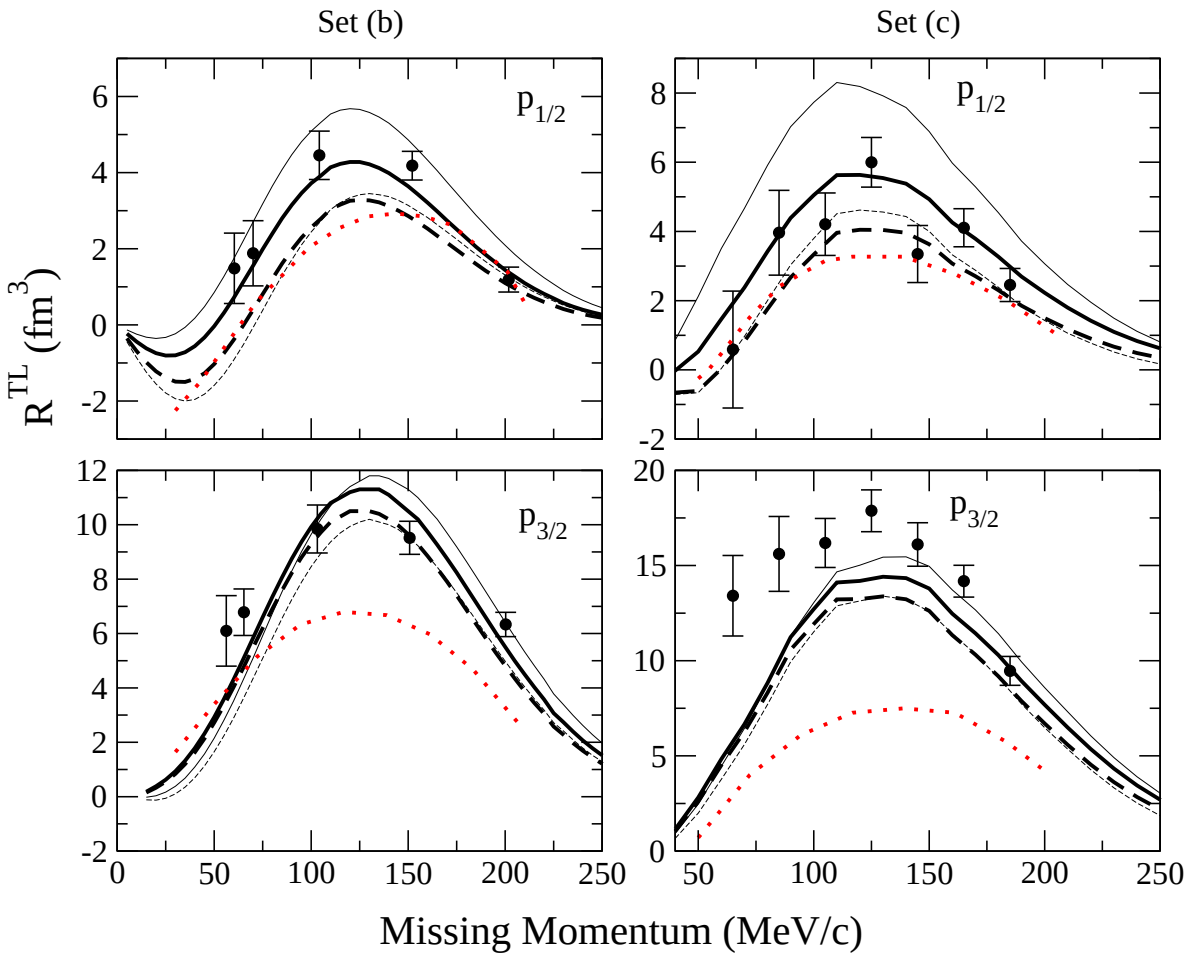

Figura 3.5: Response R^{TL} for proton knockout from ^{16}O for $1p_{1/2}$ (top panels) and $1p_{3/2}$ (bottom panels). Results and data shown correspond to kinematics of data set (b) [21] (left) and set (c) [22] (right). Line conventions as in Figs. 3.1 and 3.3 (NLSH-P wave function and EDAI-O optical potential). The curves have been scaled by the spectroscopic factors in Table 3.3. Additional dotted curves correspond to the nonrelativistic analyses of ref. [22].

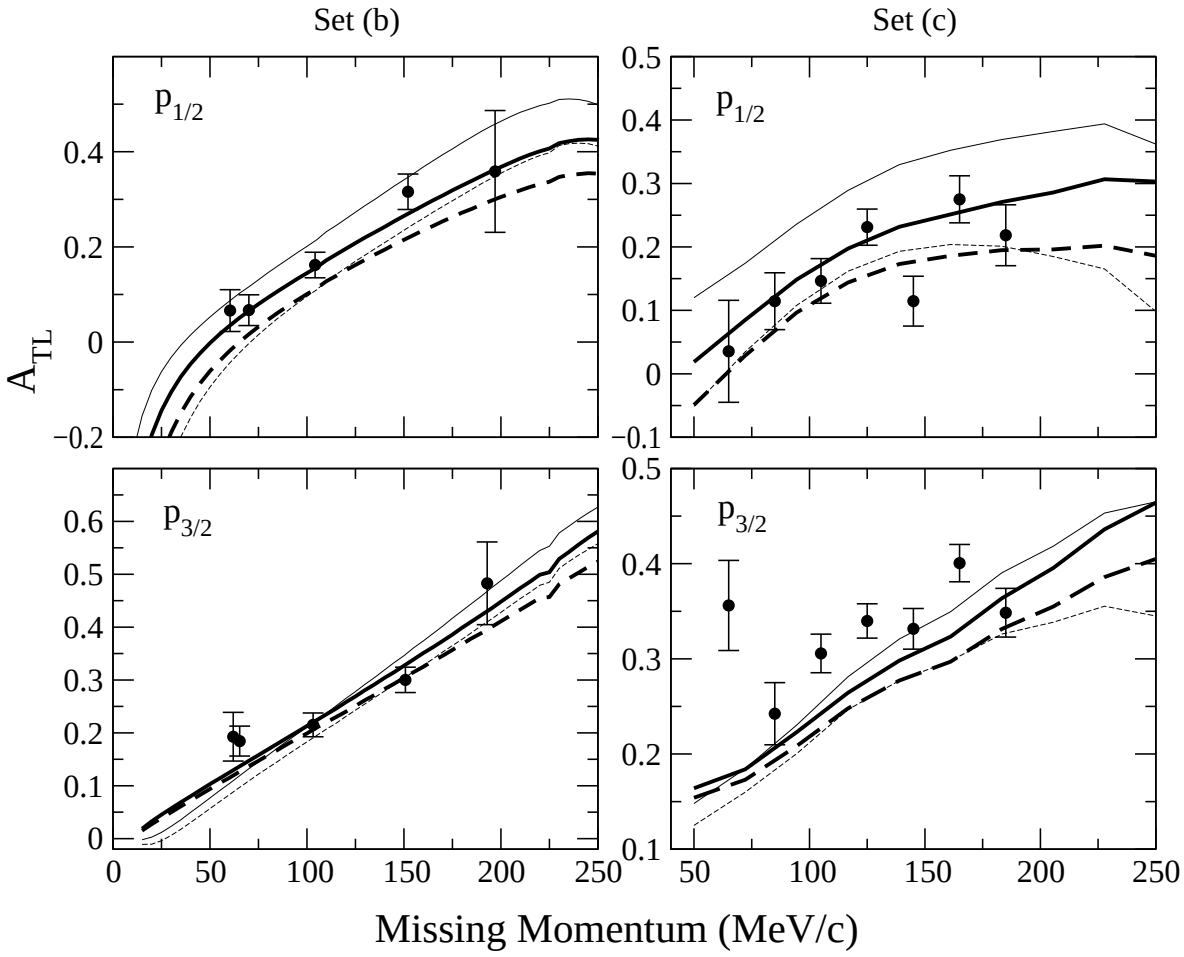

Figura 3.6: Same as Fig. 3.5 for the A_{TL} asymmetry. We recall that this observable is independent on the spectroscopic factor.

	Set (b)				Set (c)			
	$p_{1/2}$		$p_{3/2}$		$p_{1/2}$		$p_{3/2}$	
	N_{TL}	χ^2/N_{DF}	N_{TL}	χ^2/N_{DF}	N_{TL}	χ^2/N_{DF}	N_{TL}	χ^2/N_{DF}
RCC1	0.83(10)	0.65	0.95(17)	5.3	0.63(10)	1.1	1.09(12)	3.2
PCC1	1.32(42)	4.5	1.14(22)	5.8	1.15(17)	1.1	1.28(12)	2.5
RCC2	1.14(12)	0.49	1.02(15)	3.4	0.90(13)	1.0	1.17(12)	2.5
PCC2	1.48(32)	2.2	1.11(17)	3.8	1.26(19)	1.0	1.28(11)	2.1
NR	1.56(12)		1.66(9)		1.50(12)		2.05(10)	

Tabla 3.4: Extra scale factor N_{TL} needed to fit the experimental R^{TL} response. These factors would multiply those in Table 3.3 to scale theory to experiment on R^{TL}. A value of 1 indicates that no extra enhancement or quenching of the response is found. The numbers in parentheses show the statistical error only. The quality of the fit (χ^2/N_{DF}) is also quoted in every case. NR corresponds to the nonrelativistic analysis of ref. [22]. These numbers correspond to EDAI-O potential. Very similar numbers are obtained with EDAD-1, EDAD-2 or EDAD-3.

comparison to previous studies in refs. [21,22], we quote in Table 3.4 the factor required to scale the theoretical predictions to the R^{TL} data, additional to the factors in Table 3.3. A value of one in this table indicates that the same spectroscopic factor fits *both* the reduced cross section and R^{TL}, *i.e.,* indicates that the TL strength is consistently predicted by the theory.

Let us first discuss the comparison between theory and experiment for data set (b). From the results shown in Figs. 3.5 and 3.6, it is clear that the effects of the negative-energy components show up more in R^{TL} and A_{TL} than in the cross sections (Fig. 3.3). In the case of the $p_{1/2}$ shell (left-top panel of Fig. 3.5), the RCC2 calculation agrees with experimental data within statistical errors, while PCC1 and PCC2 results for R^{TL} (dashed lines) lie about a 30-50% below the data, and the RCC1 calculation (thin solid line) overestimates the R^{TL} response by around 20% (see Table 3.4). In the case of the $p_{3/2}$ orbit (left-bottom panel), all the approximations predict similar curves: The projected results are much closer to fully relativistic ones than for the $p_{1/2}$ shell. Overall, the fully relativistic calculations seem to be favored by the data. The fact that in this shell the variation introduced by the negative energy components is much smaller than for the $p_{1/2}$ shell explains why the difference between RCC1 and RCC2 results is smaller for the

$p_{3/2}$ than for the $p_{1/2}$ shell. These results agree with the conclusion reached from RPWIA calculations in ref. [18] about the behavior of $j = \ell \pm 1/2$ spin-orbit partners which was also corroborated in RDWIA calculations at high $|Q^2|$ [8].

With regards to the TL observable, independent on the spectroscopic factor, we may conclude that for $p_{1/2}$ shell, A_{TL} is best reproduced by RCC2 results, while for $p_{3/2}$ shell the four theoretical results are very close together, and the experimental data agree with all of them.

In the right panels of Figs. 3.5 and 3.6 we see the results corresponding to data set (c). Most of the comments on data set (b) apply also here, though the data are somewhat more scattered and have larger error bars. In the case of the $p_{1/2}$ shell, PCC1 and PCC2 results are very similar and lie below the data; among the fully relativistic calculation, the RCC2 result reproduces the data within statistical errors, while RCC1 overestimates them by a 35%. In the case of the $p_{3/2}$ shell (bottom-right panel), all the calculations underestimate the experimental TL response by around 17-28%, except RCC1 for which the "additional" factor in Table 3.4 is compatible with one within statistical errors.

In Fig. 3.7 we show the results for the responses $R^L + v_{TT}/v_L R^{TT}$ (top panels) and R^T (bottom panels) for the $p_{1/2}$ and $p_{3/2}$ shells compared to the data from NIKHEF [22]. Each curve is scaled with the spectroscopic factors quoted in Table 3.3. Notice that these responses are rather insensitive to dynamical enhancement of lower components. This is consistent with the behavior observed in Fig. 3.1 and also with results of RPWIA calculations [18]. The results in Fig. 3.7 indicate that the separated responses are in general well reproduced by the relativistic as well as by the projected calculations for both shells, exception made of the data point at the lowest missing momenta where, as indicated by the large error bars, the L/T separation is more problematic.

Summarizing, for the $p_{1/2}$ shell the RCC2 results agree well with all observables and data sets, while RCC1 (projected) calculations show a too large (small) R^{TL} and A_{TL}. For the $p_{3/2}$ shell the theoretical calculations lie much closer together, and generally agree with all data sets and observables, except for R^{TL} and A_{TL} of data set (c). Although the R^{TL}, A_{TL} data on $p_{3/2}$ in set (c) lie higher than theoretical calculations, they are almost compatible with RCC1 and RCC2 calculations within statistical errors. This situation is quite different from the one found in ref. [22], which is also shown for comparison in Fig. 3.5. The dotted lines in this figure show the nonrelativistic results of ref. [22] that were obtained with nonrelativistic spectroscopic factors (0.61(3) for $p_{1/2}$ and 0.53(3) for $p_{3/2}$) and standard (Woods-Saxon type) nonrelativistic optical potentials and bound wave

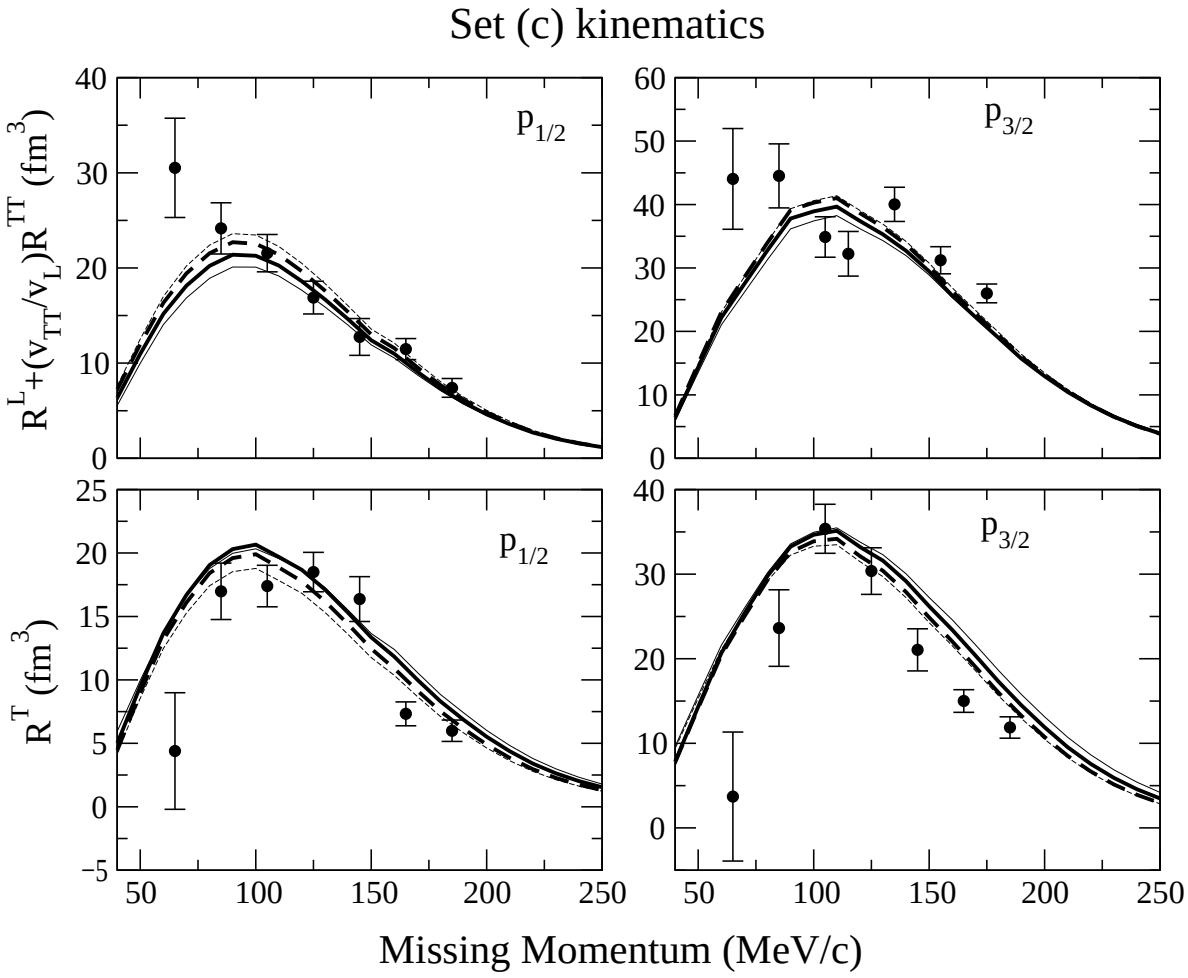

Figura 3.7: Response functions $R^L + v_{TT}/v_L R^{TT}$ and R^T for the kinematics of data set (c) [22]. Curves and calculations as in Fig. 3.3. The theoretical results are scaled with spectroscopic factors for this same experiment in Table 3.1.

functions. The latter were also fitted to Leuschner data [23].

3.3.3 Further Discussion on TL observables

In this section we focus in Fig. 3.5 comparing our results to previous nonrelativistic ones. The dotted curves -representing the nonrelativistic calculations by Spaltro *et. al.* [22]- clearly underestimate TL responses for all shell and data sets. The deviation from data is larger for $p_{3/2}$ shell, particularly in data set (c), where the dotted curve gives roughly one half of the experimental TL response. Why is it that relativistic results in this figure are so much closer to data that nonrelativistic ones?.

We have examined in detail effects due to the various aspects that are relevant in comparing relativistic to nonrelativistic results. The effects of Darwin term are already taken into account as they basically affect the spectroscopic factors. The effects of the negative energy components, as already mentioned, are very small for R^L, R^T responses in all data sets (a), (b) and (c) but, as seen in Fig. 3.5 and Table 3.4, they are important for TL observables in data sets (b) and (c), particularly for the $p_{1/2}$ shell. We are then left to consider the effect of truncation of the current operator (TCO). TCO produces also a negligible effect at the kinematics of data set (a), but it is more important at the kinematics of data sets (b) and (c). This again affects more the TL responses and asymmetries where it may represent up to a 15% effect (see also ref. [4]). Thus for $p_{1/2}$ shell, TCO roughly explains the difference at the maxima between dotted curves and the curves obtained with projected calculations. However for $p_{3/2}$ shell TCO explains only a small fraction of the difference between dotted curves and results of projected calculations. The largest fraction of this difference is due to the use of a too small spectroscopic factor (see ref. [22]) that was taken from ref. [23] and that by no means fits the data on reduced cross sections in set (c). As seen in Tables 3.1,3.3 and Fig. 3.4 the spectroscopic factor deduced from reduced cross sections in data set (c) is $25-30\%$ larger than that from data set (a).

The message from this is, not only that relativistic effects are important in perpendicular kinematics at low $|Q^2|$, but also that a careful analysis of all pieces of information has to be done to get a consistent picture of the three different sets of data. Since R^{TL} responses are known to be sensitive not only to relativistic effects but also to exchange currents, or other possible many-body effects, it is important to establish a clear framework that allows to look for the proper magnitude of such effects.

Indeed if we compare our results to data for the A_{TL} observable that is free from spectroscopic factor ambiguities, we find that all data are well reproduced with the standard CC2 current operator, except the $p_{3/2}$ data in set (c) which are only larger than theory by a factor ~ 1.17. This is to be compared to the 2.05 factor that one could expect from ref. [22].

3.4 Summary and Conclusions

In summary we find that the fully relativistic treatment improves substantially the description of reduced cross sections and individual responses of all three sets of data on $^{16}O(e,e'p)$ at low $|Q^2|$. Although predictions from CC1 and CC2 current operators are rather close in most cases, data seem to favor the CC2 current operator. Therefore our remarks here will focus mainly on results with CC2 and with the improved NLSH-P bound nucleon wave functions, that have the correct r.m.s. radius. Using the most complete set of data on reduced cross sections in parallel kinematics of Leuschner *et al.* [23] (set (a)) we obtain spectroscopic factors ranging from 0.58 to 0.64 for $p_{1/2}$ and from 0.45 to 0.55 for $p_{3/2}$, depending on whether we use A-independent (EDAI-O) or A-dependent (EDAD-1,2,3) optical potentials. In ^{16}O, the latter potentials produce a larger Darwin effect, thus larger spectroscopic factors. Compared to the cases studied in previous works on ^{40}Ca and ^{208}Pb, the determination of spectroscopic factors in ^{16}O with the relativistic approach is different in several respects. In the former cases, the standard NLSH wave functions were found to reproduce well the shapes of reduced cross sections and the only fitted parameter was the spectroscopic factor. The latter was practically independent on the optical potential used and was ~ 0.7 for the levels just below the Fermi level. On theoretical grounds smaller spectroscopic factors for ^{16}O are expected. In particular, from shell model Monte Carlo calculations on ^{16}O [46], one may expect $S_\alpha \sim 0.5$ though other theories predict somewhat larger values [47, 48]. Larger spectroscopic factors are obtained from Spaltro *et al.* data [22] on reduced cross sections in perpendicular kinematics (set (c)), while Chinitz's *et al.* data [21] also in perpendicular kinematics (set (b)) give similar spectroscopic factors than set (a). As one can see in Fig. 3.4, within error bars, spectroscopic factors derived from all data sets with EDAD-1 are compatible with each other. To overcome the uncertainty due to the optical potential (see also Fig. 3.4) one would need to fit the relativistic potential to both elastic and inelastic proton scattering data from ^{16}O in a manner similar to what has been done for nonrelativistic potentials [43].

The analyses of individual responses is practically independent on the optical potential, once they are scaled by the corresponding spectroscopic factors.

There is a long standing controversy surrounding the TL data for the $p_{1/2}$ and $p_{3/2}$ shells measured at Saclay [21] and NIKHEF [22]. We have therefore paid particular attention to TL responses and asymmetries and we conclude that there is not a fundamental inconsistency. Even at the low $|Q^2|$ values considered here, the TL response is much more sensitive than L and T responses to relativistic effects, in particular to the dynamical enhancement of the lower components. The role played by the latter is appreciated comparing fully relativistic results (RCC2 or RCC1) to those obtained using wave functions projected on the positive energy sector (PCC2 or PCC1). RCC2 results agree well with experimental TL responses on $p_{1/2}$ (as well as with TL asymmetries) which are underestimated by PCC2 and overestimated by RCC1, because CC1 current operator overemphasizes the role of negative energy components. The overall agreement with data on TL responses and asymmetries from set (b) and set (c) is quite satisfactory, with the exception of data on $p_{3/2}$ shell from set (c), but even in this case theory is much closer to experiment than previously found in ref. [22]. In particular, the large difference between data on TL responses from the two different sets is well accounted for by the present analyses. This is in contrast with the situation depicted in ref. [22], which is represented by dotted lines in Fig. 3.5.

In short, the puzzle of the large discrepancy in the TL-response obtained in Saclay [21] and NIKHEF [22], and the "additional" TL-strength found in both experiments is, to a large extent, explained by the effect of the negative energy components in the wave functions –a dynamical relativistic effect that may not have been expected at low transfer and missing momentum.

The large general mismatch of data set (c) on $p_{3/2}$ shell seems to point to a normalization problem which would require experimental verification. Our analyses indicate that the problem is not so much connected to the TL response, but rather to the normalization used. Nevertheless, since meson exchange currents and particularly isobar currents are claimed to affect more the $p_{3/2}$ than the $p_{1/2}$ orbitals [49], it would be interesting to see whether our fully relativistic calculation extended to include the isobar and other meson exchange effects would lead to better agreement with TL $p_{3/2}$ data from set (c). It will also be interesting to see how relativistic and nonrelativistic approaches compare to new data expected from future experiments that have been approved to measure reduced cross sections and TL-responses in ^{16}O with unprecedented precision at Jefferson Lab.

Acknowledgements

This work was partially supported under Contracts No. PB/98-1111, PB/98-0676, PB/96-0604 and by the Junta de Andalucía (Spain). J.R.V. and A.E. acknowledge support from doctoral fellowships of the Consejería de Educación de la Comunidad de Madrid and Ministerio de Educación y Cultura (Spain), respectively.

Bibliografía

[1] S. Boffi, C. Giusti, F.D. Pacati, Phys. Rep. **226**, 1 (1993); S. Boffi, C. Giusti, F. Pacati, M. Radici, *"Electromagnetic Response of Atomic Nuclei"*, (Oxford-Clarendon Press, 1996); J.J. Kelly, Adv. Nucl. Phys. **23**, 75 (1996).

[2] I. Bobeldijk *et al.*, Phys. Rev. Lett. **73**, 2684 (1994).

[3] L. Lapikás, Nucl. Phys. **A553**, 297c (1993).

[4] A. Meucci, C. Giusti, F. Pacati, nucl.-th/0101034 (Jan. 2001)

[5] J.M. Udías, P. Sarriguren, E. Moya de Guerra, E. Garrido, J.A. Caballero, Phys. Rev. C **48**, 2731 (1993).

[6] J.M. Udías, P. Sarriguren, E. Moya de Guerra, E. Garrido, J.A. Caballero, Phys. Rev. C **51**, 3246 (1995).

[7] J.M. Udías, P. Sarriguren, E. Moya de Guerra, J.A. Caballero, Phys. Rev. C **53**, R1488 (1996).

[8] J.M. Udías, J.A. Caballero, E. Moya de Guerra, J.E. Amaro, T.W. Donnelly, Phys. Rev. Lett. **83**, 5451 (1999).

[9] A. Picklesimer, J.W. Van Orden, Phys. Rev. C **35**, 266 (1987); **40**, 290 (1989).

[10] Y. Jin, D.S. Onley, Phys. Rev. C **50**, 377 (1994).

[11] S.Gardner, J.Piekarewicz, Phys.Rev. C **50**, 2882 (1994).

[12] C.J. Horowitz, D.P. Murdock, B.D. Serot, *Computational Nuclear Physics*, Eds. K. Langanke, J.A. Maruhn, S.E. Koonin (Springer, Berlin, 1991).

[13] E.D. Cooper, S. Hama, B.C. Clark, R.L. Mercer, Phys. Rev. C **47**, 297 (1993).

[14] J.E. Amaro, J.A. Caballero, T.W. Donnelly, A.M. Lallena, E. Moya de Guerra, J.M. Udías, Nucl. Phys. **A602**, 263 (1996); J.E. Amaro, J.A. Caballero, T.W. Donnelly, E. Moya de Guerra, **A611**, 163 (1996).

[15] J. Gao *et al.*, Phys. Rev. Lett. **84**, 3265 (2000).

[16] J.P. McDermott, Phys. Rev. Lett. **65**, 1991 (1990); Y. Jin, D.S. Onley, L.E. Wright, Phys. Rev. C **45**, 1311 (1992).

[17] J.A. Caballero, T.W. Donnelly, E. Moya de Guerra, J.M. Udías, Nucl. Phys. **A632**, 323 (1998).

[18] J.A. Caballero, T.W. Donnelly, E. Moya de Guerra, J.M. Udías, Nucl. Phys. **A643**, 189 (1998).

[19] R.J. Woo *et. al.,* Phys. Rev. Lett. **80**, 456 (1998).

[20] J.M. Udías, J.R. Vignote, Phys. Rev. C **62**, 034302 (2000).

[21] L. Chinitz *et al.*, Phys. Rev. Lett. **67**, 568 (1991).

[22] C.M. Spaltro, H.P. Blok, E. Jans, L. Lapikás, M. van der Schaar, G. van der Steenhoven, P.K.A. de Witt Huberts, Phys. Rev. C **48**, 2385 (1993).

[23] M. Leuschner *et al.*, Phys. Rev. C **49**, 955 (1994).

[24] P. Schwandt, H.O. Meyer, W.W. Jacobs, A.D. Bacher, S.E. Vigdor, M.D. Kaitchuck, T.R. Donoghue, Phys. Rev. C **26**, 55 (1982).

[25] V. Van der Sluys, J. Ryckebusch, M. Waroquier, Phys. Rev. C **54**, 1322 (1996).

[26] J.E. Amaro, A.M. Lallena, J.A. Caballero, Phys. Rev. C **60**, 014602 (1999).

[27] A.S. Raskin, T.W. Donnelly, Ann. of Phys. (NY) **191**, 78 (1989).

[28] J.E. Amaro, T.W. Donnelly, Ann. Phys. (NY) **263**, 56 (1998); Nucl. Phys. **A646**, 187 (1999).

[29] T. de Forest, Nucl. Phys. **A392**, 232 (1983).

[30] H. Überall, *Electron Scattering from Complex Nuclei*, Academic, N.Y., (1971). M.E. Rose, *Relativistic Electron Scattering*, Wiley, N.Y., (1961).

[31] B.D. Serot, J.D. Walecka, Adv. Nucl. Phys. **16**, 1 (1986).

[32] J.A. Caballero, T.W. Donnelly, G.I. Poulis, Nucl. Phys. **A555**, 709 (1993).

[33] J.D. Bjorken, S.D. Drell, *Relativistic Quantum Mechanics*, Mc Graw-Hill, N.Y., (1964)

[34] C. Giusti, F. Pacati, Nucl. Phys. **A473**, 717 (1987).

[35] S. Jeschonnek, T.W. Donnelly, Phys. Rev. C **57**, 2438 (1998); S. Jeschonnek, Phys. Rev. C **63**, 034609 (2001); S. Jeschonnek, J.W. Van Orden, Phys. Rev. C **62**, 044613 (2000).

[36] G.H. Rawitscher, Phys. Rev. C **31**, 1173 (1985).

[37] S. Boffi, C. Giusti, F.D. Pacati, F. Cannata, Nuovo Cimento **98**, 291 (1987).

[38] M. Hedayati-Poor, J.I. Johansson, H.S. Sherif, Phys. Rev. C **51**, 2044 (1995); Nucl. Phys. **A593**, 377 (1995); J.I. Johansson, H.S. Sherif, G.M. Lotz, Nucl. Phys. **A605**, 517 (1996).

[39] J.J. Kelly, Phys. Rev. C **56**, 2672 (1997); **59**, 3256 (1999).

[40] H.W.L. Naus, S. Pollock, J.H. Koch, U. Oelfke, Nucl. Phys. **A509**, 717 (1990); S. Pollock, H.W.L. Naus, J.H. Koch Phys. Rev. C **53**, 2304 (1996).

[41] M.M. Sharma, M.A. Nagarajan, P. Ring; Phys. Lett. B **312**, 377 (1993).

[42] G.A. Lalazissis, J. König, P. Ring, Phys. Rev. C **55**, 540 (1997).

[43] J.J. Kelly *et al.*, Phys. Rev. C **39**, 1222 (1989); J.J. Kelly, Phys. Rev. C **39**, 2120 (1989); J.J. Kelly *et al.* Phys. Rev. C **41**, 2504 (1990); Q. Cheng, J.J. Kelly, P.P. Singh, M.C. Radhakrishma, W. P. Jones and H. Nann, Phys. Rev. C **41**, 2514 (1990); R.S. Flanders *et al.*, Phys. Rev. C **43**, 2103 (1991).

[44] L. Chinitz, Ph.D. Thesis, University of Virginia (1990).

[45] C.M. Spaltro, M.Sci. Thesis, University of Utrecht (1992).

[46] T. Otsuka, in *Proceedings of the International NATO-Advanced Study Institute on Nuclei far from Stability and Astrophysics*, edited by D. N. Poenareau *et al.* (Kluwer Academic, The Netherlands, 2001), p. 91.

[47] D. Van Neck, M. Waroquier, A.E.L. Dieperink, Steven C. Pieper, V.R. Pandharipande, Phys. Rev. C **57**, 2308 (1998).

[48] W.J.W. Geurts, K. Allaart, W.H. Dickhoff and H. Müther, Phys. Rev. C **53**, 2207 (1996); H. Müther, W.H. Dickhoff, Phys. Rev. C **49**, R17 (1994).

[49] J. Ryckebusch, D. Debruyne, W.V. Nespen, S. Janssen, Phys. Rev. C **60**, 034604 (1999).

Capítulo 4

La reacción $^4He(e, e'p)^3H$

The European Physical Journal A - Hadrons and Nuclei 22 (2004) 449-454

Measurement of R_{LT} and A_{TL} in the $^4He(e,e'p)^3H$ Reaction at p_{miss} of 130-300 MeV/c

K. A. Aniol[1], M. B. Epstein[1], E. Gama[1], D. J. Margaziotis[1] W. Bertozzi[2], J. P. Chen[2], D. Dale[2], R. E. J. Florizone[2], S. Gilad[2], A. J. Sarty[2], J. A. Templon[2], S. P. Van Verst[2], J. Zhao[2], Z.-L. Zhou[2], P. Bartsch[3], W. U. Boeglin[3], R. Boehm[3], M. O. Distler[3], I. Ewald[3], J. M. Friedrich[3], R. Geiges[3], P. Jennewein[3], M. Kahrau[3], K. W. Krygier[3], A. Liesenfeld[3], H. Merkel[3], K. Merle[3], U. Muller[3], R. Neuhausen[3], E. A. J. M. Offermann[3], Th. Pospischil[3], G. Rosner[3], H. Schmieden[3], A. Wagner[3], Th. Walcher[3], M. Kuss[4], A. Richter[4], G. Schrieder[4], K. Bohinc[5], M. Potokar[5], S. Širca[5], J. M. Udias[6], Javier R. Vignote[6],and R. Schiavilla[7]

[1]*Department of Physics and Astronomy, California State University, Los Angeles, Los Angeles, California 90032, USA*

[2]*Laboratory for Nuclear Science, MIT, Cambridge, Massachusetts 02139, USA*

[3]*Institut für Kernphysik, Universität Mainz, D-55099 Mainz, Germany*

[4]*Institut für Kernphysik, Technische Universität Darmstadt, D-64289 Darmstadt, Germany*

[5]*Institute "Jožef Stefan" and University of Ljubljana, SI-1001 Ljubljana, Slovenija*

[6]*Departamento de Fisica Atomica, Molecular y Nuclear, Facultad de Ciencias Fisicas, Universidad Complutense de Madrid, E-28040 Madrid, Spain*

[7]*Department of Physics, Old Dominion University, Norfolk, Virginia 23529, USA*

We have measured the $^4He(e,e'p)^3H$ reaction at missing momenta of 130-300 MeV/c using the three-spectrometer facility at the Mainz microtron MAMI. Data were taken in perpendicular kinematics to allow us to determine the response function R_{LT} and the asymmetry term A_{TL}. Then data are compared to both relativistic and non-relativistic calculations.

PACS numbers: 25.10+s, 25.30.RW, 21.45.+v, 27.10+h

4.1 Introduction

There have been many studies of the (e,e'p) reaction with the overall objective of learning more about the detailed single nucleon distributions in nuclei. Of special interest are investigations of few body systems and light nuclei since they are more amenable to more complete and detailed theoretical calculations. Interpretation of the experimental results in terms of single nucleon properties is most readily done in the simple non-relativistic Plane Wave Impulse Approximation (PWIA). However, it has been clear for sometime now that the simple non-relativistic PWIA is not able to account for the observed cross sections. One has to understand the nature of the competing processes, particularly in the more interesting kinematic regions of high missing momenta. An important experimental tool in this regard is the response function decomposition of the cross sections. In the one photon exchange approximation the cross section can be written as [1] :

$$\frac{d^5\sigma}{d\Omega_e d\Omega_p dE_e} = K\ \sigma_{Mott}[\nu_L R_L + \nu_T R_T + \nu_{LT} R_{LT} cos\phi + \nu_{TT} R_{TT} cos2\phi] \qquad (4.1)$$

where ϕ is the angle between the electron scattering plane and the plane containing the momentum transfer $\vec{q}$ and the detected proton, K is a kinematic factor $\frac{mp_p}{(2\pi)^3}$ (where p_p is the momentum of the ejected proton), σ_{Mott} is the Mott cross section, the ν_i are additional kinematic factors and the R_i and R_{ij} are the response functions. The response functions describe the interaction of the longitudinal, L, and transverse, T, polarization states of the virtual photon with the nuclear charge and current. Theoretical calculations suggest that each of these response functions can exhibit selective sensitivity to particular reaction mechanisms in the (e,e'p) process. For example, past measurements of the R_{LT} interference response function have indicated that it is sensitive to relativistic effects and meson exchange currents (MEC). Measurements of the $^2H(e,e'p)n$ reaction [2] have shown that it is sensitive to inclusion of relativistic terms in the nucleon current while a previous study [3] of the $^4He(e,e'p)^3H$ reaction indicated the need to include meson exchange terms in order to reproduce both the cross sections and the R_{LT} response function measured for missing momentum $p_{miss} = 265$ MeV/c. Studies of the $^{16}O(e,e'p)^{15}N$ reaction have suggested that the R_{LT} response function is sensitive to both MEC [4] and a fully relativistic treatment [5] of the reaction.

The ^4He system is of particular interest since it is a tightly bound system for which

one can obtain the nuclear wavefunction from microscopic calculations based on realistic NN interactions. In this paper we report on a measurement of the R_{LT} interference response function in the $^4He(e,e'p)^3H$ reaction. These particular measurements were motivated in part by the measurement of R_{LT}, performed at the MIT-Bates Laboratory, for the $^4He(e,e'p)^3H$ reaction at missing momentum $p_{miss} = 265\ MeV/c$, incident electron energy, $E_o = 572.5\ MeV$, momentum transfer, $|\vec{q}| = 360\ MeV/c$, and energy transfer, $\omega = 200\ MeV$ [3]. The present experiment was designed to provide measurements of R_{LT} under similar kinematic conditions but over a wider range of p_{miss}.

4.2 The Experiment

The research reported here was done with the three-spectrometer facility at the Mainz microtron, MAMI, by the A1 collaboration. Data were taken at incident beam energies of 675 and 855 MeV and cover a range of p_{miss} from 131 MeV/c to 300 MeV/c. As was the case for the data of Ref. [3] ω was set at approximately 200 MeV and kept relatively constant in an attempt to keep final state interaction (FSI) effects constant for all measurements and also to minimize FSI effects since proton-nucleus energies of around 200 MeV are near the minimum of the $p - ^4He$ optical model potential derived by Van Oers et al [6].

The experimental setup was almost identical to that described in Ref. [7] and Ref. [8] except that for the present measurements the electron and proton spectrometers were interchanged, i.e. Spectrometer A was used to detect protons and Spectrometer B was used to detect electrons. (Details of the MAMI three spectrometer facility are described in Ref. [9].) Spectrometer C was used as a luminosity monitor. The angular acceptance of Spectrometer B, as defined by the data analysis cuts, was 2.29^o in the horizontal direction and 7.45^o in the vertical direction. The large angular acceptance of the proton spectrometer, spectrometer A, allowed us to break each angular setting into three data points of angular acceptance of 4.30^o (vertical acceptance is 11.46^o). The target consisted of cold ^4He gas (T = 20-23 K and P = 5-10 atm) encapsulated in an 8 cm diameter stainless steel quasi-spherical cell whose walls were 82 μm thick [10].

The target density was determined [8] by measuring elastic scattering from ^4He in Spectrometer B and normalizing the measured counts to the elastic scattering data and

form factor parametrization of Ref. [11]. Spectrometer C was configured to detect negatively charged particles and data were taken in Spectrometer C during the elastic scattering runs. For each beam energy the angle and momentum settings for Spectrometer C were kept fixed. Thus, with appropriate cuts to eliminate background, the recorded counts in Spectrometer C, along with the measured beam current, provided a measurement of the target density for any particular data run relative to what was determined from the elastic scattering data runs. The effective target length, as defined by the data analysis cuts, varied depending on the particular kinematic settings between 5.2 to 6.0 cm. The combined effective solid angles and target length of the two-spectrometer extended-target system was determined using the Monte Carlo code AEEXB [12].

Beam energies of 855 and 675 MeV were used with average beam currents of 40 μA. Due to constraints imposed by the available beam energies and the geometry of the experimental hall we were not able to keep $\vec{q}$ constant and $|\vec{q}|$ varied from 404.6 to 639.5 MeV/c. These changes in $|\vec{q}|$ are responsible for the discontinuities that are seen when the data are plotted as a function of p_{miss}.

To determine the asymmetry term, A_{TL}, and the interference response function, R_{LT}, data were taken in perpendicular kinematics.

$$A_{TL} = \frac{\sigma_f - \sigma_b}{\sigma_b + \sigma_f} \tag{4.2}$$

R_{LT} is defined in Equation 4.1. For each value of p_{miss} two measurements were made, the first with the proton spectrometer set at an angle forward of $\vec{q}$ (closer to the beam direction) to meaure σ_f, and the second with the proton spectrometer set at an equal angle backward of $\vec{q}$ (further away from the beam direction) to measure σ_b. Under these conditions the central value of p_{miss} is the same for both measurements.

Data were taken at one set of angles at the 855 MeV beam energy and three different sets of angles at the 675 MeV beam energy. After breaking up the horizontal angular acceptance of the proton spectrometer into three angular regions, each angular setting yielded three data points, with each data point spanning a total width in p_{miss} between 25 to 58 MeV/c. The kinematics for these data are shown in Table 4.1. To determine A_{TL} and R_{LT} the same cuts were put on $|\vec{q}|$, ω, and p_{miss} for each data point of the pair of angular settings used.

The combined energy resolution of spectrometers A and B along with the approximately 100 keV spread in the beam energy resulted in an E_{miss} spectrum in which the two-body breakup peak had a FWHM of approximately 700 keV. (See Figure 4.1) This

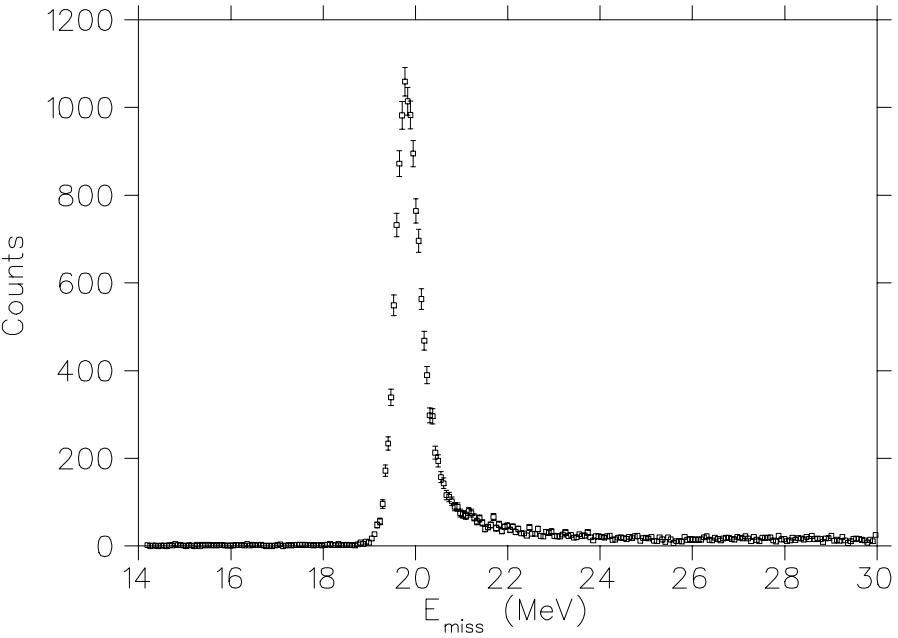

Figura 4.1: $^4He(e,e'p)^3H$. E_{miss} spectrum for $p_{miss} = 150\ MeV/c$. The three body breakup threshold is at $E_{miss} = 26.1\ MeV$.

was more than sufficient to provide clean separation between the two-body breakup peak and the threshold for the three-body continuum. Total combined systematic errors for individual cross section measurements were approximately 6%. Data are presented here only for the $^4He(e,e'p)^3H$ reaction, that is only for the two-body final state E_{miss} peak. The data were corrected for radiative losses due to internal and external bremsstrahlung processes [13], [14].

4.3 Results

The cross section data for proton angles forward of $\vec{q}$ (σ_f) are shown in Figure 4.2 and those for angles back of $\vec{q}$ (σ_b) are shown in Figure 4.3. Only statistical errors, which range between 1% to 7% , are plotted and these are almost always smaller than the size of the data points. The cross section data are tabulated in Table 4.1. Also shown in Figures 4.2 and 4.3 are four different theoretical predictions. We show two PWIA calculations, one using a ^4He wavefunction derived from the Argonne V14 nucleon-nucleon potential [15] and the other using a ^4He wavefunction derived from the Argonne V18 nucleon-nucleon potential and the Urbana IX three nucleon potential [16]. The calculations labeled Schiavilla incorporate the orthonormal-correlated states method described by Schiavilla [17] and include the effects of short range correlations, orthogonality corrections, final state interactions, and two-body charge and current operators.

The curves labeled RDWIA are fully relativistic distorted wave impulse approximation (RDWIA) calculations by Udias using the Madrid code [18]. This calculation uses the same ingredients as in the corresponding ones in ref. [19] that were compared to the transferred polarization ratio data at similar energies of the ejected proton as in this experiment. Namely: a) a relativistic mean field wave function fit to reproduce the rms radius and binding energy of ^4He which reproduces the momentum distributions from the ^4He data in Ref. [8]. b) an optical potential obtained by folding a density-dependent empirical effective p-N interaction (EEI) [20] with the measured charge density for tritium. Here we use the same potential as in Ref. [19], derived from parameters that were adjusted by Kelly to fit proton scattering data from ^4He, obtaining a better fit to the proton elastic scattering data in this nucleus than any previous optical potential. c) The CC1 current operator.

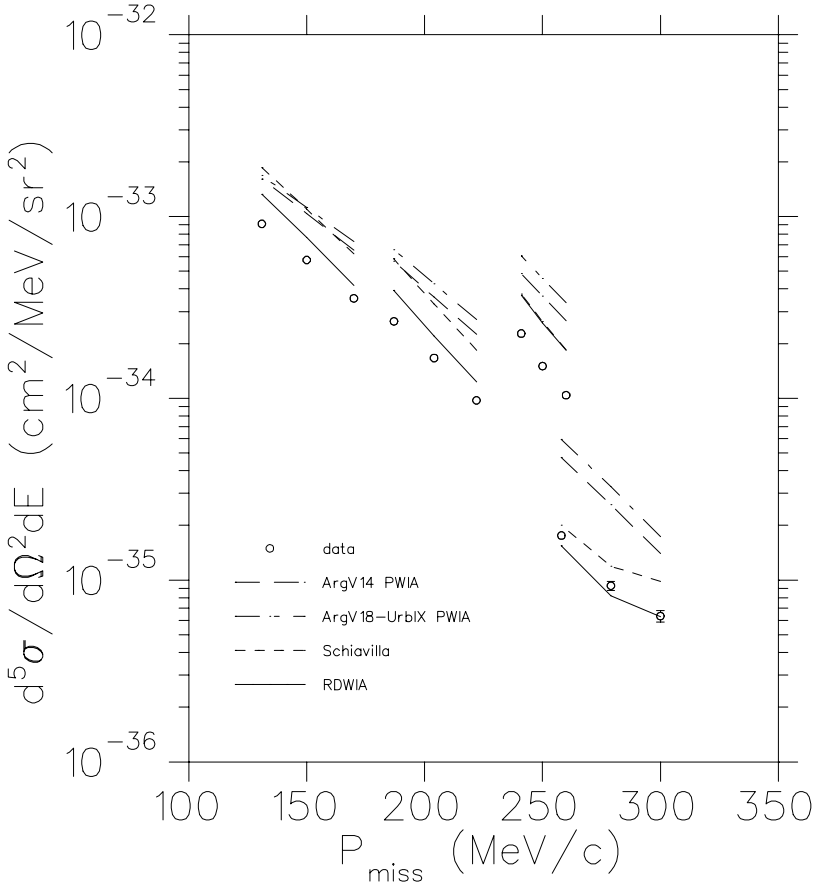

Figura 4.2: $^4He(e,e'p)^3H$. Cross sections for proton angles forward of q

The PWIA calculations were averaged over the finite acceptances of the spectrometers while the full Schiavilla and the RDWIA calculations of Udias were done only at the central point of these acceptances. Using the Argonne V14 PWIA calculation we compared the effects of acceptance averaging these calculations. The difference between the point and acceptance averaged calculations were typically less than 8 %.

Figure 4.4 shows the asymmetry term A_{TL} and Figure 4.5 shows R_{LT}. In these figures the two sets of error bars represent the statistical and systematic errors separately. Except for A_{TL} at $p_{miss} = 300\ MeV/c$ the systematic errors are always larger than the random errors. The theoretical predictions shown in Figures 4.4 and 4.5 are derived from the cross section calculations shown in Figures 4.2 and 4.3. To investigate the effects of MEC on R_{LT} and A_{TL} the Schiavilla calculations were also run without the MEC term but with everything else included. Figures 4.6 and 4.7 show these results.

In comparing theory with the cross section, R_{LT}, and A_{TL} data it is difficult to draw any firm conclusions. There is some indication from A_{TL} that the RDWIA calculations

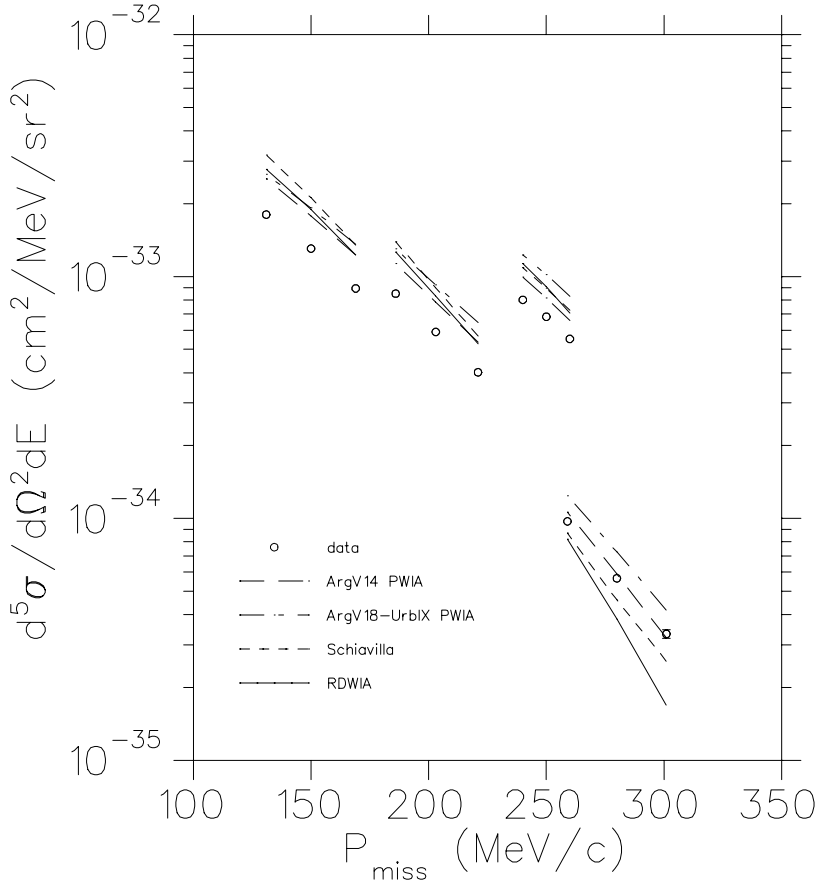

Figura 4.3: $^4He(e,e'p)^3H$. Cross sections for proton angles backward of q

of Udias or the full calculation of Schiavilla is necessary to produce the qualitative shape of the data. The inclusion of MEC terms in the Schiavilla calculation also substantially improves agreement with the R_{LT} data as was seen in the earlier MIT-Bates results [3]. However it is less clear which predictions produce the best fits to the cross section data. The full calculation of Schiavilla or the RDWIA calculations of Udias agree best with the forward angle cross section data while the simple PWIA calculation seems to do better for the back angle cross sections.

We note that the data measured at 855 MeV have Bjorken x = 1.08 and the largest value of Q^2. From the point of view of the electron kinematics the 855 MeV data should have been the best case for quasi-elastic scattering (x near 1) with the smallest contribution from meson exchange currents. In contrast, at 675 MeV and $\theta = 50^o$, x= 0.58 which should imply a greater role for meson exchange currents. However Figures 4.6 and 4.7 indicate that, at least in the context of the Schiavilla calculation, meson exchange currents are more important for the 855 MeV data than for the 675 MeV data. Overall

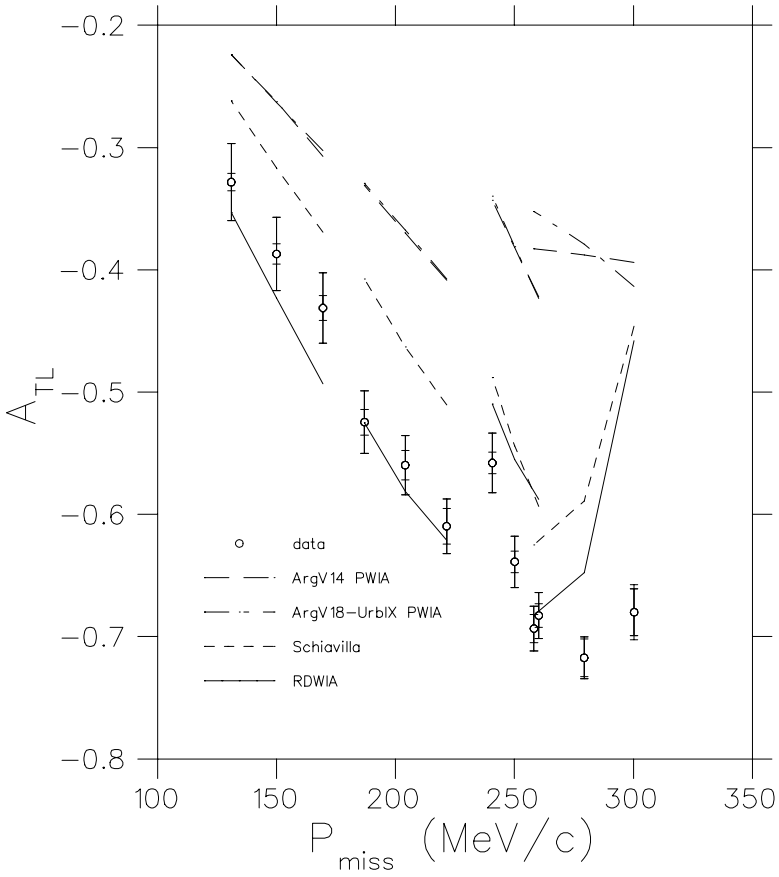

Figura 4.4: $^4He(e,e'p)^3H$. The transverse-longitudinal asymmetry A_{TL}

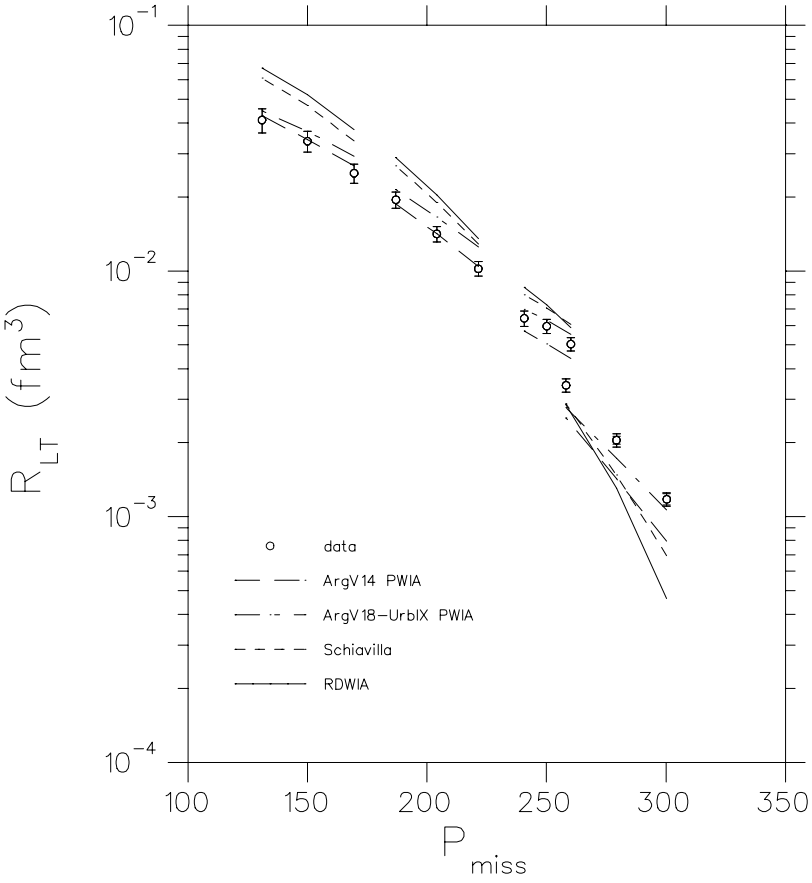

Figura 4.5: $^4He(e,e'p)^3H$. The longitudinal-transverse response function R_{LT}

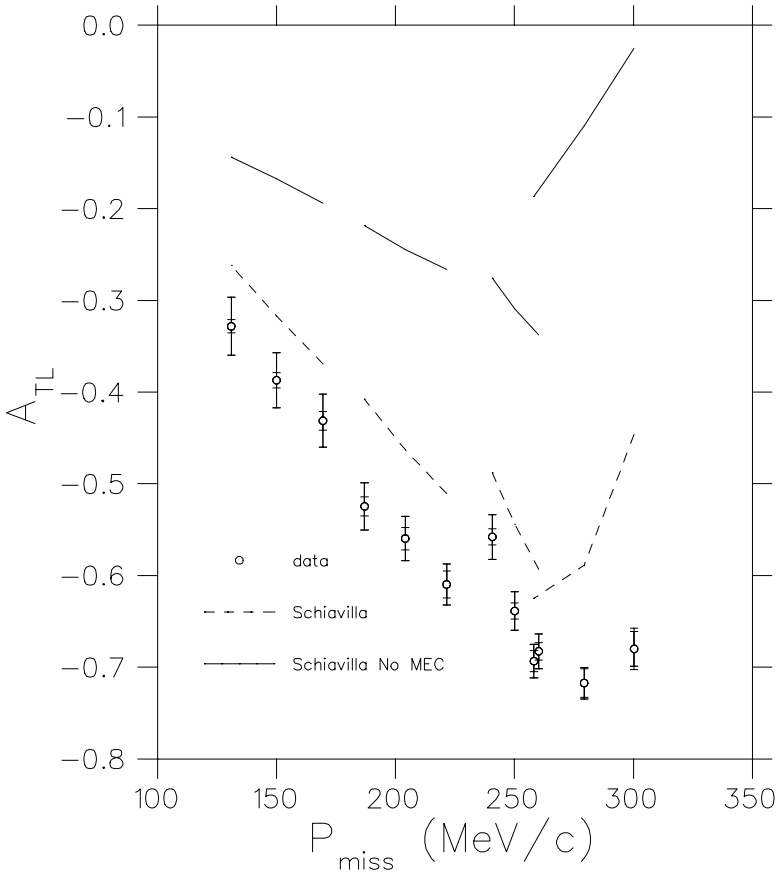

Figura 4.6: $^4He(e,e'p)^3H$. A_{TL} Schiavilla calculations with and without MEC terms

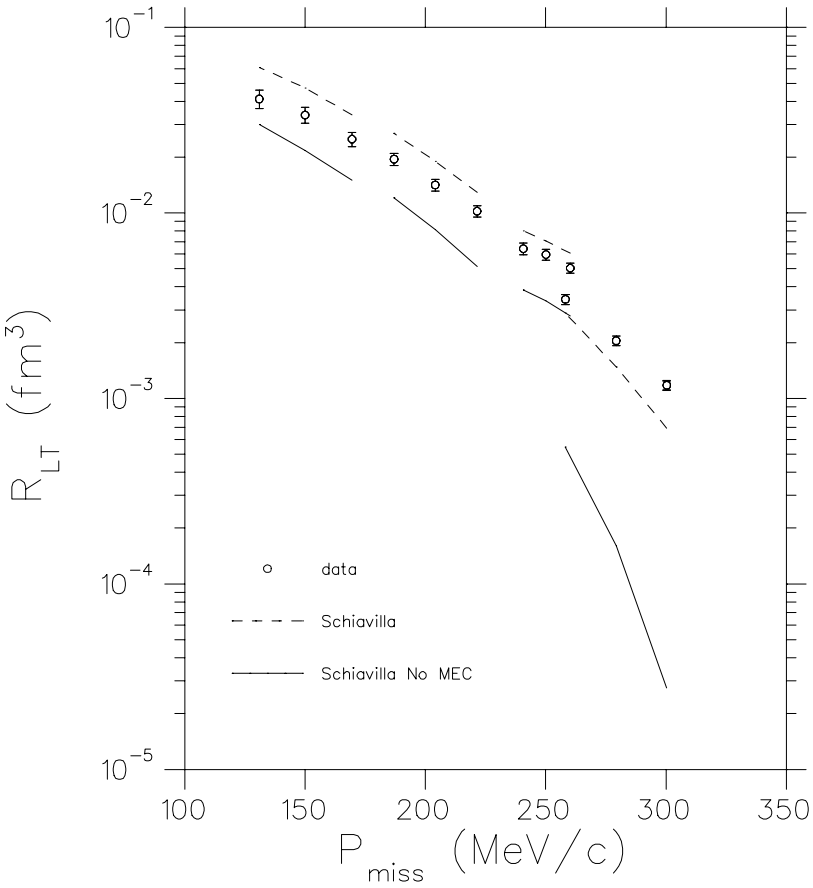

Figura 4.7: $^4He(e,e'p)^3H$. R_{LT} Schiavilla calculations with and without MEC terms

these data suggest that the inclusion of MEC terms and/or a fully relativistic calculation is necessary but at this time we are unable to conclude which effect is dominant.

4.4 Summary

We have taken data for the $^4He(e,e'p)^3H$ reaction in perpendicular kinematics that allowed us to determine R_{LT} and A_{TL} for p_{miss} from 130 to 300 MeV/c. Reasonable agreement with theory appears to require inclusion of final state interaction effects and the addition of meson exchange reaction terms and/or a fully relativistic treatment of the entire reaction. Additional data might clarify this situation. In this regard there is a proposal under review for a new series of measurements of the $^4He(e,e'p)^3H$ reaction to be done at Jefferson Lab.

We wish to thank the MAMI staff for their support during these experiments. This work was supported by the Deutsche Forschungsgemeinshaft (SFB 201) and Ri 242/15-2, by the U.S. National Science Foundation, and by the U.S. Department of Energy.

E_o MeV	θ_e deg.	q MeV/c	θ_p deg.	ω MeV	p_p MeV/c	p_{miss} MeV/c	$d^5\sigma/d\Omega^2 dE$ $cm^2/\text{MeV}/sr^2$	% error stat.
855.11	47.70	639	22.86	185.11	549.95	300.3	$6.34\ x\ 10^{-36}$	7
855.11	47.70	639	25.01	185.11	554.19	279.3	$9.31\ x\ 10^{-36}$	6
855.11	47.70	639	27.16	185.11	558.14	258.2	$1.76\ x\ 10^{-35}$	4
855.11	47.70	639	78.85	185.11	549.76	301.2	$3.33\ x\ 10^{-35}$	4
855.11	47.70	639	76.70	185.11	554.01	280.3	$5.65\ x\ 10^{-35}$	3
855.11	47.70	639	74.55	185.11	557.97	259.1	$9.72\ x\ 10^{-35}$	2
675.11	55.00	559	27.50	208.11	614.26	169.5	$3.55\ x\ 10^{-34}$	2
675.11	55.00	559	29.65	208.11	616.28	150.0	$5.77\ x\ 10^{-34}$	2
675.11	55.00	559	31.80	208.11	618.02	131.0	$9.12\ x\ 10^{-34}$	1
675.11	55.00	559	58.93	208.11	614.28	169.4	$8.93\ x\ 10^{-34}$	1
675.11	55.00	559	56.78	208.11	616.30	149.9	$1.31\ x\ 10^{-33}$	1
675.11	55.00	559	54.63	208.11	618.03	130.8	$1.80\ x\ 10^{-33}$	1
675.11	36.00	404	22.86	208.11	601.55	260.2	$1.04\ x\ 10^{-34}$	3
675.11	36.00	404	25.01	208.11	603.24	250.1	$1.50\ x\ 10^{-34}$	3
675.11	36.00	404	27.16	208.11	604.75	240.7	$2.27\ x\ 10^{-34}$	2
675.11	36.00	404	62.56	208.11	601.60	259.9	$5.52\ x\ 10^{-34}$	2
675.11	36.00	404	60.41	208.11	603.28	249.8	$6.82\ x\ 10^{-34}$	2
675.11	36.00	404	58.26	208.11	604.79	240.4	$8.01\ x\ 10^{-34}$	2
675.11	50.00	518	22.86	208.11	607.65	221.5	$9.74\ x\ 10^{-35}$	4
675.11	50.00	518	25.01	208.11	610.07	204.1	$1.67\ x\ 10^{-34}$	3
675.11	50.00	518	27.16	208.11	612.24	187.0	$2.65\ x\ 10^{-34}$	3
675.11	50.00	518	64.41	208.11	607.74	220.9	$4.02\ x\ 10^{-34}$	2
675.11	50.00	518	62.26	208.11	610.15	203.4	$5.90\ x\ 10^{-34}$	2
675.11	50.00	518	60.11	208.11	612.32	186.4	$8.50\ x\ 10^{-34}$	2

Tabla 4.1: Kinematics (Central Angles and Momenta) and Cross Sections

Bibliografía

[1] A. Picklesimer, J. W. Van Orden, and S. J. Wallace, Phys. Rev. C **32**, 1312 (1985)

[2] M. van der Schaar et al., Phys. Rev. Lett. **68**, 776 (1992).

[3] M. B. Epstein et al., Phys. Rev. Lett. **70**, 2868 (1993).

[4] J. Ryckebusch, D. Debruyne, W. Van Nespen, and S. Janssen, Phys. Rev. C **60**, 034604 (1999).

[5] J. Gao et al., Phys. Rev. Lett. **84**, 3265 (2000).

[6] W. T. H. van Oers et al., Phys. Rev. C **25**, 390 (1982).

[7] R. E. J. Florizone et al., Phys. Rev. Lett. **83**, 2308 (1999).

[8] R. E. J. Florizone, Ph.D. thesis, MIT, 1995 (unpublished).

[9] K. I. Blomqvist et al., Nucl. Instr. Meth.in Phys. Research A **403**, 263 (1998).

[10] K. I. Blomqvist et al., Nucl. Phys. A**626**, 871 (1997).

[11] C. R. Ottermann, G. Köbschall, K. Maurer, K. Röhrich, Ch. Schmitt, and V. H. Walther, Nuclear Physics **A436**, 688 (1985).

[12] E. A. J. M. Offermann and J. Mandeville, AEEXB: A program to model the A(e,e'X)B Reaction.

[13] J. Schwinger, Phys. Rev. **75**, 898 (1949).

[14] H.Überall, Electron Scattering from Complex Nuclei Vol. B, Academic Press (1971).

[15] R. Schiavilla, V. R. Pandharipande, and R. B. Wiringa, Nucl. Phys. **A449**, 219 (1986).

[16] J. L. Forest, V. R. Pandharipande, S. C. Pieper, R. B. Wiringa, R. Schiavilla and A. Arriaga, Phys. Rev. C **54**, 646 (1996).

[17] R. Schiavilla, Phys. Rev. Lett. **65**, 835 (1990).

[18] J. M. Udias, P. Sarriguren, E. Moya de Guerra, and J. A. Caballero, Phys. Rev. C **48**, 2731 (1993).

[19] S. Dieterich et al. Phys. Lett. B **500**, 47 (2001).

[20] J. Kelly and S. Wallace, Phys. Rev. C **49**, 1315 (1994).

Capítulo 5

Polarizaciones inducidas

PHYSICAL REVIEW C **62**, 034302 (2000)

Relativistic nuclear structure effects in $(e, e'\vec{p})$

J.M. Udías and Javier R. Vignote

Departamento de Física Atómica, Molecular y Nuclear, Facultad de Ciencias Físicas, Universidad Complutense de Madrid, E-28040 Madrid, Spain

---

Results for recoil nucleon induced polarization for $(e, e'\vec{p})$ are presented using various approximations for the relativistic nucleonic current, at the kinematics of a recent experiment at Bates. We see that the dynamical relativistic effects improve the agreement with the data. We make predictions for the induced normal polarization and responses for TJNAF 89-033 and Mainz A1/2-93 experiments.

PACS number(s): 25.30.Fj, 25.30.Rw, 24.10.-i, 21.60.Cs

5.1 Introduction

Several experiments have been proposed or have been carried out to measure the polarization of the ejected nucleon in $(e, e'\vec{p})$ reactions [1–3]. In this way, new sets of polarization response functions can be isolated [4–7].

If we write the cross section for the coincidence $(e, e'\vec{p})$ reaction in terms of recoil nucleon polarization dependent and independent terms, we have [4, 6, 7]:

$$\frac{d^3\sigma_s}{d\epsilon_e d\Omega_e d\Omega'} = \frac{\sigma_0}{2}\left[1 + \vec{P}\cdot\vec{\sigma}\right], \tag{5.1}$$

where ϵ_e is the scattered electron energy, σ_0 is the unpolarized cross section, s denotes the nucleon spin projection upon $\vec{\sigma}$, and $\vec{P}$ is the induced polarization. Each of these observables can be written in terms of response functions that are bilinear combinations of the nuclear electromagnetic current operator [4,5,7]. If the electron beam is unpolarized and the experiment is performed in coplanar kinematics ($\phi' = 0, \pi$), the relationship between the nuclear responses and the cross section is given by:

$$\begin{aligned}\frac{d^3\sigma_s}{d\epsilon_e d\Omega_e d\Omega'} &= \frac{E'|\vec{P}'|}{2(2\pi^3)}\left[\frac{d\sigma}{d\Omega_e}\right]_{Mott} \times \\ &\Big\{V_L(R_L + R_L^n\hat{S}_n) + V_T(R_T + R_T^n\hat{S}_n) + \\ &\cos\phi' V_{TL}(R_{TL} + R_{TL}^n\hat{S}_n) + \cos 2\phi' V_{TT}(R_{TT} + R_{TT}^n\hat{S}_n)\Big\}\end{aligned} \tag{5.2}$$

The kinematical factors are $V_L = \lambda^2$, $V_T = \lambda/2 + \tan^2\theta_e/2$, $V_{TT} = \lambda/2$, $V_{TL} = \lambda\sqrt{\lambda + \tan^2\theta_e/2}$ and $\lambda = 1 - (\omega/|\vec{q}|)^2$ where ω and $\vec{q}$ are the energy and momentum transfer in the reaction, θ_e is the electron scattering angle and E', $|\vec{P}'|$ are the energy and momentum of the ejected nucleon. Hence, for coplanar kinematics, *i.e.*, when the ejected nucleon lies within the electron scattering plane $\vec{P}$, the net ejectile polarization for an unpolarized beam or induced polarization (P_n), is normal to the scattering plane. In the one-photon exchange approximation P_n is zero when no final state interactions (FSI) between the ejected nucleon and the residual system are considered [4, 5, 7]. Thus, P_n is an observable well suited to study FSI effects in nuclear systems and measurements of P_n at different Q^2 would give information about the onset of nuclear transparency. If nuclear transparency is present at certain Q^2 value, that is, if FSI effects are quenched, we would see a decrease of P_n what would be a clear signature of nuclear transparency free from the ambiguities on the occupancies of the shells under study [9].

The first analysis of the experiment performed at BATES by Woo *et al.* that measured P_n in $^{12}C(e, e'\vec{p})$ [1] was made in a non relativistic framework. Other non relativistic results

for this experiment were recently presented in Ref. [8]. The non relativistic approach to $(e, e'\vec{p})$ is based on the impulse approximation, *i.e.*, assuming the one-photon exchange picture in which the single photon interacts only with the nucleon that is detected [4]. If no FSI are considered, the ejected nucleon is described by a plane wave (plane wave impulse approximation or PWIA). FSI are taken into account using potentials that distort the final nucleon wave function (distorted wave impulse approximation or DWIA) [4]. The non relativistic analyses found a a systematic underestimation of P_n of around 10% at best [1].

There are two main sources of an induced nonzero normal polarization in proton knockout reactions caused by the interaction with the residual nucleus in the final state. One is due to the absorption, that is, the flux lost into inelastic channels, parametrized in the imaginary part of the optical potential. Semi-classically, for scattering on a given side of $\vec{q}$, ejecting a nucleon from the front or the rear face of the nucleus would select out different directions of the angular momentum $\vec{l} = \vec{r} \times \vec{p}$ and, as the absorption depends on how much the nucleon travels in the nuclear medium before being detected, the effect is a net induced polarization due to absorption. This is well known from hadronic reactions and is named as the Maris Effect or Newns polarization [10]. It is, however, a small source of P_n [1]. The bulk of the induced polarization is primarily due to the real part of the spin-orbit potential, that parametrizes the explicitly spin-dependent terms in the optical potential [1].

Since the spin is a property intrinsically related to relativity, one may *a priori* consider that a relativistic approach is better suited to describe nucleon polarization observables. In recent years, the relativistic mean-field approximation has been successfully used for the analyses of $(e, e'p)$ reactions in the so-called relativistic distorted wave impulse approximation (RDWIA) [11–15]. The polarization degrees of freedom for the electron and the ejected nucleon have been included in this formalism years ago [7]. In RDWIA, the nucleon current

$$J^{\mu}_{N}(\omega, \vec{q}) = \int d\,\vec{p}\,\bar{\psi}_{F}(\vec{p}+\vec{q})\,\hat{J}^{\mu}_{N}(\omega, \vec{q})\,\psi_{B}(\vec{p}) \tag{5.3}$$

is calculated with relativistic ψ_B and ψ_F wave functions for initial bound and final outgoing nucleons, respectively. $\hat{J}^{\mu}_{N}$ is the relativistic nucleon current operator of $cc1$ or $cc2$ forms [16]. As bound state wave function, Dirac-Hartree solutions from relativistic Lagrangian with scalar and vector (S-V) meson terms [17] or solutions of Dirac equation with phenomenological Woods-Saxon wells are customarily used. The wave function with asymptotic momentum $\vec{P}'$ for the outgoing proton is a solution of the Dirac equation

containing S-V optical potentials. Recently a relativistic calculation of P_n following those general lines has appeared [18]. In Ref. [18] it was found that the agreement with the data improved slightly compared to the non relativistic analyses of Ref. [1]. However, relativistic effects for this improvement remained unspecified in [18].

Some of the differences between the relativistic and non relativistic approaches are independent of the dynamics, having to do with the proper (relativistic) kinematics being taken into account. Also, the non relativistic operators are normally obtained from an expansion and truncation in powers of p/M and sometimes also of q/M and ω/M. When the momenta and energy involved in the reaction are of the order of the nucleon mass, as it may be the case for $(e, e'\vec{p})$ reactions, one must be very careful with the behavior of the expanded and truncated operator. In Ref. [19] different non relativistic expansions were studied and new expressions that compared better with the unexpanded result were deduced. In Ref. [8] improved non relativistic operators were used, particularly with the inclusion of the extra spin-orbit term in the charge density operator as described in Ref. [19]. This term proves to be necessary to reproduce at least qualitatively [15, 20] the features seen in the R_{TL} response and TL asymmetry

$$A_{TL} = \frac{\sigma(\phi' = \pi) - \sigma(\phi' = 0)}{\sigma(\phi' = 0) + \sigma(\phi' = \pi)}\,, \tag{5.4}$$

as measured in a recent TJNAF experiment at $Q^2 \simeq 0.8$ (GeV/c)^2 [21].

The non relativistic approach can be better compared to the relativistic one thinking in terms of the direct Pauli reduction [13]. Starting from a non relativistic formalism based on bispinors χ solutions of a Schrödinger-like equation, one may at best construct properly normalized four-spinors of the form

$$\psi_{NR} = \frac{1}{\sqrt{N}} \left(\chi(\vec{p}), \frac{\vec{\sigma} \cdot \vec{p}}{E + M} \chi(\vec{p}) \right) \tag{5.5}$$

to be introduced in Eq. (5.3) in order to calculate a relativistic-like nucleon current matrix element. In this way the relativistic kinematics is fully taken into account and no expansions in p/M are needed. One further step to *relativize* the calculations is done by rewriting the Dirac equation for the upper component as a Schrödinger-like equation and introducing its *non relativistic* bispinor solution χ in Eq. (5.5). This 'non relativistic' bispinor is phase-shift and energy eigenvalue equivalent to the relativistic solution [13, 22, 25–27]. Comparing this solution of the Schrödinger-like equation to the upper component of the fully relativistic wave functions, one finds an additional factor (i) so that the upper component of the full Dirac solution is quenched in the nuclear interior compared to the non

relativistic solution [13, 22, 25, 27]. This quenching can be associated to the Darwin factor [28] that appears from an extra term linear in $\vec{p}$ that must be dealt with to obtain the Schrödinger-like equation and that is not present in the usual non relativistic treatment.

One can then build a non relativistic formalism based on the Schrödinger-like equation, with central and spin-orbit potentials that are phase-shift equivalent to the relativistic potentials, incorporating *a posteriori* the Darwin term in order to recover exactly the same upper component as in RDWIA and, by means of Eq. (5.5), avoid the expansions in p/M. This formalism would incorporate all the kinematical and operator-related relativistic effects, as well as the dynamical quenching of the relativistic upper components due to the Darwin term.

This is done for instance by Kelly in several works [29] though with an additional approximation, the effective momentum approach (EMA) for the lower components. This amounts to approximate the $\vec{\sigma}\cdot\vec{p}$ term that appears for the lower components in Eq. (5.5)

$$\left(\chi(\vec{p})_{lower} = \frac{\vec{\sigma}\cdot\vec{p}}{E+M}\chi(\vec{p})_{upper}\right) \tag{5.6}$$

by $\vec{\sigma}\cdot\vec{p}_{as}$, with $\vec{p}_{as}$ the momentum corresponding to the asymptotic kinematics at the nucleon vertex. Results obtained within this approximation both with relativistic and non relativistic potentials were compared to experiment in Ref. [1].

The differences between the calculations of [18] and those presented in [1] can be either due to the EMA procedure, or to an additional dynamical relativistic effect different from the Darwin term, namely the enhancement of the lower components (ii): The lower components of the fully relativistic solutions are enhanced at the nuclear interior due to the presence of negative energy components [13, 30, 40]. Solving the Dirac equation with scalar and vector potentials we see that the lower components are related to the upper ones by

$$\chi(\vec{p})_{lower} = \frac{\vec{\sigma}\cdot\vec{p}}{E+M+S-V}\chi(\vec{p})_{upper}. \tag{5.7}$$

Comparing with Eq. (5.5), we see that the lower components are enhanced with respect to the ones of free positive energy spinors by a factor

$$A^{-1}(r) = \frac{E+M}{E+M+S(r)-V(r)} \tag{5.8}$$

(we recall: $S<0$, $V>0$, and $A^{-1}(r)$ is $\simeq 2$ at the nuclear interior for the usual values of the potentials). $A^{-1}(r)$ equals the inverse of the Darwin factor squared. This enhancement

of the lower components with regard to free spinors has been sometimes referred as *spinor distortion* [29].

As one can see from Eqs. (5.5) and (5.7), for small values of the momentum $\vec{p}$ the lower components would play a minor role with respect to the upper ones, due to the factor $\vec{p}/(E+M)$. In this low-p region ($p < 300$ MeV), the enhancement of the lower components is not important for the $(e,e'p)$ cross sections [13] and the most visible difference between RDWIA and non relativistic (kinematically corrected) DWIA results is caused by the effect mentioned above in point (i), namely the Darwin term. Due to dynamical effects, relativistic cross sections at low-p are smaller than the non relativistic ones and RDWIA–deduced spectroscopic factors from the low-p data are 10% to 15% higher than the non relativistic ones [11, 12]. With increasing p, however, the lower components cease to be small and their enhancement, present in the fully relativistic wave functions but not in Eq. (5.5) or in similar non relativistic expressions, increases the cross sections at $p > 300$ MeV/c, compared to the non relativistic ones. This improves sizeably the agreement with the data of the RDWIA $(e,e'p)$ cross sections [14, 15]. In short, in regions where the momenta of the bound and/or final nucleon are comparable to the nucleon mass, the RDWIA cross sections are *larger* than the non relativistic DWIA ones, in spite of the Darwin factor that in these kinematical regions would play a minor role. The more visible dynamical effect in high-p regions would be the one mentioned in paragraph (ii) that is, the enhancement of the lower components. This enhancement is crucial to obtain good agreement [15,20] with the recent data for R_{TL} response and A_{TL} in ^{16}O taken at TJNAF for $Q^2 \simeq 0.8$ $(GeV/c)^2$ [20, 21].

To compare with non relativistic calculations, one can project the negative energy sector out of the fully relativistic solutions, thus removing the enhancement of the lower components described in paragraph (ii). More specifically, if the negative-energy components are projected out, the nucleon current is calculated as

$$J^{\mu}_{proj}(\omega,\vec{q}) = \int d\vec{p}\,\bar{\psi}^{(+)}_{F}(\vec{p}+\vec{q})\hat{J}^{\mu}(\omega,\vec{q})\psi^{(+)}_{B}(\vec{p}), \tag{5.9}$$

where $\psi^{(+)}_{B}$ ($\psi^{(+)}_{F}$) is the positive-energy component of ψ_B (ψ_F), *i.e.*, $\psi^{(+)}_{B}(\vec{p}) = \Lambda_{(+)}(\vec{p})\psi_B(\vec{p})$, $\Lambda_{(+)}(\vec{p}) = (M+\bar{\not{p}})/2M$, with $\bar{p}_\mu = (\sqrt{\vec{p}^2+M^2},\vec{p})$ (similarly for $\psi^{(+)}_{F}$). That is, the matrix element of the current is computed in a truncated space with only positive energy spinors without enhancement of the lower components. This truncation is inherent to all non relativistic calculations. The dynamical enhancement of the lower components is contained in the current of Eq. (5.3) but not in Eq. (5.9). Apart from kinematical effects, the matrix

elements obtained with the prescription of Eq. (5.9) are equivalent to the ones computed in non relativistic approaches based upon either the Foldy-Wouthuysen reduction [6, 31] or the direct Pauli reduction [13, 32].

The EMA approach (or more properly the EMA-noSV one where, as we have said, no spinor distortion is considered [29]) also removes the enhancement of the lower components but it is not completely equivalent to the exact projection method. Indeed, it is equivalent to neglecting the p-dependence of the projection operators in Eq. (5.9), using instead the asymptotic values of the momenta at the nucleon vertex. We can say that the EMA-noSV approach computes the matrix element with spinors that have the same structure as the ones that enter in the scattering of free nucleons, because it enforces the relationship between upper and lower components to be driven by the asymptotic value of the momenta at the nucleon vertex. The EMA-noSV calculation lacks any 'spinor distortion', exactly as in the scattering of free nucleons. In particular, the Gordon transformation is exact for the EMA-noSV approach and $cc1$ and $cc2$ operators would lead to identical results within EMA-noSV, if the same choices for the off-shell values of ω, E, E', $\vec{P}$ and $\vec{P}'$ are made in both cases.

The projected results, on the other hand, though lacking the large (around a factor of two) enhancement of the lower components seen in the fully relativistic calculation, are based on spinors whose upper/lower components verify Eq. (5.5) but with a wider value of momenta than in scattering from free nucleons. Thus, even projected (non relativistic) results can have a certain degree of spinor distortion compared to the free case due to the dispersion by the nuclear potentials.

We must keep in mind that both projected and EMA-noSV results still incorporate the dynamical quenching of the upper components (Darwin term) and, if they are to be compared with non relativistic calculations, care must be taken of the Darwin term in the non relativistic result. Relativistic optical potentials normally give rise to increased absorption and stronger spin-orbit potentials. Due to this, it is expected that they would also lead to a stronger induced normal polarization.

We want to emphasize that the possible differences with the former EMA-noSV analyses of Woo *et al.* [1] are not due to the use of a relativistic optical potential. In both Refs. [1] and [18], results were presented with the same potential EDAI-C that we use in the present work. The Darwin term (leading to increased absorption) was also included in a similar way to us. Thus, if there are differences between our results and those of Ref. [1], they must be due to relativistic effects additional to the Darwin term and different from

the fact that the optical potential is relativistic or not.

5.2 Results

For the bound state wave functions we use the parameters of the set NL3 [33] that reproduces adequately the known momentum distributions at low-p [34]. We have also computed results with other bound state wave functions and found the effects in P_n to be very small up to $p \leq 250$ MeV/c. For the scattered proton wave function, we use the energy-dependent A-independent potentials derived by Clark *et al.* for ^{12}C (EDAI-C) and ^{16}O (EDAI-O) [35]. To study the sensitivity to different optical potentials, we also compute results with the energy-dependent A-dependent parametrization 1 (EDAD-1) of Ref. [35].

5.2.1 Comparison with former results from Bates

In Fig. 5.1, P_n is presented against the momentum of the recoiling residual nucleus or *missing momentum* p_m, related to the momentum of the nucleon inside the target nucleus before being knocked-out [4]. The results are computed for the kinematics of Ref. [1], namely beam energy of 580 MeV, kinetic energy of the final nucleon of 270 MeV, $|\vec{q}| \simeq 760$ MeV/c, $\omega \simeq 290$ MeV in q-ω constant kinematics with $Q^2 \simeq 0.5$ (GeV/c)^2. We use the Coulomb gauge in all the cases. We included the Coulomb distortion of the electron wave function and found its effect in P_n to be small. With solid (dotted) lines we present the fully relativistic results obtained with the $cc1$ ($cc2$) operator. We also show results after projecting out the negative energy components (short-dashed lines for $cc1$, long-dashed lines for $cc2$).

We see that for the fully relativistic results, the agreement with the data is excellent in both shells, except perhaps for the highest p_m and missing energy data points in the $s_{1/2}$ shell, where the contribution from continuum states not considered in the present work begins to be important. Looking at the projected results, we see that the removal of the negative energy components worsens the agreement with the data for both the $cc1$ and $cc2$ operators. In all cases P_n is smaller (less positive or more negative) for the projected calculations. We also see that the Gordon ambiguities, *i.e.,* the differences between $cc1$ and $cc2$ results, are rather small. Compared to the theoretical results of Ref. [1], the agreement with experiment is better for any of the curves presented in Fig. 5.1. This cannot be due

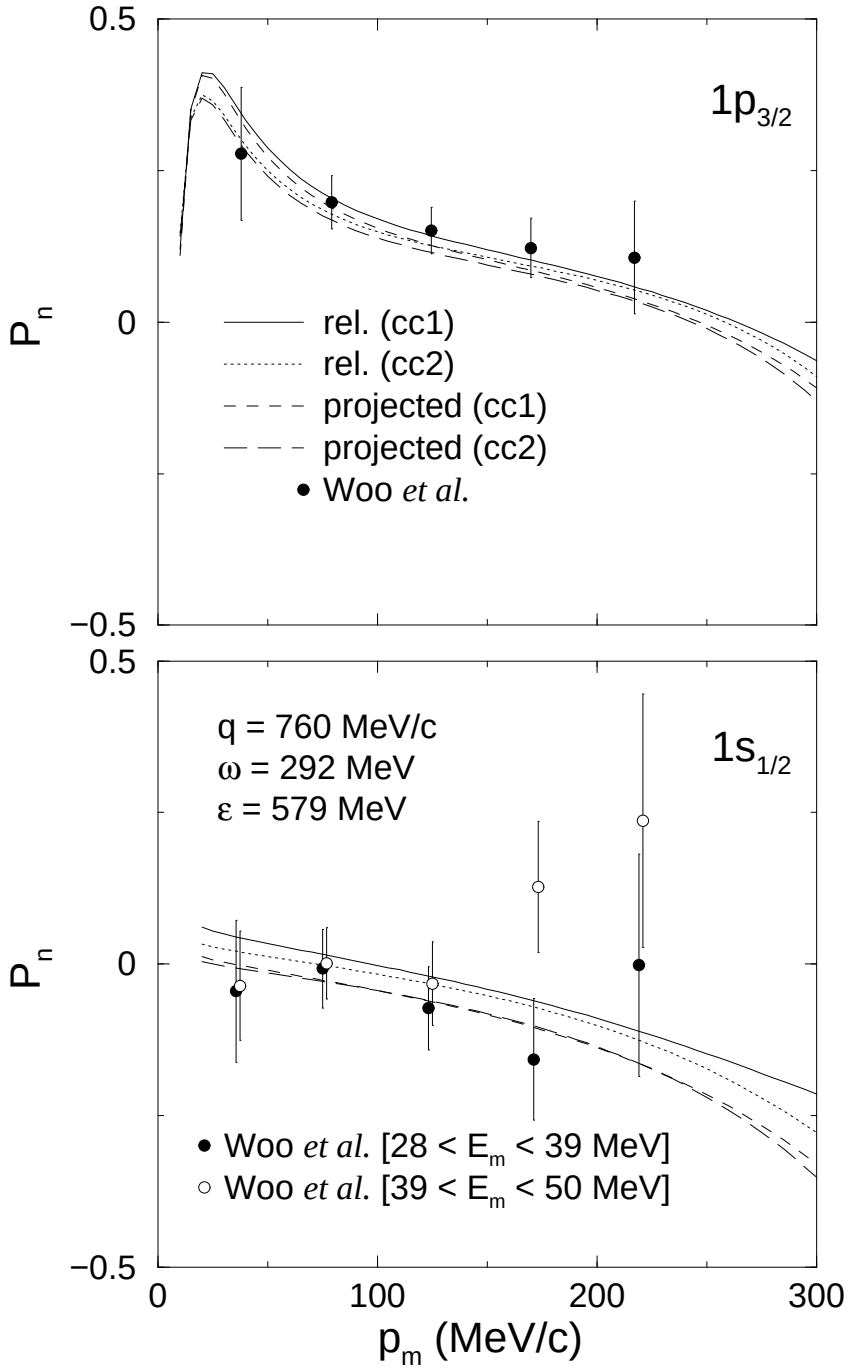

Figura 5.1: P_n from ^{12}C for the $1p_{3/2}$ (upper panel) and $1s_{1/2}$ (lower panel) orbits, versus missing momentum p_m in MeV/c. Results shown correspond to a fully relativistic calculation with the *cc*1 (solid) and *cc*2 (dotted) operators. Also shown are the results after projecting the bound and scattered proton wave functions over positive-energy states (short-dashed and long-dashed lines respectively). Data points are from Ref. [1].

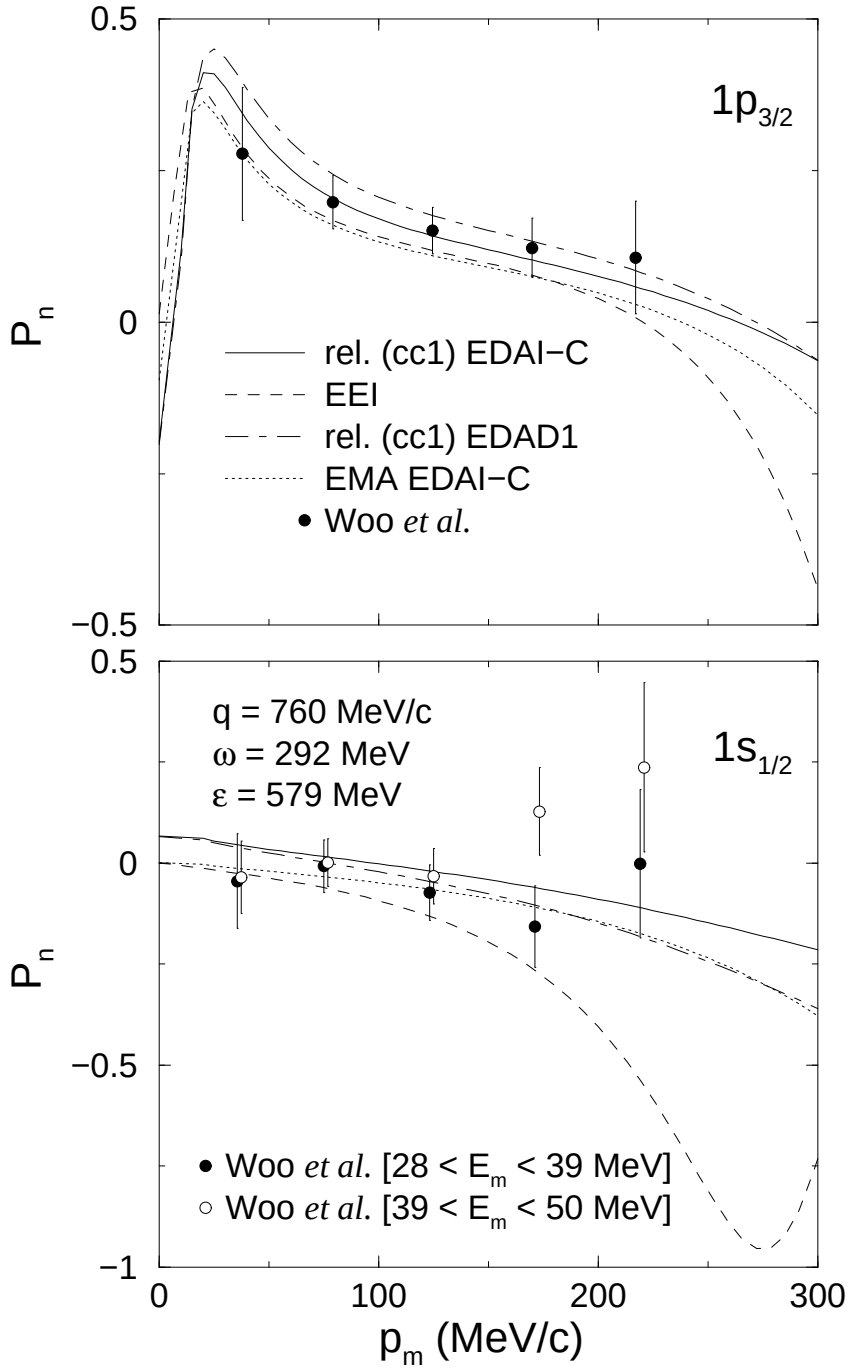

Figura 5.2: P_n from ^{12}C for the $1p_{3/2}$ (upper panel) and $1s_{1/2}$ (lower panel) orbits, versus missing momentum p_m in MeV/c. Results shown correspond to a fully relativistic calculation with the *cc*1 and the EDAI-C (solid), and the EDAD1 (dash-dotted) potentials. Also shown are the EMA results (dotted line) for the EDAI-C case. Former EMA-EEI results (dashed line) and data points are from Ref. [1].

only to the negative energy components because the effect of projection is rather modest as the results in Fig. 5.1 show. To disentangle the reasons for this difference in Fig. 5.2 we show (dotted lines) a calculation obtained with the EDAI-C potential within the EMA-noSV approach with the operator $cc1$ (very similar results are obtained with the $cc2$ operator and are not shown here). As a guidance, the solid line in Fig. 5.2 corresponds to the same one of Fig. 5.1. We see in Fig. 5.2 that for the EMA-noSV results the reduction of P_n is noticeable and the agreement with the data is worse. Our EMA-noSV results are in the line of the ones obtained with the same optical potential EDAI-C in Ref. [1]. We note that our $cc1$ and $cc2$ results are not identical within EMA-noSV due to the different off-shell prescription we use in each case for the values of the kinematical quantities that enter in the evaluation of the current matrix element. Following Ref. [16] for $cc2$ we have

$$\hat{j}^{\mu}_{cc2} = F_1\gamma^{\mu} + i\frac{\sigma^{\mu\nu}q_{\nu}}{2M}F_2, \tag{5.10}$$

with $q^{\nu} = (\omega, \vec{q})$ at the electron vertex. For $cc1$ we have

$$\hat{j}^{\mu}_{cc1} = (F_1 + F_2)\gamma^{\mu} - \frac{F_2}{2M}(P' + p_m)^{\mu}, \tag{5.11}$$

with $p_m = (\overline{E}, \vec{p}_m)$, $\vec{p}_m = \vec{P}' - \vec{q}$, $E' = \sqrt{\vec{P}'^2 + M^2}$ (the final nucleon is asymptotically on-shell) and $\overline{E} = \sqrt{\vec{p}_m{}^2 + M^2}$. Thus, ω used in Eq. (5.10) is different from $\overline{\omega} = E' - \bar{E}$ as implied in Eq. (5.11). If we had used $\overline{\omega}$ in $cc2$ instead of ω, the results of our $cc1$ and $cc2$ EMA-noSV calculations would be identical. At present, there is no definite prescription for handling this off-shell kinematical ambiguity in ω, $\overline{\omega}$ and other kinematical variables to be used in the current operator [23,24]. This ambiguity arises because, contrary to the scattering of free nucleons, part of the energy and momentum of the exchanged photon is transferred to the recoiling system instead of being completely absorbed by the detected nucleon. We have chosen the original prescription of de Forest of using $\overline{E}$ in $cc1$ but ω in $cc2$. We find that, in this way, off-shell kinematics ambiguity effects and Gordon ambiguity ones reinforce each other so that the differences between the $cc1$ and $cc2$ results are enhanced by our choice. The EMA-noSV results are free from Gordon ambiguities. This is the reason why $cc1$ and $cc2$ results obtained in such approach are much closer than the corresponding ones of the full RDWIA calculations. Kinematical ambiguities will cause differences of up to 15% between our $cc1$ and $cc2$ EMA-noSV unpolarized cross sections results for all the cases considered in the present work. However, the effect of these ambiguities in the P_n predictions is almost negligible (typically less than 1%). We have plotted only the $cc1$ EMA-noSV result for P_n. Our $cc2$ EMA-noSV result is almost identical to this curve.

Recently, Kelly has incorporated the effect of spinor distortion within his EMA approach by including the relativistic potentials in the lower component of the spinors as in Eq. (5.7), while still substituting the $\vec{\sigma}\cdot\vec{p}$ term by $\vec{\sigma}\cdot\vec{p}_{as}$. This is called EMA-SV approach in Ref. [29] in contrast to EMA-noSV. This procedure reintroduces the dynamical enhancement of the lower components. For modest values of the momentum (up to around 275 MeV/c), where the role of the lower components is less relevant, this approximation goes close [39] to the results obtained with the exact treatment that we do in the present work. It tends, however, to minimize the effect of enhancement of the lower components beyond the value of p_m mentioned above and, as the momentum of the ejected nucleon is normally well above 275 MeV/c, it underestimates the effect of spinor distortion for the ejected nucleon. We conclude that an important reason for the differences of our full RDWIA results with those of [1], using the same optical potential EDAI-C, is the EMA-noSV approach employed in Ref. [1].

For the purpose of comparison, we present (dash-dotted line in Fig. 5.2) results obtained with the same bound state wave functions as for the other curves, the full RDWIA approach with the *cc*1 operator but a different optical potential, namely the EDAD-1 of ref. [35]. We emphasize that the EDAI-C potential should be a more suitable choice than EDAD-1 for ^{12}C because it describes better the elastic proton scattering data for this particular nucleus. The effect of using EDAD-1 instead of EDAI-C is sizeable. EDAD-1 yields a larger P_n for the $p_{3/2}$ shell, worsening the agreement with the data and a smaller P_n for the $s_{1/2}$ shell, with no significant worse (or better) agreement with the data in this shell. We observed that both EDAI-C and EDAD-1 produce almost identical unpolarized cross sections or unpolarized response. However, the P_n values they produce are noticeably different. This shows the sensitivity of P_n to details of the FSI.

The comparison between the results of both potentials follows the same general trend as shown in Ref. [18]. In Ref. [18], P_n changes in the same relative direction in going from EDAI-C to EDAD-1 as in our calculation but, contrary to our case, the differences between the EDAI-C and EDAD-1 are larger for the $1s_{1/2}$ shell than for the $1p_{3/2}$ one and in this latter shell, their results seem to agree better with experiment for the EDAD-1 potential than for the EDAI-C. We find, in general, that our results with EDAI-C agree better with the data. These minor discrepancies with Ref. [18] should be traced back to the different bound state wave functions and possibly other parts of the formalism (current operator, Coulomb distortion) employed in both cases.

In Fig. 5.2 we also show the EMA-noSV results of Ref. [1] with the EEI potential

(dashed line). In Ref. [1] a more positive P_n for the $p_{3/2}$ shell and better agreement with the data was obtained with the EEI potential than with the EDAI-C one. For the $1s_{1/2}$ shell, however, a more negative P_n and worse agreement with the data was found.

The EMA-noSV-EEI calculation of Ref. [1] underestimated the data by about 10%. The EEI is a non relativistic optical potential obtained after folding a density-dependent empirical effective interaction with the nuclear density [37]. The interaction is fitted to proton-nucleus elastic *and inelastic* scattering data for several states of several targets simultaneously. The relativistic optical potentials, on the other hand, are fitted only to elastic scattering data. It is well known that elastic data can only constrain the asymptotic part of the potentials. Given the fact that the nucleus is almost transparent to electrons (compared to nucleons), phase-shift equivalent potentials that differ only in the nuclear interior would produce the same good fits to elastic proton scattering observables, leading however to different electron scattering results. The EEI approach solves this ambiguity by phenomenologically constraining the potentials in the nuclear interior by means of simultaneous fits to inelastic data. In the relativistic case, on the other hand, the shape of the potentials at the nuclear interior is assumed to be of simple Woods-Saxon + surface terms, not very different from what one finds in the relativistic mean field approximation. Thus, the fact that the relativistic model gives a very fair account of $(e, e'\vec{p})$ observables such as P_n cannot be attributed merely to the incorporation of the right phenomenology, as it could be the case with the EEI potentials, but to a merit of the model itself.

5.2.2 Predictions for Mainz and TJNAF in parallel kinematics

In a recent work [15, 20, 38], it has been shown that the dynamical enhancement of the lower components shows up differently in the $j = l - 1/2$ and $j = l + 1/2$ spin-orbit partners, specially for the R_{TL} response and the A_{TL} asymmetry. We remind that for ^{12}C the two shells studied correspond to $j = l + 1/2$ spin-orbit partners. New sets of induced polarization P_n are being obtained at TJNAF [2] in ^{16}O at a more relativistic kinematics, namely beam energy of 2450 MeV, kinetic energy of the ejected nucleon of about 420 MeV, and $Q^2 \simeq 0.8$ (GeV/c)^2. There is also a proposal at Mainz [3] to do similar measurements at a smaller value of the kinetic energy of the ejected nucleon, namely 200 MeV. In what follows, we analyze whether these experiments may provide signatures of relativistic dynamics in P_n similar to the ones found in R_{TL} and A_{TL}.

In parallel kinematics only two responses, R_L and R_T, contribute to the unpolarized

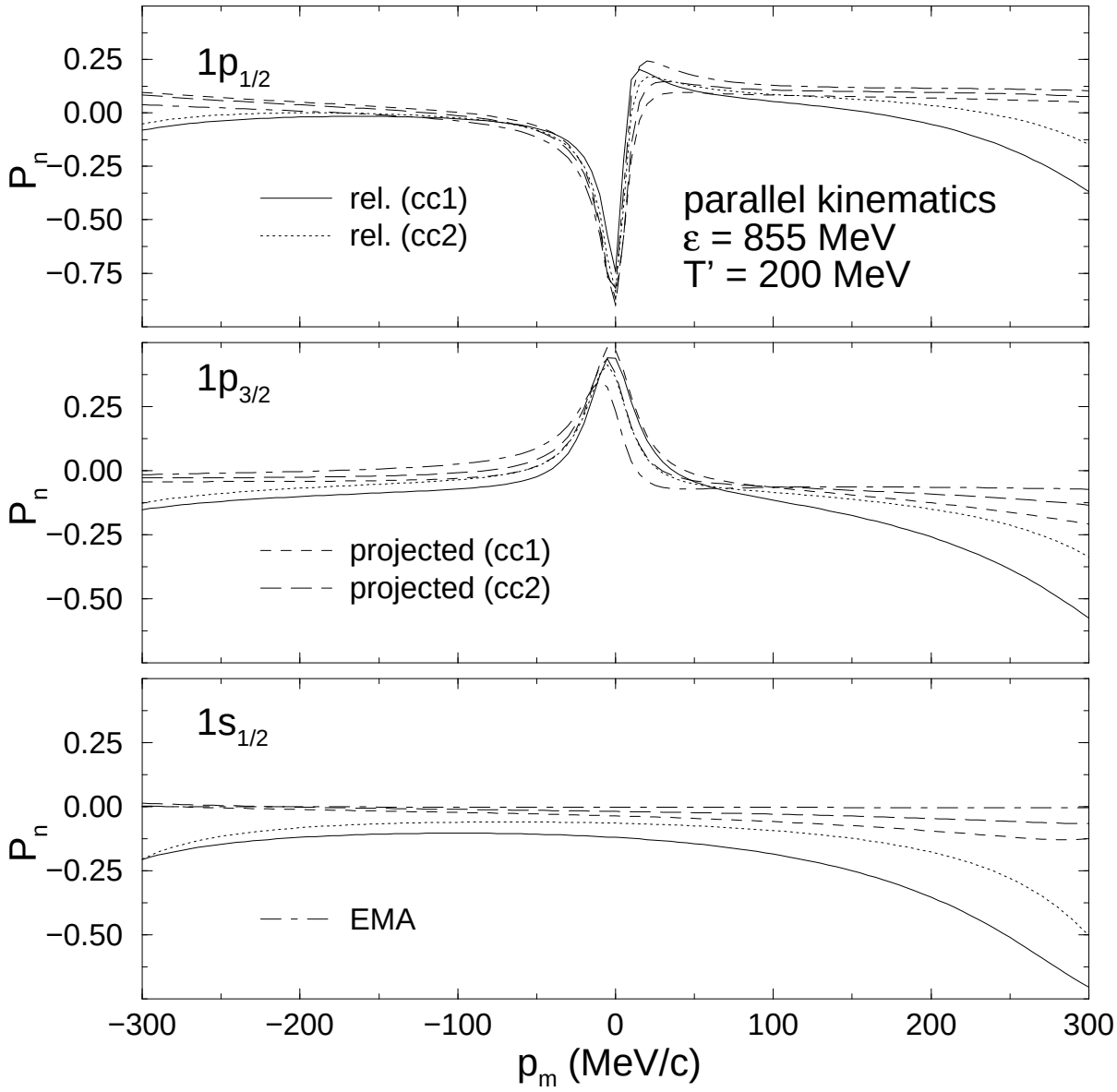

Figura 5.3: P_n from ^{16}O for the $1p_{1/2}$ (upper panel), $1p_{3/2}$ (mid panel) and $1s_{1/2}$ (lower panel) orbits, versus missing momentum p_m in MeV/c. Results shown correspond to a fully relativistic calculation with the $cc1$ (solid line) and $cc2$ (dotted line) operators. Also shown are the projected results (short and long-dashed lines) and the EMA-$cc1$ ones (dash-dotted line). Results in parallel kinematics corresponding to ref. [3] and the EDAI-O potential is used.

cross section and just one, R^n_{TL}, to P_n, so that for this kinematics the analyses are simplified. We present in Fig. 5.3 fully RDWIA results with $cc1$ (solid line), $cc2$ (dotted line), projected results (short-dashed lines for $cc1$ and long-dashed lines for $cc2$) and EMA-noSV results with the $cc1$ operator (dash-dotted line) for the two p-shell spin-orbit partners of ^{16}O, plus the deep s-shell, in parallel kinematics and with beam energy and transfer energy suitable for Mainz [3] (beam energy of 855 MeV, kinetic energy of the ejected nucleon of 200 MeV).

For the three shells we see the opposite pattern to the one depicted in Fig. 5.1: the removal of the negative energy components drives here P_n towards higher values, and even more so does using the EMA-noSV approach. For the kinematics of Fig. 5.3, the effect of projection and Gordon ambiguities is much larger than it was in Fig. 5.1.

A very characteristic feature is seen in the $s_{1/2}$ shell for this case of parallel kinematics: A zero value of P_n is predicted within the EMA-noSV approach. A small value of P_n is obtained by the projected calculations, while the full RDWIA approach yields a relatively large (in absolute value) P_n due to spinor distortions. The choice $cc1$, that emphasizes the effect of the enhancement of the lower components [30], yields the largest prediction for P_n in absolute value. Should the experiments at TJNAF or Mainz provide us with P_n values with equal or smaller uncertainty that the ones already measured at BATES, it will undoubtedly disentangle the role played in P_n by the enhancement of the lower components.

The responses involved in the evaluation of P_n for this case are displayed in Fig 5.4. The only nonzero contribution to P_n comes from R^n_{TL} and the link between the responses shown in the bottom panel of Fig. 5.4 and the results for P_n of Fig. 5.3 is straightforward. As it could be deduced from the values of P_n displayed in Fig. 5.3, R^n_{TL} for the $s_{1/2}$ shell is zero within EMA-noSV, it is very small for the projected results and reaches the largest absolute value for the full RDWIA $cc1$ calculation. The results for the $p_{3/2}$ shell follow the same trend as shown for the $s_{1/2}$ shell, only that here the more complex spin-orbit structure of the bound state causes a nonzero value of P_n even for the EMA-noSV results. The projected and EMA-noSV results display small (in absolute value) predictions for R^n_{TL}. The $cc2$ RDWIA prediction exhibits larger R^n_{TL}, while the full $cc1$ result yields the largest value of R^n_{TL}. This gradation of R^n_{TL} is similar to what one finds generally for the unpolarized R_{TL} (in q-ω constant kinematics): As the $cc1$ operator enhances the role of the negative energy components [30] with regards to other choices of the operator, it produces the largest value of R_{TL}. Thus, at least for the $j = l + 1/2$ spin orbit partner, we

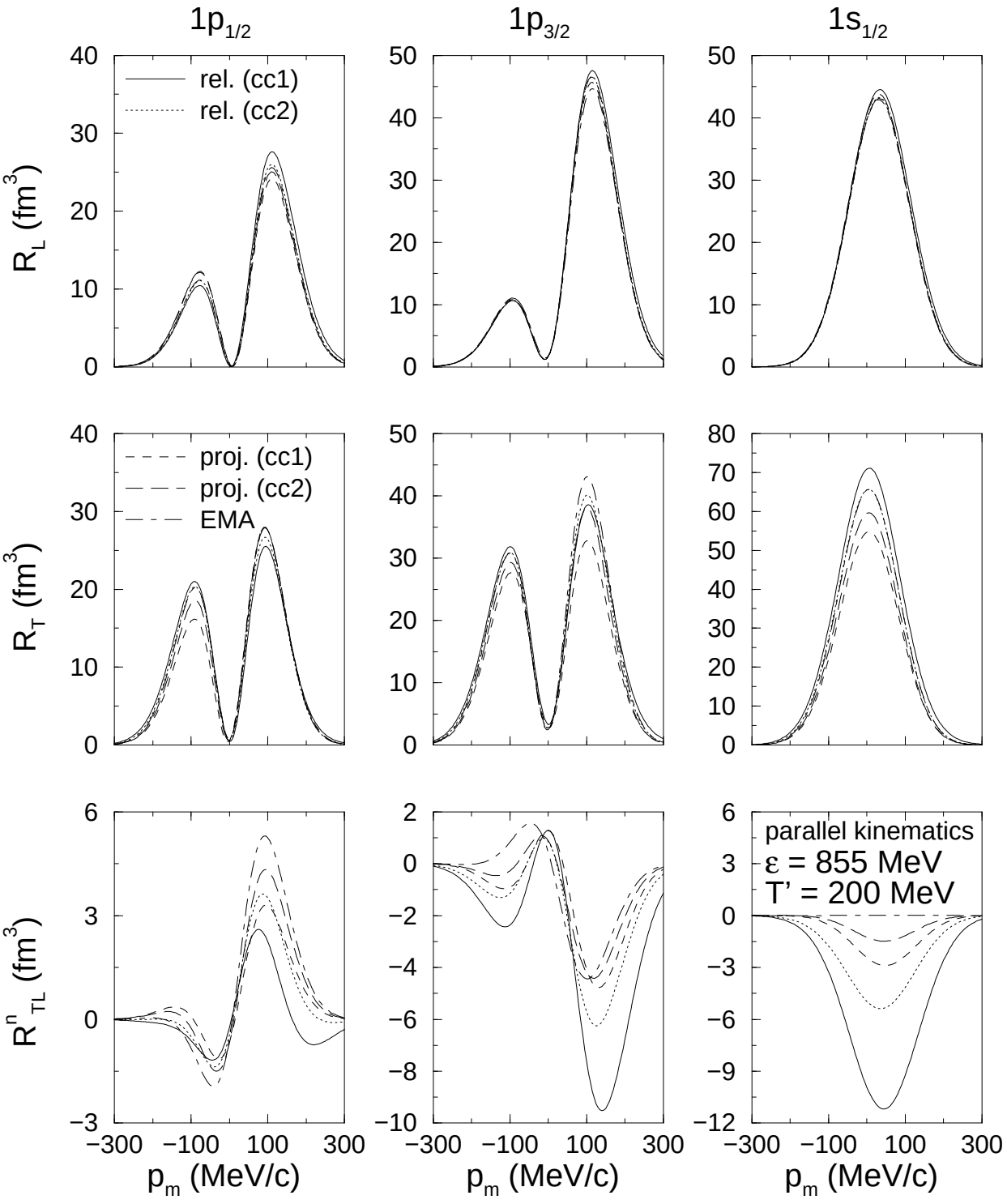

Figura 5.4: Response functions corresponding to the kinematics of Fig. 5.3.

observe the same behavior for R^n_{TL} and R_{TL} with regards to the effect of negative energy components.

On the other hand, we find that projection and Gordon ambiguities effects show up differently for the $p_{1/2}$ shell. For this case R_L, R_T and R^n_{TL} are shown in the leftermost panel of Fig. 5.4 at the same kinematics of Fig. 5.3. While for R^n_{TL} in the $j = l + 1/2$ shells the larger was the role given to the negative energy components the larger (in absolute value) R^n_{TL} response was obtained, for the $p_{1/2}$ shell ($j = l - 1/2$) one sees the opposite behavior: the full $cc1$ calculation yields the smallest R^n_{TL} while the EMA-noSV prediction displays the largest one. This is at variance with the behavior observed for the unpolarized R_{TL} response [38] and indicates an interference between positive and negative energy component contributions to R^n_{TL}. This interference is constructive for the $j = l + 1/2$ shells so that the calculations with large contribution from negative energy components yield a large R^n_{TL}, while it is largely destructive for the $j = l - 1/2$ shells for which large effects of negative energy components translate into small values of R^n_{TL}.

In Ref. [36] results were presented for the EMA-noSV case within the IA and also in a calculation beyond IA that included channel coupling to several configurations in the final state. Our EMA-noSV result of Fig. 5.4 and the one shown in Fig. 14 of Ref. [36] are very similar, with small differences due to the different wave functions and optical potentials. The most interesting outcome of this comparison is that the effect of spinor distortion increases R^n_{TL}, in particular for the case of the $s_{1/2}$ shell that would have a zero value without spinor distortion within IA. Due to channel coupling (CC), a nonzero R^n_{TL} for this shell was obtained in Ref. [36]. The effect of spinor distortion, however, is at least twice to four times (depending on whether one considers the RDWIA $cc2$ or $cc1$ result) larger than the one of CC shown in Ref. [36]. We conclude that coupled channel contributions would not mask the large negative value of P_n caused by spinor distortion. The R^n_{TL} response in this $s_{1/2}$ shell is sensitive to Gordon ambiguities and overall constitutes a very clear signature for the presence of negative energy components in the nucleon wave function.

For the other shells, the effects of CC shown in Ref. [36] were small at moderate values of p_m for the cases we studied in the present work and the IA results shown here should not change much if CC effects were considered.

Still in parallel kinematics but with a larger value of Q^2 that is suitable at TJNAF, we have obtained very similar results to the ones just presented. We plot in Fig. 5.5 only the results for P_n.

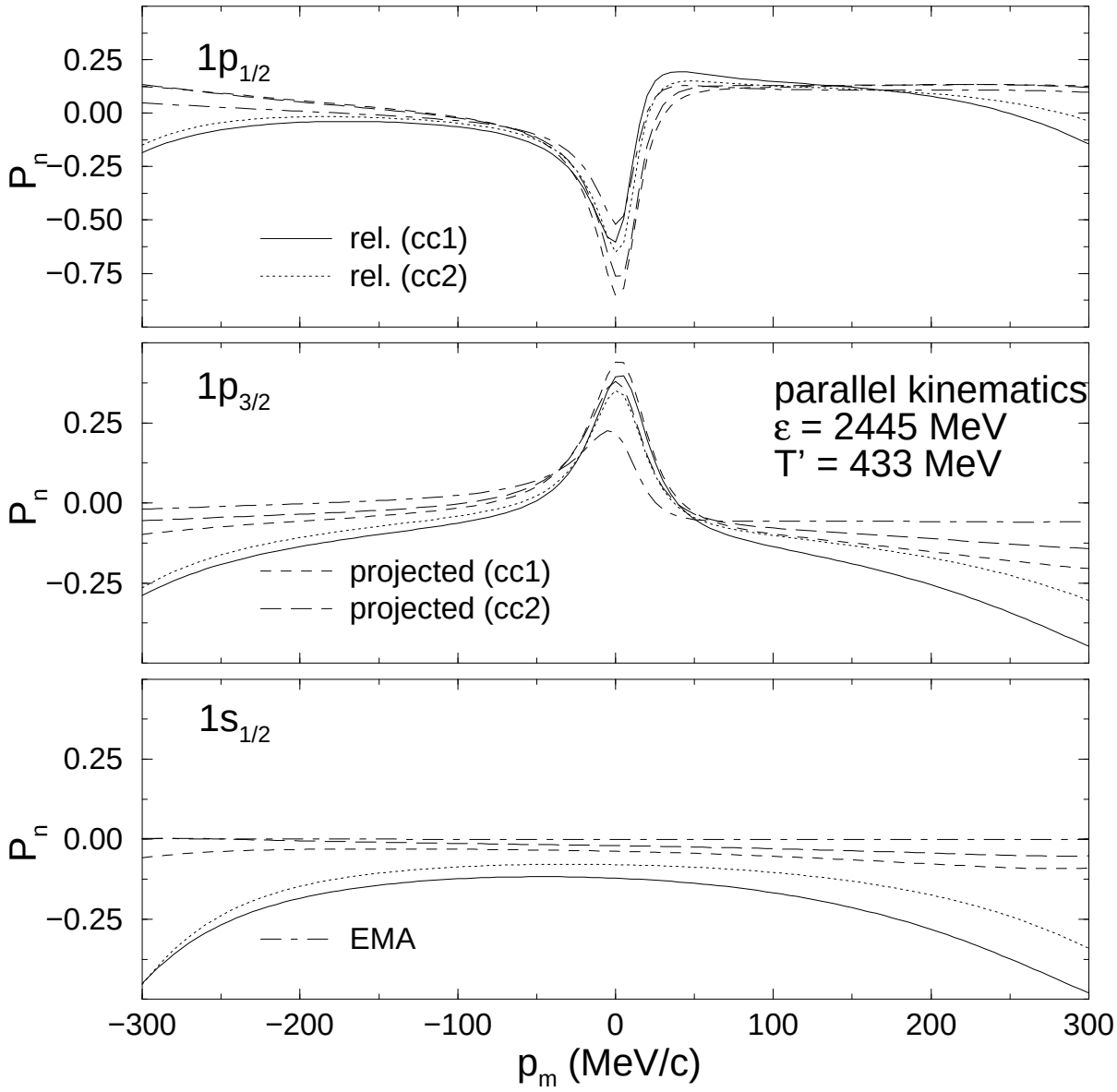

Figura 5.5: P_n from ^{16}O for the $1p_{1/2}$ (upper panel), $1p_{3/2}$ (mid panel) and $1s_{1/2}$ (lower panel) orbits, versus missing momentum p_m in MeV/c. Results shown correspond to a fully relativistic calculation with the $cc1$ (solid line) and $cc2$ (dotted line) operators. Also shown are the projected results (short and long dashed lines) and the EMA(noSV)-$cc1$ ones (dash-dotted line). Parallel kinematics suitable at TJNAF [2] and the EDAI-O potential is used.

5.2.3 q-ω constant kinematics

	TJNAF	MAMI	BATES
θ_e	23.4°	48.8°	118.8°
Q^2 $(GeV/c)^2$	0.8	0.4	0.5
ω (MeV)	445	215	292
V_L	0.643	0.792	0.727
V_T	0.444	0.651	3.283
V_{TL}	0.737	0.932	1.642
V_{TT}	0.401	0.445	0.426

Tabla 5.1: Approximated values of the kinematical variables and the factors in Eq. (5.2) for the q-ω constant experimental setups discussed in the present work.

The experiment of Bates was performed in q-ω constant kinematics and in the same side of $\vec{q}$ for the scattered proton, $\phi' = \pi$, which corresponds to $p_m > 0$ in our figures. The analysis of this case is more complicated because all the eight responses of Eq. (5.2), in combination with the factors shown in Table 5.1, contribute to the cross section and P_n. In Figs. 5.6 and 5.7 we present the responses for the Bates results depicted in Fig. 5.1. The effect of spinor distortion and Gordon ambiguities in the R_L, R_T, R_{TL} and R_{TT} has been studied previously in the context of RPWIA [30, 38]. It was found there that for the $j = l + 1/2$ partners, as it is the case of the two shells in ^{12}C, the differences are relatively small, at least for the 'large' responses R_L and R_T.

For the normal responses the situation is less clear. One must remember that unpolarized and normal responses share the same structure in terms of components of the hadronic current, differing only in the signs with which the contribution for every value of ejected nucleon spin projection upon the normal direction enters into the unpolarized or normal responses [5, 7]. Thus, large unpolarized responses usually come from constructive interference of the two spin contributions and are associated with a correspondingly small normal response coming from destructive interference. The converse is also true: small unpolarized responses have a correspondingly large polarized normal response [7]. If there were no FSI, both normal projection contributions (spin up and spin down) would be identical, all the responses shown in Fig. 5.7 would vanish and no normal polarization

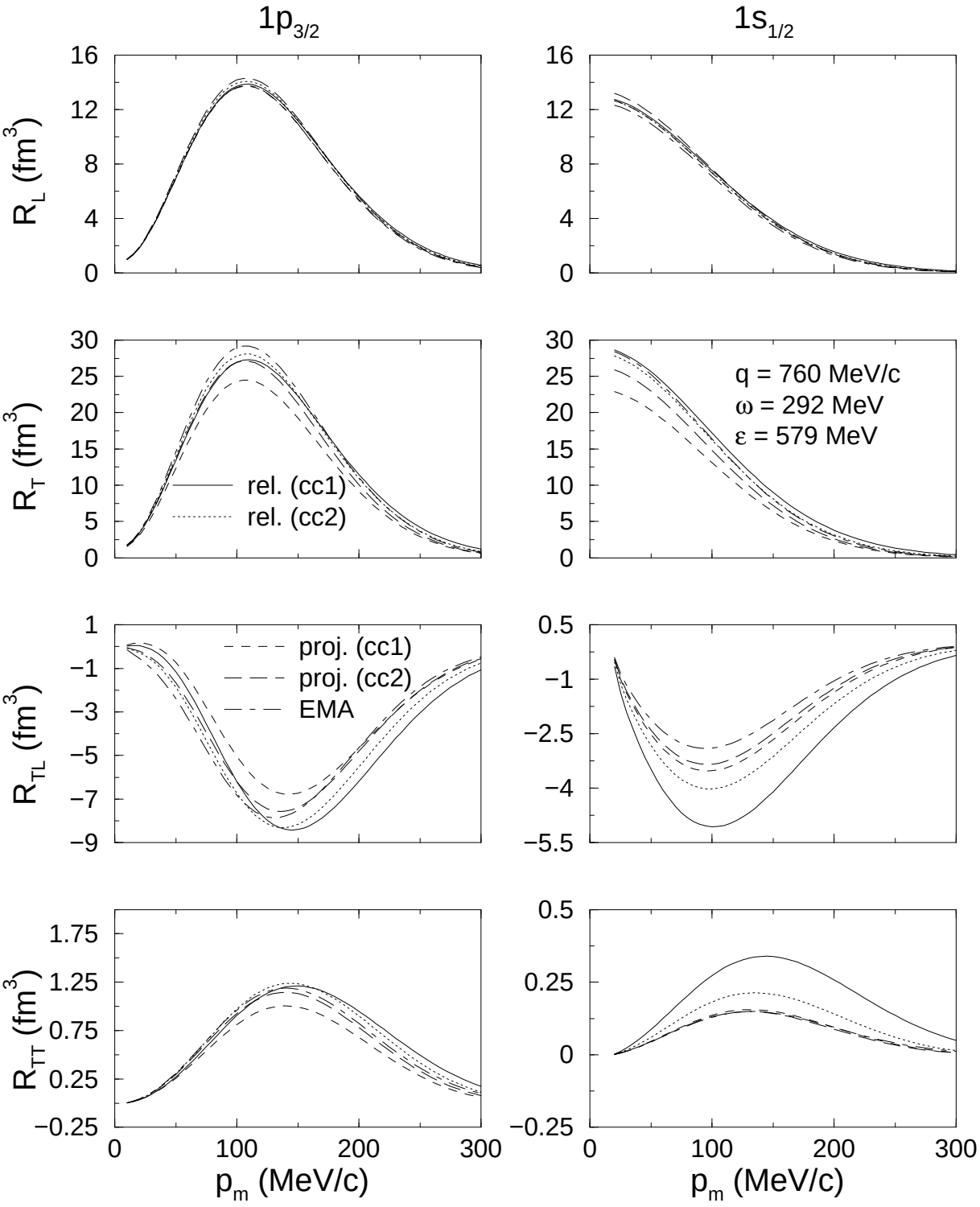

Figura 5.6: Unpolarized responses for the kinematics of Fig. 5.1.

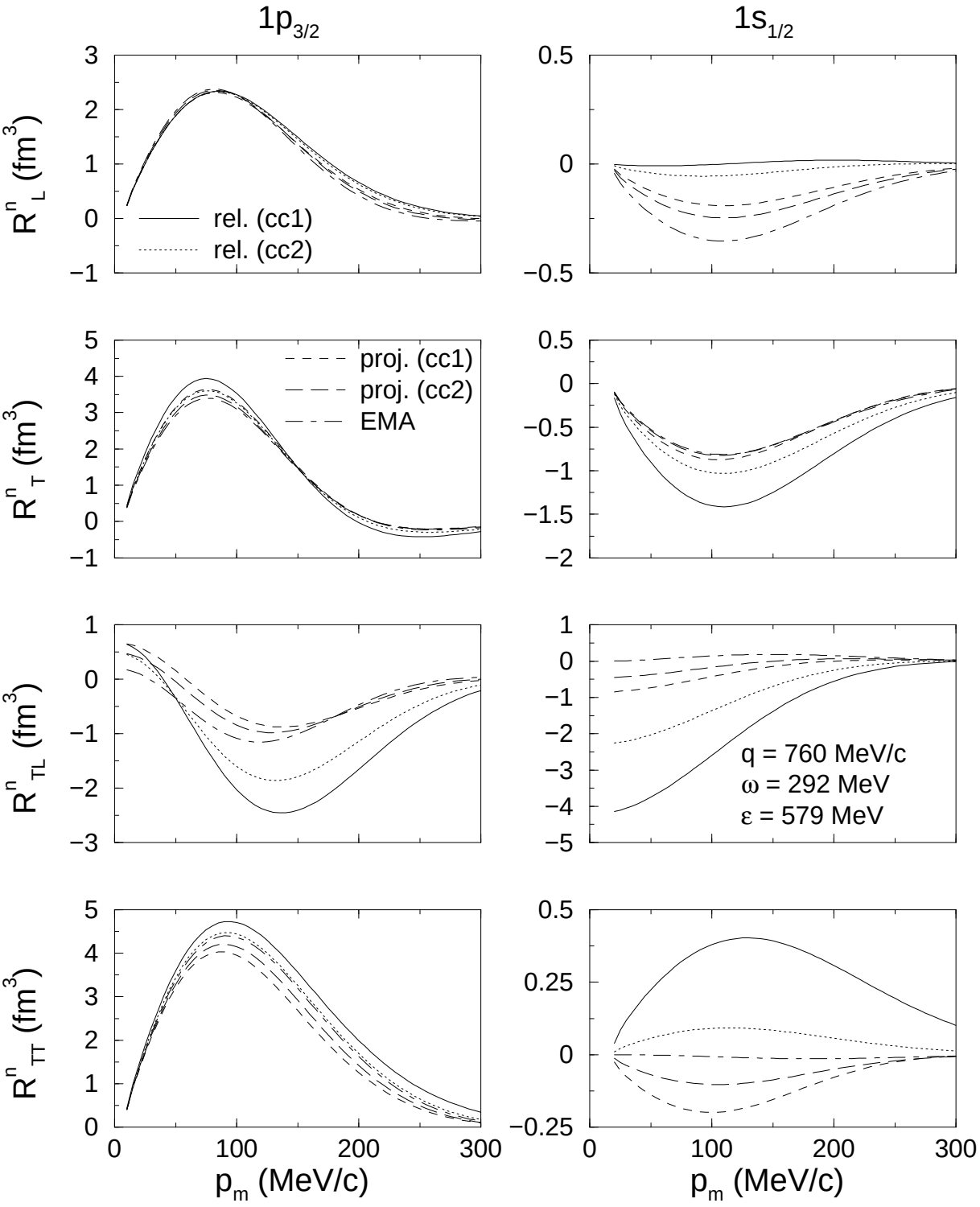

Figura 5.7: Normal responses for the kinematics of Fig. 5.1.

would be observed.

Taking into account the value of the kinematical factors in front of each response (see Table 5.1), the main contributions to P_n for the $s_{1/2}$ shell comes from R_T^n and R_{TL}^n responses. In the case of the full RDWIA results, the R_{TL}^n response is responsible for most of the net P_n. Due to this, P_n will change sign with p_m because of the $\cos\phi'$ factor in Eq. (5.2). We also see that R_{TL}^n is larger (in absolute value) for the calculation with larger effect of the negative energy components, *i.e.,* the full $cc1$ result. In Fig. 5.6 we can see the same feature in the unpolarized R_{TL} response. This characteristic has been explained before [20,30,38]. For the p shell, the largest contribution comes from R_T^n that shows little dependence on spinor distortion. This is why the effect of negative energy components is small for this shell.

We plot also P_n and responses (Figs. 5.8, 5.9 and 5.10) for a kinematics suitable at TJNAF (namely $|\vec{q}| = 1000$ MeV/c, $\omega = 445$ MeV and energy of the beam $\epsilon = 2445$ MeV). Apart from what has been already said, we find that for the $p_{3/2}$ shell and $p_m < 0$ there are small Gordon ambiguities and a very clear separation of the fully RDWIA results from the projected or EMA-noSV ones is seen. Therefore, this is a good region to look for the effects of spinor distortion. We can explain this better by looking at the results in the second column of Fig. 5.10: There, all calculations lie very close except for R_{TL}^n. In the $p_{3/2}$ shell the projected and EMA-noSV curves group together, while both fully relativistic calculations clearly deviate from the others. Going back to P_n in the second panel of Fig. 5.8, we observe these differences only in the region $p_m < 0$, due to the different sign with which the $\cos\phi' R_{TL}^n$ term contributes in the $p_m < 0$ and $p_m > 0$ regions. This behavior is characteristic of the kinematics chosen at TJNAF. Indeed, as we can see in Fig. 5.11, at different kinematics conditions such as the ones suitable at Mainz, (*i.e., q*-ω constant kinematics with $|\vec{q}| = 648$ MeV/c, $\omega = 215$ MeV and $\epsilon = 855$ MeV), there is not such a clear separation of the fully relativistic curves from the others in the $p_{3/2}$ shell for $p_m < 0$ as the one found for the TJNAF kinematics.

Another interesting feature that was already found in parallel kinematics is that, for the $j = l + 1/2$ shells, R_{TL}^n has larger values when the calculation emphasizes the role of negative energy components while the converse is seen for the $p_{1/2}$ ($j = l - 1/2$) shell.

For the two p shells at the kinematics of TJNAF and Mainz, the largest contribution to P_n would come from $V_{TT} R_{TT}^n$. For the $p_{3/2}$ shell in the $p_m < 0$ region, however, this contribution is canceled to a large extent by the $V_{TL} R_{TL}^n$ one. This explains why P_n is mainly negative for $p_m < 0$ for the $p_{3/2}$ shell. On the other hand, the $v_{TL} R_{TL}^n$ contribution

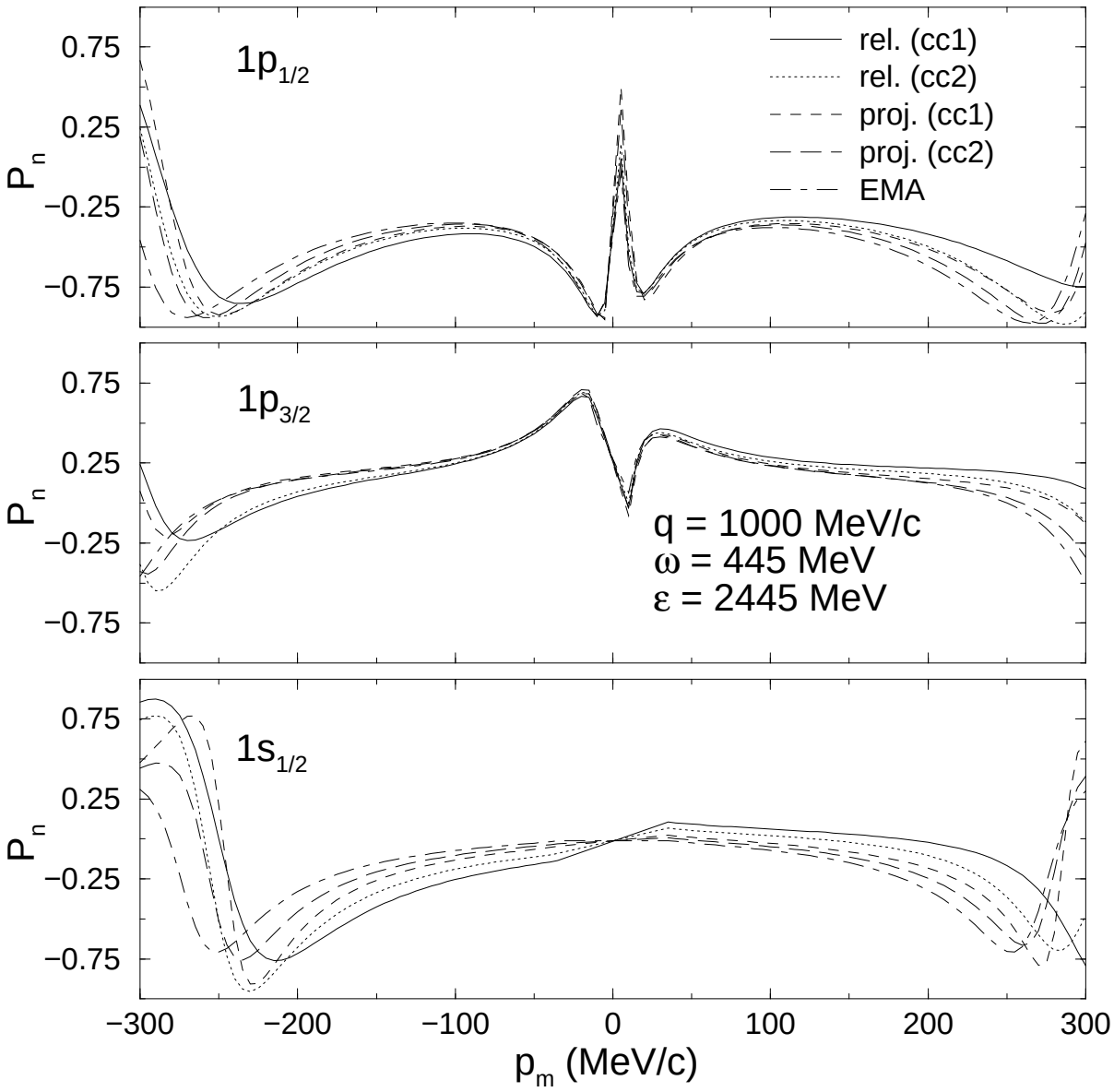

Figura 5.8: P_n from ^{16}O for the $1p_{1/2}$ (upper panel), $1p_{3/2}$ (mid panel) and $1s_{1/2}$ (lower panel) orbits, versus missing momentum p_m in MeV/c. Results shown correspond to a fully relativistic calculation with the $cc1$ (solid line) and $cc2$ (dotted line) operators. Also shown are the projected results (short and long dashed lines) and the EMA(noSV)-$cc1$ ones (dash-dotted line). Results in q-ω constant kinematics corresponding to ref. [2] and the EDAI-O potential is used.

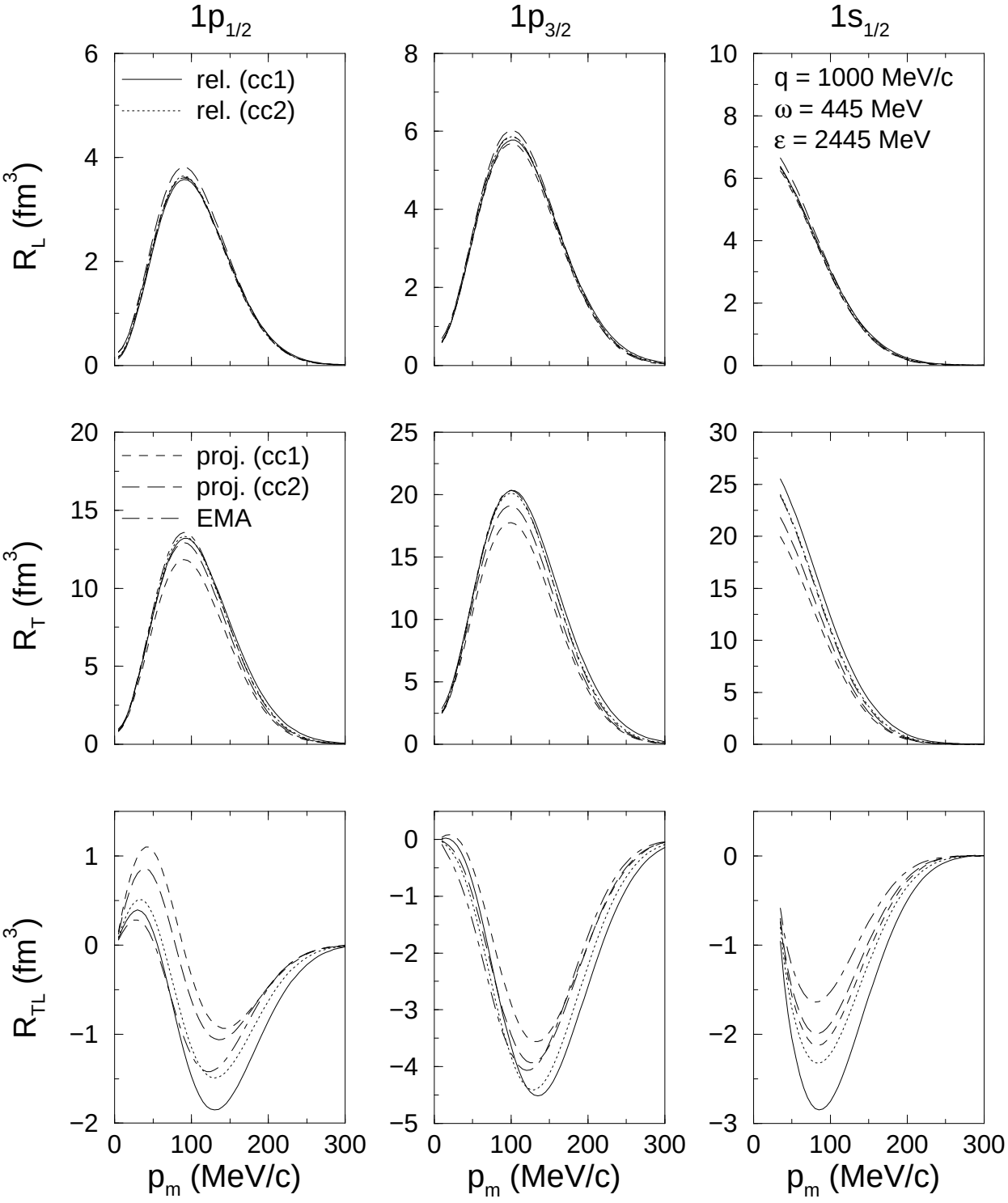

Figura 5.9: Unpolarized responses for the kinematics of Fig. 5.8. The response R_{TT} is not plotted, because it is much smaller than the ones shown.

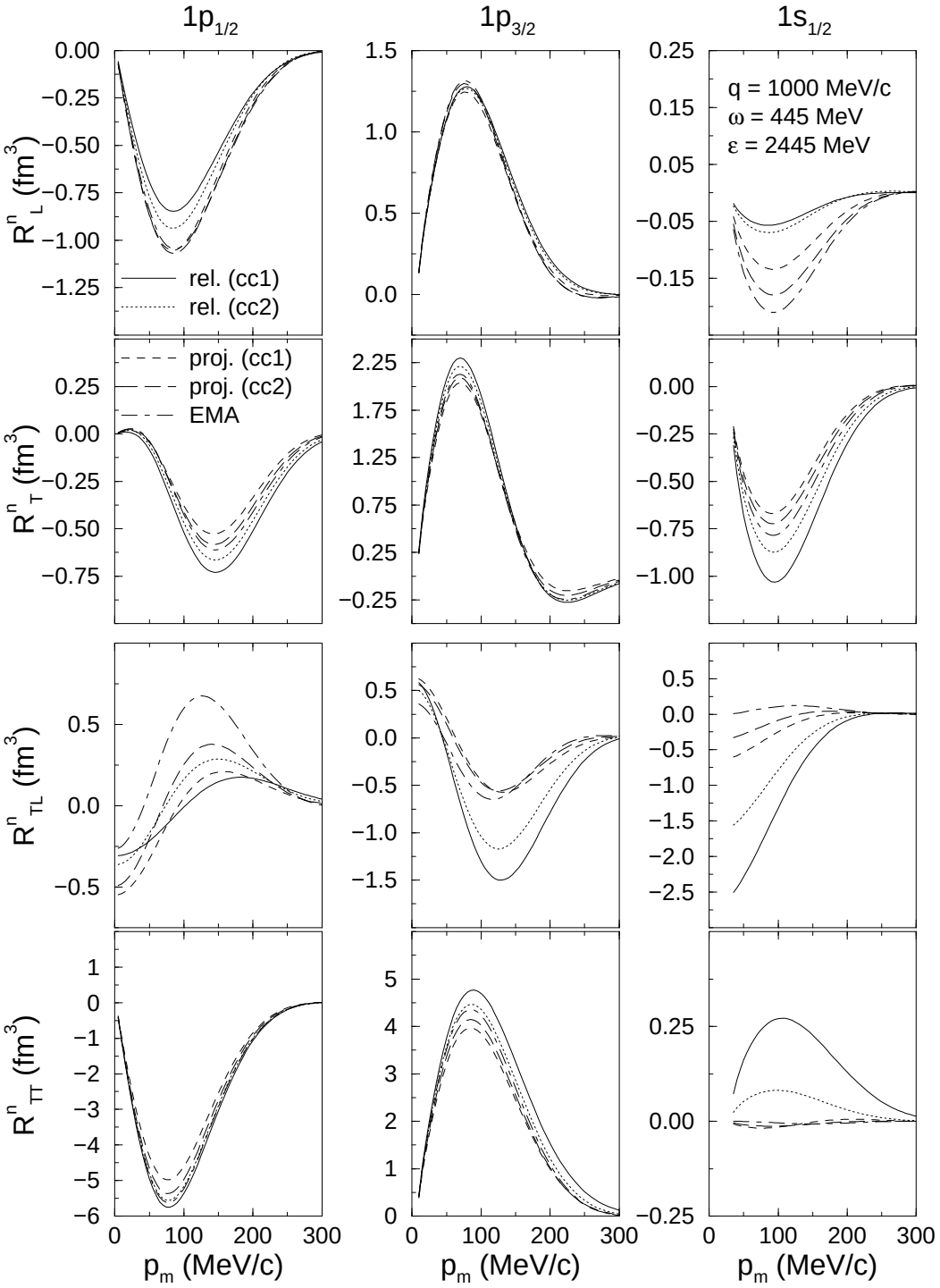

Figura 5.10: Normal responses for the kinematics of Fig. 5.8.

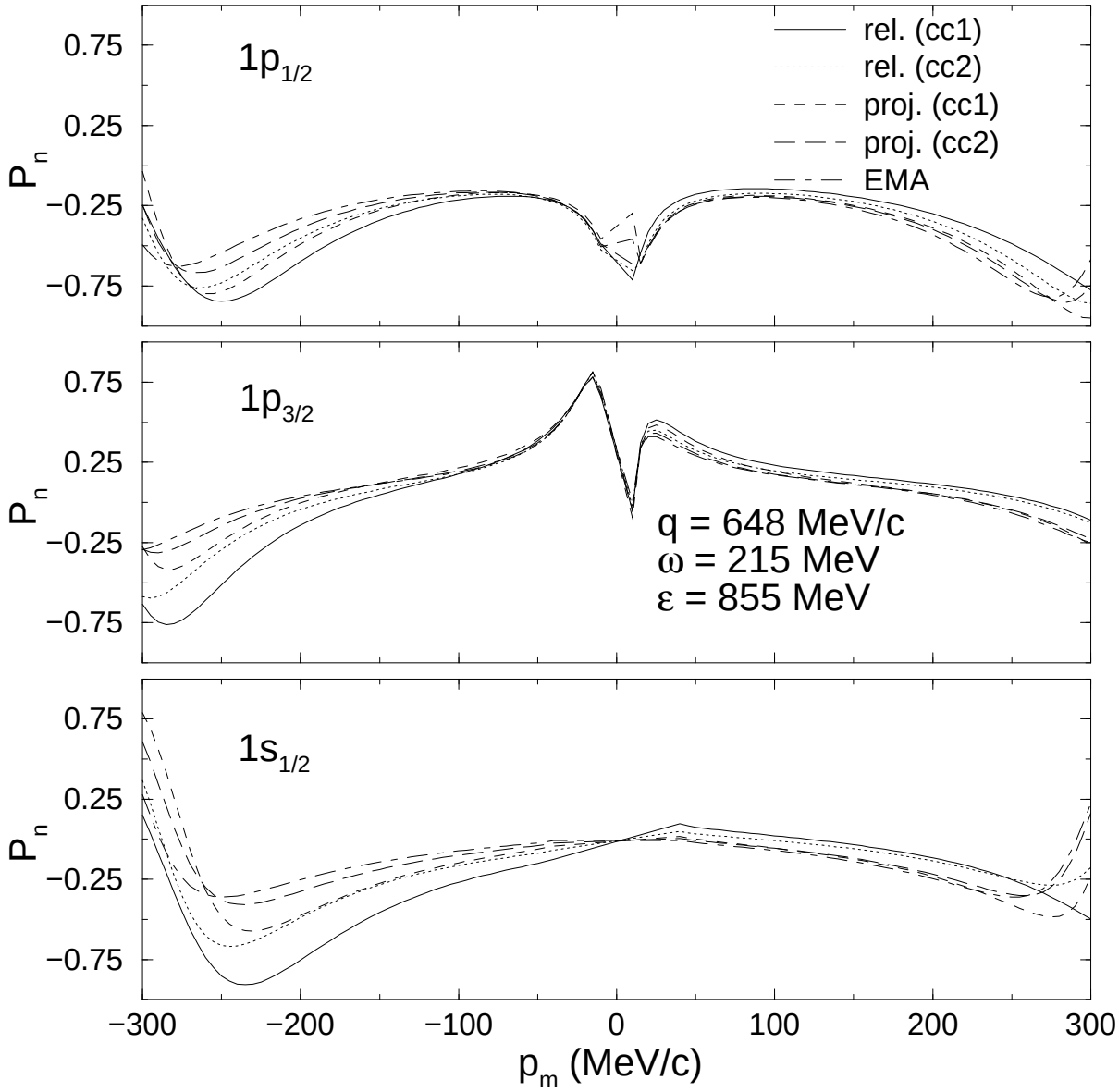

Figura 5.11: The same as Fig. 5.8 except for slightly smaller values of q and P' as expected at Mainz [3].

is less important for the $p_{1/2}$ shell and practically does not influence the total polarization. Therefore P_n for this shell is negative irrespectively of the sign of p_m.

A serious concern is the issue of current conservation. The use of an optical potential breaks Gauge invariance in DWIA. We estimated the uncertainty associated to the choice of Gauge by comparing the results we show in the present work with the ones obtained in the Landau Gauge. We find that the fully relativistic results in perpendicular kinematics at the highest value of Q^2 are the less sensitive ones to this procedure. On the other hand, the unpolarized cross sections can differ by as much as 50% in parallel kinematics for large values of $|p_m|$. However, P_n is much less sensitive to the choice of Gauge than unpolarized cross sections: For the fully RDWIA results of the present work, using the Landau or Coulomb Gauge produces P_n results within 5%. Gauge ambiguity is much less important than the one due to the $cc1$ or $cc2$ choice.

5.3 Conclusions

We have found that the relativistic dynamical effect mentioned in paragraph (ii), the enhancement of the lower components, increases noticeably P_n with respect to both the projected and, more sizeably, the EMA-noSV results, driving the fully RDWIA results for P_n into excellent agreement with the data of Ref. [1]. For the kinematics of the TJNAF 89-033 [2] and Mainz [3] experiments we find the differences between the RDWIA and projected results to be important.

P_n proves to be very sensitive to the choice of optical potential, allowing this observable to be used to constrain the theoretical model for FSI so that these effects can be included with confidence when making predictions for other observables much less sensitive to the choice of FSI, such as the polarization transfer observables P'_x and P'_z [29].

Previous explorations of the role of meson exchange currents (MEC) for Bates, based upon a non relativistic picture, showed very little effect in P_n at moderate p_m [8]. MEC are expected to play an even minor role for higher Q^2 at quasi-elastic kinematics ($x \simeq 1$) [8] and its inclusion will not modify substantially the predictions for P_n presented in the present work. The same can be said of coupled channel effects analyzed within the EMA-noSV approach in Ref. [36]. However, Gordon and kinematical off-shellness ambiguities are large for high Q^2 experiments. We have looked for kinematical regions where these ambiguities are minimized. In parallel kinematics, we conclude that the $p_m < 0$ region

($|\vec{q}| > |\vec{P}'|$) is optimal because it displays a minimum effect of Gordon ambiguities while a high sensitivity of the calculations to the presence of negative energy components is found. In q-ω constant kinematics the same favorable situation is seen again for $p_m < 0$ ($\phi' = 0$) but only for the $p_{3/2}$ shell at $|\vec{q}| = 1$ GeV/c, adequate to TJNAF.

In parallel kinematics we found very clear signatures for negative energy components in the wave functions, that cause P_n to be driven towards more negative values with respect to the non relativistic prediction, particularly for the $s_{1/2}$ and $p_{3/2}$ ($j = l + 1/2$) shells. This feature should remain even in the presence of MEC and CC.

In q-ω constant kinematics the effect of the negative components is manifested as an increase (decrease) of P_n for $p_m > 0$ ($p_m < 0$) of the relativistic predictions with regards to the non relativistic ones.

Finally, we hope that future experiments will shed light on the theoretical uncertainties that are still present in the calculations such as which current operator should be used and will help to disentangle the role played by the negative energy components of the wave functions.

Acknowledgements

This work was partially supported under Contracts PB/96-0604 (DGES, Spain) and PR156/97 (Complutense University, Spain). J.M.U. thanks E. Moya de Guerra and J.A. Caballero for many useful comments. We also thank J.J. Kelly for providing us with files with his calculations and interesting comments. J.R.V. acknowledges financial support from the Consejería de Educación y Cultura de la Comunidad de Madrid.

Bibliografía

[1] R.J. Woo *et al.*, Phys. Rev. Lett. **80** (1998) 456.

[2] TJNAF proposal 89-033, C. Glashausser contact person.

[3] R. Neuhasen *et al.*, Measurement of Polarized Protons from Quasi-elastic Electron Scattering on ^{16}O, MAMI Proposal A1/2-93, 1993.

[4] S. Boffi, C. Giusti, F.D. Pacati, Phys. Rep. 226 (1993) 1. S. Boffi, C. Giusti, F. Pacati, M. Radici in *"Electromagnetic Response of Atomic Nuclei"*, (Oxford-Clarendom Press, 1996). J.J. Kelly, Adv. Nucl. Phys. V 23 (1996) 75.

[5] A.S. Raskin and T.W. Donnelly, Ann. Phys. (N.Y.) **191** (1989) 78.

[6] C. Giusti and F.D. Pacati, Nucl. Phys. **A504** (1989) 685.

[7] A. Picklesimer, J.W. Van Orden, Phys. Rev. C **35** (1987) 266; *ibidem* **40** (1989) 290.

[8] J. Ryckebusch, D. Debruyne, W.V. Nespen, S. Janssen, Phys. Rev. C **60** (1999) 034604.

[9] L. Lapikás, G. van der Steenhoven, L. Frankfurt, M. Strikman and M. Zhalov, Phys. Rev. C61 (2000) 064325.

[10] G. Jacob, T.A.J. Maris, C. Schneider and M.R. Teodoro, Nucl. Phys. **A257** (1976) 517.

[11] J.P. McDermott, Phys. Rev. Lett. **65** (1990) 1991; Y. Jin, D.S. Onley, L.E. Wright, Phys. Rev. C **45** (1992) 1311.

[12] J.M. Udías, P. Sarriguren, E. Moya de Guerra, E. Garrido, J.A. Caballero, Phys. Rev. C **48** (1993) 2731

[13] J.M. Udías, P. Sarriguren, E. Moya de Guerra, E. Garrido, J.A. Caballero, Phys. Rev. C **51** (1995) 3246.

[14] J.M. Udías, P. Sarriguren, E. Moya de Guerra, J.A. Caballero, Phys. Rev. C **51** (1996) R1488.

[15] J.M. Udias et al, in "Proceedings of the 4th workshop on Electromagnetically Induced two-hadron Emission, Granada May 26-29 1999", C. Garcia Recio, P. Grabmayr, A.M. Lallena and R. Owens, Eds., ISBN 84-699-1645-9, page 318.

[16] T. de Forest, Nucl. Phys. **A392** (1983) 232.

[17] B.D. Serot and J.D. Walecka, Adv. Nucl. Phys. 16 (1986) 1.

[18] J.J. Johansson and H.S. Sherif, Phys. Rev. C **59** (1999) 3481.

[19] J.E. Amaro *et al.*, Nucl. Phys. **A602** (1996) 263.

[20] J.M. Udías *et al.*, Phys. Rev. Lett. **83** (1999) 5451.

[21] J. Gao *et al.*, Phys. Rev. Lett. **84**, (2000) 3265.

[22] S. Boffi, C. Giusti, F.D. Pacati, F. Cannata, Nuovo Cimento **98**, (1987) 291.

[23] S.J. Pollock, H.W.L. Naus, J.H. Koch, Phys. Rev. C **53** (1996) 2304.

[24] S. Jeschonnek and T.W. Donnelly, Phys. Rev.C **57** (1998) 2438. J.A. Caballero, T.W. Donnelly, G.I. Poulis, Nucl. Phys.**A555** (1993) 709.

[25] G.H. Rawitscher, Phys. Rev. C **31** (1985) 1173.

[26] J.J. Kelly, Phys. Rev. C **54**, (1996) 2547.

[27] Y. Jin, D.S. Onley, Phys. Rev. C **50**, (1994) 377.

[28] C.G. Darwin, Proc. Roy. Soc. (London) A **118** (1928) 654.

[29] J.J. Kelly, Phys. Rev. **C56** (1997) 2672; **C60** (1999) 044609.

[30] J.A. Caballero, T.W. Donnelly, E. Moya de Guerra, J.M. Udías, Nucl. Phys. **A632** (1998) 323.

[31] K.V. McVoy and L. van Hove, Phys. Rev. **125** (1962) 1034.

[32] H.W. Fearing, G. Poulis and S. Scherer, Nucl. Phys. **A570**, (1994) 657.

[33] G.A. Lalazissis, J. König, P. Ring, Phys. Rev. C **55** (1997) 540.

[34] G. van der Steenhoven *et al.*, Nucl. Phys **A480** (1988) 547.

[35] E.D. Cooper, S. Hama, B.C. Clark, R.L. Mercer, Phys. Rev. C **47** (1993) 297.

[36] J.J. Kelly, Phys.Rev. C **59** (1999) 3256.

[37] J.J. Kelly, Phys. Rev. C **39** (1989) 2120.

[38] J.A. Caballero, T.W. Donnelly, E. Moya de Guerra, J.M. Udías, Nucl. Phys. **A643** (1998) 189.

[39] J.J. Kelly, private communication.

[40] S. Ulrych and H. Müther, Nucl. Phys. **A641** (1998) 499.

Capítulo 6

Polarizaciones transferidas

PHYSICAL REVIEW C **69**, 034604 (2004)

Analysis of polarized ^{16}O$(\vec{e}, e'\vec{p})$ observables within the relativistic distorted wave impulse approximation

M.C. Martínez[1], J.R. Vignote[2], J.A. Caballero[1], T.W. Donnelly[3], E. Moya de Guerra[4], and J.M. Udías[2]

[1]*Departamento de Física Atómica, Molecular y Nuclear, Universidad de Sevilla, Apartado postal 1065, E-41080 Sevilla, Spain*

[2]*Departamento de Física Atómica, Molecular y Nuclear, Universidad Complutense de Madrid, E-28040 Madrid, Spain*

[3]*Center for Theoretical Physics, Laboratory for Nuclear Science and Department of Physics, Massachusetts Institute of Technology, Cambridge, Massachusetts 02139, USA*

[4]*Instituto de Estructura de la Materia, CSIC, Serrano 123, E-28006 Madrid, Spain*

Recoil nucleon transferred polarization observables in coincidence quasielastic electron scattering are studied within the relativistic distorted wave impulse approximation. Results for response functions and polarization asymmetries are discussed for proton knockout from $p_{1/2}$, $p_{3/2}$ and $s_{1/2}$ shells in ^{16}O. The impact of spinor distortion is examined by comparing the fully relativistic calculation with results obtained by projecting out the negative-energy components. In particular, a careful analysis of effects linked to the description of the bound and scattered relativistic nucleon wave functions is presented. The high sensitivity of some polarization observables to the dynamical enhancement of the lower components, already shown within the relativistic plane wave impulse approximation, is proven to be maintained in the relativistic distorted wave approach. Semi-relativistic approaches based on the effective momentum approximation are also studied. Finally, comparison with experimental data and a brief analysis of effects linked to medium modified form factors is presented.

PACS number(s): 25.30.Rw, 14.20.Gk, 24.10.Jv, 24.30.Gd

6.1 Introduction

A very topical issue in nuclear physics at present is the search for evidence of possible modification of the nucleon form factors inside the nuclear medium. A number of double polarized $(\vec{e}, e'\vec{p})$ experiments have been proposed or carried out recently to measure polarization transfer asymmetries, motivated by the hope that such observables may provide valuable information that can shed some light on this issue. Importantly, transferred polarization observables have been identified as being ideally suited for such studies: they are believed to be the least sensitive to most standard nuclear structure uncertainties and accordingly to provide the best opportunities for studying the nucleon form factors in the nuclear medium. Polarization transfer data have been reported recently for the case of $^{16}\mathrm{O}(\vec{e}, e'\vec{p})^{15}\mathrm{N}$ in [1] and for $^{4}\mathrm{He}(\vec{e}, e'\vec{p})^{3}\mathrm{H}$ in [2, 3]. Although the experimental uncertainties in both cases make it difficult to draw unambiguous conclusions on the nucleon form factors inside the nuclei, the data in [3] do seem to favour such a possibility. Specifically, this means that comparisons of measured polarization asymmetries with those computed using the best currently available nuclear models for the states and operators involved in the coincidence reaction in fact show disagreements, and that these can be removed by modifying the nucleon form factors in a reasonable way.

Of course, what constitutes the "best currently available nuclear models"must be judged carefully. In particular, the kinematic regime where the measurements have been undertaken is at relatively high energy — to make the reaction sufficiently impulsive to be at all interpreted as a simple single-nucleon knockout reaction — and it is clear that relativistic effects in wave functions and operators are essential. So, for instance, the data in [2] disagree significantly with the standard non-relativistic calculations; however, this cannot be taken as evidence for nucleon modifications, since one finds that the results are (not unexpectedly) much more in accord with a fully relativistic approach. Also recent data on induced polarization in $^{12}\mathrm{C}$ [4] strongly support an analysis based on the fully relativistic formalism [5]. These results are not surprising since spin and relativity are intrinsically related, and hence one may *a priori* consider the relativistic formalism to be better suited to describe polarization observables.

Indeed, most electron scattering experiments performed in the last decade have involved energies and momenta high enough to invalidate the non-relativistic approximations assumed within the standard non-relativistic distorted wave impulse approximation (DWIA), *i.e.,* bound and scattered wave functions given as solutions of the Schrödinger

equation, and one-body current operator resulting from a non-relativistic reduction. In the relativistic distorted wave impulse approximation (RDWIA), nucleon wave functions are described by solutions of the Dirac equation with scalar and vector (S-V) potentials, and the relativistic free nucleon current operator is used.

Relativistic effects can be classified into two basic categories according to their origin, namely kinematical and dynamical effects. The former are due to the truncation of the current operator within the non-relativistic approach, the latter, dynamical effects, come from the difference between the relativistic and non-relativistic wave functions. Here one may distinguish a dynamical depression of the upper component of the scattered nucleon wave function in the nuclear interior (Darwin term) and a dynamical enhancement of the lower components, mainly that corresponding to the bound nucleon wave function.

So far, RDWIA calculations for cross sections and response functions at low and high missing momenta [6–10] have clearly improved the comparison with experimental data over the previous non-relativistic approaches. Moreover, RDWIA also predicts larger spectroscopic factors which are more in accord with theoretical calculations which incorporate correlations [6, 10].

Concerning the current operators, in some recent studies [11–15] new so-called 'semi-relativistic' approaches have been introduced to describe $(e, e'p)$ reactions. Here the 'semi-relativistic' current operators are obtained by expanding only in missing momentum over the nucleon mass while treating the transferred energy and momentum exactly. This new approach has been proven to retain important aspects of relativity, and hence its predictions, compared with the standard DWIA, agree much better with the RDWIA calculations.

Concerning dynamical effects, the enhancement of the lower components of bound Dirac spinors [9, 10] (not present in the semi-relativistic approaches) has been shown to play a crucial role in the description of the interference TL response and left-right asymmetry A_{TL}. Meson exchange currents and the Δ-isobar contribution have recently been analyzed in [16,17] within the semi-relativistic approach, also showing very significant effects, particularly due to the Δ, at large missing momentum $p \geq 300$ MeV/c.

In this paper we focus on the analysis of polarized A$(\vec{e}, e'\vec{p})$B observables within the framework of the RDWIA. Our aim is to study the role played by both kinematical and dynamical relativistic effects in a consistent description of the polarized responses and asymmetries. This work extends the previous analyses presented in [18,19] within the plane

wave approach, now including a realistic description of the final-state interactions (FSI) through relativistic optical potentials. The magnitude of relativistic effects on various transfer polarization observables is carefully examined, disentangling the role played by the various ingredients that enter in the fully relativistic formalism. In particular, we extend the study of [18] where within RPWIA we demonstrated the importance of the negative-energy components of the relativistic bound nucleon in the description of the polarized responses and transferred polarization asymmetries. The RDWIA analysis performed here allows one to examine also the dynamical enhancement of the lower components in the scattered Dirac wave functions and moreover, makes it possible to carry out meaningful comparisons with measured observables.

Returning to the issue of potential medium modifications of the nucleon form factors, the current study has the following goal: we wish to explore a selected set of model "variations on a theme" of the type discussed above. In all cases we choose only modeling that is, within the context of the general relativistic approach being adopted, consistent with what we know about initial- and final-state wave functions and one-body electromagnetic operators. Since equally acceptable relativistic potentials exist when obtaining the states and since alternative descriptions of the current operators are likewise acceptable, it is impossible at present to define what is "the best" model. Our goal is to explore these acceptable models and where the resulting polarization observables differ with the choice of model to ascribe these variations to a (minimal) theoretical uncertainty. Needless to say, all of this is within the general context of relativistic mean-field modeling and so the resulting uncertainties are minimal in the sense that effects that go beyond the scope of the modeling might increase the uncertainties. In the final analysis, only if medium modification effects are larger than the uncertainties we find here, and only if the uncertainties that arise from ingredients not in the present model can ultimately be shown to be small, will a convincing case be made for the necessity of having such medium modification effects.

The paper is organized as follows: in Sec. 6.2 we briefly introduce the general formalism for A$(\vec{e}, e'\vec{p})$B reactions focusing on the relativistic distorted wave impulse approximation. Within this context, we also introduce the projected approach, the effective momentum approximation (EMA-noSV) and the use of semi-relativistic current operators. By comparing them one may get a clear image of the importance of relativity in these processes. In Sec. 6.3 we present and discuss the results, paying special attention to the polarized responses and transferred polarization asymmetries. Finally, in Sec. 6.4 we summarize our

conclusions.

6.2 Description of $A(\vec{e}, e'\vec{p})B$ reactions

6.2.1 General formalism. RDWIA

In this section we briefly review the general formalism needed to describe coincidence $(\vec{e}, e'\vec{p})$ reactions. We consider plane waves for the incoming and outgoing electron (treated in the extreme relativistic limit) and the Born approximation (one virtual photon exchanged). When the incoming electron is polarized and the final nucleon polarization is measured, the differential cross section can be written as [20–24]

$$\frac{d\sigma}{d\varepsilon_e d\Omega_e d\Omega_F} = \frac{\sigma_0}{2}[1 + \boldsymbol{P}\cdot\boldsymbol{\sigma} + h(A + \boldsymbol{P'}\cdot\boldsymbol{\sigma})]\,, \tag{6.1}$$

where the variables $\{\varepsilon_e, \Omega_e\}$ refer to the scattered electron and Ω_F to the ejected nucleon. The term σ_0 is the unpolarized cross section, h is the incident electron helicity, A denotes the electron analyzing power, and $\boldsymbol{P}$ ($\boldsymbol{P'}$) represents the induced (transferred) polarization. Note that both $\boldsymbol{P}$ and $\boldsymbol{P'}$ depend on the outgoing nucleon polarization, but $\boldsymbol{P'}$ only becomes accessible when the incoming electron beam is polarized. The cross section in Eq. (6.1) can also be written in terms of nuclear responses as follows:

$$\begin{aligned}
\frac{d\sigma}{d\varepsilon_e d\Omega_e d\Omega_F} &= K\sigma_M f_{rec}^{-1}\left\{v_L\left(R^L + R_n^L\widehat{S}_n\right) + v_T\left(R^T + R_n^T\widehat{S}_n\right)\right. \\
&+ v_{TL}\left[\left(R^{TL} + R_n^{TL}\widehat{S}_n\right)\cos\phi + \left(R_l^{TL}\widehat{S}_l + R_s^{TL}\widehat{S}_s\right)\sin\phi\right] \\
&+ v_{TT}\left[\left(R^{TT} + R_n^{TT}\widehat{S}_n\right)\cos 2\phi + \left(R_l^{TT}\widehat{S}_l + R_s^{TT}\widehat{S}_s\right)\sin 2\phi\right] \\
&+ h\left\{v_{TL'}\left[\left(R_l^{TL'}\widehat{S}_l + R_s^{TL'}\widehat{S}_s\right)\cos\phi + \left(R^{TL'} + R_n^{TL'}\widehat{S}_n\right)\sin\phi\right]\right. \\
&+ \left.\left. v_T\left[R_l^{T'}\widehat{S}_l + R_s^{T'}\widehat{S}_s\right]\right\}\right\}\,,
\end{aligned} \tag{6.2}$$

where ϕ is the azimuthal angle that determines the outgoing nucleon momentum. The term K is a kinematical factor given by $K = p_F M_N M_B/M_A$, with p_F the outgoing nucleon momentum, M_N the nucleon mass, and M_B (M_A) the mass of the residual nucleus (target), respectively. The Mott cross section is represented by σ_M, f_{rec} is the recoil factor given by $f_{rec} = 1 + (\omega p_F - qE_F\cos\theta_F)/M_A p_F$, where E_F is the outgoing nucleon energy and θ_F is the angle between $\boldsymbol{p}_F$ and the transferred momentum, and the v_K, $K = L, T, ...$ are the standard electron scattering kinematical factors (see [24, 25]). The indices l, s, n refer as usual to the directions selected to specify the recoil nucleon polarization: $\boldsymbol{l}$ (parallel to the

momentum $\boldsymbol{p}_F$), $\boldsymbol{n}$ (perpendicular to the plane containing $\boldsymbol{p}_F$ and the transfer momentum $\boldsymbol{q}$), and $\boldsymbol{s}$ (determined by $\boldsymbol{n}\times\boldsymbol{l}$). From this large number of possible response functions some selection can be made to limit the focus:

- Assuming coplanar kinematics, *i.e.*, $\phi = 0°, 180°$, from the total set of eighteen responses in Eq. (6.2) only twelve survive.
- From these twelve responses, the four transferred polarization ones $R_{l,s}^{K'}$ only contribute when the electron is polarized, while the four induced polarization ones R_n^K only enter when FSI are taken into account.

Following the analysis presented in [18], in this work we limit our attention to those observables that survive in the plane wave limit, *i.e.*, transferred polarization responses $R_l^{TL'}$, $R_l^{T'}$, $R_s^{TL'}$, $R_s^{T'}$ and transferred asymmetries P_l', P_s'. A detailed study of the induced polarization observables within RDWIA has been presented in [5].

The response functions in Eq. (6.2) are constructed directly by taking the appropriate components of the hadronic tensor $W^{\mu\nu}$ which, within the RDWIA, comes from bilinear combinations of the nucleon current matrix elements

$$J_N^{\mu}(\omega,\boldsymbol{q}) = \int d\boldsymbol{p}\overline{\Psi}_F(\boldsymbol{p}+\boldsymbol{q})\hat{J}_N^{\mu}\Psi_B(\boldsymbol{p})\,, \tag{6.3}$$

where Ψ_B and Ψ_F are relativistic wave functions describing the initial bound and final outgoing nucleons, respectively, and $\hat{J}_N^{\mu}$ is the relativistic one-body current operator. The bound wave function Ψ_B is a four-spinor with well-defined parity and angular momentum quantum numbers κ_b, μ_b, obtained within the framework of the relativistic independent particle shell model. The mean field in the Dirac equation is determined through a Hartree procedure from a phenomenological relativistic Lagrangian with scalar (S) and vector (V) terms. It may be written

$$\Psi_B(\boldsymbol{p}) = \Psi_{\kappa_b}^{\mu_b}(\boldsymbol{p}) = \frac{1}{(2\pi)^{3/2}}\int d\boldsymbol{r}e^{-i\boldsymbol{p}\cdot\boldsymbol{r}}\Psi_{\kappa_b}^{\mu_b}(\boldsymbol{r}) = (-i)^{\ell_b}\begin{pmatrix} g_{\kappa_b}(p) \\ S_{\kappa_b}f_{\kappa_b}(p)\dfrac{\boldsymbol{\sigma}\cdot\boldsymbol{p}}{p}\end{pmatrix}\Phi_{\kappa_b}^{\mu_b}(\hat{\boldsymbol{p}}) \tag{6.4}$$

with $\Phi_{\kappa_b}^{\mu_b}(\hat{\boldsymbol{p}})$ the usual spinor harmonics. The wave function for the ejected proton Ψ_F is a scattering solution of a Dirac-like equation, which includes S-V global optical potentials obtained by fitting elastic proton scattering data. This wave function, obtained as a partial wave expansion, is given in momentum space by

$$\Psi_F(\boldsymbol{p}) = 4\pi\sqrt{\frac{E_F+M_N}{2E_F}}\sum_{\kappa\mu m}e^{-i\delta_\kappa^*}i^{\ell}\langle\ell m\frac{1}{2}s_F|j\mu\rangle Y_\ell^{m*}(\hat{\boldsymbol{p}}_F)\Psi_\kappa^{\mu}(\boldsymbol{p})\,, \tag{6.5}$$

where $\Psi^{\mu}_{\kappa}(\boldsymbol{p})$ are four-spinors of the same form as in Eq. (6.4), but the phase-shifts and radial functions are complex because of the complex optical potential involved.

Finally, for the nucleon current operator we consider the two choices denoted as CC1 and CC2 [26]

$$\hat{J}^{\mu}_{CC1} = (F_1 + F_2)\gamma^{\mu} - \frac{F_2}{2M_N}(\overline{P} + P_F)^{\mu} \tag{6.6}$$

$$\hat{J}^{\mu}_{CC2} = F_1\gamma^{\mu} + i\frac{F_2}{2M_N}\sigma^{\mu\nu}Q_{\nu}\,, \tag{6.7}$$

where F_1 and F_2 are the Dirac and Pauli nucleon form factors related to the electric and magnetic Sachs form factors in the usual form. The variable $\overline{P}^{\mu}$ in Eq. (6.6) is the four-momentum of the initial nucleon for on-shell kinematics, *i.e.*, $\overline{P}^{\mu} = (\overline{E}, \boldsymbol{p})$ ($\overline{E} = \sqrt{\boldsymbol{p}^2 + M_N^2}$ and $\boldsymbol{p} = \boldsymbol{p}_F - \boldsymbol{q}$).

6.2.2 Dynamical effects: projected approach and effective momentum approximation

In recent years a considerable effort has been devoted to the analysis of quasielastic $(e, e'p)$ reactions using a fully relativistic formalism. Within this framework, particular emphasis has been placed on comparison between relativistic and non-relativistic approaches, trying to identify and disentangle clearly the ingredients which lead to different results in the two types of calculations. In some recent works [27] relativistic effects have been analyzed by comparing directly results obtained from a standard non-relativistic DWIA code (DWEEPY) with those provided by a relativistic calculation. These investigations were aimed at providing systematic and precise information on the magnitude of the effects introduced by relativity when compared with the standard non-relativistic description based on DWEEPY. The latter was widely used in the 1980s to analyze low-energy experimental data. However, although interesting, this study did not allow one to identify clearly the role played by the various ingredients entering into the relativistic formalism. Note that apart from the four-spinor versus two-spinor structure involved in relativistic and non-relativistic calculations, respectively, also the potentials used in the Dirac and Schrödinger equations for the bound and scattered nucleon are different. Moreover, the non-relativistic current operator results from an expansion in a basis of free nucleon plane waves and a Pauli reduction with the operator expanded in powers of p/M_N, q/M_N and/or ω/M_N, p being the missing momentum, q and ω the transfer

momentum and energy, respectively. In this work we focus on the separate analysis of the various ingredients that enter in the general formalism, and evaluate their impact on the transferred polarization observables. Hence, in order to minimize the mismatch coming from the different assumptions involved in relativistic and non-relativistic approaches, all of the results presented in this work have been evaluated using the same potentials and code.

Dynamical effects arise from the differences between relativistic and non-relativistic potentials and wave functions. A detailed study on this subject has been already presented in [9, 10, 28], so here we simply summarize the basic concepts needed for later discussion of the results. As is well known, interacting Dirac wave functions have a non-zero overlap with the Dirac sea [29]. The presence of the S-V potentials leads to a significant dynamical enhancement of the lower components of the Dirac solution at the nuclear interior. This fact is clearly illustrated by realizing that for a general solution of the Dirac equation with scalar and vector potentials, its upper and lower components are related by

$$\Psi^{down} = \frac{\boldsymbol{\sigma} \cdot \boldsymbol{p}}{E + M_N + S - V} \Psi^{up} \tag{6.8}$$

with $S < 0$ and $V > 0$. Note that these lower components are enhanced with respect to the ones corresponding to free positive energy spinors where $S = V = 0$. This effect has been referred to as dynamical enhancement of the lower components, and more recently as *spinor distortion* [30].

The analysis of these dynamical effects can be done by constructing properly normalized four-spinor wave functions where the negative-energy components have been projected out. Thus, instead of the fully relativistic expression given in Eq. (6.3), the nucleon current is evaluated as

$$J_N^{\mu(+,+)}(\omega, \boldsymbol{q}) = \int d\boldsymbol{p} \overline{\Psi}_F^{(+)}(\boldsymbol{p} + \boldsymbol{q}) \hat{J}_N^{\mu} \Psi_B^{(+)}(\boldsymbol{p}) \,, \tag{6.9}$$

where $\Psi_B^{(+)}(\boldsymbol{p})$, $(\Psi_F^{(+)}(\boldsymbol{p}))$ is the positive-energy projection of $\Psi_B(\boldsymbol{p})$, $(\Psi_F(\boldsymbol{p}))$, *i.e.,*

$$\begin{aligned} \Psi_B^{(+)}(\boldsymbol{p}) &= \Lambda_{(+)}(\boldsymbol{p}) \Psi_B(\boldsymbol{p}) \\ \Psi_F^{(+)}(\boldsymbol{p} + \boldsymbol{q}) &= \Lambda_{(+)}(\boldsymbol{p} + \boldsymbol{q}) \Psi_F(\boldsymbol{p} + \boldsymbol{q}) \,, \end{aligned} \tag{6.10}$$

where $\Lambda_{(+)}(\boldsymbol{p}) = (M_N + \overline{P\!\!\!/})/2M_N$ is the positive energy projector. Then the effects due to the dynamical enhancement of the lower components show up clearly by comparing the results obtained using the fully relativistic amplitude given in Eq. (6.3) with those evaluated by using Eq. (6.9).

Notice that the relationship between lower and upper components in the projected wave functions is similar to that corresponding to free nucleon wave functions, but with the positive-energy projectors depending explicitly on the integration variable $\boldsymbol{p}$. An additional approach, referred to as asymptotic projection, consists of introducing the asymptotic values of the momenta into the positive-energy projectors acting on the bound and scattered wave functions. This asymptotic projection is very similar (although it is not completely equivalent) to the effective momentum approximation (EMA-noSV) introduced originally by Kelly [30]. Within the EMA-noSV approach, the four spinors used have the same upper components as those of the Dirac equation solutions, but the lower components are obtained by enforcing the "free" relationship between upper and lower components and using the asymptotic momenta at the nucleon vertex. Note that these wave functions also lack the dynamical enhancement of the lower components.

Finally, one also has the dynamical quenching of the upper component of the Dirac wave function in the nuclear interior compared with the non-relativistic solution. This effect, associated with the Darwin term, is implicitly included in all calculations presented in this work. Hence the differences between the EMA-noSV approach (or equivalently the asymptotic projection) and the fully relativistic calculation can be solely ascribed to the negative-energy components.

6.2.3 Kinematical effects: semi-relativistic reductions

Another ingredient which leads to differences between the relativistic and non-relativistic approaches concerns the specific form of the current operator used to evaluate Eq. (6.3). Instead of the fully relativistic operator considered in RDWIA, truncated expressions up to first or higher orders in p/M_N, ω/M_N and/or q/M_N are employed in standard non-relativistic DWIA calculations. These effects, here referred to as kinematical relativistic effects [9, 10, 19], include not only the relativistic kinematics of the nucleon energies and momenta [16, 31] (which must be accounted for in order to describe properly the form of the momentum distribution), but also the effects linked to the use of the relativistic nucleon current operator.

Improved non-relativistic expansions of the nucleon current operator, denoted as semi-relativistic approaches, which contain important aspects of relativity, have been derived recently and are available in the literature [12–15]. In this paper we investigate the kinematical effects associated with these expansions in polarized $(\vec{e}, e'\vec{p})$ observables. To this

end we have also incorporated the semi-relativistic expressions in the relativistic code, so that a direct comparison between the fully relativistic calculation and the semi-relativistic approach becomes more meaningful because the effects due to the choice of wave functions and/or potentials are minimized.

To make the analysis clearer, in what follows we explain in some detail the procedure used to get the semi-relativistic results. In the case in which spinor distortion is neglected and asymptotic momenta are used, the relativistic (4×4) current matrix element can be recast in an equivalent form that involves an effective (2×2) current operator $\overline{J}^{\mu}_{eff}$ that occurs between the upper two component spin $\frac{1}{2}$ spinors. The (2×2) operator $\overline{J}^{\mu}_{eff}$ is obtained without any approximation concerning non-relativistic reductions; it corresponds to an exact expression for the on-shell electromagnetic current operator [15]. This means that the results obtained using $\overline{J}^{\mu}_{eff}$ between bispinors corresponding to the upper components of the relativistic wave functions should coincide exactly with those obtained using the original relativistic (4×4) electromagnetic current operator within the EMA-noSV approach [30]. Finally, a comparison between these results and those provided by making use of the semi-relativistic expressions for the operator, leads to direct information on the magnitude associated with the kinematical relativistic effects. It is important to point out that the semi-relativistic reduction is done in the context of the effective momentum approximation, *i.e.,* using asymptotic momenta.

The semi-relativistic (SR) expression of the electromagnetic current operator relies on the direct Pauli reduction method, by expanding only in the missing momentum (p) over the nucleon mass. The transfer energy and momentum are treated exactly. Up to first-order in p/M_N, the following results for the electromagnetic current operators are obtained:

$$\overline{J}^0 = \frac{\kappa}{\sqrt{\tau}}G_E + \frac{i}{\sqrt{1+\tau}}\left(G_M - \frac{G_E}{2}\right)(\boldsymbol{\kappa}\times\boldsymbol{\eta})\cdot\boldsymbol{\sigma}\,, \tag{6.11}$$

$$\begin{aligned}\overline{\boldsymbol{J}} &= \frac{1}{\sqrt{1+\tau}}\left\{iG_M(\boldsymbol{\sigma}\times\boldsymbol{\kappa}) + \left(G_E + \frac{\tau}{2}G_M\right)\boldsymbol{\eta} + G_E\boldsymbol{\kappa}\right.\\ &- \frac{G_M}{2(1+\tau)}(\boldsymbol{\kappa}\cdot\boldsymbol{\eta})\boldsymbol{\kappa} - \frac{iG_E}{2(1+\tau)}(\boldsymbol{\sigma}\times\boldsymbol{\kappa})\boldsymbol{\kappa}\cdot\boldsymbol{\eta}\\ &- \left. i\tau\left(G_M - \frac{G_E}{2}\right)(\boldsymbol{\sigma}\times\boldsymbol{\eta}) + \frac{i(G_M-G_E)}{2(1+\tau)}(\boldsymbol{\kappa}\times\boldsymbol{\eta})\boldsymbol{\sigma}\cdot\boldsymbol{\kappa}\right\}\,,\end{aligned} \tag{6.12}$$

where we have introduced the usual dimensionless variables: $\tau = |Q^2|/4M_N^2$, $\boldsymbol{\kappa} = \boldsymbol{q}/2M_N$ and $\boldsymbol{\eta} = \boldsymbol{p}/M_N$. Obviously, when computing response functions, evaluated by taking

bilinear combinations of the electromagnetic current matrix elements, terms of order η^2 should be dismissed.

As shown, the spin-orbit part of the charge and the relativistic correction to the transverse current, the first-order convective spin-orbit term, are included in Eqs. (6.11,6.12). Although the above expressions have been already presented in the literature [12–15, 31], in most of these previous works the analysis of the observables has been performed adopting additional approximations on the vector current, namely, $\overline{\boldsymbol{J}}$ is simply taken as the standard non-relativistic reduction except for a global kinematical factor $(1+\tau)^{-1/2}$ that includes relativistic corrections coming from the Dirac spinors (see [12–15] for details). Here we evaluate the recoil nucleon polarized observables by making use of the full SR currents in Eqs. (6.11,6.12) taken between the upper components of the original relativistic wave functions.

6.3 Results and discussion

In this section we analyze the recoil nucleon transferred polarization observables for proton knockout from ^{16}O. Although we focus on results for the $1p_{1/2}$ shell, similar conclusions are reached for the $1p_{3/2}$ and $1s_{1/2}$ shells unless otherwise specified. Results are computed for both CC1 and CC2 choices of the current operator in Eqs. (6.6,6.7), and the Coulomb gauge is assumed. A detailed study on gauge ambiguities in RPWIA has been presented in Ref. [18] showing that the Coulomb and Landau gauges lead to very similar results, differing significantly from the ones corresponding to the Weyl gauge. These results are proven to persist within the relativistic distorted approach. The bound nucleon wave function is obtained using the parameters of the set NLSH [32]. Results computed with other parameterizations are found to be similar and do not change the general conclusions. For the outgoing nucleon wave function, we use the energy-dependent, A-independent potential derived by Clark *et al.* for ^{16}O (EDAIO) [33] which describes fairly well the existing elastic proton-^{16}O scattering data. Although our main interest in this work concerns the effects introduced by dynamical and kinematical relativistic effects, a brief study of the sensitivity of the polarized observables to the description of final-state interactions is also presented. Hence in next section, results evaluated with different relativistic optical potentials are shown and compared. Finally, the Coulomb distortion of the electron wave functions is accounted for by using the effective momentum approximation with the nuclear Coulomb potential equal to 3.5 MeV (see [6, 7] for details). All the results

shown throughout this work correspond to the nucleon form factor parameterization of Gari and Krumplemann [34].

6.3.1 Final-State Interactions: relativistic optical potentials

We start our discussion with the analysis of the longitudinal and sideways transferred polarization asymmetries and their dependence on FSI. In Fig. 6.1, P'_l and P'_s are presented as functions of the missing momentum p. The kinematics are chosen with (q,ω) constant, $q = 1$ GeV/c and $\omega = 439$ MeV, yielding $|Q^2| = 0.8$ (GeV/c)^2. This roughly corresponds to the experimental conditions of experiments E89-003 and E89-033 performed at JLab [35–37]. Left panels correspond to the $p_{1/2}$ shell and right panels to $p_{3/2}$. In each case, RDWIA results obtained with the EDAIO optical potential parameterization [33] are compared with the RPWIA results. Plane wave calculations after projecting out the negative-energy components of the bound nucleon wave function, denoted as PWIA, are also shown. Note that PWIA polarization transfer asymmetries coincides with what one would obtain using free Dirac spinors wave functions for both nucleons in Eq. (6.3). The electron beam energy has been fixed to $\varepsilon_{beam} = 2.445$ GeV which corresponds to an electron scattering angle $\theta_e = 23.4^\circ$ (forward scattering).

First note the difference between the RPWIA calculations (dot-dashed lines) and the RDWIA results (solid lines). For low missing momentum values $p \lesssim 200$ MeV/c, the effects of FSI do not modify substantially the behaviour of the polarization asymmetries, particularly for P'_l. However, in the case of P'_s, the difference is of the order of 20–25% for $p \simeq 100$ MeV/c which corresponds to the momentum where the responses reach their maxima for the $p_{1/2}$ shell. Similar comments also apply to the results obtained for the $p_{3/2}$ and $s_{1/2}$ shells, although in these cases a smaller effect of FSI is observed for P'_s. It is important to point out that FSI lead to a significant reduction of the individual response functions: ∼50–60% ($R_l^{TL'}$) and ∼25% ($R_s^{TL'}$ and $R_l^{T'}$) at $p \simeq 100$ MeV/c. The response $R_s^{T'}$ is very small and its contribution to the transferred polarization is hardly visible. Hence, the results in Fig. 6.1 clearly indicate that for low p-values, FSI effects are partially cancelled when constructing the transferred polarization asymmetries. Note also that, for these low-p values, the PWIA approach is more in accord with the RDWIA. This means that in RPWIA the role of dynamical relativity stands out more clearly.

For high missing momentum, $p \gtrsim 200$ MeV/c, FSI strongly modify the behaviour of the polarizations, which is in accord with the peculiar sensitivity to the interaction pre-

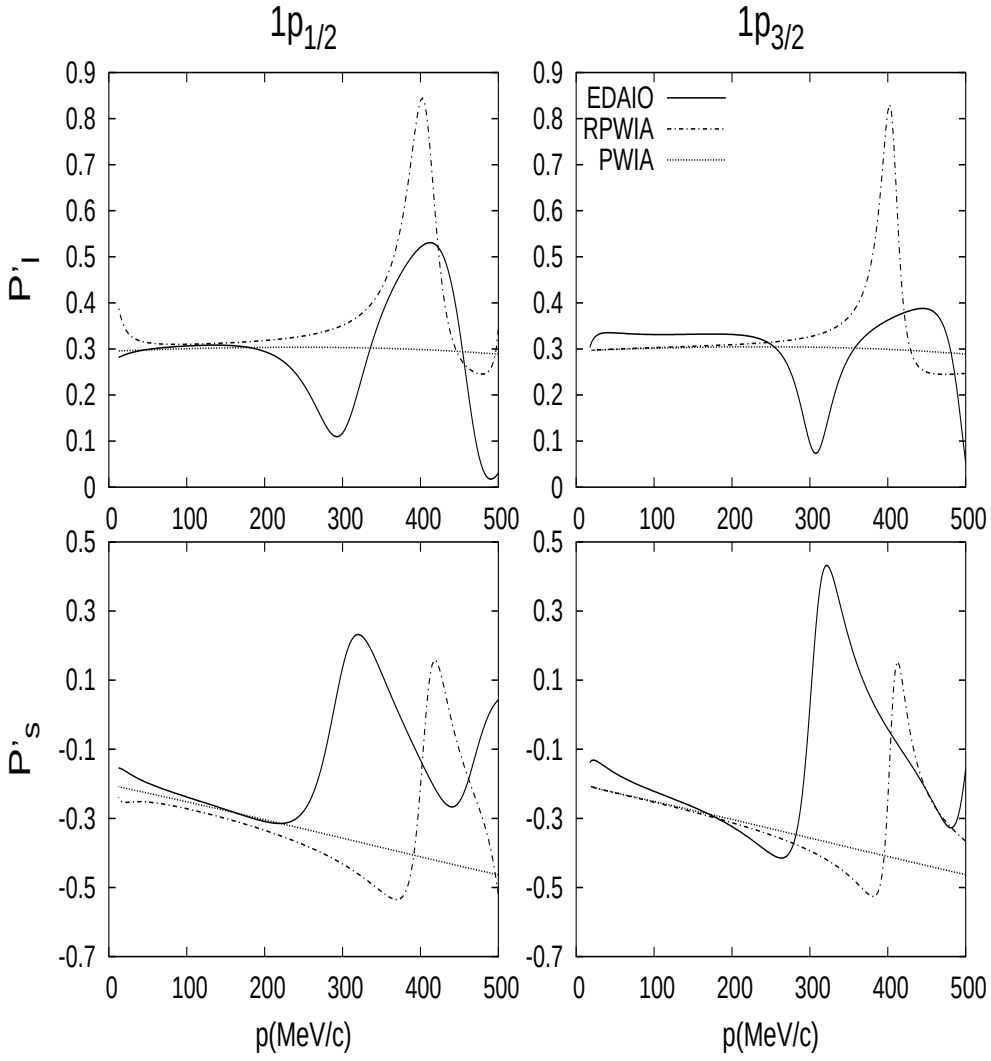

Figura 6.1: Transferred polarization asymmetries for the $p_{1/2}$ (left panels) and $p_{3/2}$ (right panels) shells in (q,ω)-constant kinematics (see text). Top and bottom panels correspond to the longitudinal and sideways components, respectively. RPWIA results (dot-dashed lines) are compared with RDWIA calculations using EDAIO (solid lines), and with the PWIA (dotted line) (see text for details). All calculations correspond to the CC2 current operator.

sented by each response function. When comparing RDWIA with RPWIA we see that the main effect is a global displacement to lower momenta of the polarization profiles. Let us recall that the oscillatory behaviour shown by P'_l and P'_s within RPWIA is a direct consequence of the dynamical enhancement of the lower components in the bound Dirac wave functions [18]; thus disappearing within PWIA. The oscillations are also present in the relativistic distorted wave calculations, although being very different from the RPWIA results with the maxima and minima located at different p-values. Let us note that the oscillatory behaviour of the polarization asymmetries persists even when non-relativistic distorted wave approaches are assumed (see [17, 27, 38]). This outcome emerges due to the fact that both FSI and dynamical relativistic effects cause a breakdown of factorization. A study of the later is presently in progress and the results will be presented in a forthcoming publication [39].

Let us next focus on the analysis of the uncertainties introduced by different relativistic optical potentials. In Fig. 6.2 we present the transferred ratios P'_l and P'_s for the $p_{1/2}$ shell evaluated using three different relativistic optical potential parameterizations: EDAIO, EDAD1 and EDAD2 [33]. Results with EDAD3 parameterization are practically identical to those obtained with EDAD1 and therefore have not been plotted. The left panels refer to calculations involving the CC1 current operator and right panels to CC2. As pointed out in previous papers [17, 21, 27, 30], transferred polarization asymmetries are expected to be relatively insensitive to the choice of optical potential at low missing momenta. This can be seen in Fig. 6.2, at least up to $p = 150$ MeV/c which is where the cross section reaches its maximum value [37]. This trend is also followed in the other two shells, $p_{3/2}$ and $s_{1/2}$.

However, as shown in Fig. 6.2, P'_l exhibits a strong dependence on the optical potential parametrization, resulting in important differences for larger values of the missing momentum: $\sim$20% (CC1) and $\sim$40% (CC2) for $p \simeq 250$ MeV/c. Note that in this kinematical region the cross section [37] has already decreased by almost two orders of magnitude with regards to the maximum, making measurements of transferred polarization responses very difficult. This result contrasts with non-relativistic (NR) and semirelativistic (SR) approaches where the effects introduced by different non-relativistic optical potentials are small [17]. Note also that the current operator choice, CC1 versus CC2, gives rise to very significant differences in P'_l within this p-region, being of the same order as those introduced by the optical potentials. Only for high p-values, $p \gtrsim 350$ MeV/c, is the uncertainty associated with FSI larger than that due to the choice of current operator. In the case of

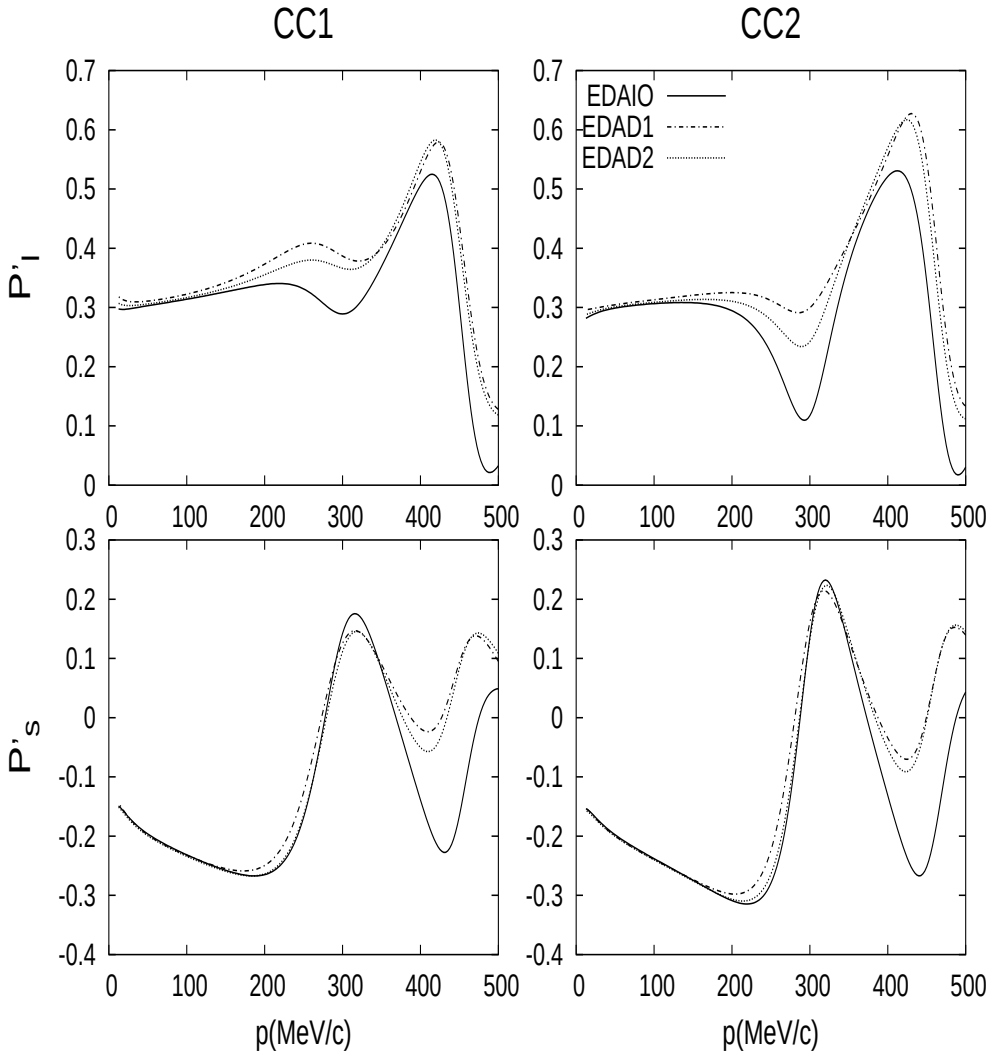

Figura 6.2: Transferred polarization asymmetries for the $p_{1/2}$ shell in (q,ω)-constant kinematics. Top and bottom panels correspond to the longitudinal and sideways components, respectively. Right panels refer to results obtained with the CC2 current operator and left ones to the CC1 current. RDWIA calculations using EDAIO (solid lines), EDAD1 (dot-dashed lines) and EDAD2 (dotted lines) optical potential parameterizations are compared.

the sideways polarization P'_s, in general less dependence on the interaction model as well as on the current is seen, which is more in accord with non-relativistic analyses. Finally, notice that for very high momentum values $p \gtrsim 400$ MeV/c, P'_l and P'_s evaluated with the EDAIO potential deviate from the results corresponding to the EDAD1 and EDAD2 parameterizations.

To end with this discussion, we conclude that both transferred polarization asymmetries at moderate p values ($p \simeq 100$ MeV/c) are independent of the optical potential choice. Increasing p from here, each optical potential starts to follow a different curve especially in the case of P'_l. For very high p ($p \gtrsim 350$ MeV/c), both transferred polarizations present large sensitivity to the choice of optical potential. However, caution should be placed on drawing general conclusions from the results given here in this kinematical region because other ingredients beyond the impulse approximation, such as meson exchange currents (MEC), Δ-isobar, short-range correlations, *etc.,* may also play a crucial role.

6.3.2 Dynamical relativistic effects

This section, which constitutes the main focus of the present work, is devoted to the analysis of dynamical relativistic effects for nucleon polarized observables within the framework of the RDWIA. With this aim we present in Fig. 6.3 the longitudinal and sideways transferred polarization asymmetries for the three shells involved in ^{16}O: $p_{1/2}$, $p_{3/2}$ and $s_{1/2}$. All of the results have been obtained using the EDAIO optical potential parameterization [33], and the choice of kinematics is the same as in the previous figures. To make explicit the effects introduced by spinor distortion, in each graph we compare the fully relativistic calculations (solid lines) using both current operators, CC1 (thin lines) and CC2 (thick lines), with the results after projecting out the negative-energy components (see Eqs. (6.9,6.10)) (dashed lines). Finally we also present for reference the results corresponding to the EMA-noSV approach evaluated with the CC2 current operator (dot-dashed line). Within EMA-noSV, the results provided by the two current operators are very similar, differing only due to the off-shell kinematical quantities involved in the operator [19, 28].

A detailed analysis of the transferred polarizations within the relativistic plane wave approach was presented in [18]. In said reference, it is shown that the dynamical enhancement of the lower components in the bound nucleon wave function leads to strong oscillations in $P'_{l,s}$ for high missing momentum values, $p \geq 300$ MeV/c. This behaviour

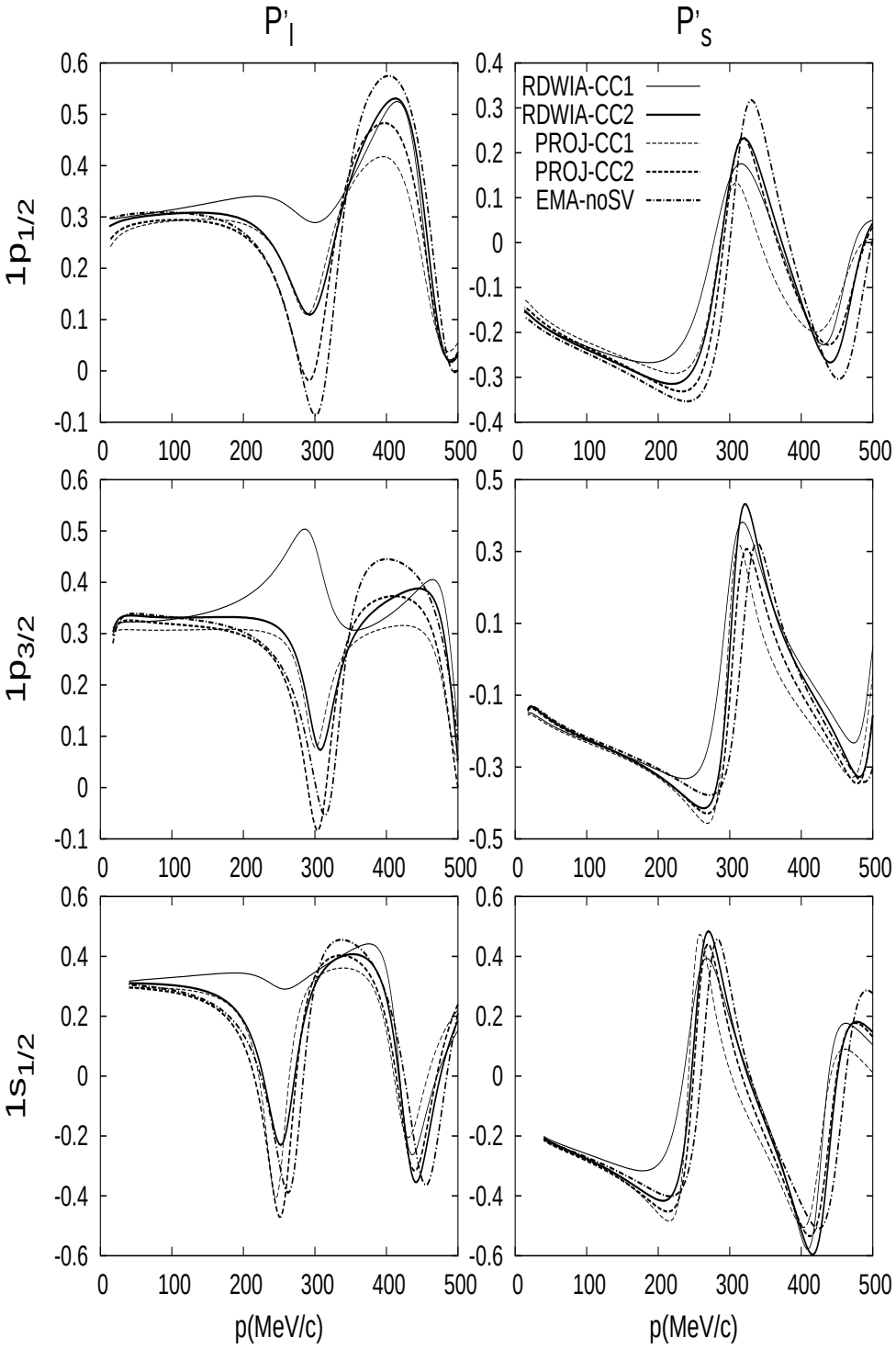

Figura 6.3: Same observables as in Fig. 6.1. Right panels correspond to P'_s and left ones to P'_l. On top, middle and bottom panels, results for the $1p_{1/2}$, $1p_{3/2}$ and $1s_{1/2}$ shells are plotted, respectively. In each graph, RDWIA calculations evaluated with EDAIO (solid line) are compared with positive-energy projection results (dashed line) and EMA-noSV approach (dot-dashed line). Thick lines correspond to the CC2 current operator and thin lines to CC1.

disappears after projecting out the negative-energy components. From the results shown in Fig. 6.3, it is clear that, within the relativistic distorted wave approximation, the oscillatory behaviour in the polarization asymmetries persists even after projecting the bound and scattered proton wave functions over positive-energy states. The same comment applies to the EMA-noSV approach. On the contrary, this last fact is not applicable to the behaviour shown by the left-right asymmetry A_{TL} [9,10], defined as the difference of unpolarized cross sections evaluated at $\phi = 0^\circ$ and $\phi = 180^\circ$ divided by their sum. These results are connected with the interplay between polarization degrees of freedom and dynamical relativistic effects. Whereas in RPWIA, projecting out the negative-energy components of the bound nucleon wave function leads to factorization, hence destroying the oscillatory behaviour in $P'_{l,s}$, in RDWIA factorization breaks down even after projection over positive-energy components.

From inspection of Fig. 6.3, and in accord with previous results for unpolarized observables [9, 10, 28] and polarized ones in RPWIA [18], we note that dynamical relativistic effects are maximized for the CC1 current operator. This applies to both polarization ratios and the three shells considered. Particularly noteworthy is the behaviour displayed by P'_l even at intermediate p-values in the case of the fully relativistic CC1 calculation. This result deviates significantly from the others, modifying even the global shape of the observable. This contrasts with the situation for P'_s where, apart from the specific discrepancies introduced by relativity, the five calculations follow the same general oscillatory pattern. Hence it would be interesting to investigate further this intermediate p-region where new high quality data on P'_l could make it possible to constrain the theoretical choices for current operator.

As shown in [9, 28], the contribution from the negative-energy components to the current are of the same order as the positive-energy ones with the CC2 operator, whereas with the CC1 choice the negative-energy terms may become much larger. This explains the much wider spread shown by the CC1 results, particularly the large effects introduced by the dynamical enhancement of the lower components in P'_l. As we will show later, this emerges from the polarized responses that enter in the longitudinal polarization in contrast with the sideways case. Note also that the CC1 projected calculations get closer to the CC2 ones and to the EMA-noSV approach. This may indicate that the CC1 current emphasizes the role played by the lower components in the wave functions, agreeing with the findings for unpolarized responses [10]. Precise comparisons with data would yield definite conclusions on the reliability of the various approximations.

Finally, it is also interesting to compare the effects arising from dynamical relativity with those due to FSI models. As shown in Figs. 6.1– 6.3, P_l' presents the strongest sensitivity to both kinds of effects for intermediate p-values, $200 \leq p \leq 350$ MeV/c. This can make it difficult to isolate the role played by each ingredient when compared with data; however, note that the important deviation between the results obtained with the two currents tends to persist, no matter which optical potential is used. Hence, precise measurements of P_l' in this p-region, in conjunction with P_s' data, may give us important clues to constrain final-state interactions and the choice of current operator.

To complete the analysis of dynamical relativistic effects, we focus on the four separate responses that contribute when the polarization of the outgoing nucleon is measured and the electron beam is polarized: $R_l^{T'}$, $R_l^{TL'}$, $R_s^{T'}$ and $R_s^{TL'}$ ($R_n^{TL'}$ does not enter for coplanar kinematics). Results are shown in Fig. 6.4 for proton knockout in ^{16}O from the $p_{1/2}$ shell. Let us recall that Coulomb distortion of the electron waves breaks the simplicity of Eq. (6.2), leading to responses which also depend on the electron kinematic variables. However, the effective momentum approximation for the electrons adopted in this work makes Eq. (6.2) reliable when analyzing the response functions. For ^{16}O we have proven [10] that Coulomb distortion effects, and consequently the dependence of the responses with θ_e, are very small.

As a general rule we observe that $R_s^{T'}$ and $R_l^{TL'}$ show the highest sensitivity to relativistic dynamics, while the uncertainties in $R_l^{T'}$ and $R_s^{TL'}$ are much smaller. This coincides with the analysis already performed in RPWIA [18] and, although not shown here for simplicity, applies also to the $p_{3/2}$ and $s_{1/2}$ shells. In addition, Gordon ambiguities are also significantly enhanced for $R_s^{T'}$ and $R_l^{TL'}$. Finally, note that the largest spread due to relativistic dynamical effects arises for the CC1 current operator, which is in accord with RPWIA results [18], and can be traced back to the strong influence of the negative-energy projections of the wave functions in this case.

Let us study in more detail each individual response. As shown in Fig. 6.4, the contributions of $R_l^{T'}$ and $R_s^{TL'}$ are rather similar, and moreover, the EMA-noSV predictions almost coincide (evaluated at the maxima) with the fully relativistic calculations, the largest difference being of the order of 3.6% for the CC1 current in $R_s^{TL'}$. Positive-energy projected results also follow the RDWIA curves closely, although sizeable differences are observed for the CC1 current, particularly in the case of $R_l^{T'}$ ($\sim$11% at the maximum).

Concerning $R_l^{TL'}$, we observe that the projected calculations differ substantially from the RDWIA results, especially for the CC1 current operator. This resembles the large

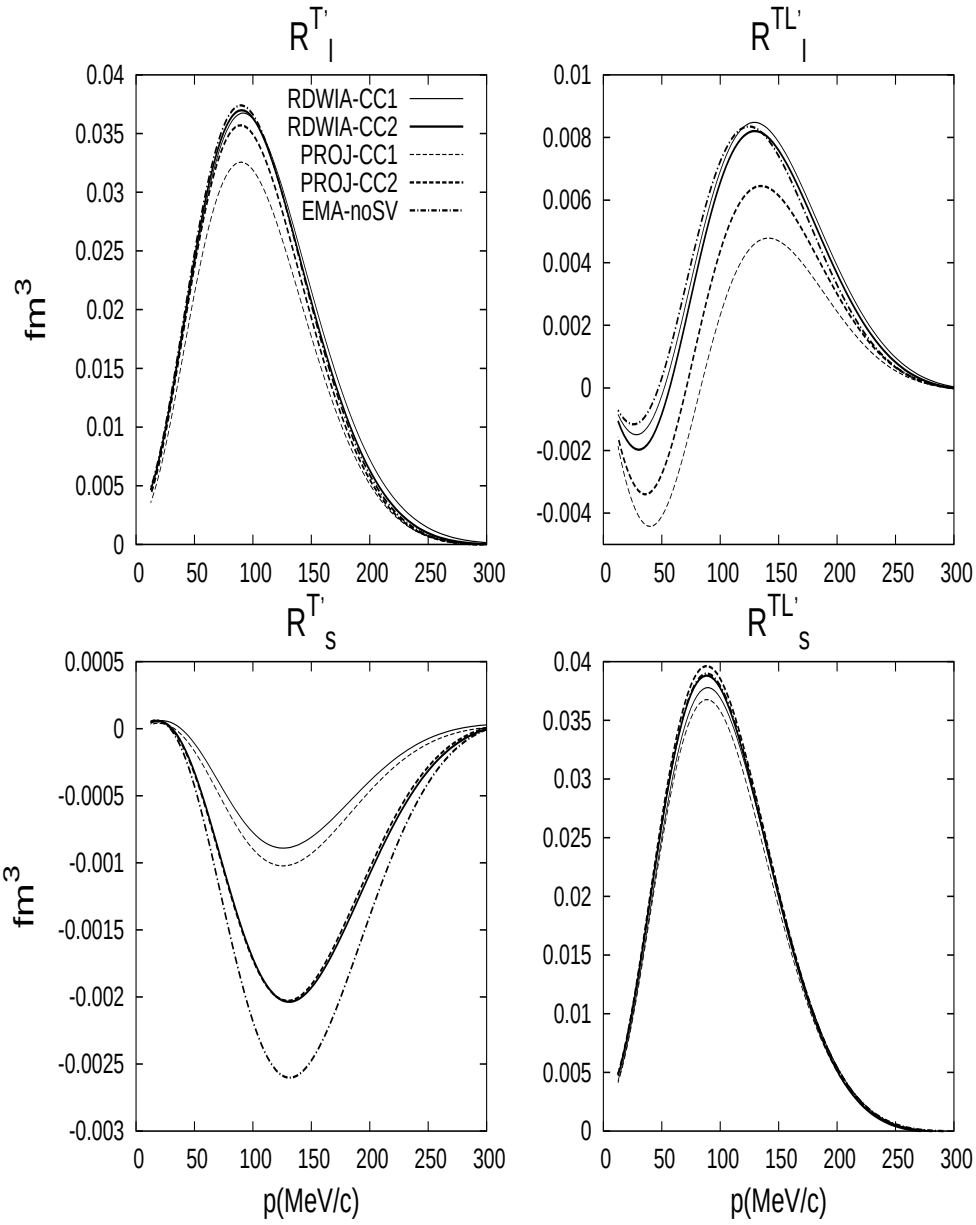

Figura 6.4: Transferred polarized responses for the $1p_{1/2}$ shell. Same kinematics as in previous figures, and the labelling as in Fig. 6.2.

relativistic dynamical effects shown by this response in RPWIA [18]. On the contrary, it is interesting to note that different choices of the current operator within RDWIA lead to very similar results, which is somewhat opposed to the situation observed in the plane wave limit [18]. Finally, the EMA-noSV approach provides a description of $R_l^{TL'}$ that basically coincides with the two RDWIA calculations, the largest difference being observed at very low-p values. In fact, this result is proven to be valid only at $q = 1$ GeV/c, where the effective momentum approach (EMA) applied to the bound wave function, leads to effects which cancel almost exactly those coming from the ejected nucleon. For lower values of q this cancellation does not occur, and so an important discrepancy between the EMA-noSV prediction and the RDWIA calculations emerges.

The smallest $R_s^{T'}$ response presents a large dependence on the current operator choice. This applies to the full RDWIA calculation as well as to the positive-energy projected approach. Note, however, that the difference between RDWIA and projected results is tiny, almost negligible for the CC2 current. Contrary to $R_l^{TL'}$ case, the EMA-noSV approach for $R_s^{T'}$ deviates significantly from the fully relativistic and projected results, the uncertainty spread (significantly enhanced for the CC1 current) being even larger than that obtained in RPWIA [18]. We should also recall that $R_s^{T'}$ is strongly affected by the choice of the optical potential (results corresponding to the parameterizations EDAIO and EDAD2 are very different from those for EDAD1 and EDAD3). Although not shown in the figure, it is also important to point out that at low q ($q \leq 350$ MeV/c), the projection over positive-energies in the bound nucleon wave function clearly dominates, while at higher q, the reverse occurs. This result contrasts with the behaviour seen for the unpolarized observables and also with the other three polarized responses, where for high enough transfer momentum projecting out the negative-energy components in the ejected nucleon wave function is proven not to alter the fully relativistic predictions.

The behaviours presented by the four polarized responses, their relative contributions and their sensitivity to dynamical relativistic effects, give us important clues to understanding the results obtained for the longitudinal and sideways transferred polarization asymmetries. The large effects introduced by relativity in P_l', particularly when comparing full relativistic and projected calculations for CC1, can be traced back to the similar contributions given by the two responses, $R_l^{T'}$ and $R_l^{TL'}$, that enter in P_l'. Although relativistic dynamics affect $R_l^{TL'}$ more, their effect on $R_l^{T'}$ is also sizeable. The case of P_s' is clearly different. Here the two polarized responses involved contribute very differently, $R_s^{T'}$ being much smaller (more than one order of magnitude). Therefore, the asymmetry P_s'

is almost given uniquely by $R_s^{TL'}$, whose uncertainty due to dynamical relativistic effects presents the lowest spread. Although results for $p_{3/2}$ and $s_{1/2}$ show basically similar behaviour to those of the $p_{1/2}$ shell, off-shell and dynamical relativity play a less significant role for the $p_{3/2}$ shell in $R_s^{T'}$ and $R_l^{TL'}$.

As already mentioned, in RDWIA spinor distortion affects both the bound and ejected nucleon wave functions. Hence in what follows, we analyze the role of dynamical relativity, isolating the spinor distortion contribution in each nucleon wave function separately. We show results for the ratios $P'_{l,s}$ and the left-right asymmetry A_{TL}, focusing on the CC2 current, which minimizes dynamical effects, and the $p_{1/2}$ shell. Results for $p_{3/2}$ and $s_{1/2}$ follow the same general trends, but with a significant reduction of the effects due to relativistic dynamics. In Fig. 6.5 we show the observables for three values of the momentum transfer q. In each case, quasiperpendicular kinematics (q, ω constant) have been selected, and RDWIA and projected calculations are compared. Within the projected results, we distinguish the EMA-noSV approach, where negative-energy components of the bound and scattered nucleon wave functions have been projected out, from the results where the projection over positive-energy components affects only one of the nucleon wave functions: bound (referred to as EMAb) and ejected (EMAf).

From inspection of Fig. 6.5, a clear difference emerges in the behaviour observed for A_{TL} and the polarized ratios $P'_{l,s}$. The asymmetry A_{TL} presents a well established pattern: for low-medium p-values the largest effect shows up when projection over positive-energy states in the bound nucleon wave function is assumed (a consequence of the dominance of the direct term in the reaction mechanism for low-p). On the contrary, for high-p ($p \geq 250, 300$ MeV/c), the separate influence of each nucleon wave function depends very much on q. At very low-q the most sizeable effects correspond to projection of the ejectile wave function state. However, as q increases so does the ejected nucleon momentum p_F; thus FSI effects are expected to be smaller and consequently the contributions of the negative-energy states in the ejected nucleon play a minor role. As noted, the results for $P'_{l,s}$ do not match this general behaviour, and it is hard to state which nucleon wave function plays the major role concerning relativistic dynamical effects.

Finally, a basic difference between A_{TL} and $P'_{l,s}$ connects with the oscillatory behaviour shown by these observables. While it remains in $P'_{l,s}$ for all q-values and all approaches, in the case of A_{TL}, the oscillations disappear when projection is assumed. This effect, connected with factorization breakdown, is analyzed in [39].

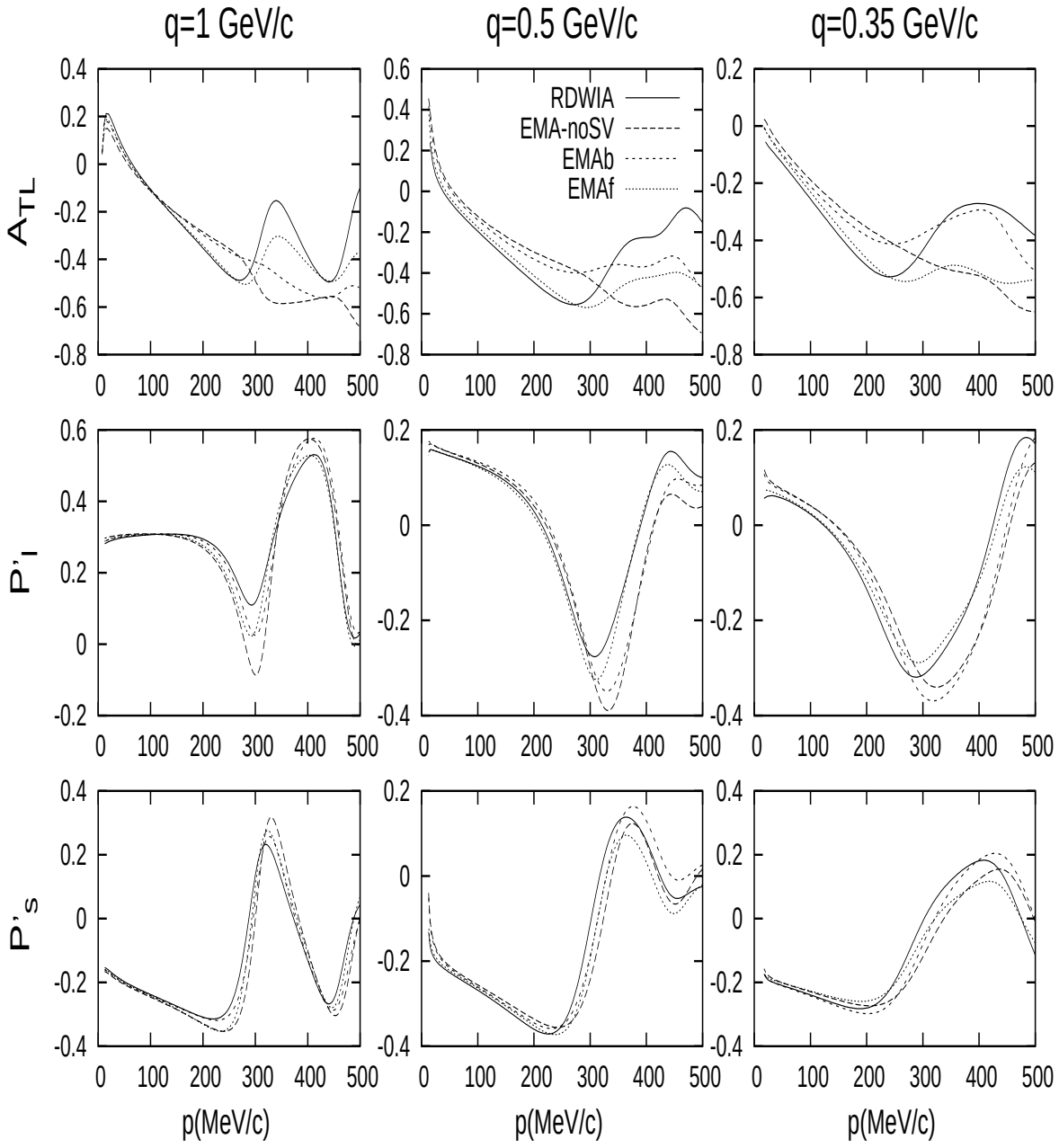

Figura 6.5: Left-right asymmetry A_{TL} (top panels) and transferred polarized ratios, P'_l (middle panels) and P'_s (bottom panels) for proton knockout from ^{16}O for the $p_{1/2}$ shell. Results correspond to (q,ω)-constant kinematics with $q = 0.35$ GeV/c (right panels), $q = 0.5$ GeV/c (middle panels) and $q = 1$ GeV/c (left panels). In each case the transfer energy ω is fixed to the quasielastic peak value. RDWIA calculations (solid line) are compared with the EMA-noSV approach (dashed line) and with the results after projecting over positive-energy states for the bound nucleon wave function only (short-dashed line) and for the ejected nucleon only (dotted line).

6.3.3 Semirelativistic reductions

In this section we focus on the kinematical relativistic effects, *i.e.,* effects associated with the non-relativistic reduction of the nucleon current operator. In Fig. 6.6 we present the polarization ratios and TL asymmetry for the $p_{1/2}$ shell and same kinematics as in Fig. 6.1. We compare the RDWIA results (solid line) with the EMA-noSV (dotted line) and semi-relativistic approaches. For the latter we distinguish the following: SR (dot-dashed line), corresponding to the expressions in Eqs. (6.11,6.12), and Nonrel (dashed line) where additional approximations on the vector current have been assumed (see Sec. 6.2.3 and Refs. [14, 31] for details). As shown, the semi-relativistic curves follow the shape of the EMA-noSV ones, particularly for A_{TL} where oscillations are largely supressed within EMA-noSV and semi-relativistic approaches. Kinematical effects are observed by comparing EMA-noSV and SR calculations. As expected, they are very small in the low-p region, increasing for high missing momenta. This same general pattern emerges for other transfer momentum values and similar conclusions hold for the $p_{3/2}$ and $s_{1/2}$ shells.

To complete the analysis of kinematical effects we study the individual responses. First, let us consider the unpolarized ones, which are presented in Fig. 6.7 (top panels) for the $p_{1/2}$ shell and CC2 current operator. The labelling of the curves is as in previous figure. We observe that the pure longitudinal and transverse responses, R^L and R^T, hardly show any dependence on either kinematical or dynamical relativistic effects. This coincides with some previous findings [9, 10], but clearly disagrees with the results obtained by Meucci and collaborators [27], who found very different results for R^T using relativistic and non-relativistic approximations. Concerning R^{TL}, it shows a significant dependence with relativistic nucleon dynamics. This is in accord with our previous analyses [9,28], and also with the results of the Pavia group [27], although in this latter case, the behaviour found for R^{TL} within the RDWIA calculation, clearly differs from ours for very low missing momentum. Moreover, notice that the difference between EMA-noSV, SR and Nonrel is negligible. Finally, the response R^{TT} also shows a high sensitivity to both dynamical and kinematical relativistic ingredients, though its smallness makes it difficult to isolate from cross section measurements. Let us also recall that our results do not match those obtained by the Pavia group, particularly for high q-values.

Focusing on the transferred polarized responses (bottom panels of Fig. 6.7), we observe that relativistic ingredients play a very minor role in $R_s^{TL'}$ and $R_l^{T'}$. On the contrary, dynamical relativitic effects are sizeable for $R_l^{TL'}$ and especially for $R_s^{T'}$, while the kinematical relativistic effects are strongly cancelled. Notice that the EMA-noSV and semi-

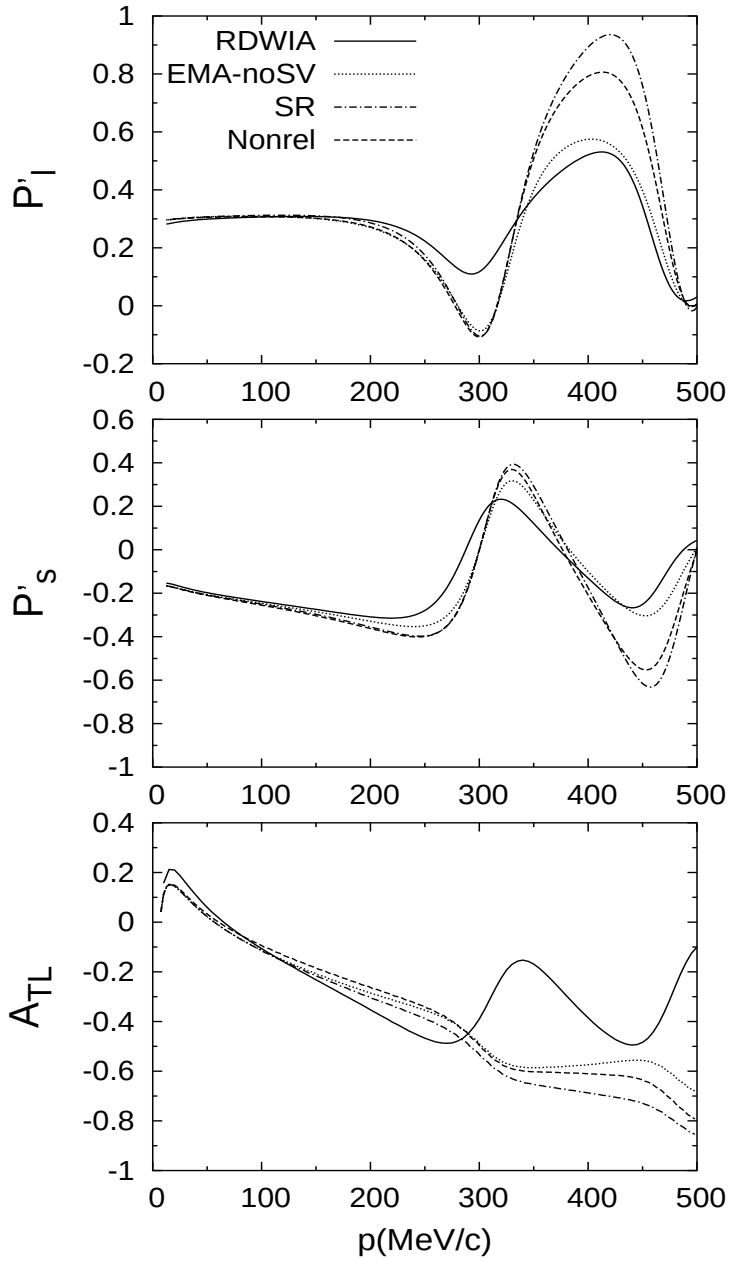

Figura 6.6: Transferred polarizations P'_l (top panel) and P'_s (middle panel), and A_{TL} asymmetry (bottom panel) for proton knockout from the $p_{1/2}$ shell in ^{16}O. Results correspond to the RDWIA calculation with the CC2 current operator (solid line), the EMA-noSV approach (dotted line), the semi-relativistic (SR) current given in Eqs. (6.11,6.12) (dot-dashed line) and the Nonrel approach (dashed line) (see text for details). All curves have been obtained using the EDAIO optical potential.

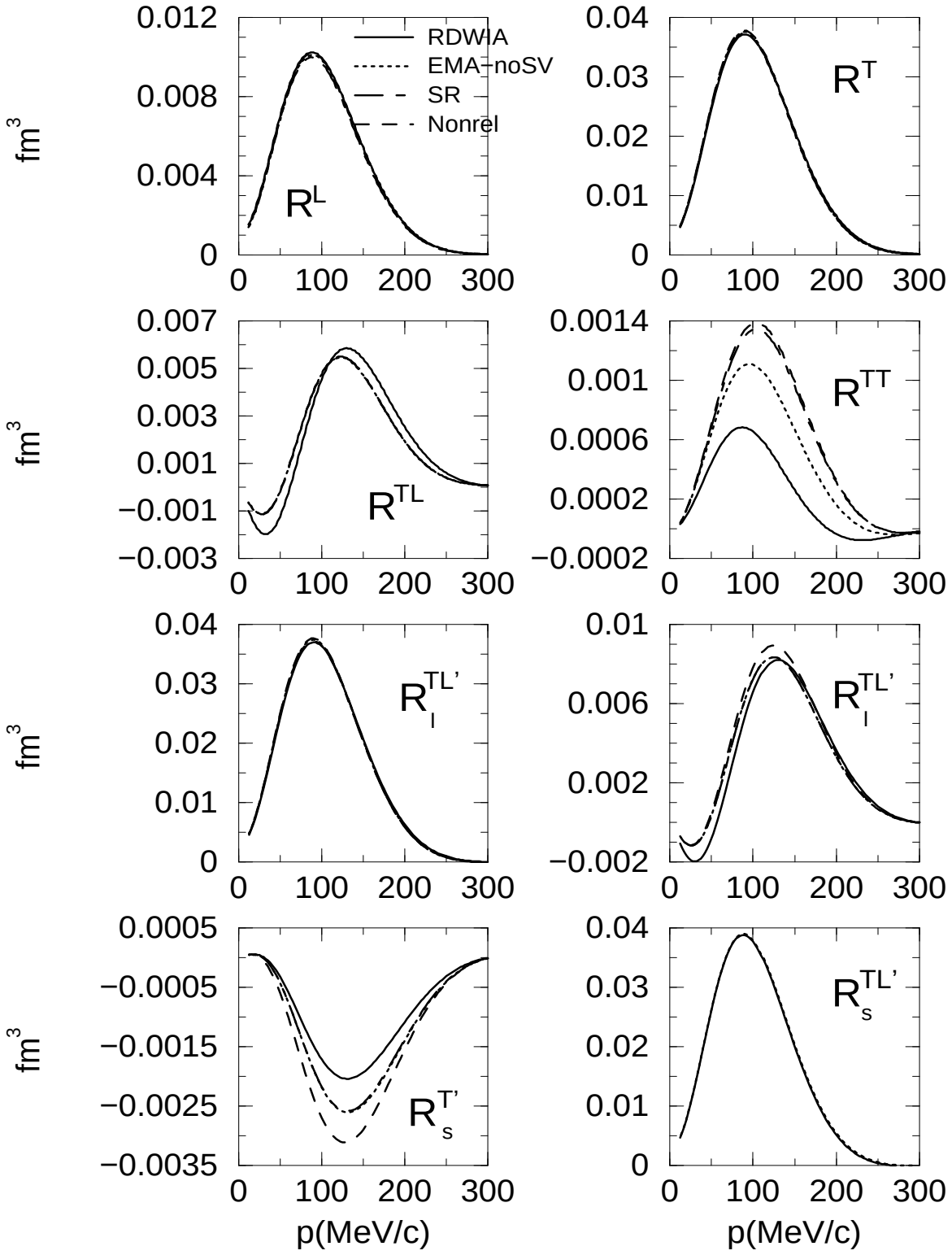

Figura 6.7: Unpolarized (top panels) and recoil nucleon polarized (bottom panels) responses for proton knockout from the $p_{1/2}$ shell in ^{16}O. Kinematics as in Fig. 6.1 and the same labelling as in Fig. 6.6.

relativistic approaches give rise to almost identical results. Additional restrictions on the non-relativistic procedure to get the current operator [12–14, 31] (Nonrel approach) leads to more visible effects which increase when the transferred energy goes up.

6.3.4 Comparison with experimental data

We proceed to compare our calculations with the experimental data recently measured at JLab [1]. The kinematics of the experiment was the same as used in previous figures except that the azimuthal angle was $\phi = 180°$ instead of $\phi = 0°$. As shown later, this makes an important difference concerning the effects introduced by relativistic dynamics and/or optical potentials. Fig. 6.8 shows P'_l (top panels), P'_t (middle panels) and the ratio P'_t/P'_l (bottom panels) for proton knockout in ^{16}O from the $1p_{1/2}$ (left panels), $1p_{3/2}$ (middle panels) and $1s_{1/2}$ (right panels) shells. Note the change of notation for the transverse polarization transfer observable. In reference [1], and only for $\phi = 180°$, the vector perpendicular to the plane containing $\boldsymbol{p}_F$ and the transfer momentum $\boldsymbol{q}$, is chosen in the opposite direction that we have made in this paper. Consequently there is also a change of sign in the transverse vector. In order to present the experimental data taken in [1] in the same form as in the original paper, we have prefered to show our curves for P'_t polarization in Fig. 6.8. P'_t is equal to P'_s for $\phi = 0°$ and differs only in a sign with P'_s when $\phi = 180°$. Curves corresponding to RDWIA, positive-energy projected and EMA-noSV calculations are presented. The labelling is as in Fig. 6.3, and all of the results have been obtained using the EDAIO potential.

To make explicit the differences between $\phi = 0°$ (kinematics assumed in the previous figures) and $\phi = 180°$ (kinematics of the experiment), in each graph we present the polarized observables as functions of the missing momentum, whose range goes from -300 MeV/c to $+300$ MeV/c. Positive p-values refer to $\phi = 180°$, where the two experimental data are located, and negative ones to $\phi = 0°$.

As shown in Fig. 6.8, all theoretical calculations satisfactorily reproduce the data, improving somehow the general agreement compared with previous SR analyses [17]. However, it is hard to draw specific conclusions concerning the reliability of the various approaches within this low-p region. For higher p, relativistic dynamics, off-shell effects and FSI start to play an important role. In this sense, from inspection of Fig. 6.8, it is interesting to point out that choosing $\phi = 0°$ clearly enhances dynamical relativistic effects for P'_l at intermediate p-values, $p \simeq 200 - 300$ MeV/c. The same comment applies

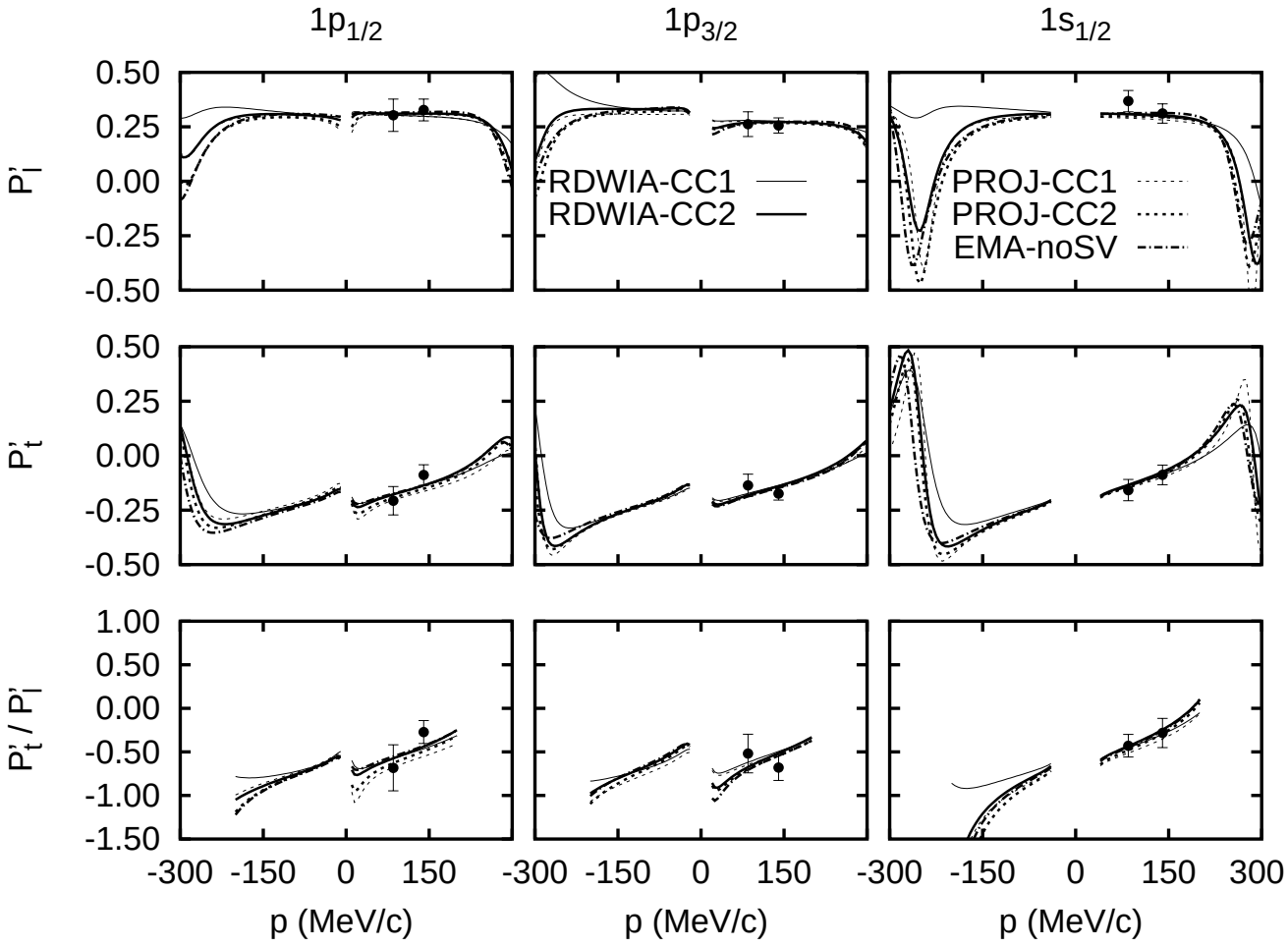

Figura 6.8: Transferred polarizations P'_l, P'_t and the ratio P'_t/P'_l compared with experimental data. Positive (negative) p-values refer to $\phi = 180°$ ($0°$). The labelling of the curves is as in Fig. 6.3. Left, middle and right panels correspond to $p_{1/2}$, $p_{3/2}$ and $s_{1/2}$ shells, respectively.

to off-shell and FSI effects. Hence, high quality P_l' data measured for coplanar, $\phi = 0^\circ$ kinematics at intermediate p-values can provide precise information to constrain the theoretical models. In the case of P_t', dynamical uncertainties (also off-shell and FSI effects) are shown to be rather similar for both coplanar $\phi = 0^\circ$ and 180° kinematics.

6.3.5 Effects of medium modified form factors

To finish, we present a brief analysis of the effects introduced by possible changes in the nucleon form factors in the nuclear medium. We limit our attention to the same kinematics as in previous sections. A more exhaustive analysis ranging over different Q^2 values, where the models predict different sensitivity to in-medium effects, will be presented in a forthcoming publication.

The procedure we have used to include these effects in our calculations is as follows. We have taken density-dependent form factors as predicted by the quark-meson coupling model (QMC) [40], computed for a bag radius of 0.8 fm. In order to get well behaved modified form factors in the free case, we have scaled the ones parametrized by Gari and Krumplemann [34] (labelled as GK) with the ratio between the QMC form factors at a given density and those predicted for free conditions,

$$G_{E,M}(Q^2, \rho(\boldsymbol{r})) = G_{E,M}^{GK}(Q^2) \frac{G_{E,M}^{QMC}(Q^2, \rho(\boldsymbol{r}))}{G_{E,M}^{QMC}(Q^2, 0)}, \tag{6.13}$$

where $G_{E,M}^{QMC}(Q^2, \rho(\boldsymbol{r}))$ are the density-dependent Sachs form factors of the proton immersed in nuclear matter with local baryon density $\rho(\boldsymbol{r})$. By analogy with the free case, we define density-dependent Dirac and Pauli form factors related to $G_{E,M}(Q^2, \rho(\boldsymbol{r}))$. Finally, we compute the current matrix elements in coordinate space by introducing these modified form factors into Eqs. (6.6) and (6.7), evaluated for the corresponding local density in ^{16}O.

The results obtained for the ratio of transferred polarization asymmetries are presented in Fig. 6.9 for both current operators. Only the $\phi = 180^\circ$ region, where data have been measured, is analysed. As in the previous section, we plot P_t'/P_l' instead of P_s'/P_l'. The upper, middle and bottom panels correspond to $1p_{1/2}$, $1p_{3/2}$ and $1s_{1/2}$ knockout, respectively. For completeness, in the right panels of Fig. 6.9 we also present the uncertainties due to the choice of the optical potential parametrization. As shown, for the p shells our model dependence due to the description of FSI is very small in the region $75 \leq p \leq 175$ MeV/c ($p \leq 100 - 125$ MeV/c for $1s_{1/2}$), starting to increase for higher p. Within this

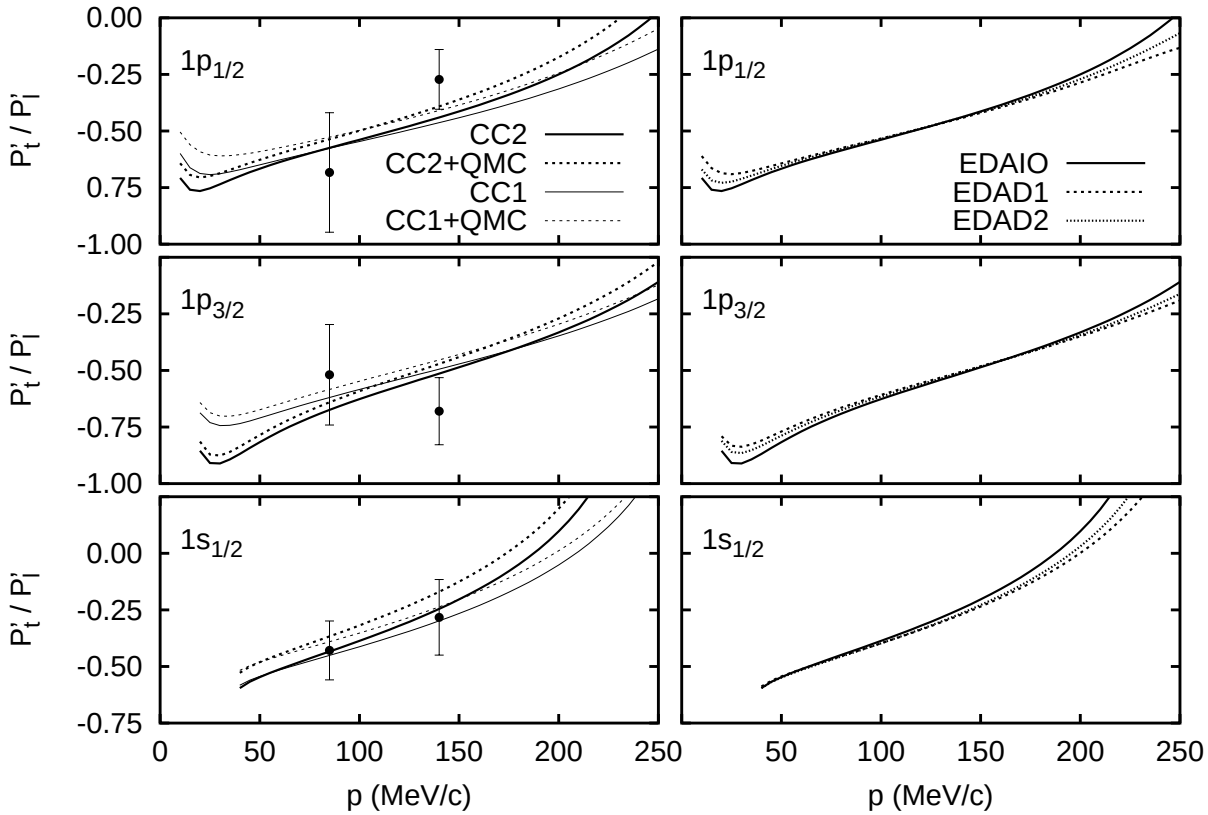

Figura 6.9: Effects of medium modified form factors (left panels) and FSI uncertainties (right panels) on the transferred polarization ratio P'_t/P'_l. Results correspond to $\phi = 180°$. Upper, middle and bottom panels represent the results for $1p_{1/2}$, $1p_{3/2}$ and $1s_{1/2}$, respectively. For the left panels, the free (medium modified) results calculated by using the EDAIO optical potential are represented by solid (dashed) lines. Thick (thin) lines refer to the CC2 (CC1) results, respectively. For the right panels all of the curves have been obtained using CC2. Solid lines correspond to the EDAIO results, dashed lines to EDAD1 and dotted to EDAD2.

"safe" region, medium modification effects for the $p_{1/2}$ amount to $\sim 9\%$ ($\sim 7\%$) for the CC1 (CC2) operator at $p \simeq 100$ MeV/c. Note however that even when these effects are sizeable, the uncertainties introduced by the current operator choice can also be noticeable. The situation worsens for the $1p_{3/2}$ shell, for which the free and QMC calculations get mixed due to the off-shell uncertainties. The precision of the actual experimental data [1] does not allow one to state which specific calculation is preferred. However, more precise data, particularly in the region $100 \leq p \leq 175$ MeV/c for $p_{1/2}$, could help to constrain the theoretical model. In this sense, note that the QMC results differ more clearly from the free calculations in this shell.

For the $1s_{1/2}$, the effects of the medium are larger in the vecinity of $p = 100$ MeV/c ($\sim 18\%$ for CC2 and $\sim 15\%$ for CC1). Indeed, medium effects are expected to be more important for the inner orbits, due to their higher average densities. The QMC calculations differ substantially from the calculations with free form factors in the p region from 40 to 100 MeV/c, where off-shell ambiguities are very small. In this region it can be possible to disentangle density dependence effects if the error bars of the data are of the order of 10% or less. At larger p values, off-shell ambiguities can make it difficult to contrast our predictions including density-dependence of the form factors versus the free ones, as was the case for the p-shells. Moreover, other effects beyond the impulse approximation, not considered in this work, could also play an important role in order to provide a precise description of experimental data for the s shell. We have also computed results with other form factor parametrizations (different from the dipole one), and they change the P'_t/P'_l ratio by about $2-3\%$ for both the free and modified case, keeping the relative differences almost unchanged.

In view of these results we conclude that inferring medium modifications from transfer polarization in ^{16}O at this Q^2 value seems not to be free from ambiguities because of the off-shell effects. However, more precise data and an analysis of other kinematical situations and/or for different nuclei could surely help to draw more definite conclusions.

6.4 Summary and conclusions

The analysis of recoil nucleon polarized $(\vec{e}, e'\vec{p})$ observables presented in [18] within RPWIA has been extended here to include FSI described through relativistic optical potentials. The study is restricted to proton knockout from the $p_{1/2}$, $p_{3/2}$ and $s_{1/2}$ shells

in ^{16}O and quasi-perpendicular kinematics with $q = 1$ GeV/c, which roughly corresponds to the experimental setting. A comparison with data is provided.

The main focus of this paper is to study the role played by the dynamical enhancement of the lower components in the bound and scattered nucleon wave functions; along this line, a systematic investigation on the effects linked to FSI and off-shell descriptions is also done. We show results evaluated with the two usual choices of the nucleon current operator, CC1 and CC2, and three different relativistic parameterizations of the optical potential, EDAIO, EDAD1 and EDAD2. Finally, kinematical relativistic effects, associated with the non-relativistic truncation of the current operator, are also investigated in detail. Additional ingredients, such as the different relativistic models to describe the bound nucleon wave function and nucleon form factors, are seen not to modify our conclusions.

From the results shown in previous sections, we may summarize our basic findings as follows:

- FSI constitutes a basic ingredient in order to get reliable results to be compared with data. Transferred polarization ratios as well as polarized responses do modify very significantly their structure when FSI are taken into account. However, a kind of cancellation of the FSI effects is observed to occur in P'_l and P'_s for low missing momenta, $p \leq 100$ MeV/c. Concerning the role of the optical potential, a clear difference emerges for the two asymmetries at very high p-values, $p \geq 400$ MeV/c, when comparing results for the EDAIO and EDAD-type potentials. This is due to the different reduction of the scattered wave function in the nuclear interior produced by the two kinds of optical potentials. Finally, at intermediate p-values ($p \simeq 250$ MeV/c), P'_l shows a strong dependence on the interaction model, whereas the uncertainty in P'_s is tinier. A similar comment applies also to the off-shell ambiguities.

- Dynamical relativistic effects are shown to be very important, being enhanced for the CC1 current operator. Concerning the responses, $R_s^{T'}$ and $R_l^{TL'}$ present the highest dependence with dynamical effects, as also found in the RPWIA studies. However, contrary to the plane wave limit, where the dynamical enhancement of the lower components of the bound nucleon completely modifies the shape of the transferred asymmetries, in the case of the distorted wave approach the general oscillatory behaviour of P'_l and P'_s persists even after projecting-out the negative-energy components. This differs also with the behaviour of the unpolarized observable A_{TL}.

This effect is linked to the breakdown of factorization. At intermediate p-values, P_l' shows a stronger sensitivity to relativistic dynamics.

- Results corresponding to SR reductions are proven to be very similar (depending on the truncation) to the EMA-noSV approach, differing more from the RDWIA calculations. As expected, the difference between the three approaches increases as p goes up. The SR approaches also lead to a significant cancellation of the oscillatory behaviour in A_{TL}, while maintaning the general shape of P_l' and P_s'. This is again connected with the factorization property and its possible breakdown.

From the comparison with experimental data, we show the reliability of our general description of $(\vec{e}, e'\vec{p})$ reactions, and conclude that new high quality data measured at intermediate p-values ($150 - 200$ MeV/c) may help to constrain the various theoretical approximations involved in our calculations.

As pointed out in [17], other ingredients that go beyond the impulse approximation, such as those arising from meson exchange currents and the Δ-isobar contribution, may also play a very important role in properly describing the transferred polarization asymmetries. These remain to be investigated in a relativistic context, although, in on-going work, the inclusion of two-body currents within the fully relativistic formalism is presently in progress. In the final analysis, any interpretation in terms of medium modified nucleon form factors requires having excellent control of all of these model dependences, both those discussed in the present work and those that go beyond the impulse approximation. Within our model we have found that for the kinematical conditions of E89003 and E89033 [35,36] it is difficult to separate effects introduced by density-dependent form factors from off-shell ambiguities due to the choice of current operator. However, for the $s_{1/2}$ and $p_{1/2}$ shells there is a region in between 40 and 100 MeV/c that is relatively free from off-shell uncertainties and where the effect of medium modifications would be easier to assess. In a future publication we will present the results of a more extensive study in the context of the nuclear model uncertainties and will assess the impact of including medium modifications of the form factors at different values of Q^2.

Acknowledgements

This work was partially supported by funds provided by DGI (Spain) and FEDER funds, under Contracts Nos BFM2002-03315, BFM2002-03562, FPA2002-04181-C04-04

and BFM2000-0600 and by the Junta de Andalucía (Spain) and in part by the U.S. Department of Energy under Cooperative Research Agreement No. DE-FC02-94ER40818. M.C.M. and J.R.V. acknowledge financial support from the Fundación Cámara (University of Sevilla) and the Consejería de Educación de la Comunidad de Madrid, respectively.

Bibliografía

[1] S. Malov *et al.,* Phys. Rev. **C62** (2000) 057302. S. Malov, PhD thesis, New Brunswick, New Jersey, (1999), unpublished.

[2] S. Dieterich *et al.,* Phys. Lett. **B500** (2001) 47.

[3] S. Strauch *et al.,* Phys. Rev. Lett. **91** (2003) 052301

[4] R.J. Woo *et al.,* Phys. Rev. Lett. **80** (1998) 456.

[5] J.M. Udías, J.R. Vignote. Phys. Rev. **C62** (2000) 034302.

[6] J.M Udías, P. Sarriguren, E. Moya de Guerra, E. Garrido, J.A. Caballero, Phys. Rev. **C48** (1993) 2731.

[7] J.M Udías, P. Sarriguren, E. Moya de Guerra, E. Garrido, J.A. Caballero, Phys. Rev. **C51** (1995) 3246.

[8] J.M. Udías, P. Sarriguren, E. Moya de Guerra, J.A. Caballero, Phys. Rev. **C53** (1996) R1488.

[9] J.M. Udías, J.A. Caballero, E. Moya de Guerra, J.E. Amaro, T.W. Donnelly, Phys. Rev. Lett. **83** (1999) 5451.

[10] J.M. Udías, J.A. Caballero, E. Moya de Guerra, J.R. Vignote, A. Escuderos, Phys. Rev. **C64** (2001) 024614.

[11] J.M. Udías, J.R. Vignote, E. Moya de Guerra, A. Escuderos, J.A. Caballero, nucl-th/0109077. Proceedings of the 5th Workshop on "e.-m. induced two-hadron emission", Lund, 2001.

[12] J.E. Amaro, J.A. Caballero, T.W. Donnelly, A.M. Lallena, E. Moya de Guerra, J.M. Udías, Nucl. Phys. **A 602** (1996) 263.

[13] J.E. Amaro, J.A. Caballero, T.W. Donnelly, E. Moya de Guerra, Nucl. Phys. **A 611** (1996) 163.

[14] J.E. Amaro, M.B. Barbaro, J.A. Caballero, T.W. Donnelly, A. Molinari, Nucl. Phys. **A643** (1998) 349.

[15] S. Jeschonnek, T.W. Donnelly, Phys. Rev. **C57** (1998) 2438.

[16] J.E. Amaro, M.B. Barbaro, J.A. Caballero, F. Kazemi Tabatabei, Phys. Rev. **C68** (2003) 014604.

[17] F. Kazemi Tabatabei, J.E. Amaro, J.A. Caballero, Phys. Rev. **C68** (2003) 034611.

[18] M.C. Martínez, J.A. Caballero, T.W. Donnelly, Nucl. Phys. **A707** (2002) 83.

[19] M.C. Martínez, J.A. Caballero, T.W. Donnelly, Nucl. Phys. **A707** (2002) 121.

[20] S. Boffi, C. Giusti, F.D. Pacati, M. Radici, "Electromagnetic Response of Atomic Nuclei", (Oxford University Press, Oxford, 1996); Phys. Rep. **226** (1993) 1.

[21] J.J. Kelly, Adv. Nucl. Phys. **23** (1996) 75.

[22] A. Picklesimer and J.W. Van Orden, Phys. Rev. **C35** (1987) 266.

[23] A. Picklesimer and J.W. Van Orden, Phys. Rev. **C40** (1989) 290.

[24] A.S. Raskin, T.W. Donnelly, Ann. of Phys. **191** (1989) 78.

[25] T.W. Donnelly, A.S. Raskin, Ann. of Phys. **169** (1986) 247.

[26] T. de Forest, Nucl. Phys. **A392** (1983) 232.

[27] A. Meucci, C. Giusti, and F.D. Pacati, Phys. Rev. **C64** (2001) 014604; nucl-th/0211023.

[28] J.A. Caballero, T.W. Donnelly, E. Moya de Guerra, J.M. Udías, Nucl. Phys. **A632** (1998) 323; **A643** (1998) 189.

[29] B.D. Serot, J.D. Walecka, Adv. Nucl. Phys. **16** (1986) 1.

[30] J.J. Kelly, Phys. Rev. **C56** (1997) 2672; **59** (1999) 3256.

[31] J.E. Amaro, M.B. Barbaro, J.A. Caballero, T.W. Donnelly, A. Molinari, Phys. Rep. **368** (2002) 317.

[32] M.M. Sharma, M.A. Nagarajan, P. Ring, Phys. Lett. **B312** (1993) 377.

[33] E.D.Cooper, S. Hama, B.C. Clark, R.L. Mercer, Phys. Rev. **C47** (1993) 297.

[34] Manfred Gari, W. Krumpelmann, Z. Phys. **A322** (1985) 689.

[35] JLab Experiment E89-003, Spokespersons: W. Bertozzi, K. Fissum, A. Saha, L. Weinstein, unpublished.

[36] JLab Experiment E89-033, Spokespersons: C.C. Chang, C. Glashausser, S. Nanda, P. Rutt, unpublished.

[37] J. Gao *et al.,* Phys. Rev. Lett. **84** (2000) 3265

[38] J. Ryckebusch, D. Debruyne, W. Van Nespen, S. Janssen, Phys. Rev. **C60** (1999) 034604; **C64** (2001) 044606.

[39] J.R. Vignote, M.C. Martínez, J.A. Caballero, E. Moya de Guerra, J.M. Udías, nucl-th/0312076.

[40] D.H. Lu, K. Tsushima, A.W. Thomas, A.G. Williams and K. Saito, Phys. Lett. **B417** (1998) 217 and Phys. Rev. **C60** (1999) 068201.

Capítulo 7

Cociente de polarizaciones transferidas en $^4He(\vec{e}, e'\vec{p})$ (I)

Physics Letters B 500 (2001) 47-52

Polarization transfer in the ^{4}He$(\vec{e},e'\vec{p})^3$H reaction

S. Dieterich,[1] P. Bartsch,[2] D. Baumann,[2] J. Bermuth,[3] K. Bohinc,[2,4] R. Böhm,[2] D. Bosnar,[2,a] S. Derber,[2] M. Ding,[2] M. Distler,[2] I. Ewald,[2] J. Friedrich,[2] J.M. Friedrich,[2,b] R. Gilman,[1,5] C. Glashausser,[1] M. Hauger,[6] P. Jennewein,[2] J. Jourdan,[6] J.J. Kelly,[7] M. Kohl,[8] A. Kozlov[2], K.W. Krygier,[2] G. Kumbartzki,[1] J. Lac,[1,c] A. Liesenfeld,[2] H. Merkel,[2] U. Müller,[2] R.Ñeuhausen,[2] Th. Pospischil,[2] R. D. Ransome,[1] D. Rohe,[6] G. Rosner,[2,d] H. Schmieden,[2] M. Seimetz,[2] I. Sick,[6] S. Strauch,[1] J.M. Udias,[9] J.R. Vignote,[9] A. Wagner,[2] Th. Walcher,[2] G. Warren,[6] M. Weis[2]

[1] *Rutgers, The State University of New Jersey, Piscataway, New Jersey, USA*

[2] *Institut für Kernphysik, Universität Mainz, Mainz, Germany*

[3] *Institut für Physik, Universität Mainz, Mainz, Germany*

[4] *Institut Jozef Stefan, Ljubljana, Slovenia*

[5] *Thomas Jefferson National Accelerator Facility*

[6] *Universität Basel, Basel, Switzerland*

[7] *University of Maryland, College Park, Maryland, USA*

[8] *Institut für Kernphysik, Technische Universität Darmstadt,Darmstadt, Germany*

[9] *Universidad Complutense de Madrid, Madrid, Spain*

Polarization transfer in the ^{4}He$(\vec{e},e'\vec{p})^3$H reaction at a Q^2 of 0.4 (GeV/c)^2 was measured at the Mainz Microtron MAMI. The ratio of the transverse to the longitudinal polarization components of the ejected protons was compared with the same ratio for elastic *ep* scattering. The results are consistent with a recent fully relativistic calculation which includes a predicted medium modification of the proton form factor based on a quark-meson coupling model.

PACS numbers: 13.40.Gp, 13.88.+e, 24.70.+s, 25.30.Dh, 27.20.+h

A long standing question in nuclear physics is the effect of the nuclear medium on the properties of the nucleon. The close proximity of nucleons in the nucleus would lead one to expect effects on the spatial distribution of the nucleon's constituent particles. However, experimentally distinguishing changes of the nucleon structure from other conventional nucleus-related effects, such as meson-exchange currents (MEC), isobar configurations (IC), and final state interactions (FSI) has proven difficult. The form factor of a bound nucleon is not directly observable; it must be inferred from calculations which predict how a modification of the form factor will affect measurable quantities such as cross sections or polarizations.

In this Letter we report on the first measurement of polarization transfer in the ^{4}He$(\vec{e}, e'\vec{p})^3$H reaction in quasielastic parallel kinematics. Polarization provides a sensitive test of any model and should be more sensitive to changes in the form factor than cross section measurements.

Several recent calculations [1–3] have demonstrated the importance of dynamic enhancement of lower components of Dirac spinors (spinor distortions) for the $(e, e'p)$ reaction. The R_{LT} response function is sensitive to distortion of the bound-state spinor while recoil polarization is more sensitive to distortion of the ejectile spinor. The relativistic calculations of Udias *et al.* provide excellent descriptions of A_{TL} in ^{16}O$(e, e'p)$ [4] and the induced polarization for ^{12}C$(e, e'\vec{p})$ [5]. The sensitivity of recoil polarization to possible density dependence of nucleon form factors was investigated first by Kelly [6] using a local density approximation for the current operator and an effective momentum approximation (EMA) for spinor distortion. Udias then performed a fully relativistic calculation which shows that the accuracy of the EMA for the recoil polarization is better than 1% for missing momentum $p_m < 100$ MeV/c. Both groups have shown that recoil polarization for modest p_m is relatively insensitive to gauge and Gordon ambiguities and to variations of the optical potential and have concluded that polarization transfer provides a promising probe of density-dependent modifications of nucleon electromagnetic form factors.

Polarization transfer was first used to study nuclear medium effects in deuterium [7–9]. Within statistical uncertainties, no evidence of medium modifications was found. Malov *et al.* [10] made the first measurement of polarization transfer in a complex nucleus, ^{16}O. Their results were consistent with predictions of relativistic calculations, with limited statistical precision.

Cross section data indicate only upper limits on possible modifications of the form factors in the nucleus. The limits come primarily from quasielastic electron scattering

with separation of the longitudinal and transverse response functions [11–14] and from y-scaling [15–17] of inclusive electron scattering. In the Q^2 range of 0.1 to 0.5 $(GeV/c)^2$ L/T separations limit modifications to 3% for the magnetic and 5-10% for the electric form factor. The limits from y-scaling at higher Q^2, in the range of 1 to 5 $(GeV/c)^2$, are about the same.

While the data exclude substantial form factor modification, especially of the magnetic form factor, recent theoretical work predicts modifications within the experimental limits [18–21]. Lu *et al.* [18], using a quark-meson coupling model (QMC), and Frank *et al.* [19], using a light front constituent quark model, both predicted changes of a few percent in the form factors. Lu calculated the change for both ^{16}O and ^4He and found little difference in the size of the modification. We shall later examine the effect on the predicted polarization of the QMC modification.

In the case of electron-nucleon scattering, there is a direct relationship between the form factors and the polarization transfer components [22]:

$$\frac{G_E}{G_M} = -\frac{P'_x}{P'_z} \cdot \frac{E + E'}{2m_N} \tan(\theta/2) \tag{7.1}$$

where E and E' are the energies of the incident and scattered electron, θ is the electron scattering angle, m_N is the nucleon mass, and the longitudinal and transverse polarization transfer observables are P'_z and P'_x, respectively. The relation in Eq. (7.1) was recently used to extract G_E/G_M for the proton [8, 23]. This relationship is only approximately correct for electron scattering from a bound nucleon; one must calculate the expected polarization ratio in the context of some model.

We use the coordinate system with unit vectors pointing in the direction of the three momentum transfer $\hat{z} = \hat{q}$, normal to the electron scattering plane $\hat{y} = (\hat{k}_i \times \hat{k}_f)/|\hat{k}_i \times \hat{k}_f|$, and transverse $\hat{x} = \hat{y} \times \hat{z}$, where the initial and final electron momenta are $\vec{k}_i$ and $\vec{k}_f$. The results are presented in terms of P'_x and P'_z, the projections of the transferred polarizations on these axes.

The advantage of using polarization is that the polarizations do not depend on the target thickness or total current; the beam polarization and analyzing power both cancel in the ratio of polarizations. The difference between the asymmetries measured with positive and negative beam helicity cancels instrumental asymmetries to first order. The only significant experimental systematic uncertainty is the determination of the spin precession in the spectrometer.

This experiment was done at MAMI at the Johannes Gutenberg-Universität, Mainz, Germany, using the spectrometer facilities of the A1 collaboration Ref. [24]. A proton focal plane polarimeter (FPP) was installed in Spect. A [25]. The beam energy was 854.5 MeV. The nominal settings were 625 MeV/c central momentum at 50.24° for the electron arm (Spect. B) and 660 MeV/c and 46.56° for the proton arm (Spect. A). The data covered the Q^2 range of 0.35 to 0.42 $(\mathrm{GeV/c})^2$. To measure the polarization ratio for the free proton and to study systematic effects, $\vec{e}p$ elastic scattering data were taken at the same nominal settings as for the ^{4}He measurement except that the central angle for the proton arm was set to 48.16° in order to better match the kinematic acceptance.

The FPP includes a graphite analyzer with a thickness of 11.9 g/cm^2 (7 cm). The spectrometer vertical drift chambers serve as the tracking detectors before the analyzer and two horizontal drift chambers track scattered protons after the analyzer. The basic design of the FPP is similar to several used previously [26]. For further details, see Ref. [25].

The helium target consisted of a gas cell 8 cm long, at a temperature of 19 K and pressure of 19 bar. The target thickness was about 250 mg/cm^2. The same cell was used for liquid hydrogen, with a thickness of about 560 mg/cm^2, in order to minimize any systematic differences. The beam current used for hydrogen was typically 0.5 μA, set by the data acquisition rate, and for helium 14 μA. The beam polarization was approximately 75%, as determined from the recoil polarization measured for hydrogen using the analyzing power from Ref. [27]. The invariant mass resolution was approximately 0.8 MeV, which allowed clear separation of the ^{3}Hp final state from the ^{2}Hpn and $ppnn$ final states.

In the data analysis the criteria for selected events included, among others, tests on spectrometer acceptance, target geometry, missing mass, and FPP polar scattering angle ($7^\circ < \theta_c < 35^\circ$). The physical quantities of interest, P'_x and P'_z, were determined by means of the maximum likelihood technique, utilizing the azimuthal distribution of the protons scattered from the graphite analyzer

$$I = I_0 \left[1 + \epsilon_y \cos(\phi_c) + \epsilon_x \sin(\phi_c)\right]. \tag{7.2}$$

The asymmetries ϵ_x and ϵ_y are proportional to the analyzing power and to the proton's polarizations perpendicular to its momentum as it enters the analyzer and are linear functions of the proton's polarization components at the target. The relationship is given by a rotation which takes into account the change of coordinate system and the proton spin precession [25] in the spectrometer's magnetic fields and is calculated on an event by

Target	P'_x/P'_z	Ref.
^{4}He	-0.862 $\pm$ 0.020 $\pm$ 0.03	this work
^{1}H	-0.978 $\pm$ 0.044 $\pm$ 0.03	this work
^{1}H	-0.952 $\pm$ 0.008	[8, 23, 29]

Tabla 7.1: Polarization ratios with statistical and estimated systematic uncertainties. The world average, last row, is derived from measurements of G_E and G_M.

event basis.

The systematic uncertainty in the determination of P'_x/P'_z can be estimated by introducing artificial shifts in various parameters and finding the effect on the ratio. The total systematic uncertainty was estimated to be ± 0.03 on the ratio, for both helium and hydrogen.

Table 7.1 lists the extracted polarization ratios for ^{4}He and ^{1}H. No radiative corrections have been applied; they are expected to have an effect which is of order 1% [28]. The hydrogen ratio is found to be in agreement with the polarization ratio derived from the world average of G_E/G_M [8, 23, 29] for data between Q^2 of 0.3 and 0.5 (GeV/c)^2.

Since systematic effects on the polarization ratio for hydrogen and helium were nearly the same in both size and sign, the effect of systematic uncertainties on the ratio of helium to hydrogen data

$$R = (P'_x/P'_z)_{\mathrm{He}} \; / \; (P'_x/P'_z)_{\mathrm{H}} \tag{7.3}$$

nearly canceled. This "super-ratio" is estimated to have a systematic uncertainty of less than 0.01. The uncertainty on R is then limited by the statistical uncertainty, mainly of the hydrogen ratio measured in this experiment. Using the ratio of G_E/G_M derived from the world average for hydrogen would give a smaller statistical uncertainty but larger systematic uncertainty. Table 7.2 lists the super-ratio, using the hydrogen ratio from this experiment, as a function of p_m, along with the value averaged over the entire data set. Negative values of p_m correspond to the recoiling nucleus having a momentum component along the direction of $\vec{q}$.

A meaningful interpretation of the polarization ratio measured for ^{4}He with that of hydrogen can only be made by utilizing theoretical calculations which include the effects

p_m (MeV/c)	$(P'_x/P'_z)_{\mathrm{He}}$ / $(P'_x/P'_z)_{\mathrm{H}}$
-53	$0.88 \pm 0.05 \pm 0.01$
55	$0.89 \pm 0.05 \pm 0.01$
mean	$0.88 \pm 0.04 \pm 0.01$

Tabla 7.2: R as a function of missing momentum.

of FSI, the off-shell current operator, relativistic effects, MEC, and IC on the ratio. In addition, any calculation must be averaged over the spectrometer acceptance.

We now proceed as follows. The polarization transfer is predicted using a model which includes the free form factors and the best phenomenologically determined optical potentials and bound state wave functions (BSWF), and FSI. MEC and IC are included in one nonrelativistic model. If the value predicted using the free form factor does not describe the measured value well, within the theoretical uncertainties, the effect of a modified form factor will be considered. If the new value predicted provides a better description of the data, we can take it as evidence that the proton form factors inside ^{4}He differ from those of a free proton.

Figure 7.1 shows a comparison of the experimental result R, the ^{4}He polarization ratio normalized to the hydrogen ratio, with the acceptance-averaged calculations. The hydrogen calculation made use of the same form factor parameterization as does the corresponding ^{4}He calculation.

We first examined the effect of MEC and IC using the non-relativistic calculations of Laget [30]. The result of the full Laget calculation was found to be nearly identical to the PWIA result, points 2 and 1, respectively, in Fig. 7.1, indicating that MEC and IC do not contribute significantly in our kinematics. There is a discrepancy of over two standard deviations between the observed value and both calculations of Laget.

We next use the model of Udias *et al.* to determine the magnitude of relativistic effects. Udias solves the Dirac equation and uses relativistic optical potentials, but does not include MEC or IC. For each case, we give the result for two different de Forest [31] off-shell current operators, *cc*1 and *cc*2. The PWIA calculation of Udias (points 3 and 4) includes positive and negative energy components for the bound state, but only positive energy components for the ejected nucleon. It gives nearly the same results as that of Laget, indicating that R is insensitive to the negative energy components of the bound state. The calculations are insensitive to differences between the two forms of the current

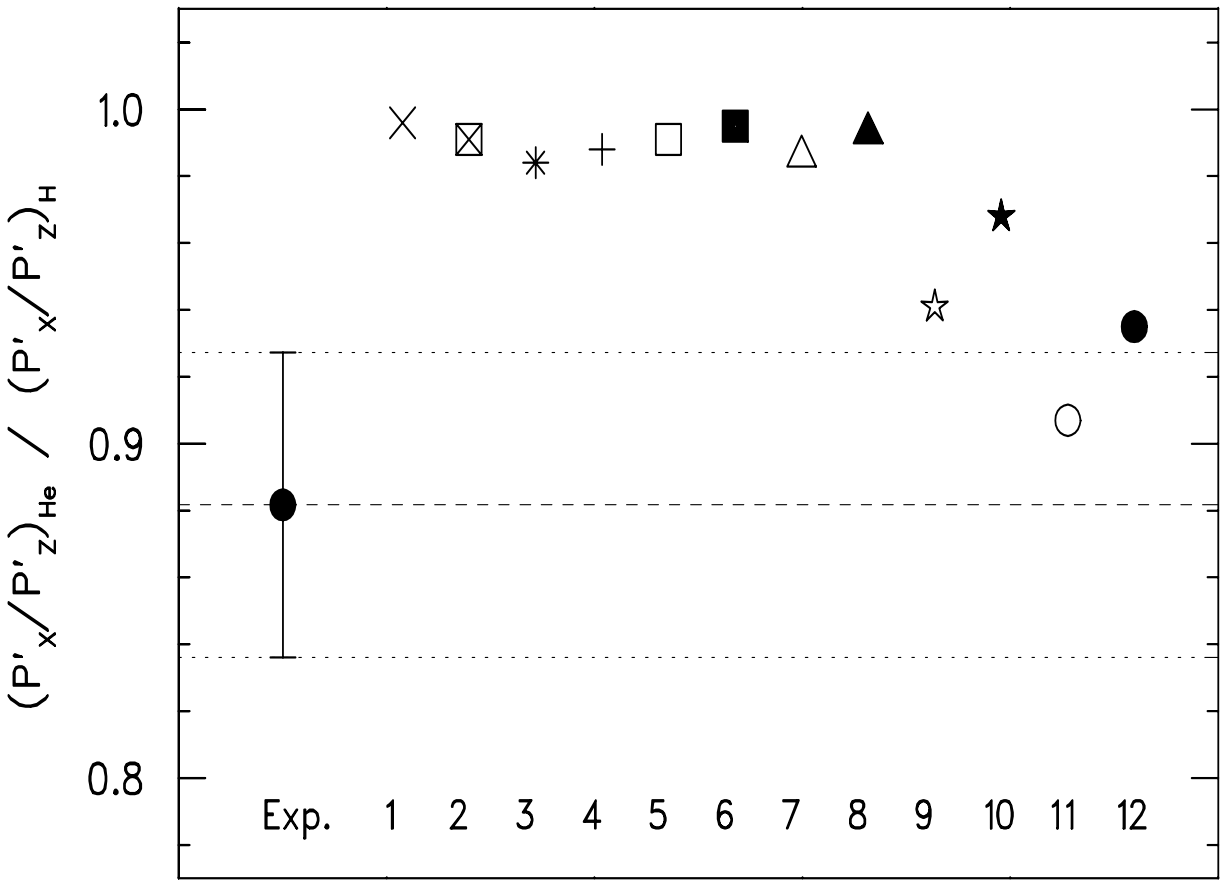

Figura 7.1: Comparison of measured R (Exp.) with theoretical calculations. Laget - PWIA (1); full calculation (2). Udias - PWIA, $cc1$ (3), $cc2$ (4); positive energy projection, $cc1$ (5), $cc2$(6); no spinor distortions, $cc1$ (7), $cc2$ (8); fully relativistic, $cc1$ (9), $cc2$ (10); fully relativistic, and QMC, $cc1$ (11), $cc2$ (12).

operator.

The optical potential for p+^{3}H was obtained by folding a density-dependent empirical effective pN interaction (EEI) with the measured charge density for tritium. Kelly and Wallace [32] derived an effective interaction for nucleon-nucleus scattering for $9 \leq A \leq 208$, designated IA2, in which spinor distortion is represented by density-dependent modifications that are very similar to those of the EEI model fitted to proton elastic and inelastic scattering data. Some parameters were adjusted to fit p^4He data yielding a better fit to the proton elastic scattering data than any previous optical potential. Furthermore, the dominant source of density dependence is consistent with the spinor distortion employed by relativistic $(e, e'p)$ calculations. We investigated the sensitivity to final-state interactions by using several other optical models and found variations of ± 0.02 in the polarization ratio.

In principle, the result should not depend on the gauge used. However, the calculations do show a small gauge dependence. We show the result using the Coulomb gauge, which gives nearly the same ratio as the Landau gauge; the Weyl gauge gives a larger ratio by 0.04.

The results of the Udias relativistic calculation projecting out the negative energy sector (points 5 and 6) and with no spinor distortion (points 7 and 8), called EMA-noSV in Ref. [3], are also nearly the same as the PWIA calculation (points 3 and 4), demonstrating the small influence of relativistic effects, other than the negative energy components of the outgoing nucleon wave function, which are not included in any of the calculations 1 to 8, and of FSI, on R. The fully relativistic calculations are shown as points 9 and 10. The ratio decreases noticeably, in particular with $cc1$, but it remains slightly larger than the observed ratio. Both results are between one and two standard deviations from the observed value.

Finally, we include the density dependent form factor modifications predicted by the QMC model of Lu *et al.* [18], using a bag constant of 0.8 fm (points 11 and 12). These decrease the ratio further by about 4%. The difference between the $cc1$ and $cc2$ results are about the same as for points 9 and 10. The effect on the ratio is less than the 10% effect discussed in Ref. [18]. However, the calculations of Ref. [18] averaged over the bound state wavefunction. As discussed in Ref. [10], an integration over the final state, including the effects of absorption and non-locality corrections, reduces the effect. The addition of QMC brings the calculation into good agreement with the observed value.

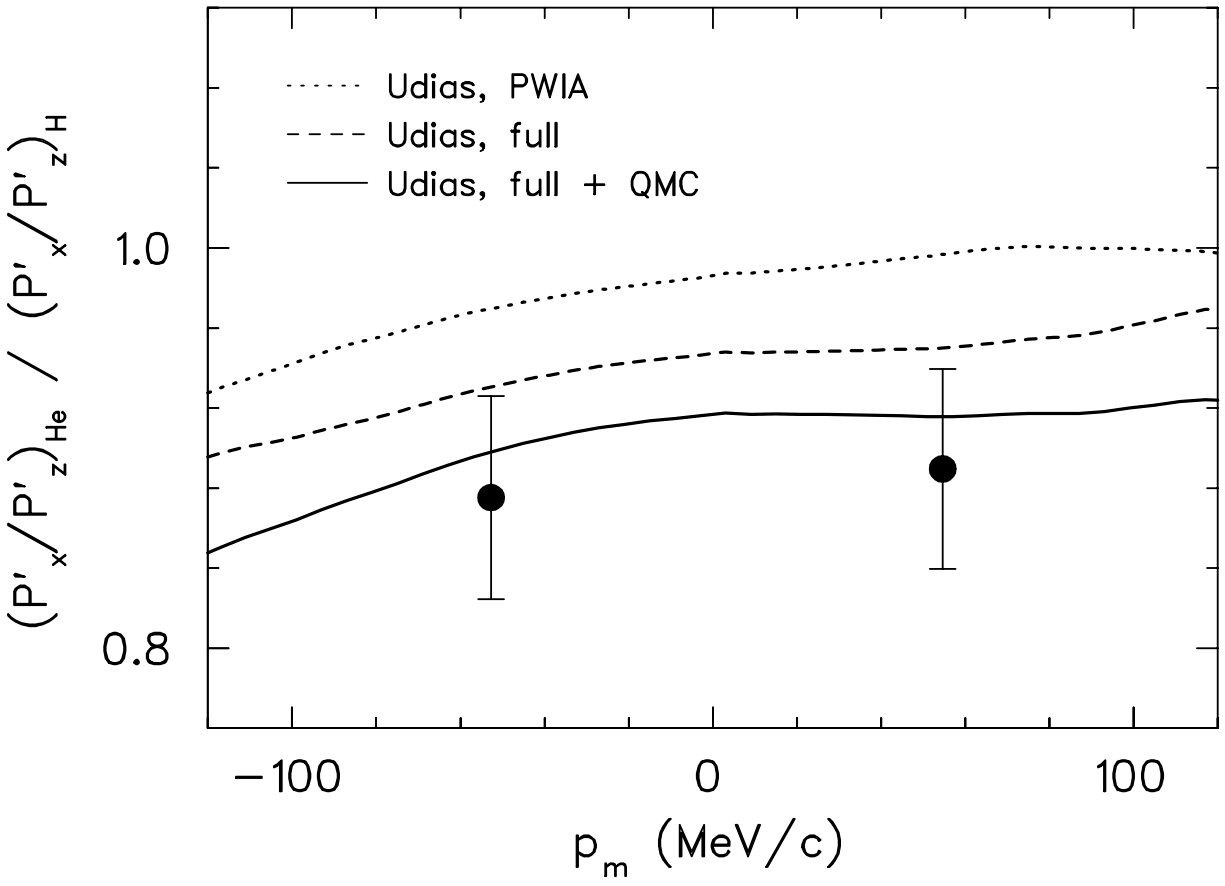

Figura 7.2: R as a function of missing momentum. Using the labels of Fig. 7.1, the curves are dotted (3), dashed (9), and solid (11).

Calculations using Kelly's EMA for similar conditions give very similar results. The variations in the result due to choice of the BSWF and the effect of Coulomb distortions were negligible in both models.

The dependence of R on the missing momentum was found to be small, as shown in Fig. 7.2. A sample of the calculations given in Fig. 7.1 are shown in Fig. 7.2. The other calculations give curves nearly parallel to those shown, with separations about the same as the separations of the averages shown in Fig. 7.1.

In conclusion, we have measured polarization transfer in the reaction ^{4}He$(\vec{e}, e'\vec{p})^3$H for the first time. The P'_x/P'_z ratio is in clear disagreement with PWIA and non-relativistic calculations. A full relativistic calculation agrees at the two standard deviation level. The variation in the result for different choices of the bound-state wave function, optical model, and current operator, added in quadrature, is less than one standard deviation. These measurements give the first evidence that a fully relativistic calculation that includes negative energy components giving rise to spinor distortions, is required for a correct description of spin transfer in $(\vec{e}, e'\vec{p})$ for ^{4}He, even at low missing momentum. The addition of a modified proton form factor to the calculation, predicted by the QMC model, brings the result into good agreement with the data. Although the data do favor the models with a modified form factor, the statistical significance is not sufficient to exclude calculations without form factor modification.

We wish to thank the MAMI accelerator staff for their excellent work during this experiment. The authors gratefully acknowledge the assistance of J.-M. Laget with theoretical calculations. This work was supported in part by the Deutsche Forschungsgemeinschaft, U.S. National Science Foundation, and the Schweizerische Nationalfond.

[a]Permanent address: Department of Physics, University of Zagreb, Zagreb, Croatia
[b]Present address: Physik Department E18, T.U. München, Germany
[c]Present address: Netherlands Industrial Property Office, Rijswijk, The Netherlands
[d]Present address: Glasgow University, Glasgow, Scotland, UK

Bibliografía

[1] J.M. Udias, J.A. Caballero, E. Moya de Guerra, J.E. Amaro and T.W. Donnelly, Phys. Rev. Lett. **83**, 5451 (1999); J.A. Caballero, T.W. Donnelly, E. Moya de Guerra, and J.M. Udias, Nucl. Phys. **A632**, 323 (1998).

[2] J.J. Kelly, Phys. Rev. C **60**, 044609 (1999).

[3] J.M. Udias and J.R. Vignote, Phys. Rev. C **62**, 034302 (2000).

[4] J. Gao *et al.*, Phys. Rev. Lett. **84**, 3265 (2000).

[5] R.J. Woo *et al.*, Phys. Rev. Lett. **80**, 456 (1998).

[6] J.J. Kelly, Phys. Rev. C **56**, 2672 (1997); Adv. in Nucl. Phys. **23**, 75 (1996).

[7] D. Eyl *et al.*, Z. Phys. A **352**, 211 (1995).

[8] B.D. Milbrath, J. McIntyre *et al.*, Phys. Rev. Lett. **80**, 452 (1998) and Phys. Rev. Lett. **82**, 2221 (1999).

[9] D.H. Barkhuff *et al.*, Phys. Lett. B **470**, 39 (1999).

[10] S. Malov *et al.*, Phys. Rev. C **62**, 057302 (2000).

[11] A. Zghiche *et al.*, Nucl. Phys. **A572**, 513 (1994).

[12] R. Schiavilla, V.R. Pandharipande and A. Fabrocini, Phys. Rev. C **40**, 1484 (1989).

[13] J.E. Ducret *et al.*, Nucl. Phys. **A556**, 373 (1993).

[14] K.I. Blomqvist *et al.*, Z. Phys. A **351**, 353 (1995).

[15] I. Sick, Comm. Nucl. Part. Phys. **18**, 109 (1988).

[16] D.B. Day *et al.*, Ann. Rev. Nucl. Part. Sci. **40**, 357 (1990).

[17] D.B. Day *et al.*, Phys. Rev. Lett. **59**, 427 (1987).

[18] D.H. Lu *et al.*, Nucl. Phys. **A634**, 443 (1998); D.H. Lu *et al.*, Phys. Lett. B **417**, 217 (1998); D.H. Lu *et al.*, Phys. Rev. C **60**, 068201 (1999).

[19] M.R. Frank, B.K. Jennings and G.A. Miller, Phys. Rev. C **54**, 920 (1996).

[20] Ulf-G. Meissner, Phys. Rev. Lett. **62**, 1013 (1989).

[21] I.T. Cheon and M.T. Jeong, J. Phys. Soc. Jpn. **61**, 2726 (1992).

[22] A.I. Akhiezer and M.P. Rekalo, Sov. J. Part. Nucl. **4**, 277 (1974); R. Arnold, C. Carlson and F. Gross, Phys. Rev. C **23**, 363 (1981).

[23] M.K. Jones *et al.*, Phys. Rev. Lett. **84**, 1398 (2000).

[24] K.I. Blomqvist *et al.*, Nucl. Inst. Meth. **A403**, 263 (1998).

[25] Th. Pospischil, Ph.D. thesis, Mainz (unpublished), and Th. Pospischil *et al.*, submitted to Nucl. Inst. Meth., LANL preprint nucl-ex/0010007.

[26] G. Waters *et al.*, Nucl. Inst. Meth. **153**, 401 (1978); D. Besset *et al.*, Nucl. Inst. Meth. **166**, 379 (1979); R.D. Ransome *et al.*, Nucl. Inst. Meth. **201**, 309 (1982); E. Aprile-Giboni *et al.*, Nucl. Inst. Meth. **215**, 147 (1983).

[27] M.W. McNaughton *et al.*, Nucl. Inst. Meth. **A241**, 435 (1985).

[28] A. Afanasev, I. Akusevich and N. Merenkov, private communication.

[29] G. Höhler *et al.*, Nucl. Phys. **B114**, 505 (1976); Ch. Berger *et al.*, Phys. Lett. **35B**, 87 (1971); L.E. Price *et al.*, Phys. Rev. D **4**, 45 (1971); J. Litt *et al.*, Phys. Lett. **31B**, 40 (1970).

[30] J.-M. Laget, Nucl. Phys. **A579**, 333 (1994).

[31] T. de Forest, Jr., Nucl. Phys. **A392**, 232 (1983).

[32] J.J. Kelly and S.J. Wallace, Phys. Rev. C **49**, 1315 (1994).

Capítulo 8

Cociente de polarizaciones transferidas en $^4He(\vec{e}, e'\vec{p})$ (II)

PHYSICAL REVIEW LETTERS **91**, 052301 (2003)

Polarization Transfer in the ^{4}He$(\vec{e}, e'\vec{p})^3$H Reaction up to $Q^2 = 2.6$ (GeV/c)^2

S. Strauch,[1] S. Dieterich,[1] K.A. Aniol,[2] J.R.M. Annand,[3] O.K. Baker,[4,5] W. Bertozzi,[6] M. Boswell,[7] E.J. Brash,[8] Z. Chai,[6] J.-P. Chen,[5] M.E. Christy,[4] E. Chudakov,[5] A. Cochran,[4] R. De Leo,[9] R. Ent,[5] M.B. Epstein,[2] J.M. Finn,[10] K.G. Fissum,[11] T.A. Forest,[12] S. Frullani,[13] F. Garibaldi,[13] A. Gasparian,[4] O. Gayou,[10,14] S. Gilad,[6] R. Gilman,[1,5] C. Glashausser,[1] J. Gomez,[5] V. Gorbenko,[15] P.L.J. Gueye,[4] J.O. Hansen,[5] D.W. Higinbotham,[6] B. Hu,[4] C.E. Hyde-Wright,[12] D.G. Ireland,[3] C. Jackson,[4] C.W. de Jager,[5] X. Jiang,[1] C. Jones,[4] M.K. Jones,[16] J.D. Kellie,[3] J.J. Kelly,[16] C.E. Keppel,[4] G. Kumbartzki,[1] M. Kuss,[5] J.J. LeRose,[5] K. Livingston,[3] N. Liyanage,[5] R.W. Lourie,[17] S. Malov,[1] D.J. Margaziotis,[2] D. Meekins,[18] R. Michaels,[5] J.H. Mitchell,[5] S.K.Ñanda,[5] J.Ñappa,[1] C.F. Perdrisat,[10] V.A. Punjabi,[19] R.D. Ransome,[1] R. Roché,[18] G. Rosner,[3] M. Rvachev,[6] F. Sabatie,[12] A. Saha,[5] A. Sarty,[18] J.M. Udias,[20] P.E. Ulmer,[12] G.M. Urciuoli,[13] J.F.J. van den Brand,[21] J.R. Vignote,[20] D.P. Watts,[3] L.B. Weinstein,[12] K. Wijesooriya,[22] and B. Wojtsekhowski[5]

[1] *Rutgers, The State University of New Jersey, Piscataway, New Jersey 08854*
[2] *California State University, Los Angeles, California 90032*
[3] *University of Glasgow, Glasgow, G12 8QQ, Scotland, United Kingdom*
[4] *Hampton University, Hampton, Virginia 23668*
[5] *Thomas Jefferson National Accelerator Facility, Newport News, Virginia 23606*
[6] *Massachusetts Institute of Technology, Cambridge, Massachusetts 02139*
[7] *Randolph-Macon Woman's College, Lynchburg, Virginia 24503*
[8] *University of Regina, Regina, Saskatchewan, Canada S4S 0A2*
[9] *INFN, Sezione di Bari and University of Bari, I-70126, Bari, Italy*
[10] *College of William and Mary, Williamsburg, Virginia 23187*
[11] *University of Lund, SE-221 00 Lund, Sweden*
[12] *Old Dominion University, Norfolk, Virginia 23529*

[13] *INFN, Sezione Sanitá and Istituto Superiore di Sanitá, Laboratorio di Fisica, I-00161 Rome, Italy*

[14] *Université Blaise Pascal, F-63177 Aubière, France*

[15] *Kharkov Institute of Physics and Technology, Kharkov 310108, Ukraine*

[16] *University of Maryland, College Park, Maryland 20742*

[17] *State University of New York at Stony Brook, Stony Brook, New York 11794*

[18] *Florida State University, Tallahassee, Florida 32306*

[19] *Norfolk State University, Norfolk, Virginia 23504*

[20] *Universidad Complutense de Madrid, E-28040 Madrid, Spain*

[21] *Vrije Universiteit, NL-1081 HV Amsterdam, Netherlands*

[22] *University of Illinois at Urbana-Champaign, Urbana, Illinois 61801*

We have measured the proton recoil polarization in the ^{4}He$(\vec{e}, e'\vec{p})^3$H reaction at Q^2 = 0.5, 1.0, 1.6, and 2.6 (GeV/c)^2. The measured ratio of polarization transfer coefficients differs from a fully relativistic calculation, favoring the inclusion of a predicted medium modification of the proton form factors based on a quark-meson coupling model. In contrast, the measured induced polarizations agree reasonably well with the fully relativistic calculation indicating that the treatment of final-state interactions is under control.

PACS number(s): 13.40.Gp, 13.88.+e, 25.30.Dh, 27.10.+h

The underlying theory of strong interactions is Quantum ChromoDynamics (QCD), yet there are no ab-initio calculations of nuclei available. Nuclei are effectively and well described as clusters of protons and neutrons held together by a strong, long-range force mediated by meson exchange, whereas the saturation properties of nuclear matter arise from the short-range, repulsive part of the strong interaction [1]. Whether the nucleon bound in the nuclear medium changes structure has been a long-standing issue in nuclear physics. At nuclear densities of about 0.17 fm^{-3} nucleon wave functions have significant overlap. In the chiral limit, one expects nucleons to lose their identity altogether and nuclei to make a transition to a quark-gluon plasma.

Unfortunately, distinguishing possible changes in the structure of nucleons embedded in a nucleus from more conventional many-body effects is only possible within the context of a model. Nucleon modifications can be described in terms of coupling to excited states, and such changes are intrinsically intertwined with many-body effects, such as meson-exchange currents (MEC) and isobar configurations (IC). Therefore, interpretation of an experimental signature as an indication of modifications of the nucleon form factors only makes sense if this results in a more economical effective description of the bound, quantum, nuclear many-body system.

The quark-meson coupling (QMC) model of Lu *et al.* [2] suggests a measurable deviation of the ratio of the proton's electric (G_E) and magnetic (G_M) form factors from its free space value over the Q^2 range accessible by experiment. This calculation is consistent with present constraints on possible medium modifications for both G_E (from the Coulomb Sum Rule, with $Q^2 < 0.5$ $(\mathrm{GeV/c})^2$ [3–5]), G_M (from a y-scaling analysis [6], for $Q^2 > 1$ $(\mathrm{GeV/c})^2$), and limits on the scaling of nucleon magnetic moments in nuclei [7]. Similar effects have been calculated in the light-front constituent quark model of Frank *et al.* [8] and in the modified Skyrme model of Yakhshiev *et al.* [9].

In unpolarized $A(e,e'p)$ experiments involving light- and medium-heavy nuclei, deviations were observed in the longitudinal/transverse character of the nuclear response compared to the free proton case [10–12]. Below the two-nucleon emission threshold, these deviations were originally interpreted as changes in the nucleon form factors within the nuclear medium. However, strong interaction effects on the ejected proton (final state interactions [FSI]) later also succeeded in explaining the observed effect [13]. This illustrates that any interpretation in terms of medium modifications to nucleon form factors requires having excellent control of FSI effects.

For free electron-nucleon scattering, the ratio of the electric to magnetic Sachs form factors, (G_E/G_M), is directly proportional to the ratio of the transverse and longitudinal transferred polarizations, (P'_x/P'_z) [14, 15]. This relationship was recently used to extract G_E/G_M for the proton [16–19]. Polarization transfer in quasielastic nucleon knockout remains sensitive to this ratio of form factors (possibly modified by the nuclear medium). A variety of calculations for the A$(\vec{e}, e'\vec{p})$ reaction indicate that FSI and MEC effects on polarization transfer observables are small, amounting to only a $< 10\%$ correction [20–22]. In addition, these nuclear interaction effects tend to largely cancel in the ratio of polarization transfer coefficients P'_x/P'_z.

Recently, polarization transfer for the ^{4}He$(\vec{e}, e'\vec{p})\,^3$H reaction at $Q^2 = 0.4$ (GeV/c)^2 was studied [23]. The addition of medium-modified proton form factors, as predicted by the QMC model, to a state-of-the-art fully relativistic model [21] gave a good description of the data. The authors concluded that, within the model space examined, the data favor models with medium-modified form factors over those with free form factors, but the latter could not be excluded. Examination of this finding over a larger range in Q^2 seems an obvious step for further investigation.

The experiment reported here includes measurements of the polarization transfer coefficients over the range of Q^2 from 0.5 to 2.6 (GeV/c)^2, and as a function of missing momentum in the range 0 to 240 MeV/c, in order to maximize sensitivity to the electric to magnetic form factor ratio for protons bound in the ^{4}He nucleus. This nucleus was selected for study because its relative simplicity allows realistic microscopic calculations and its high density enhances any possible medium effects. As the experiment was designed to detect differences between the in-medium polarizations and the free values, both ^{4}He and ^{1}H targets were employed (except at $Q^2 = 2.6$ (GeV/c)^2, where only ^{4}He data were acquired due to beam time constraints).

Kinematics settings for the present experiment in Hall A at Jefferson Lab (JLab) are given in Table 8.1. The experiment used beam currents of 40 μA for the lower Q^2 values and up to 70 μA for the highest Q^2 value, combined with beam polarizations of 66% for the lowest Q^2 value and $\approx 77\%$ for the other Q^2 values. The beam helicity was flipped pseudorandomly to reduce systematic errors of the extracted polarization transfer observables. The proton spectrometer was equipped with a focal plane polarimeter (FPP) [24, 25]. Polarized protons lead to azimuthal asymmetries after scattering in the carbon analyzer of the FPP. These distributions, in combination with information on the beam helicity, were analyzed by means of a maximum likelihood method to obtain the

Beam Energy (MeV)	Q^2 (GeV/c)^2	Electron Momentum (MeV/c)	Electron θ_{LAB} (degrees)	Proton Momentum (MeV/c)	Proton θ_{LAB} (degrees)
3400	0.5	3102	12.47(12.50)	766	61.43(63.12)
4239	1.0	3667	14.56	1150	54.55(54.82)
4237	1.6	3340	19.35	1549	45.75(46.77)
4237	2.6	2796	27.10	2161	36.20

Tabla 8.1: Kinematics for the present experiment. For the electron and proton angles we indicate between parentheses the angles for the ^{1}H$(\vec{e},e'\vec{p})$ reaction, if different from the ^{4}He$(\vec{e},e'\vec{p})\,^3$H reaction.

induced and transferred polarization components. More details on the analysis can be found in Refs. [16, 26, 27].

Our results are shown in Fig. 8.1 as R/R_{PWIA} for all four values of Q^2. R_{PWIA} is the prediction based on the relativistic plane-wave impulse approximation (RPWIA) calculation. Here, R is defined as

$$R = \frac{(P'_x/P'_z)_{^4\mathrm{He}}}{(P'_x/P'_z)_{^1\mathrm{H}}} \tag{8.1}$$

for the data, whereas R_{PWIA} is the same ratio based on the relativistic plane-wave impulse approximation (RPWIA) calculation. The helium polarization ratio is normalized to the hydrogen polarization ratio measured at the same setting. Such a polarization double ratio nearly cancels all systematic uncertainties. As a cross check, the hydrogen results were also used to extract the free proton form factor ratio G_E/G_M and found to be in excellent agreement with previous data [16, 17]. In addition, our result at $Q^2 = 0.5$ (GeV/c)^2 closely coincides with the recent results at $Q^2 = 0.4$ (GeV/c)^2 of Mainz [23], also shown in Fig. 8.1. Our experimental results for helium and hydrogen separately, in terms of (P'_x/P'_z), are tabulated in Table 8.2. Systematic uncertainties are mainly due to possible minor misalignments of the magnetic elements of the proton spectrometer and uncertainties in the spin transport through these magnetic elements. They are estimated to contribute less than 1.7% to R.

The theoretical calculations by the Madrid group [21] are averaged over the experimental acceptance. We note that these relativistic calculations provide good descriptions of, *e.g.*, the induced polarizations measured at Bates in the ^{12}C$(e,e'\vec{p})$ reaction [30] and of A_{TL} in ^{16}O$(e,e'p)$ as previously measured at JLab [31].

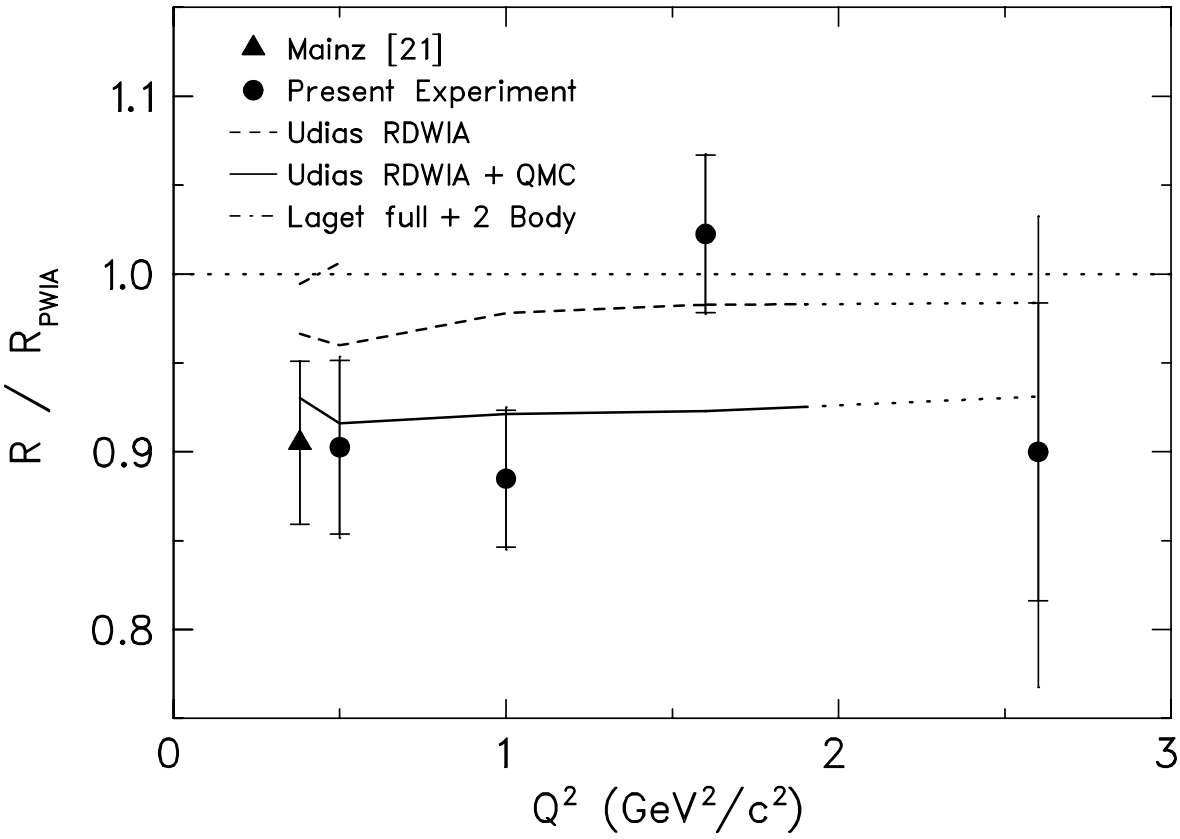

Figura 8.1: Superratio R/R_{PWIA} as a function of Q^2. R is defined as the double ratio $(P'_x/P'_z)_{He}/(P'_x/P'_z)_H$. In PWIA (short-dashed curve) this superratio is identically unity, barring acceptance-averaging effects. The dashed curve shows the results of the full relativistic calculation of Udias *et al.* [21]. The dot-dashed curve shows the results of Laget's full calculation, including two-body currents [20]. The solid curve indicates the full relativistic calculation of Udias including medium modifications as predicted by a quark-meson coupling model [2]. For $Q^2 > 1.8$ (GeV/c)^2 the Udias calculations maintain a constant relativistic optical potential and are indicated as short-dashed curves. Lines connect the acceptance-averaged theory calculations and are to guide the eye only.

Q^2	$(P'_x/P'_z)_{He}$	$(P'_x/P'_z)_H$	R
0.5	-0.804±0.035±0.006	-0.898±0.029±0.011	0.895±0.048±0.015
1.0	-0.502±0.018±0.005	-0.578±0.014±0.005	0.868±0.038±0.011
1.6	-0.393±0.014±0.011	-0.395±0.010±0.009	0.992±0.043±0.007
2.6	-0.231±0.022±0.016	(-0.265±0.024)	0.869±0.081±0.099

Tabla 8.2: Polarization ratios with statistical and estimated systematic uncertainties. The polarization ratio value for ^{1}H($\vec{e}$,e'$\vec{p}$) at $Q^2 = 2.6$ (GeV/c)^2 is from the fit of Ref. [16]. The uncertainty in this ratio and in R reflects the typical systematic uncertainty of the data of Ref. [16] at this Q^2.

At $Q^2 = 0.5$ and 1.0 (GeV/c)^2 the RPWIA calculation overestimates the data by $\approx 10\%$. The relativistic distorted-wave impulse approximation (RDWIA) calculation gives a slightly smaller ($\approx 3\%$) value of R but still overpredicts the data. After including the (density-dependent) medium-modified form factors as predicted by Lu *et al.* [2] in the RDWIA calculation, excellent agreement is obtained at both settings. All calculations shown use the Coulomb gauge, the *cc*1 current operator as defined in [32], and the MRW optical potential of [33]. The *cc*2 current operator gives slightly higher values of R, worsening agreement with the data. In general, various choices for, *e.g.*, spinor distortions, current operators, and relativistic corrections, affect the theoretical predictions by $\leq 3\%$, and can presently not explain the disagreement between the data and the RDWIA calculations. In contrast, the datum at $Q^2 = 1.6$ (GeV/c)^2 is well described by the RPWIA and RDWIA calculations, whereas all calculations are consistent with the datum at $Q^2 = 2.6$ (GeV/c)^2.

A statistical analysis of the measured double ratios, including the result of the Mainz experiment [23], and various theoretical predictions was performed. The model space we examined encompassed the RPWIA and RDWIA calculations of Udias *et al.* [21], the latter with and without medium modifications as predicted by a quark-meson coupling model [2], the full nonrelativistic model of Debruyne *et al.* [28, 29], and the full nonrelativistic calculation of Laget including two-body currents [20]. For the latter calculation only data up to $Q^2 = 0.5$ (GeV/c)^2 are taken into account. A significantly better description is given by the RDWIA calculation when medium modifications are included.

Figure 8.2 shows the polarization double ratio R as a function of missing momentum for the lower three Q^2 kinematics (the statistics at the $Q^2 = 2.6$ (GeV/c)^2 kinematics are not sufficient to make a meaningful comparison with calculations). Negative values of missing

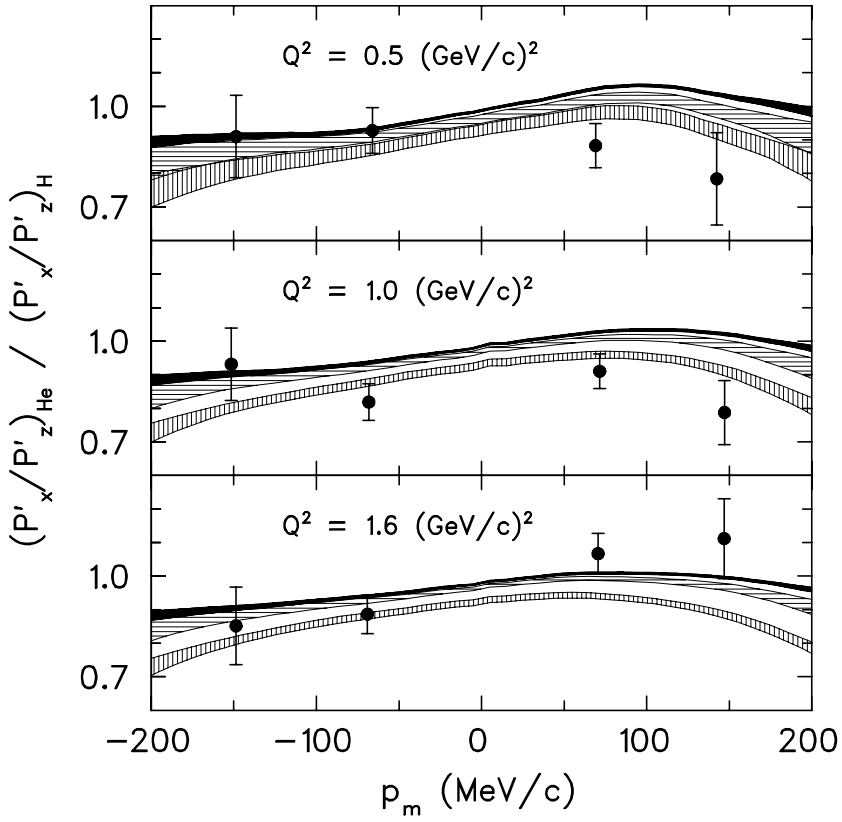

Figura 8.2: Measured values of the polarization double ratio R for ^{4}He$(\vec{e}, e'\vec{p})^3$H at Q^2 = 0.5 (GeV/c)^2 (top), Q^2 = 1.0 (GeV/c)^2 (middle), and Q^2 = 1.6 (GeV/c)^2 (bottom). The shaded bands represent RPWIA calculations (solid), relativistic DWIA calculations (horizontal dashes) and relativistic DWIA calculations including QMC medium–modified form factors [2] by Udias *et al.* [21] (vertical dashes). The bands reflect variations due to choice of current operator, optical potential, and bound-state wave function (see also Ref. [23]).

momentum correspond to the recoiling nuclei having a momentum component antiparallel to the direction of the three-momentum transfer. Both the RPWIA and the RDWIA give a reasonable, but not perfect, description of the missing momentum dependence of the data. As already seen in Fig. 8.1, the difference in magnitude between the RDWIA calculation and the data at $Q^2 = 0.5$ and 1.0 $(\mathrm{GeV/c})^2$ can be largely eliminated by including the QMC medium modifications, whereas at $Q^2 = 1.6$ $(\mathrm{GeV/c})^2$ the calculation without QMC medium modifications already gives a satisfactory description. More precise data could unambiguously settle whether this is just a statistical fluctuation, and would constitute a demanding test of modern nucleon-meson descriptions of nuclear physics.

Lastly, we show in Fig. 8.3 the induced polarization, P_y, obtained by properly averaging over the two beam helicities, and corrected for (small) false asymmetries, as a function of Q^2. P_y is identically zero in the absence of FSI effects (in the one-photon exchange approximation) and constitutes a stringent test of the validity of the inclusion of FSI effects in the calculations. For example, an underestimate of reaction mechanism effects in the present calculation may be due to the neglect of the charge exchange $(\vec{e},\mathrm{e}'\vec{n})(\vec{n},\vec{p})$ reaction in the RDWIA calculations. However, the measured induced polarizations agree well with the RDWIA calculations. In addition, the $^{12}\mathrm{C}(\vec{e},e'\vec{p})$ and $^{16}\mathrm{O}(\vec{e},e'\vec{p})$ reactions were calculated to be insensitive to this effect [22].

One sees in Fig. 8.3 that the induced polarizations are small for all measured Q^2 values. The dashed and dot-dashed curves represent RDWIA calculations by Udias *et al.* [21] with the MRW [33] and RLF [34] relativistic optical potentials. For the induced polarization case, the RDWIA curves with and without medium modifications are identical: as mentioned earlier the QMC model incorporates modifications only to the one-body form factors. For a rigorous calculation of the $^4\mathrm{He}(e,e'\vec{p})^3\mathrm{H}$ results presented here, one would need to take into account possible medium modifications to both one-body form factors and many-body FSI effects. Figure 8.3 confirms the expected small values of the induced polarizations, and indicates reasonable agreement with the RDWIA calculations.

In summary, we have measured recoil polarization in the $^4\mathrm{He}(\vec{e},e'\vec{p})\,^3\mathrm{H}$ reaction in the range from $Q^2 = 0.5$ to 2.6 $(\mathrm{GeV/c})^2$. The datum at the lowest Q^2 agrees well with the results of a recently reported Mainz measurement [23]. Such polarization transfer data are calculated to be only slightly dependent ($< 10\%$ effect) on nuclear structure effects and fine details of the reaction mechanism. Furthermore, these effects tend to cancel in the P'_x/P'_z polarization transfer ratio. Within our model assumptions we find strong evidence for a medium modification; a calculation incorporating a predicted medium modification based

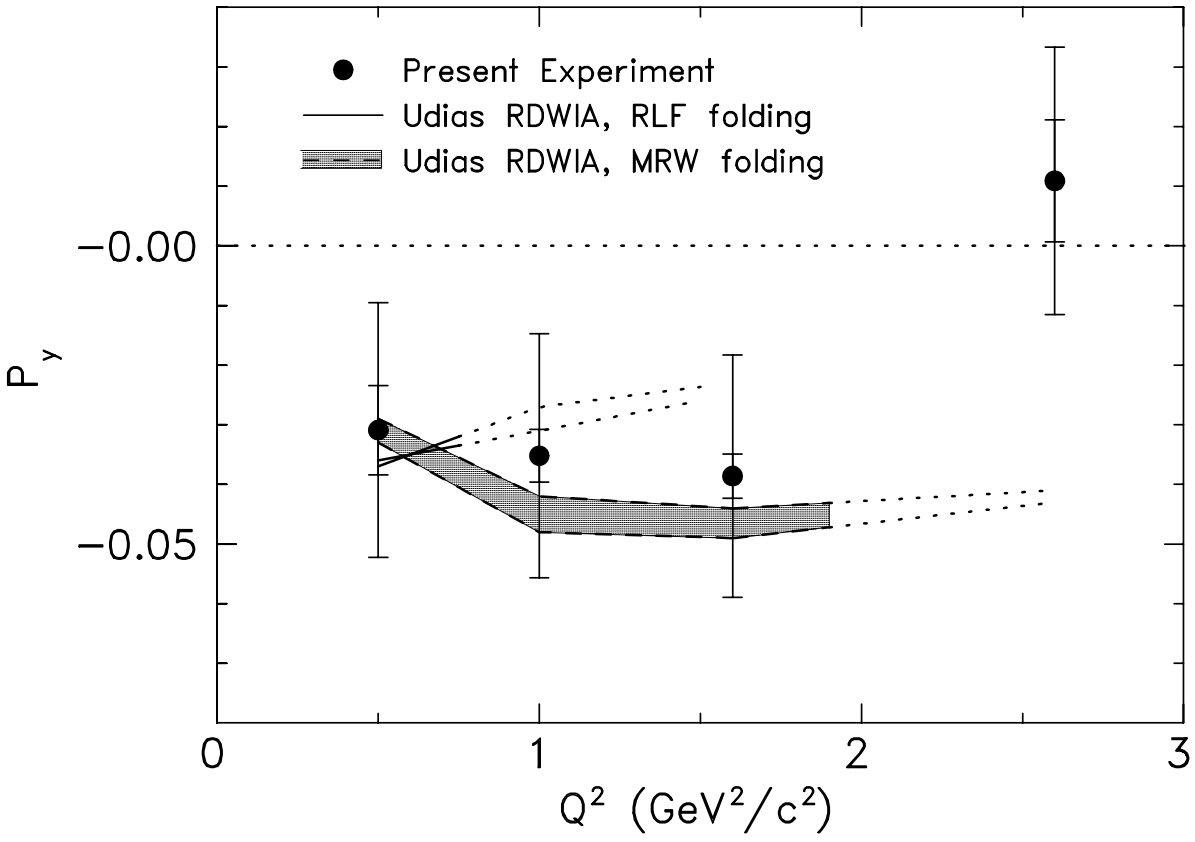

Figura 8.3: Measured values of the induced polarizations for the ^{4}He$(e, e'\vec{p})\,^3$H reaction. The inner uncertainty is statistical only; the total uncertainty includes a systematic uncertainty of ± 0.02, due to imperfect knowledge of the false asymmetries. The solid and dashed curves show the results for the full relativistic RDWIA calculations of Udias *et al.* [21], using differing relativistic optical potentials [33,34]. For the dashed curves, variation within the chosen optical potential parameters is indicated by the shaded area. The short-dashed lines indicate the Q^2 regions beyond the validity of the relativistic optical potentials used.

on the quark-meson coupling model [2] gives a good description of our data. Moreover, the calculated induced polarizations agree well with our data, giving credibility to the validity of the treatment of FSI effects in the model. These data provide the most stringent test to date of the applicability of conventional meson-nucleon calculations.

The collaboration wishes to acknowledge the Hall A technical staff and the Jefferson Lab Accelerator Division for their outstanding support. The Southeastern Universities Research Association (SURA) operates the Thomas Jefferson National Accelerator Facility for the United States Department of Energy under contract DE-AC05-84ER40150. This work was supported by research grants from the United States Department of Energy and the National Science Foundation, the Italian Istituto di Fisica Nucleare (INFN), the Natural Sciences and Engineering Council of Canada (NSERC), the Swedish Natural Science Research Council, and the Comunidad de Madrid and Ministerio de Ciencia y Technologia (Spain).

Bibliografía

[1] S.A. Moszkowski and B.L. Scott, Ann. Phys. **11** (1960) 65.

[2] D.H. Lu, K. Tsushima, A.W. Thomas, A.G. Williams and K. Saito, Phys. Lett. **B417** (1998) 217 and Phys. Rev. C **60** (1999) 068201.

[3] J. Jourdan, Phys. Lett. **B353** (1995) 189.

[4] J. Morgenstern and Z.-E. Meziani, Phys. Lett. **B515** (2001) 269.

[5] J. Carlson, J. Jourdan, R. Schiavilla, and I. Sick, to be submitted.

[6] I. Sick, Comm. Nucl. Part. Phys. **18** (1988) 109.

[7] T.E.O. Ericson and A. Richter, Phys. Lett. **B183** (1987) 249.

[8] M.R. Frank, B.K. Jennings, and G.A. Miller, Phys. Rev. C **54** (1996) 920.

[9] U.T. Yakhshiev, U-G. Meissner, and A. Wirzba, Eur. Phys. J. A **16**, (2003) 569.

[10] G. van der Steenhoven *et al.*, Phys. Rev. Lett. **57** (1986) 182; **58** (1987) 1727.

[11] P. Ulmer *et al.*, Phys. Rev. Lett. **59** (1987) 2259.

[12] D. Reffay-Pikeroen *et al.*, Phys. Rev. Lett. **60** (1988) 776.

[13] T.D. Cohen, J.W. Van Orden, and A. Picklesimer, Phys. Rev. Lett. **59** (1987) 1267.

[14] A.I. Akhiezer and M.P. Rekalo, Sov. J. Part.Ñucl. **3** (1974) 277; R. Arnold, C. Carlson, and F. Gross, Phys. Rev. C **23** (1981) 363.

[15] With the initial and final electron momentum $\vec{k}_i$ and $\vec{k}_f$, the coordinate system is given by the unit vectors $\hat{z} = (\vec{k}_i - \vec{k}_f)/|\vec{k}_i - \vec{k}_f|$, $\hat{y} = (\vec{k}_i \times \vec{k}_f)/|\vec{k}_i \times \vec{k}_f|$, and $\hat{x} = \hat{y} \times \hat{z}$.

[16] M.K. Jones *et al.*, Phys. Rev. Lett. **84** (2000) 1389.

[17] O. Gayou *et al.*, Phys. Rev. C **64** (2001) 038202.

[18] O. Gayou *et al.*, Phys. Rev. Lett. **88** (2002) 092301.

[19] T. Pospichil *et al.*, Eur. Phys. J. **12**, (2001) 125.

[20] J.-M. Laget, Nucl. Phys. **A579** (1994) 333.

[21] J.M. Udias *et al.*, Phys. Rev. Lett. **83** (1991) 5451; J.A. Caballero, T.W. Donnelly, E. Moya de Guerra, and J.M. Udias, Nucl. Phys. **A632** (1998) 323; J.M. Udias and J.R. Vignote, Phys. Rev. C **62** (2000) 034302.

[22] J.J. Kelly, Phys. Rev. C **59** (1999) 3256; **60** (1999) 044609.

[23] S. Dieterich *et al.*, Phys. Lett. **B500** (2001) 47.

[24] M.K. Jones *et al.*, in *Proceedings of the 6th Conference on Intersections between Particle and Nuclear Physics*, edited by T. W. Donnelly, AIP Conf. Proc. No. 412 (AIP New York, 1997), p. 342.

[25] V. Punjabi *et al.* (to be published).

[26] S. Malov *et al.*, Phys. Rev. C **62** (2000) 057302.

[27] S. Dieterich, Ph.D. thesis, Rutgers University (2002).

[28] J. Ryckebusch, D. Debruyne, W. Van Nespen, and S. Janssen, Phys. Rev. C **60** (1999) 034604.

[29] D. Debruyne, Ph.D. thesis, University of Gent (2001).

[30] R.J. Woo *et al.*, Phys. Rev. Lett. **80** (1998) 456.

[31] J. Gao *et al.*, Phys. Rev. Lett. **84** (2002) 3265.

[32] T. de Forest, Nucl. Phys. **A392** (1983) 232.

[33] J.A. McNeil, L. Ray, and S.J. Wallace, Phys. Rev. C **27**, (1983) 2123.

[34] C.J. Horowitz, Phys. Rev. C **31** (1985) 1340; D.P. Murdock and C.J. Horowitz, Phys. Rev. C **35** (1987) 1442.

Capítulo 9

Discusión

En esta tesis hemos revisado en su formulación actual, la aproximación de impulso relativista al proceso $(e, e'p)$ así como la comparación con los datos experimentales disponibles y la confrontación con los análisis no relativistas.

En el primer capítulo se ha introducido el proceso $(\vec{e}, e'\vec{p})$ y definido las condiciones de cinemática exclusiva en las que nos hemos centrado en esta tesis. También se ha revisado brevemente el formalismo y se resume la derivación de la sección eficaz que aparece de forma más completa en el apéndice.

En el capítulo 2 se ha revisado en detalle la aproximación factorizada al proceso $(\vec{e}, e'\vec{p})$ en la aproximación de ondas distorsionadas para el protón. La aproximación de factorización ha sido ampliamente utilizada para interpretar los datos experimentales. Dicha aproximación había sido analizada con cierto detalle en el formalismo no relativista, pero no en el relativista. Existen diferencias notables entre ambos casos, en particular, en el caso relativista, no hay factorización ni siquiera en ondas planas para el nucleón final, contrariamente al caso no relativista [1]. También se demuestran de forma muy general varios resultados conocidos en el caso no relativista, como el hecho de que puede haber factorización de la sección eficaz (en el caso no relativista y bajo hipótesis adicionales) si no se considera interacción de espín-órbita o bien en el estado inicial (es decir, para ser realistas, sólo en onda s, resultado nuevo no conocido) o bien en el estado final, éste último resultado sí que era ya conocido [2], o bien si no hay interacción de espín-órbita ni en el estado inicial ni en el final. De forma importante, se han definido y aclarado algunas de las condiciones adicionales que se solían imponer a la derivación de la sección eficaz factorizada en el caso no relativista [2] y se ha encontrado el adecuado significado físico, que no es otro que el imponer que la relación entre las componentes inferiores y superiores

del cuadriespinor que describe, en el caso relativista, a los nucleones, venga dada por la misma relación que para nucleones libres, es decir, venga mediada por la ecuación de Dirac libre. Esta condición está implícita en la mayoría de los tratamientos no relativistas de la corriente electromagnética, que por tanto factorizan en mayor medida que en el caso relativista. En dicho capítulo 2 se ha extendido el análisis de la validez de la aproximación de factorización más allá de las secciones eficaces, para incluir todos los demás observables que se pueden determinar en experimentos de $(\vec{e}, e'\vec{p})$ sin medir polarizaciones del núcleo blanco. Más interesante aún, se ha encontrado una lógica correlación entre observables que son "robustos", dado que factorizan con menos hipótesis, y cuyas predicciones se alejan en menor medida de las predicciones para nucleones libres. Dicho observables son adecuados para estudiar posibles modificaciones del comportamiento de los nucleones en los núcleos. Por otro lado, otros observables menos "robustos" son aquéllos que no factorizan en ningún caso, ya que son nulos para nucleones libres. Estos observables dependen en mucha mayor medida de los ingredientes del modelo y son útiles para restringir el rango de los parámetros de éste, como el operador de corriente adecuado, la interacción de estados finales, el modelo utilizado para los nucleones iniciales, etc. En definitiva, en este capítulo se exponen todos los aspectos más novedosos del análisis del proceso de $(\vec{e}, e'\vec{p})$ en la aproximación de impulso relativista y se identifica un observable relativamente moderno, la asimetría A_{TL}, como una medida muy robusta que da información sobre la estructura cuadriespinorial de los nucleones.

En el capítulo 3 se aplica el formalismo RDWIA al análisis de datos experimentales de secciones eficaces y observables A_{TL} en oxígeno. Para este núcleo, existía una controversia muy antigua [3] por la aparente discrepancia entre los datos experimentales obtenidos en Saclay y en NIKHEF, en condiciones cuasielásticas relativamente similares ($Q^2 = 0.3$ y 0.2 $(\mathrm{GeV/c})^2$ respectivamente). Dicha discrepancia se reflejaba especialmente en la respuesta R^{TL}, que se puede separar experimentalmente realizando medidas con los protones salientes "a la derecha" y "a la izquierda" del momento transferido q. La discrepancia entre ambos conjuntos de datos se explica debido a las contribuciones relativistas a la estructura de los nucleones, especialmente de los nucleones ligados. Mientras que en un análisis no relativista que mantenga la relación entre componentes inferiores y superiores de los espinores nucleónicos similar a la relación para espinores libres, el observable A_{TL} se desvía moderadamente de la predicción para nucleones libres, en los modelos de campo medio relativista, en los que se produce de forma automática un incremento de la contribución de las componentes inferiores para nucleones ligados y del continuo, el observable A_{TL} au-

menta considerablemente en magnitud con respecto a la predicción libre. La comparación de la teoría relativista con los datos de Saclay y de NIKHEF no muestra ninguna discrepancia ni inconsistencia entre ambos conjuntos de datos y sí unos valores de A_{TL} en buen acuerdo con las predicciones relativistas [4]. También se analizó la posible variación con Q^2 del factor espectroscópico, medido a través del factor de escala necesario para ajustar las predicciones de campo medio a los datos experimentales, incluyendo todos los datos en ^{16}O desde Q^2 0.2 hasta 0.8 $(\mathrm{GeV/c})^2$. Se encontró, contrariamente a lo que habían sugerido algunos estudios no relativistas [5], que no hay evidencia de una dependencia de dicho factor de escala con el momento transferido.

En el capítulo 4 se realiza un estudio de datos obtenidos en el ciclotrón MAMI de Mainz para la reacción $^4He(e,e'p)^3H$ a momentos transferidos moderados. La particularidad de este experimento radica en la amplia aceptancia de los espectrómetros. La comparación de la teoría con los datos requiere de la incorporación de los efectos de los detectores en la respuesta experimental. Para esto, se introducen los resultados teóricos en una simulación MonteCarlo que incluyen, entre otras, las propiedades de los detectores, energía y características específicas del haz de electrones incidente, tipo del blanco y disposición geométrica del mismo, con el fin de generar pseudodatos experimentales que posteriormente son analizados con los mismos procedimientos que los datos reales. Esta simulación de Monte Carlo se realizó en este estudio con los cálculos PWIA. Los cálculos RDWIA fueron evaluados simplemente para la cinemática correspondiente a los valores centrales de las aceptancias experimentales. En la figura 9.1 se puede ver ya el estudio completo, para otro experimento y condiciones cinemáticas, promediando también sobre las aceptancias de los espectrómetros los cálculos RDWIA mediante el uso del código MCEEP [6]. Los datos experimentales presentados en la figura 9.1 fueron medidos en Mainz por Florizone *et al.* [7].

En particular, el objetivo del experimento presentado en el capítulo 4, era comprobar si la relación T/L en ^4He era distinta de la de nucleones libres, como sugerían experimentos anteriores en Saclay. Para ello, se tomaron datos a tres valores diferentes de la energía del electrón todos correspondientes a un momento transferido similar, por lo tanto con una contribución relativa de la parte transversal y longitudinal de la corriente distinta. La comparación con la teoría no mostró diferencia con el cociente T/L experimental respecto de las predicciones relativistas, una vez incluidos los efectos de la interacción de estados finales. Las simulaciones demostraron que los experimentos serían sensibles a modificaciones del cociente T/L superiores al 10% y que, por tanto, se debería haber observado el

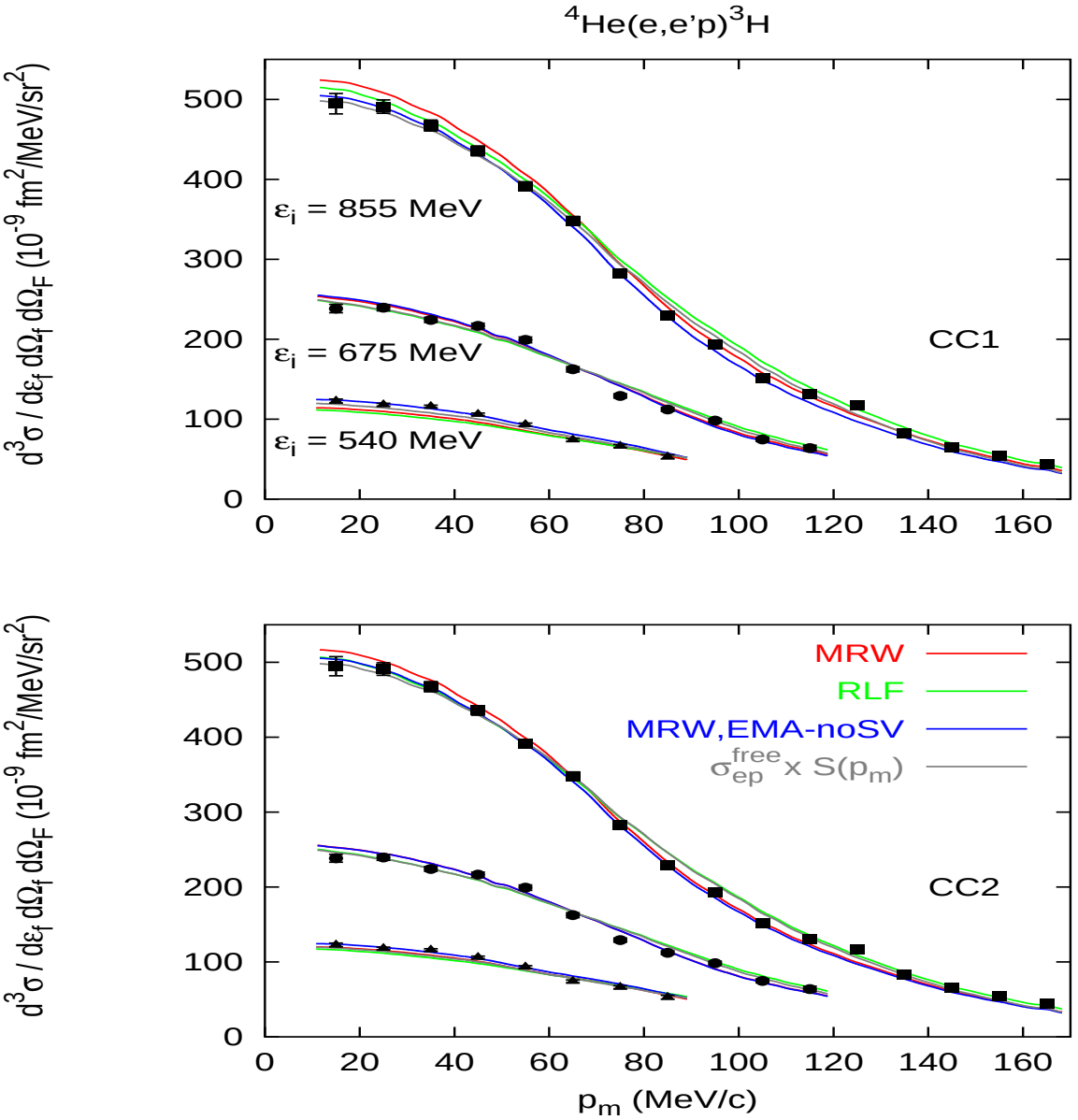

Figura 9.1: Sección eficaz de la reacción $^4He(e,e'p)^3H$ para tres energías del haz incidente medidas por Florizone *et al.* [7]. Las curvas rojas y verdes muestran el cálculo RDWIA, promediado sobre las aceptancias de los espectrómetros, con dos diferentes parametrizaciones para la interacción de estados finales [8, 9]. También se muestran la aproximación EMA-noSV [10] (curva azul) y una aproximación factorizada (curva gris). En el panel superior (inferior) se muestran los cálculos con el operador de corriente $CC1$ ($CC2$) respectivamente.

efecto si fuese tan grande como el observado en Saclay. Posibles explicaciones pasan por la dificultad de realizar correcciones radiativas en el caso de que la resolución en energía desaparecida es pequeña. En el caso del experimento de Mainz, en lugar de corregir los datos experimentales para 'deradiarlos', lo que se hizo fue 'radiar' la teoría, un proceso que tiene menos ambigüedades. Como contrapartida, el análisis realizado en esta forma, resulta menos sensible a las modificaciones del cociente T/L, La conclusión, por el momento, es que parte de los efectos observados en Saclay pueden ser debidos a un sesgo introducido por el procedimiento de deconvolucionar las correcciones radiativas [7], lo cual ha dado lugar a varios estudios independientes para revisar las aproximaciones tradicionales al proceso de deradiación de los datos experimentales en dispersión de electrones. En cuanto a otras conclusiones de este estudio, se ha observado que el efecto de la interacción de estados finales para un núcleo relativamente ligero como es el ^4He y a energías relativamente altas en condiciones cuasielásticas, es poco importante, de forma que incluso una simple aproximación en ondas planas o factorizada, describe los datos razonablemente. No obstante, el mejor ajuste con los datos se obtiene en el caso del cálculo relativista completo y no factorizado. Este experimento permitió, entre otras cosas, establecer que las aproximaciones utilizadas reproducían adecuadamente el proceso $^4He(e, e'p)$ a energías moderadas, al menos en lo que respecta a las secciones eficaces.

En los capítulos siguientes, se introducen los grados de libertad de polarización del nucleón saliente en los análisis. Los experimentos son más difíciles, ya que es necesario introducir análisis magnético para el nucleón final, lo cual típicamente reduce en un factor diez las tasas de conteo. Por tanto, los experimentos de medida de polarizaciones inducidas (o transferidas) requieren mayor tiempo de medida o más luminosidad.

En el capítulo 5 se analizan las polarizaciones inducidas en el proceso $(e, e'\vec{p})$. Es bien conocido, desde los primeros análisis de dispersión de protones por núcleos, que la interacción entre el nucléon final y el núcleo residual, induce un polarización en el protón saliente, en particular debido, por ejemplo, a la interacción de espín-órbita. De forma análoga, este mismo efecto se produce en el caso $(e, e'\vec{p})$. Dado que la aproximación relativista en general tiene mucho más éxito que la no relativista a la hora de reproducir observables relacionados con la interacción de espín-órbita [11], es interesante realizar un análisis relativista de la polarización inducida y compararla con los pocos datos disponibles por el momento. Se observa que la polarización inducida es muy sensible a los detalles de la interacción de estados finales. La medida de P_n puede ser de gran utilidad para determinar los valores o modelos adecuados de la interacción en el estado final. La comparación con

los datos revela que el cálculo relativista reproduce los datos mejor que el no relativista.

En el capítulo 6 se introducen de nuevo observables adicionales, en este caso las polarizaciones transferidas, cuya determinación experimental requiere, además del polarímetro magnético de los protones emitidos, la utilización de electrones polarizados [12–14]. De nuevo se incrementa el grado de dificultad requerido a los experimentos. En cuanto al formalismo, en este capítulo se derivan los observables en la aproximación relativista, se compara con varias aproximaciones no relativistas o semi-relativistas y se contrastan los resultados con los escasos datos disponibles en ^{16}O. La precisión obtenida hasta el momento en experimentos con ^{16}O no permite distinguir entre las predicciones de diferentes modelos, en particular porque las polarizaciones transferidas son un tipo de observables de los que se han denominado "robustos" en el capítulo 2, es decir, cuyo valor depende sólo moderadamente de las aproximaciones utilizadas en su cálculo. Esto hace que el cociente entre polarizaciones transferidas P'_s/P'_l, proporcional al cociente G_E/G_M de los factores de forma eléctrico y magnético del nucleón, se haya propuesto como el observable más indicado para estudiar posibles modificaciones de los factores de forma del nucléon en el seno nuclear. Los datos en ^{16}O disponibles hasta la fecha no tienen precisión suficiente como para concluir de ellos que se obtiene un cociente distinto al predicho por los diversos modelos teóricos existentes. En cambio, en el caso del ^4He, la precisión de los datos experimentales y el gran número de experimentos que se han realizado es mucho mayor y, como se ha visto en los capítulos 7 y 8, suficiente como para extraer conclusiones sobre el cociente G_E/G_M en núcleos.

En los capítulos 7 y 8 se analizan experimentos de medida de polarizaciones normales, polarizaciones transferidas y cocientes de éstas, en ^4He. Como se explicó en los capítulos anteriores, la medida combinada del cociente P'_x/P'_z junto con P_y, consigue dos objetivos complementarios: por un lado, P_y es muy sensible a la interacción de estados finales. Una buena reproducción de P_y indicará, por tanto, que esta parte del modelo está bajo control. El cociente de polarizaciones transferidas, por otro lado, es una medida muy directa de los factores de forma del nucleón que muestra muy poca sensibilidad a los efectos habituales en este tipo de procesos, como interacción de estados finales, tipo de corriente nuclear, ambigüedades off-shell o Gauge, y otras. Por tanto, los experimentos de $(\vec{e}, e'\vec{p})$ en condiciones exclusivas han sido propuestos con el fin de determinar la posible modificación de los factores de forma de los nucleones al estar ligados en el medio nuclear. Es cierto que, por definición, los factores de forma de los nucleones ligados en núcleos, como cualquier otra cantidad *off-shell*, no puede ser medida experimentalmente y realizar experimen-

tos para determinar dichos factores parece un contrasentido. Sin embargo, recordemos que las corrientes de intercambio mesónicas (MEC) [15–18] son también una cantidad *off-shell* y por tanto no medible, pese a lo cual numerosos experimentos han concluido que se ha determinado o medido el efecto de las MEC a la respuesta electromagnética de los núcleos [15]. Para entender esta aparente paradoja, hay que tener en cuenta que los experimentos, como cualquier otro fenómeno en física nuclear, se analizan en términos de modelos y es dentro de un modelo en el que cabe denominar, discernir o atribuir contribuciones a las observaciones experimentales de los diferentes efectos *off-shell*, como pueden ser la interacción de estados finales olas corrientes de intercambio mesónicas. Si en los mismos modelos que a menudo han servido para justificar la necesidad de introducir MEC, después de incluir dichas corrientes, efectos relativistas, FSI y todos los ingredientes habituales, aún no se pueden explicar los datos experimentales, cabe entonces probar con factores de forma modificados de acuerdo a algunos modelos [19] y si, como en el caso de estos experimentos, se encuentra que el acuerdo mejora hasta el punto de hacerlo perfectamente compatible con los experimentos, se ha de concluir que, al menos en el contexto de este modelo, hay una evidencia palpable y sustancial sobre la modificación de los factores de forma de los nucleones en el núcleo. En estos dos capítulos se analizan los experimentos realizados en MAMI-Mainz y Jefferson Lab, en condiciones cuasielásticas en ^4He y en un amplio rango de momento transferido, con el fin de determinar las polarizaciones normales y las polarizaciones transferidas. Para el correcto análisis del experimento, las respuestas obtenidas en el modelo relativista basado en la aproximación de impulso se introducen en un complejo programa de Monte Carlo que promedia en las aceptancias angulares [6]. La comparación con los datos revela:

1. Los efectos relativistas, sobre todo debidos a la interacción de estados finales, acercan la teoría a los datos, de forma que la diferencia entre las predicciones de la aproximación de impulso relativista para el cociente y los datos se reducen a la mitad con respecto al caso no relativista [20].

2. Pese a la mejora, se mantiene una diferencia con los datos experimentales que es estadísticamente significativa. Dicha diferencia se reduce hasta hacer la teoría compatible con los datos experimentales, si se incluyen modificaciones de los factores de forma dentro de los núcleos similares a las predichas por varios modelos [19].

3. Se ha comprobado que FSI y otros efectos más allá de la aproximación de impulso, tal como MEC, apenas modifican el cociente de respuestas transferidas [20, 21].

4. Las polarizaciones normales están bien descritas en el modelo relativista [22, 23], con el tratamiento estándar del proceso. No así en el caso no relativista [24].

Hasta el momento, sólo hay un tipo de procesos que pueden contemplarse como explicación alternativa a las modificaciones de los factores de forma en el medio nuclear: una combinación de MEC tensoriales en conjunción con canales acoplados p-n en el estado final, es decir, que el fotón transferido interacciona con un neutrón que, tras la interacción de estados finales se convierte en un protón que es el detectado en coincidencia [24]. Normalmente este proceso no contribuye de forma significativa, apenas un 1-2% [25], a la sección eficaz. Sin embargo no hay que perder de vista que el efecto experimentalmente observado es muy pequeño: Un 8% de desviación respecto de la predicción para el cociente libre, 4% del cual se explica por los efectos de interacción de estados finales relativistas y el 4% adicional puede explicarse por modificaciones de los factores de forma, o bien, en la otra alternativa [24], 4% se debe a las MEC tensoriales y otro 4% a los canales acoplados. Sin embargo, de momento esta explicación alternativa presenta varios inconvenientes:

- La interacción p-n se introduce de forma ad-hoc sin contrastar con otros procesos o resultados experimentales en los que también podría influir.
- La polarización inducida que se obtiene con el valor de interacción p-n necesario para explicar los datos de cociente P'_x/P'_z es muy grande, apenas compatible con la cota superior de los valores máximos medidos.
- Los resultados se han obtenido para cinemáticas centrales, sin promediar con las aceptancias experimentales, lo cual podría modificar los datos de forma significativa.

Ya que los datos experimentales son cada vez más precisos al continuarse acumulando estadística en sucesivos experimentos, lo cual restringe cada vez más los parámetros de los modelos teóricos utilizados, esperamos que en los próximos meses todos estos puntos puedan ser aclarados.

Bibliografía

[1] J.A. Caballero, T.W. Donnelly, E. Moya de Guerra, J.M. Udías, Nucl. Phys. **A632**, 323 (1998).

[2] S. Frullani and J. Mougey, Adv. Nucl. Phys. **14**, 1 (1985).

[3] C.M. Spaltro, H.P. Blok, E. Jans, L. Lapikás, M. van der Schaar, G. van der Steenhoven, P.K.A. de Witt Huberts, Phys. Rev. C **48**, 2385 (1993).

[4] J.M. Udías, J.A. Caballero, E. Moya de Guerra, J.R. Vignote, A. Escuderos, Phys. Rev. C **64**, 024614 (2001).

[5] L. Lapikás, Nucl. Phys. **A553**, 297c (1993).

[6] P.E. Ulmer, *MCEEP: Monte Carlo for Electro-Nuclear Coincidence Experiments*, http://www.physics.odu.edu/~ulmer/mceep/mceep.html

[7] R. Florizone, Ph.D. thesis, MIT, 1998.

[8] J.A. McNeil, L. Ray, and S.J. Wallace, Phys. Rev. C **27**, 2123 (1983).

[9] C.J. Horowitz, Phys. Rev. C **31**, 1340 (1985); D.P. Murdock and C.J. Horowitz, Phys. Rev. C **35**, 1442 (1987).

[10] J.M. Udias and J.R. Vignote, Phys. Rev. C **62**, 034302 (2000).

[11] B.C. Clark, S. Hama, R.L. Mercer, L. Ray, B.D. Serot, Phys. Rev. Lett. **50**, 1644 (1983).

[12] K. Wijesooriya, Ph.D. thesis, College of William and Mary, 1999

[13] S. Malov, Ph.D. thesis, New Brunswick, New Jersey, 1999.

[14] S. Malov *et al.,* Phys. Rev. C **62**, 057302 (2000).

[15] J.-F. Mathiot, Phys. Rep. **173**, 63 (1989).

[16] J. E. Amaro, G. Co', E. M. V. Fasanelli, A. M. Lallena, Phys. Lett. B **277**, 249 (1992).

[17] J. E. Amaro, G. Co', A. M. Lallena, Nucl. Phys. **A578**, 365 (1994).

[18] J. Ryckebusch, D. Debruyne, W. Van Nespen, S. Janssen, Phys. Rev. C **60**, 034604 (1999).

[19] D.H. Lu *et al.*, Nucl. Phys. **A634**, 443 (1998); D.H. Lu *et al.*, Phys. Lett. B **417**, 217 (1998); D.H. Lu *et al.*, Phys. Rev. C **60**, 068201 (1999).

[20] S. Dieterich *et al.*, Phys. Lett. B **500**, 47 (2001).

[21] J.-M. Laget, Nucl. Phys. **A579**, 333 (1994).

[22] S. Strauch *et al.,* Phys. Rev. Lett. **91**, 052301 (2003).

[23] P. Lava, J. Ryckebusch, B. Van Overmeire, S. Strauch, Phys. Rev. C **71**, 014605 (2005).

[24] J. Carlson, J. Jourdan, R. Schiavilla and I. Sick, Phys. Lett. B **553**, 191 (2003)

[25] James J. Kelly, Phys. Rev. C **59**, 3256 (1999).

Capítulo 10

Conclusiones

De los resultados presentados en los distintos capítulos de esta tesis doctoral podemos extraer las siguientes conclusiones:

- La aproximación de impulso relativista ha tenido mucho éxito prediciendo un amplísimo abanico de resultados experimentales en condiciones cuasielásticas exclusivas. Una muestra de esta afirmación se puede observar al comparar los cálculos relativistas, con las secciones eficaces reducidas y las respuestas hadrónicas medidas por diferentes grupos experimentales en Saclay y NIKHEF [1–3]. En general, estos datos se reproducen muy bien mediante un tratamiento completamente relativista, mejorando sensiblemente el acuerdo con el experimento respecto a los cálculos no relativistas existentes hasta ahora. Asimismo, los cálculos relativistas son capaces de explicar los datos de la respuesta R^{TL} medida a bajo momento transferido Q^2 por ambos grupos, algo que hasta ahora no era posible.

- Nuevos observables han podido ser medidos gracias a los avances efectuados en el campo experimental. Entre ellos destacan las polarizaciones inducidas y transferidas, accesibles gracias a la posibilidad de polarizar el haz de electrones incidente y/o medir la polarización del protón saliente, la asimetría de helicidad A que implica medidas de secciones eficaces fuera del plano [4] y la asimetría A_{TL} nunca medida con anterioridad [5]. Todos estos nuevos observables ponen a prueba de forma mucho más exigente los modelos teóricos. Hasta el momento, el modelo relativista compara bien con los experimentos. Como ejemplo podemos citar los datos de la polarización inducida normal P_n medidos por Woo *et al.* en ^{12}C [6] y reproducidos en el capítulo

4 de esta tesis o los datos de la asimetría A_{TL} en ^{16}O medidos por Gao *et al.* [5] y comparados con nuestro modelo RDWIA en los artículos [7, 8].

- El conocimiento preciso de las polarizaciones inducida P_n y transferidas $P'_{l,s}$ permite estudiar el comportamiento de los nucleones en el seno nuclear. La polarización inducida P_n es uno de los observables más indicados para discernir entre los diferentes modelos teóricos que describen la interacción entre el nucleón detectado y el núcleo residual. Los últimos experimentos y el análisis relativista [9, 10], son evidencia poderosa a favor de la modificación de las propiedades de los nucleones en el núcleo con respecto a los nucleones libres. Nuevos experimentos en curso determinaran con más precisión el cociente P'_s/P'_l y permitirán determinar de forma concluyente la hipótesis de modificación de las propiedades electromagnéticas de los nucleones en el núcleo.

Como conclusión final de esta tesis doctoral podríamos decir que el cálculo basado en la aproximación relativista de ondas distorsionadas (RDWIA), es en la actualidad la mejor herramienta teórica para el análisis de los experimentos de $A(\vec{e}, e'\vec{p})B$ a energías intermedias.

Bibliografía

[1] L. Chinitz *et al.*, Phys. Rev. Lett. **67**, 568 (1991).

[2] C.M. Spaltro, H.P. Blok, E. Jans, L. Lapikás, M. van der Schaar, G. van der Steenhoven, P.K.A. de Witt Huberts, Phys. Rev. C **48**, 2385 (1993).

[3] M. Leuschner *et al.*, Phys. Rev. C **49**, 955 (1994).

[4] S. M. Dolfini *et al.*, Phys. Rev. C **60**, 064622 (1999).

[5] J. Gao *et al.,* Phys. Rev. Lett. **84**, 3265 (2000).

[6] R.J. Woo *et al.,* Phys. Rev. Lett. **80** 456, (1998).

[7] J.M. Udías, J.A. Caballero, E. Moya de Guerra, J.E. Amaro, T.W. Donnelly, Phys. Rev. Lett. **83**, 5451 (1999).

[8] K. G. Fissum *et al.*, Phys. Rev. C **70**, 034606 (2004).

[9] S. Dieterich *et al.*, Phys. Lett. B **500**, 47 (2001).

[10] S. Strauch *et al.,* Phys. Rev. Lett. **91**, 052301 (2003).

Apéndice A

Sección eficaz $A(\vec{e}, e'\vec{p})B$

En este apéndice calcularemos la sección eficaz para el proceso $A(\vec{e}, e'\vec{p})B$ en la aproximación de impulso y con intercambio de un fotón. En este trabajo se utilizan unidades naturales $\hbar = c = 1$, así como los convenios para la métrica del espacio tiempo y las matrices de Dirac de las referencias [1–3]. Los vectores espaciales (tres componentes) se representan por letras en negrilla (*e.g.* $\boldsymbol{p}$) y los cuadrivectores con subíndice o superíndice griego.

A primer orden en teoría de perturbaciones, la amplitud de transición de esta reacción viene dada por la siguiente expresión [3]:

$$S^{(2)} = -ie^2 \int_V d^4x \int_V d^4y \, \tilde{j}^\mu(x) D_{\mu\nu} \tilde{J}^\nu(y) \frac{1}{V} \sum_{\boldsymbol{q}'} \int dq'_0 \frac{1}{2\pi} \frac{e^{iq'\cdot(x-y)}}{(q'\cdot q') + i\epsilon} \,, \tag{A.1}$$

donde $\tilde{j}^\mu$ y $\tilde{J}^\nu$ son las corrientes electromagnéticas leptónicas y hadrónicas respectivamente y $D_{\mu\nu}$ es un operador definido como sigue:

$$D_{\mu\nu} = g_{\mu\nu} - \frac{q'_\mu q'_\nu}{q'\cdot q'} \,. \tag{A.2}$$

Si suponemos que los estados iniciales y finales son estados de energía bien definida, es decir, $\tilde{j}^\mu(x) = e^{-i(\varepsilon_i - \varepsilon_f)x^0} j^\mu(\boldsymbol{x})$ y una expresión análoga para $\tilde{J}^\nu(y)$, la integral de la dependencia temporal de las corrientes da como resultado una delta de Dirac cuyo argumento es la suma de las energías iniciales menos las finales y por tanto implica que la energía total se conserva durante el proceso. Llegamos entonces a la siguiente expresión para la amplitud de transición

$$S^{(2)} = -ie^2 \delta(energia) \int_V d\boldsymbol{x} \int_V d\boldsymbol{y} j^\mu(\boldsymbol{x}) D_{\mu\nu} J^\nu(\boldsymbol{y}) \frac{1}{V} \sum_{\boldsymbol{q}'} \frac{e^{-i\boldsymbol{q}'\cdot(\boldsymbol{x}-\boldsymbol{y})}}{(\tilde{q}\cdot\tilde{q}) + i\epsilon} \,, \tag{A.3}$$

con $\tilde{q}=(\omega,\boldsymbol{q}')$ y $\omega=\varepsilon_i-\varepsilon_f$. Si además consideramos que las funciones de onda de los electrones vienen descritas por una onda plana, o dicho con otras palabras, trabajamos bajo la aproximación PWBA, resulta que:

$$j^{\mu}(\boldsymbol{x})=\frac{1}{\sqrt{2\varepsilon_i V 2\varepsilon_f V}}(\bar{u}_f\gamma^{\mu}u_i)e^{i\boldsymbol{x}\cdot(\boldsymbol{k}_i-\boldsymbol{k}_f)}\,, \tag{A.4}$$

siendo u_i, u_f cuadriespinores de Dirac para partículas libres [1, 2]

$$u(\boldsymbol{k},s)=\sqrt{\varepsilon+m_e}\begin{pmatrix}\chi^s_{\frac{1}{2}}\\ \frac{\boldsymbol{\sigma}\cdot\boldsymbol{k}}{\varepsilon+m_e}\chi^s_{\frac{1}{2}}\end{pmatrix}\,, \tag{A.5}$$

y por tanto podemos realizar la integral en $\boldsymbol{x}$ obteniendo el siguiente resultado:

$$S^{(2)}=i(2\pi)\delta(energia)I_V\,, \tag{A.6}$$

donde hemos definido I_V como sigue:

$$\begin{aligned} I_V &= -\frac{e^2(\bar{u}_f\gamma^{\mu}u_i)}{2V\sqrt{\varepsilon_i\varepsilon_f}}\int_V d\boldsymbol{y}\frac{1}{V}\sum_{\boldsymbol{q}'}V\delta_{\boldsymbol{k}_i-\boldsymbol{k}_f,\boldsymbol{q}'}\frac{1}{(\tilde{q}\cdot\tilde{q})+i\epsilon}D_{\mu\nu}J^{\nu}(\boldsymbol{y})e^{i\boldsymbol{q}'\cdot\boldsymbol{y}} \\ &= \frac{e^2(\bar{u}_f\gamma^{\mu}u_i)}{2V\sqrt{\varepsilon_i\varepsilon_f}}\frac{1}{Q^2}D_{\mu\nu}J^{\nu}(\boldsymbol{q}) \end{aligned} \tag{A.7}$$

siendo $q^{\mu}=(\omega,\boldsymbol{q})=(\omega,\boldsymbol{k}_i-\boldsymbol{k}_f)$; $Q^2=q^2-\omega^2$ y hemos expresado la corriente hadrónica en el espacio de momentos,

$$J^{\nu}(\boldsymbol{q})=\int_V d\boldsymbol{y}J^{\nu}(\boldsymbol{y})e^{i\boldsymbol{q}\cdot\boldsymbol{y}}\,. \tag{A.8}$$

Ahora, obviamente, el tensor $D_{\mu\nu}$ es:

$$D_{\mu\nu}=g_{\mu\nu}-\frac{q_{\mu}q_{\nu}}{Q^2} \tag{A.9}$$

Como la corriente se conserva ($q_{\mu}\bar{u}_f\gamma^{\mu}u_i=0$) es usual no considerar el término $q_{\mu}q_{\nu}$ en el tensor $D_{\mu\nu}$. Alternativamente, es conveniente introducir la expansión [4]:

$$D^{\mu\nu}=\sum_{\lambda_\gamma=\pm1,0}(-1)^{\lambda_\gamma}\epsilon^{\mu*}_{\lambda_\gamma}\epsilon^{\nu}_{\lambda_\gamma}\,, \tag{A.10}$$

donde los $\epsilon^{\mu}_{\lambda_\gamma}$ son los llamados vectores de polarización del fotón virtual que se intercambia en la reacción. El caso $\lambda_\gamma=0$ se corresponde con la polarización longitudinal y los casos $\lambda_\gamma=\pm1$ con las dos polarizaciones transversales. En el sistema de referencia en el que el núcleo blanco está en reposo (LAB), eligiendo el eje z a lo largo de la dirección del

momento transferido $\boldsymbol{q}$, las coordenadas de los vectores de polarización del fotón son las siguientes:

$$\epsilon^{\mu}_{+1} = -\frac{1}{\sqrt{2}}(0,1,i,0)\,, \tag{A.11}$$

$$\epsilon^{\mu}_{-1} = \frac{1}{\sqrt{2}}(0,1,-i,0)\,, \tag{A.12}$$

$$\epsilon^{\mu}_{0} = (\frac{q}{Q},0,0,\frac{\omega}{Q})\,. \tag{A.13}$$

Es sencillo comprobar que satisfacen la siguiente propiedad bajo el cambio de signo de λ:

$$(\epsilon^{\mu}_{\lambda})^{*} = (-1)^{\lambda}\epsilon^{\mu}_{-\lambda}\,. \tag{A.14}$$

Podemos espresar por tanto la amplitud de transición como sigue,

$$I_V = \frac{1}{2V\sqrt{\varepsilon_i\varepsilon_f}}\sum_{\lambda_\gamma}\left[\bar{u}_f\gamma_\mu u_i\epsilon^{\mu *}_{\lambda_\gamma}\right]\left[J_\nu(\boldsymbol{q})\epsilon^{\nu}_{\lambda_\gamma}\right]\frac{e^2}{Q^2}\,. \tag{A.15}$$

Es interesante recalcar que las dos cantidades entre corchetes en la Eq. (A.15) son escalares Lorentz y por lo tanto pueden ser evaluados en cualquier sistema de referencia.

A partir de la amplitud de transición antes calculada podemos hallar la sección eficaz de la reacción:

$$d\sigma = \frac{1}{\frac{1}{V}\frac{1}{V}}\sum_{B}\sum_{\boldsymbol{k}_f}\sum_{\boldsymbol{p}_F}\sum_{\boldsymbol{p}_B}\frac{\left|S^{(2)}\right|^2}{TV}\,. \tag{A.16}$$

Empleando la sustitución habitual

$$\sum_{\boldsymbol{p}} \to \frac{Vd\boldsymbol{p}}{(2\pi)^3}\,, \tag{A.17}$$

la sección eficaz diferencial también puede escribirse:

$$d\sigma = \sum_{B}\sum_{\boldsymbol{p}_B}\frac{1}{(2\pi)^5}\delta(energia)\left|I_V\right|^2 V^3 d\boldsymbol{k}_f\, d\boldsymbol{p}_F\,. \tag{A.18}$$

Ahora, $d\boldsymbol{k}_f = \varepsilon_f^2 d\varepsilon_f\, d\Omega_e$, donde hemos usado la aproximación ultrarrelativista para los electrones ($m_e = 0$), y $d\boldsymbol{p}_F = E_F p_F dE_F\, d\Omega_p$, entonces

$$\frac{d\sigma}{d\varepsilon_f\, d\Omega_e\, dE_F\, d\Omega_p} = \sum_{B}\sum_{\boldsymbol{p}_B}\frac{1}{(2\pi)^5}\delta(energia)\varepsilon_f^2 E_F p_F V^3\left|I_V\right|^2\,, \tag{A.19}$$

$$\left|I_V\right|^2 = \frac{e^4}{2\varepsilon_i 2\varepsilon_f}\frac{1}{Q^4}\frac{1}{V^2}\sum_{\lambda_\gamma,\lambda'_\gamma}L_{\lambda_\gamma\lambda'_\gamma}\left(J(\boldsymbol{q})\cdot\epsilon_{\lambda_\gamma}\right)\left(J^{\dagger}(\boldsymbol{q})\cdot\epsilon^{*}_{\lambda'_\gamma}\right)(-1)^{\lambda_\gamma+\lambda'_\gamma} \tag{A.20}$$

siendo $L_{\lambda\lambda'}$ el tensor léptonico:

$$\begin{aligned} L_{\lambda\lambda'} &= (\bar{u}_f\gamma_\mu u_i\epsilon_\lambda^{\mu *})\,(\bar{u}_f\gamma_\nu u_i\epsilon_{\lambda'}^{\nu *})^\dagger = (\bar{u}_f \not{\epsilon}_\lambda^* u_i)\,(\bar{u}_f \not{\epsilon}_{\lambda'}^* u_i)^\dagger \\ &= \bar{u}_f \not{\epsilon}_\lambda^* u_i \bar{u}_i \not{\epsilon}_{\lambda'}^* u_f = Tr\left\{\frac{1+h\gamma_5}{2}\not{k}_i \not{\epsilon}_{\lambda'}^* \frac{1+h\gamma_5}{2}\not{k}_f \not{\epsilon}_\lambda^*\right\} \\ &= 2\left[(k_i\cdot\epsilon_\lambda^*)\,(k_f\cdot\epsilon_{\lambda'}) + (k_i\cdot\epsilon_{\lambda'})\,(k_f\cdot\epsilon_\lambda^*) - (k_i\cdot k_f)\,(\epsilon_\lambda^*\cdot\epsilon_{\lambda'})\right] \\ &+ 2\,i\,h\,\epsilon^{\mu\nu\alpha\beta}\,(\epsilon_\lambda)^*_\mu\,(\epsilon_{\lambda'})_\nu\,(k_i)_\alpha\,(k_f)_\beta\ , \end{aligned} \tag{A.21}$$

con $\epsilon_{\mu\nu\alpha\beta}$ tensor antisimétrico definido por $\epsilon_{\mu\nu\alpha\beta}=1$ cuando (μ,ν,α,β) es una permutación par de (0,1,2,3), -1 para una permutación impar [2] y $h=\pm 1$ denota la helicidad del electrón incidente. Nótese que llamar tensor a $L_{\lambda\lambda'}$ no es debido a sus propiedades de transformación bajo el grupo de Lorentz ya que, como se puede observar, bajo ese grupo se comporta como un escalar.

Teniendo en cuenta que $e^4 = 4(2\pi)^2\alpha^2$, la sección eficaz resulta:

$$\frac{d\sigma}{d\varepsilon_f\,d\Omega_e\,dE_F\,d\Omega_p} = \frac{1}{(2\pi)^3}\sum_{\lambda_\gamma,\lambda'_\gamma}(-1)^{\lambda_\gamma+\lambda'_\gamma}\frac{\varepsilon_f}{\varepsilon_i}\,E_F p_F \frac{\alpha^2}{Q^4} L_{\lambda_\gamma\lambda'_\gamma} W_{\lambda_\gamma\lambda'_\gamma}\,, \tag{A.22}$$

siendo $W_{\lambda\lambda'}$ el tensor hadrónico,

$$W_{\lambda\lambda'} = V\sum_{\boldsymbol{p}_B}\sum_B \delta(energia)(J(\boldsymbol{q})\cdot\epsilon_\lambda)(J^\dagger(\boldsymbol{q})\cdot\epsilon^*_{\lambda'})\,. \tag{A.23}$$

Nótese que si el blanco A está completamente despolarizado, como es el caso, tenemos que añadir un sumatorio $\sum_{\bar{A}}$ en $W_{\lambda\lambda'}$. También es interesante recalcar de nuevo que el llamarlo "tensor" no está justificado por sus propiedades de transformación Lorentz si no por su doble dependendencia en los índices característicos de los vectores de polarización del fotón.

Supongamos que podamos factorizar una exponencial con los momentos de las partículas intervinientes en la corriente hadrónica como sigue [5, 6]:

$$J^\mu(\boldsymbol{y}) = \frac{1}{\sqrt{N_A V N_B V N_F V}} e^{i(\boldsymbol{p}_A-\boldsymbol{p}_B-\boldsymbol{p}_F)\cdot\boldsymbol{y}}\langle B\boldsymbol{p}_F|\hat{J}^\mu|A\rangle\,, \tag{A.24}$$

siendo N_A, N_B y N_F cierto factores de normalización de las funciones de onda de las partículas implicadas en la Eq.(A.24). Entonces, en espacio de momentos, la corriente hadrónica viene dada por:

$$J^\mu(\boldsymbol{q}) = \frac{1}{\sqrt{N_A V N_B V N_F V}}\langle B\boldsymbol{p}_F|\hat{J}^\mu|A\rangle V\delta_{\boldsymbol{q}+\boldsymbol{p}_A,\boldsymbol{p}_F+\boldsymbol{p}_B}\,. \tag{A.25}$$

Si a partir de ahora utilizamos la notación: $J^\mu = \langle B\boldsymbol{p}_F|\hat{J}^\mu|A\rangle$, resulta que la contracción de la corriente hadrónica con los vectores de polarización del fotón puede escribirse como:

$$(J(\boldsymbol{q})\cdot\epsilon_\lambda)(J^\dagger(\boldsymbol{q})\cdot\epsilon^*_{\lambda'}) = \frac{V^2}{N_A V N_B V N_F V}\,(J\cdot\epsilon_\lambda)\left(J^\dagger\cdot\epsilon^*_{\lambda'}\right)\delta_{\boldsymbol{q}+\boldsymbol{p}_A,\boldsymbol{p}_F+\boldsymbol{p}_B}\,, \tag{A.26}$$

lo que implica que el tensor hadrónico de la Eq. (A.23) es

$$W_{\lambda\lambda'} = \sum_{\bar{A}}\sum_{B}\sum_{\boldsymbol{p}_B}\frac{1}{N_{ABF}}\,(J\cdot\epsilon_\lambda)\left(J^\dagger\cdot\epsilon^*_{\lambda'}\right)\delta_{\boldsymbol{q}+\boldsymbol{p}_A,\boldsymbol{p}_F+\boldsymbol{p}_B}\delta(energia) \tag{A.27}$$

donde $N_{ABF} = N_A N_B N_F$. Pero como,

$$\sum_{\boldsymbol{p}}\delta_{\boldsymbol{p},\boldsymbol{p}'} = \int d\boldsymbol{p}\,\delta^3(\boldsymbol{p}-\boldsymbol{p}') \tag{A.28}$$

resulta:

$$W_{\lambda\lambda'} = \sum_{\bar{A},B}\frac{1}{N_{ABF}}\int d\boldsymbol{p}_B\,(J\cdot\epsilon_\lambda)\left(J^\dagger\cdot\epsilon^*_{\lambda'}\right)\delta^4(momentum) \tag{A.29}$$

con $\delta^4(momentum) = \delta^4(P_A + q - P_F - P_B)$. Usando la $\delta^4(momentum)$ en el sistema LAB, podemos realizar la integral en el momento del núcleo residual quedando:

$$W_{\lambda\lambda'} = \sum_{\bar{A},B}\frac{1}{N_{ABF}}(J\cdot\epsilon_\lambda)(J^\dagger\cdot\epsilon^*_{\lambda'})\,\delta(M_A+\omega-E_F-E_B) \tag{A.30}$$

y $\boldsymbol{p}_B = \boldsymbol{q} - \boldsymbol{p}_F$ una vez efectuada la integral, manifestándose la conservación de momento en el vértice hadrónico.

En la expresión para la sección eficaz del proceso que estamos teniendo en cuenta podemos extraer un término correspondiente a la sección eficaz de Mott [1], σ_M, definiendo un nuevo tensor leptónico $\ell_{\lambda\lambda'}$ como sigue:

$$L_{\lambda\lambda'} = 4\varepsilon_i\varepsilon_f\cos^2\left(\frac{\theta_e}{2}\right)\ell_{\lambda\lambda'}\,. \tag{A.31}$$

Como se cumple que el cuadrimomento transferido Q^2 es igual a

$$Q^2 = -(k_i-k_f)_\mu(k_i-k_f)^\mu = 2(k_i\cdot k_f) = 2\varepsilon_i\varepsilon_f(1-\cos\theta_e) = 4\varepsilon_i\varepsilon_f\sin^2\left(\frac{\theta_e}{2}\right)\,, \tag{A.32}$$

entonces

$$\frac{\varepsilon_f}{\varepsilon_i}\frac{\alpha^2}{Q^4}4\varepsilon_i\varepsilon_f\cos^2\left(\frac{\theta_e}{2}\right) = \frac{\varepsilon_f}{\varepsilon_i}\alpha^2\frac{4\varepsilon_i\varepsilon_f\cos^2\left(\frac{\theta_e}{2}\right)}{16\varepsilon_i^2\varepsilon_f^2\sin^4\left(\frac{\theta_e}{2}\right)} = \frac{\alpha^2\cos^2\left(\frac{\theta_e}{2}\right)}{4\varepsilon_i^2\sin^4\left(\frac{\theta_e}{2}\right)} = \sigma_M\,, \tag{A.33}$$

y la sección eficaz puede escribirse de forma más compacta como:

$$\frac{d\sigma}{d\varepsilon_f\,d\Omega_e\,dE_F\,d\Omega_p} = \frac{E_F p_F}{(2\pi)^3}\sigma_M\sum_{\lambda_\gamma,\lambda'_\gamma}(-1)^{\lambda_\gamma+\lambda'_\gamma}\,\ell_{\lambda_\gamma\lambda'_\gamma}W_{\lambda_\gamma\lambda'_\gamma}\,. \tag{A.34}$$

Si las condiciones cinemáticas son tales que garantizan que el núcleo residual no se ha fragmentado y se encuentra en un estado de energía bien definida, entonces $\sum_B$ solo da un valor y por tanto $\delta(M_A+\omega-E_F-E_B)$ puede ser usada para integrar en E_F, obteniéndose el factor de recoil [7]:

$$f_{rec} = \int dE_F\, \delta(M_A+\omega-E_F-E_B) = \left|1-\frac{E_F}{E_B}\frac{\boldsymbol{p}_B\cdot\boldsymbol{p}_F}{p_F^2}\right|^{-1} \tag{A.35}$$

Lo que implica que la sección eficaz diferencial es

$$\frac{d\sigma}{d\varepsilon_f\, d\Omega_e\, dE_F\, d\Omega_p} = \frac{E_F p_F}{(2\pi)^3}\sigma_M f_{rec} \sum_{\lambda_\gamma,\lambda'_\gamma} (-1)^{\lambda_\gamma+\lambda'_\gamma}\, \ell_{\lambda_\gamma\lambda'_\gamma} W_{\lambda_\gamma\lambda'_\gamma}\,, \tag{A.36}$$

con

$$W_{\lambda\lambda'} = \sum_{\bar{A}} \frac{1}{N_{ABF}} (J\cdot\epsilon_\lambda)(J^\dagger\cdot\epsilon^*_{\lambda'})\,. \tag{A.37}$$

Debido a que los tensores $L_{\lambda\lambda'}$ y $W_{\lambda\lambda'}$ son hermíticos y por tanto satisfacen que

$$L_{\lambda\lambda'} = L^*_{\lambda'\lambda}\,, \tag{A.38}$$

$$W_{\lambda\lambda'} = W^*_{\lambda'\lambda} \tag{A.39}$$

y además también se cumple que

$$\epsilon^{\mu*}_\lambda = (-1)^\lambda \epsilon^\mu_{-\lambda}\,, \tag{A.40}$$

podemos efectuar una serie de reducciones adicionales en la Eq. (A.36). Para ello separamos en dos sumandos el término $L_{\lambda\lambda'}$. El primero independiente de la helicidad del electrón y el segundo dependiente de ella,

$$L_{\lambda\lambda'} = L^u_{\lambda\lambda'} + hL^h_{\lambda\lambda'}\,, \tag{A.41}$$

siendo sus expresiones explícitas:

$$L^u_{\lambda\lambda'} = 2\left[(k_i\cdot\epsilon^*_\lambda)(k_f\cdot\epsilon_{\lambda'}) + (k_i\cdot\epsilon_{\lambda'})(k_f\cdot\epsilon^*_\lambda) - (k_i\cdot k_f)(\epsilon^*_\lambda\cdot\epsilon_{\lambda'})\right] \tag{A.42}$$

$$L^h_{\lambda\lambda'} = 2\,i\,\epsilon^{\mu\nu\alpha\beta}\,(\epsilon_\lambda)^*_\mu\,(\epsilon_{\lambda'})_\nu\,(k_i)_\alpha\,(k_f)_\beta \tag{A.43}$$

Se puede ver que estos tensores satisfacen las siguientes propiedades:

$$L^u_{-\lambda,-\lambda'} = (-1)^{\lambda+\lambda'} L^{u*}_{\lambda\lambda'} \tag{A.44}$$

$$L^h_{-\lambda,-\lambda'} = (-1)^{\lambda+\lambda'} L^{h*}_{\lambda\lambda'}\,. \tag{A.45}$$

Tenemos por tanto solo seis independientes, de los cuales nos quedamos con: L^u_{00}, L^u_{01}, L^u_{11}, L^u_{1-1}, L^h_{01}, L^h_{11}. Es sencillo ver que todos ellos son reales y que el resto de los términos $L^{u,h}_{\lambda\lambda'}$ o son cero o pueden obtenerse a partir de éstos.

Explícitamente, en el sistema LAB, usando los ϵ^μ_λ definidos en las Eqs. (A.11-A.13) y teniendo en cuenta que los momentos del electrón incidente y dispersado vienen dados por:

$$\boldsymbol{k}_i = \frac{\varepsilon_i}{q}(\varepsilon_f \sin\theta_e, 0, \varepsilon_i - \varepsilon_f \cos\theta_e)\,, \tag{A.46}$$

$$\boldsymbol{k}_f = \frac{\varepsilon_f}{q}(\varepsilon_i \sin\theta_e, 0, \varepsilon_i \cos\theta_e - \varepsilon_f)\,, \tag{A.47}$$

resultan las siguientes expresiones para las seis componentes antes elegidas para el tensor leptónico:

$$\ell^u_{00} = \frac{Q^2}{q^2} \tag{A.48}$$

$$\ell^u_{01} = \frac{Q}{\sqrt{2}\,q}\sqrt{\frac{Q^2}{q^2} + \tan^2\frac{\theta_e}{2}} \tag{A.49}$$

$$\ell^u_{11} = \frac{Q^2}{2q^2} + \tan^2\frac{\theta_e}{2} \tag{A.50}$$

$$\ell^u_{1-1} = -\frac{Q^2}{2q^2} \tag{A.51}$$

$$\ell^h_{01} = \frac{Q}{\sqrt{2}\,q}\tan\frac{\theta_e}{2} \tag{A.52}$$

$$\ell^h_{11} = \tan\frac{\theta_e}{2}\sqrt{\frac{Q^2}{q^2} + \tan^2\frac{\theta_e}{2}} \tag{A.53}$$

Por tanto, usando que solo hay seis $\ell_{\lambda\lambda'}$ independientes y que los $W_{\lambda\lambda'}$ son hermíticos, resulta

$$\begin{aligned}\sum_{\lambda,\lambda'}(-1)^{\lambda+\lambda'}\ell_{\lambda\lambda'}W_{\lambda\lambda'} &= \ell^u_{00}W_{00} + \ell^u_{11}\,(W_{11} + W_{-1-1}) + \ell^u_{1-1}2Re\,(W_{1-1}) \\ &- \ell^u_{01}2Re\,(W_{01} - W_{0-1}) + h\ell^h_{11}\,(W_{11} - W_{-1-1}) \\ &- h\ell^h_{01}2Re\,(W_{01} + W_{0-1})\end{aligned} \tag{A.54}$$

y la sección eficaz diferencial de la reacción $A(\vec{e},e'\vec{p})B$ podemos escribirla:

$$\begin{aligned}\frac{d\sigma}{d\varepsilon_f d\Omega_e d\Omega_p} &= \frac{E_F p_F}{(2\pi)^3}\sigma_M f_{rec}\left[v_L\tilde{R}^L + v_T\tilde{R}^T + v_{TT}\tilde{R}^{TT} + v_{TL}\tilde{R}^{TL}\right. \\ &+ \left. h\left(v_{T'}\tilde{R}^{T'} + v_{TL'}\tilde{R}^{TL'}\right)\right]\end{aligned} \tag{A.55}$$

donde hemos utilizado los factores cinemáticos v_α, $\alpha = L, T, TT, TL, T', TL'$ relacionados con los $\ell^{u,h}_{\lambda\lambda'}$ como sigue:

$$v_L = \frac{Q^2}{q^2}\ell^u_{00} = \frac{Q^4}{q^4} \tag{A.56}$$

$$v_T = \ell^u_{11} = \frac{Q^2}{2q^2} + \tan^2\frac{\theta_e}{2} \tag{A.57}$$

$$v_{TT} = \ell^u_{1-1} = -\frac{Q^2}{2q^2} \tag{A.58}$$

$$v_{TL} = \frac{Q}{q}\ell^u_{01} = \frac{Q^2}{\sqrt{2}\,q^2}\sqrt{\frac{Q^2}{q^2} + \tan^2\frac{\theta_e}{2}} \tag{A.59}$$

$$v_{T'} = \ell^h_{11} = \tan\frac{\theta_e}{2}\sqrt{\frac{Q^2}{q^2} + \tan^2\frac{\theta_e}{2}} \tag{A.60}$$

$$v_{TL'} = \frac{Q}{q}\ell^h_{01} = \frac{Q^2}{\sqrt{2}\,q^2}\tan\frac{\theta_e}{2}\,. \tag{A.61}$$

Las funciones de respuesta hadrónicas se obtienen a partir del tensor $W_{\lambda\lambda'}$ del siguiente modo:

$$\tilde{R}^L = \frac{q^2}{Q^2}W_{00} \tag{A.62}$$

$$\tilde{R}^T = W_{11} + W_{-1-1} \tag{A.63}$$

$$\tilde{R}^{TT} = 2Re\,(W_{1-1}) \tag{A.64}$$

$$\tilde{R}^{TL} = -\frac{q}{Q}2Re\,(W_{01} - W_{0-1}) \tag{A.65}$$

$$\tilde{R}^{T'} = W_{11} - W_{-1-1} \tag{A.66}$$

$$\tilde{R}^{TL'} = -\frac{q}{Q}2Re\,(W_{01} + W_{0-1}) \tag{A.67}$$

Se puede observar que las funciones de respuesta hadrónicas arriba definidas dependen del ángulo azimutal ϕ_F. Es más usual expresar explícitamente esta dependencia en ϕ_F de la sección eficaz, extrayéndola de las funciones de respuesta. Para ello elegimos un nuevo sistema de ejes $\{\boldsymbol{u}'_x, \boldsymbol{u}'_y, \boldsymbol{u}'_z\}$ definidos como:

$$\boldsymbol{u}'_y = \frac{\boldsymbol{q}\times\boldsymbol{p}_F}{|\boldsymbol{q}\times\boldsymbol{p}_F|} = -\sin\phi_F\,\boldsymbol{u}_x + \cos\phi_F\,\boldsymbol{u}_y \tag{A.68}$$

$$\boldsymbol{u}'_z = \boldsymbol{u}_z \tag{A.69}$$

$$\boldsymbol{u}'_x = \boldsymbol{u}'_y \times \boldsymbol{u}'_z = \cos\phi_F\,\boldsymbol{u}_x + \sin\phi_F\,\boldsymbol{u}_y \tag{A.70}$$

Como se puede ver una rotación relaciona ambos sistema de ejes. Ir de un sistema de ejes a otro sólo implica un cambio en las componentes transversales. En particular, es sencillo comprobar que los vectores de polarización del fotón cumplen:

$$\epsilon'_\lambda = e^{i\lambda\phi_F}\epsilon_\lambda\,, \tag{A.71}$$

donde hemos denotado ϵ'_λ a los vectores de polarización del fotón referidos respecto al nuevo sistema de ejes de coordenadas. Sabemos que:

$$W_{\lambda\lambda'} = \sum_{\overline{A}} \frac{1}{N_{ABF}} (J\cdot\epsilon_\lambda (J\cdot\epsilon_{\lambda'})^* \equiv \sum_{\overline{A}} \frac{1}{N_{ABF}} \mathcal{R}_{\lambda\lambda'} \tag{A.72}$$

obsérvese que $\mathcal{R}_{\lambda\lambda'}$ es un escalar Lorentz lo cual implica que tiene el mismo valor en cualquier sistema de referencia. En particular, se satisface la siguiente propiedad:

$$\mathcal{R}_{\lambda\lambda'} = (J\cdot\epsilon_\lambda)\,(J\cdot\epsilon_{\lambda'})^* = (J'\cdot\epsilon'_\lambda)\,(J'\cdot\epsilon'_{\lambda'})^* = e^{i\phi_F(\lambda-\lambda')}\,(J'\cdot\epsilon_\lambda)\,(J'\cdot\epsilon_{\lambda'})^*\,. \tag{A.73}$$

Hemos factorizado la dependencia en ϕ_F de los $\mathcal{R}_{\lambda\lambda'}$. Denotando con minúsculas las respuestas independientes de ϕ_F, se pueden establecer las siguientes relaciones:

$$\tilde{R}^L = r^L \tag{A.74}$$

$$\tilde{R}^T = r^T \tag{A.75}$$

$$\tilde{R}^{TT} = r^{TT\,(I)}\cos 2\phi_F + r^{TT\,(II)}\sin 2\phi_F \tag{A.76}$$

$$\tilde{R}^{TL} = r^{TL\,(I)}\cos\phi_F + r^{TL\,(II)}\sin\phi_F \tag{A.77}$$

$$\tilde{R}^{T'} = r^{T'} \tag{A.78}$$

$$\tilde{R}^{TL'} = r^{TL'\,(I)}\cos\phi_F + r^{TL'\,(II)}\sin\phi_F \tag{A.79}$$

teniendo en cuenta que tanto las $\tilde{R}^\alpha$ como las r^α dependen del espín del nucleón saliente. Asimismo, también vamos a poder separar por un lado la contribución de las funciones de respuestas independientes de la polarización del protón final, de las que si dependen de ésta. Dado que el protón tiene espín $\frac{1}{2}$ y por tanto la dependencia en la sección eficaz del espín del protón saliente ha de ser lineal, se puede demostrar que podemos descomponer las funciones de respuesta independientes de ϕ_F como sigue [4, 8, 9]:

$$r^L = \frac{1}{2}\left(R^L + R^L_n \widehat{S}_n\right) \tag{A.80}$$

$$r^T = \frac{1}{2}\left(R^T + R^T_n \widehat{S}_n\right) \tag{A.81}$$

$$r^{TT\,(I)} = \frac{1}{2}\left(R^{TT} + R_n^{TT}\widehat{S}_n\right) \tag{A.82}$$

$$r^{TT\,(II)} = \frac{1}{2}\left(R_l^{TT}\widehat{S}_l + R_s^{TT}\widehat{S}_s\right) \tag{A.83}$$

$$r^{TL\,(I)} = \frac{1}{2}\left(R^{TL} + R_n^{TL}\widehat{S}_n\right) \tag{A.84}$$

$$r^{TL\,(II)} = \frac{1}{2}\left(R_l^{TL}\widehat{S}_l + R_s^{TL}\widehat{S}_s\right) \tag{A.85}$$

$$r^{T'} = \frac{1}{2}\left(R_l^{T'}\widehat{S}_l + R_s^{T'}\widehat{S}_s\right) \tag{A.86}$$

$$r^{TL'\,(I)} = \frac{1}{2}\left(R_l^{TL'}\widehat{S}_s + R_s^{TL}\widehat{S}_s\right) \tag{A.87}$$

$$r^{TL'\,(II)} = \frac{1}{2}\left(R^{TL'} + R_n^{TL'}\widehat{S}_n\right) \tag{A.88}$$

donde las R^α son las funciones de respuesta independientes de ϕ_F y de la polarización del protón final y las R_k^α son las funciones de respuesta polarizadas a lo largo de las tres direcciones determinadas por los vectores unitarios:

$$\boldsymbol{l} = \frac{\boldsymbol{p}_F}{p_F}\,,\quad \boldsymbol{n} = \frac{\boldsymbol{q}\times\boldsymbol{p}_F}{|\boldsymbol{q}\times\boldsymbol{p}_F|}\,,\quad \boldsymbol{s} = \boldsymbol{n}\times\boldsymbol{l}\,. \tag{A.89}$$

$\widehat{S}_k$ denota la componente a lo largo de la dirección k del espín $(\boldsymbol{s}_F)_R$ del nucleón final, en el sistema de referencia en el que dicho nucleón está en reposo.

Bibliografía

[1] F. Halzen and A.D. Martin, *Quarks & Leptons: An Introductory Course in Modern Particle Physics* (John Wiley & Sons, New York, 1984).

[2] G. Sterman, *An Introduction to Quantum Field Theory* (Cambridge University Press, 1993).

[3] J.D. Bjorken and S.D. Drell, *Relativistic Quantum Mechanics* (McGraw-Hill, New York, 1964).

[4] V. Dmitrasinovic, F. Gross, Phys. Rev. C **40**, 2479 (1989).

[5] J.M. Udías, Ph.D. thesis, CSIC, Madrid, 1993.

[6] J.M. Udías, *Lepton-Nucleus Scatering in a Relativistic Framework: Electromagnetic and Neutral Current Case*, informe de uso interno, NIKHEF 95-P12, Amsterdam, 1995.

[7] J.J. Kelly, Adv. Nucl. Phys. **23**, 75 (1996).

[8] A. Picklesimer and J.W. Van Orden, Phys. Rev. C **35**, 266 (1987)

[9] A. Picklesimer and J.W. Van Orden, Phys. Rev. C **40**, 290 (1989).

Esta tesis ha sido posible gracias a la beca predoctoral que me concedió la Consejería de Educación de la Comunidad de Madrid